WYDZIAŁ FIZYKI
UNIWERSYTET WARSZAWSKI

UNIVERSITY OF WARSAW
FACULTY OF PHYSICS
DEPARTMENT OF PHOTONICS

STUDY OF SOLITONIC STEERING OF FEMTOSECOND PULSES IN SOFT GLASS DUAL-CORE OPTICAL FIBERS

Doctoral Dissertation of:
Mattia Longobucco

Supervisor:
prof. dr hab. Ryszard Buczyński

Assistant supervisor:
dr. Ignác Bugár

November 2021

Abstract

In this dissertation, a study of pulse energy-controlled solitonic steering of femtosecond pulses in highly nonlinear dual-core fibers is presented. It targets a specific area of ultrafast nonlinear fiber optics and also the general soliton theory in coupled waveguides, with high application potential in all-optical signal processing. The goal of the dissertation is to prove that specially designed dual-core fibers made of soft-glass materials support an energy-driven switching of femtosecond pulses. The fiber is made of a pair of two thermally matched glasses: a lead silicate (highly nonlinear) and borosilicate glasses for the cores and cladding, respectively. They have high contrast of the refractive indices at the level of 0.4 in the near infrared. The physical principle that allows the switching performance is the nonlinear self-trapping of high-order solitons, which is induced by the nonlinear Kerr effect in the core glass.

The first part of the dissertation shows the numerical study of the fiber structure optimization in terms of its dispersion and coupling properties. Two alternatives are studied: all-solid photonic crystal dual-core fiber and all-solid dual-core fiber with homogeneous cladding. Then, the numerical simulation results of the nonlinear propagation of femtosecond pulses with energies in the picojoule range are presented. The goal is to determine the wavelength and temporal width of hyperbolic secant pulses which support the optimal switching performance. They are in the range 1400 - 1800 nm and 75 - 150 fs, respectively. The optimal switching performance is identified in terms of highest switching contrast parameter, which indicates the capability of the excited pulse to exchange core during propagation. The optimal switching performance is predicted for a 43 mm all-solid dual-core fiber with simple cladding and 3.2 µm distance between the cores. The excitation pulses have 1500 nm wavelength, 75 fs temporal width and in-coupled energies at the level of only 20 pJ. The highest switching contrast is 46 dB calculated in the time window of the ultrashort pulses. Moreover, the predicted switching performance is uniform over 200 nm in the spectral domain. Afterwards, the dissertation proceeds with a brief description of the fabrication process of the optimized dual-core fiber. It is based on the stack-and-draw method. Then, the structure of the fabricated fiber is analyzed in terms of dual-core asymmetry. It is related to the difference between the shapes of the two cores. It is always present after the fabrication process because of the intrinsic thermodynamic fluctuation of the drawing parameters. Therefore, its influence on the coupling properties of the fiber, on the ultrafast pulse propagation, as well on the switching performance, is examined.

The second part of the dissertation presents the experimental results of self-switching, i.e. energy-driven nonlinear switching, using femtosecond pulses at wavelength of 1560 and 1700 nm. Two sets of all-solid dual-core fibers with the optimized structural parameters and different levels of dual-core symmetry were used. The following outcomes were demonstrated: 1) reversible switching performance of 1560 nm sub-nJ pulses, with soliton-like character (confirmed by numerical simulations); 2) switching performance at 1700 nm of pulses with 1-3 nJ input energy; it shows a two-time exchange of the core with a maximal switching contrast of 16.7 dB and it is broadband in a spectral window of 150 nm. In the frame of the study of the fiber length effect, the highest switching contrast of 20.1 dB at 35 mm fiber length is demonstrated at 1560 nm. The switching performance is observed in a broadband spectral range between 1450 and 1650 nm. In the case of 1700 nm excitation wavelength, the highest switching contrast is 20.6 dB at 40 mm. It is accompanied by multiple exchanges of the dominant core, which is a strong indication of the soliton-based switching process. Both reported outcomes rely on the lower dual-core asymmetry of the all-solid fiber than the one of the standard air-hole dual-core fiber, which was investigated previously.

Finally, in the last part of the dissertation a novel switching approach is presented: the so-called dual wavelength approach. It is based on the cross-interaction between two synchronized femtosecond pulses with different wavelengths: *signal* (1560 nm) and *control* (1030 nm). The adjustment of the control pulse energy enables the signal pulse to switch between the cores. The novel switching approach is based on the physical process of nonlinear balancing of dual-core asymmetry: the control pulse induces a group velocity reduction of the signal pulse, which finally switches between the cores. Switching contrasts of more than 25 dB and a shift of the signal central wavelength of only 3 nm were recorded using fibers with optimized lengths below only 20 mm. These results were confirmed also by the spectra recordings at the fiber output.

Thanks to the improved dual-core symmetry, the fiber design without microstructure and fabricated with the all-solid approach allows an efficient switching capability of optical soliton-like pulses. Moreover, it can have some practical applications in optical communications as fiber-based, low-power, compact and simple all-optical switching device.

Streszczenie

Badanie solitonowego sterowania impulsami femtosekundowymi w światłowodach dwurdzeniowych wykonanych ze szkieł wieloskładnikowych

Niniejsza rozprawa doktorska zawiera badania sterowanego energią solitonowego prze-łączania impulsów femtosekundowch w dwurdzeniowych światłowodach o wysokiej nieliniowości optycznej. Praca dotyczy zagadnień nieliniowej, światłowodowej optyki ultraszybkiej oraz ogólnie do teorii solitonów w sprzężonych falowodach i zawiera duży potencjał aplikacyjny w dziedzinie całkowicie optycznego przetwarzania sygnałów. Celem rozprawy jest dowiedzenie, ze specjalnie zaprojektowane światłowody dwurdzeniowe ze szkieł miękkich mogą posłużyć jako ośrodki do sterowanego energią przełączania impulsów femtosekundowych. Światłowód jest wykonany z pary szkieł o dopasowanych właściwościach temperaturowych: jest to szkło ołowiowo-krze-mianowe (silnie nieliniowe) oraz szkło borokrzemianowe, użyte do wytworzenia od-powiednio rdzeni optycznych oraz płaszcza świa-tłowodowego. Szkła mają bardzo duży kontrast współczynników załamania na poziomie 0,4 w zakresie spektralnym bliskiej podczerwieni. U podstaw fizycznych obserwowanych zjawisk przełączania leży mechanizm samopułapkowania solitonów wysokiego rzędu, które jest wymuszane przez nieliniowy efekt Kerra w szkle rdzeni optycznych.

Pierwsza część rozprawy została poświęcona badaniom teoretycznym (symulacjom numerycznym) optymalizacji struktury światłowodów w kontekście ich dyspersji i właściwości sprzęgania. Badane były dwa rodzaje światłowodów: w pełni szklany fotoniczny światłowód dwurdzeniowy oraz światłowód dwurdzeniowy z jednorodnym pła-szczem szklanym. Następnie zaprezentowane zostały wyniki symulacji propagacji nie-liniowej impulsów femtosekundowych o energii w zakresie piko dżuli. Celem prac było określenie długości fali oraz czasu trwania impulsów o kształcie secansa hiperbolicznego dla osiągniecia optymalnego przełączania. Otrzymano jako optymalne wyniki dla impulsów w zakresie widma 1400 – 1800 nm oraz długości 75-150 fs. Optymalne przełączania definiowano przy pomocy kryterium najwyższego kontrastu przełączania, które wskazuje na możliwość zmiany rdzenia, w którym propaguje się impuls. Optymalne przełączanie zostało przewidziane w symulacjach dla 43 mm długości całkowicie szklanego, dwurdzeniowego świa-tłowodu z jednorodnym płaszczem oraz odstępem pomiędzy rdzeniami wynoszącym 3,2 µm. Rozważane impulsy wprowadzane do świa-tłowodu miały środkową długość fali 1500 nm i czas trwania 75 fs, a energia wprzęgnięta do włókna jest na poziomie 20 pJ. Największy kontrast przełączania 46 dB jest obliczony w oknie czasowym ultrakrótkich impulsów. Ponadto, osiągnięta sprawność przełączania pozostaje utrzymana w zakresie spektralnym 200 nm. Następnie, w rozpra-wie przedstawiono zwięzły opis procesu wytwarzania światłowodu o zoptymalizowanej strukturze dwurdzeniowej. Proces ten wykorzystuje metodę mozaikową. W kolejnej części rozprawy analizowana jest struktura wytworzonego włókna w kontekście asyme-trii dwurdzeniowej, związanej z różnicą rozmiarów pomiędzy rdzeniami. Niewielkie różnice w symetrii włókna dwurdzeniowego są zawsze obecne po procesie technologicznym w wyniku nieodłącznych fluktuacji warunków termodynamicznych podczas procesu wyciągania włókna. W dalszej części pracy badany został wpływ tych zjawisk na właściwości sprzęgania we włóknie, na propagację impulsów ultraszybkich oraz na sprawność przełączania.

Druga część rozprawy zawiera wyniki prac eksperymentalnych związanych z obserwowaniem samoprzełączania, tj. przełączania nieliniowego sterowanego energią, przy użyciu impulsów femtosekundowych o środkowej długości fali 1560 nm oraz 1700 nm. Do badań wykorzystane zostały dwa w pełni szklane światłowody dwurdzeniowe o zoptymalizowanych parametrach struktury oraz o różnym stopniu asymetrii dwurdzeniowej. Zademonstrowano dwa efekty: 1) odwracalne przełączanie impulsów 1560 nm o energii poniżej 1 nJ, zachowujące charakter solitonu (potwierdzone wynikami symulacji numerycznych); 2) przełączanie na długości fali 1700 nm impulsów o energii wejściowej 1-3 nJ, które wykazuje możliwość dwukrotnego przełączenia pomiędzy rdzeniami z maksymalnym kontrastem przełączania 16,7 dB w zakresie spektralnym o szerokości 150 nm. W badaniach wpływu długości światłowodu na sprawność przełączania, największy kontrast, na poziomie 20,1 dB, osiągnięto dla włókna o długości 35 mm i na środkowej długości fali 1560 nm. Przełączanie obserwowane było w zakresie spektralnym od 1450 nm do 1650 nm. W przypadku pobudzania na długości fali 1700 nm, największy kontrast osiągnięto na poziomie 20,6 dB na długości włókna 40 mm. Towarzyszy temu wielokrotna zmiana prowadzącego rdzenia, co stanowi silne wskazanie na proces o charakterze solitonowym. Wyniki zostały uzyskane dla jednorodnego włókna o mniejszej dwurdzeniowej asymetrii, niż w przypadku standardowych włókien fotonicznych z płaszczem szklano-powietrznym, które były badane we wcześniejszych pracach.

W ostatniej części rozprawy zostało opisane nowatorskie podejście do przełączania wykorzystujące dwie długości fali. Oparte jest ono na skrośnym oddziaływaniu dwóch zsynchronizowanych impulsów na różnych długościach fali: sygnałowej (1560 nm) i sterującej (1030 nm) . Zmiana energii impulsu sterującego umożliwia przełączenie impulsu sygnałowego pomiędzy rdzeniami światłowodu. Zaobserwowany został kontrast przełączania powyżej 25 dB przy jednoczesnej zmianie środkowej długości fali o zaledwie 3 nm w światłowodach o zoptymalizowanej długości 20 mm. Wyniki zostały potwierdzone również w pomiarach widm na wyjściu światłowodu.

Dzięki poprawionej symetrii dwurdzeniowej, światłowód bez mikrostruktury i wytworzony w przy zastosowaniu jednorodnego płaszcza, pozwala na wydajne przełączanie impulsów optycznych o cechach solitonu. Otrzymane wyniki mogą mieć zastosowania praktyczne w komunikacji optycznej do budowy kompaktowych światłowodowych całkowicie optycznych przełączników o niewielkim zapotrzebowaniu na moc.

Objectives and claims

The main purpose of this dissertation is the study of input energy-driven ultrafast steering of solitonic pulses in dual-core fibers (DCFs). This dissertation would address some fundamental questions and contribute to the field of generation of complex spatial and temporal solitary waves in coupled waveguides. The self-trapping phenomenon of femtosecond solitonic pulses called light bullets has been already demonstrated experimentally in optical fiber arrays [1]. In addition, a broadband and efficient steering based on controllable self-trapping of higher-order solitons in a highly nonlinear air-glass dual-core (DC) photonic crystal fiber (PCF) was predicted by P. Stajanča and I. Bugár at 1550 nm [2]. The numerical results obtained in this study predicted sub-nanojoule switching input energies and efficient soliton switching with femtosecond hyperbolic secant pulse at 1550 nm (central wavelength of the long-distance optical telecommunication C-band). However, this successful scenario has been never demonstrated experimentally because the manufactured PCF structure did not have sufficient initial structural symmetry and the coupling efficiency between the cores was not high enough [3].

It could be possible to overcome these limitations by considering a PCF structure which is totally all-solid. Such fiber avoids air holes inside the structure and have both the cores and the cladding made of special multicomponent soft glasses. This approach has potential to achieve higher level of structural symmetry at simultaneous preservation of the anomalous dispersion regime required for the solitonic propagation. Therefore, it can support an effective steering of ultrashort pulses between the two fiber cores, requiring energies of the input pulses of only few nanojoules. Nevertheless, only a limited number of scientific works about the optimization of an all-solid DCF for such purpose could be found in the scientific literature [2, 4]. Moreover, only a few experimental works on the topic has been published [3, 5].

The dissertation focuses on the study of solitonic steering of femtosecond pulses in soft glass DCFs. This property would eventually lay the foundations for the establishment of bi-stable state for optical pulses. The result is that pulses could propagate uniquely through one of the two cores in dependence of their input energy level. To do that, I studied the properties of a totally all-solid DCF, which is made of two thermally matched soft glasses with high contrast of refractive index region and enhanced nonlinear properties in the near infrared spectral region. Due to its all-glass structure, it has potential to improve the symmetry between the two cores and, therefore, overcoming the limits shown in [3]. All the mentioned properties of the fiber could be advantageous for the demonstration of femtosecond pulse-switching at the sub-nJ level of the in-coupled pulse energies in the solitonic propagation regime. The research was carried out under the project No. 2016/23/P/ST7/02233 - POLONEZ 3 program of National Science Centre of Poland (NCN) *All-optical steering of solitonic signals in all-solid dual-core photonic crystal fibers* at Łukasiewicz Research Network - Institute of Microelectronics and Photonics (Ł-IMIF) in Warsaw, leaded by Dr. Ignác Bugár, and it is currently continued under a new NCN project, with No. 2019/33/N/ST7/03142 and title *Self-trapped solitonic switching of ultrafast pulses in dual-core high index contrast optical fibers* (PRELUDIUM 17 program), where I am the Personal Investigator.

In the scope of the thesis, I present both the numerical and the experimental studies conducted with a new DCF, which was fabricated at Ł-IMIF. The fiber is made with a pair of soft glasses synthesized in-house and using the stack-&-draw technique. The goal of the dissertation is to experimentally demonstrate a high contrast switching performance of femtosecond pulses and investigate their propagation evolution in DCF I optimized for the purpose. The whole study is also supported by numerical simulations, performed considering two fiber structures: a DCF with perfectly symmetric cores and another one with asymmetric cores, which perturbs the soliton steering effect. The numerical framework involved the use of the software Lumerical, for the identification of the linear optical properties of the fiber and Matlab, to solve the Coupled generalized nonlinear Shrödinger equations (CGNLSEs) and simulate the pulse propagation in the nonlinear regime. The experimental phase was conducted at the FUW using a C-Fiber Menlo laser at 1560 nm, and at the Photonic Institute of Technical University of Vienna (PI-TUW), in collaboration with the group of prof. Andrius Baltuška, using an amplifier-OPA system tunable in the range 1500 - 1900 nm.

Dissertation theses

Taking lessons from the numerical and experimental studies conducted on the air-glass PCF and also of the well-consolidated manufacturing technology of PCF, this dissertation has the objective to investigate solitonic steering of femtosecond pulses in a novel all-solid DCF. The claims that I aim to address with this study are the following:

- **First claim**: *The soft-glass all-solid DCF supports nonlinear controllable self-trapping of femtosecond solitons with central wavelength in the near-infrared (NIR) region, in particular at 1560 nm (optical telecom C-band)*;

- **Second claim**: *The optimized DCF allows a high-contrast switching performance enabled by the self-trapping phenomenon in a broad range of excitation wavelengths up to 1700 nm*;

- **Third claim**: *In the fabricated dual-core fiber, the influence of asymmetry on the coupling efficiency can be mitigated by taking advantage of nonlinear Kerr-effect introduced by femtosecond pulses and by the all-solid soft-glass approach. Consequently, the switching performance can be improved in a broadband wavelength* *range, when pumped at 1560 and 1700 nm wavelengths.*

In order to address these claims, the purposed strategies are the following:

1. To verify the **first claim**, I present a systematic numerical study of ultrafast nonlinear directional coupler (NLDC) performance based on soliton self-trapping in a new all-solid DCF. The fiber is made of two special multicomponent glasses synthesized at Ł-IMIF.

   First, I analyze numerically the linear characteristics of the fiber, such as dispersion profile and coupling properties. Then, I simulate the nonlinear propagation of picojoule level femtosecond pulses with the help of Lumerical and Matlab softwares. The nonlinear propagation has been simulated with an extended numerical model based on a system of CGNLSE. The aim is to study the steering performance of light pulses with central wavelengths between 1400 and 1800 nm, and pulse widths between 75 and 150 fs, which are in accordance to the commercially available lasers used for telecommunication applications. As second step, the optimized fiber was fabricated at Ł-IMIF in Warsaw. I rely also on the fiber manufacturing background of the institution, which has potential to bring further improvement of the DCF structural symmetry.

   As main proof of the first claim, I investigate the switching performance experimentally. I analyze the DCF with the help of a Menlo laser at 1560 nm, available at the Faculty of Physics of the University of Warsaw (FUW).

2. In order to address the issues of the **second claim**, I perform a study of switching performance of femtosecond pulses using the DCF at longer excitation wavelengths than 1560 nm, i.e. at 1700 nm. In cooperation with PI-TUW, I have the motivation to verify the tuneable and broadband character of the switching performance using the novel DCF, covering the optical telecommunication from C- (1530-1565 nm) to U-bands (1625-1675 nm).

3. To verify the **third claim**, I perform a complex experimental study of the fiber length effect on the switching performance in two generations of high index contrast DCFs: the first generation of fabricated DCFs, which was used to observe a high-contrast switching at 1700 nm, and the second generation of DCF with improved DC symmetry, enabling a first time observation of switching at 1560 nm. I compare the sets of experimental results at 1700 and 1560 nm, including the fiber length dependence of the switching performance, and provide a summary of the observed switching performances using the two generations of DCFs.

   To give a stronger proof of the third claim, I present the results of the dual wavelength switching experiment, realized at PI-TUW. It includes two sources of femtosecond pulses, one centered at 1560 nm (signal) and the other at 1030 nm (control). The main purpose is to improve the switching performance using the first generation DCF. This new control/signal approach, in fact, will show cause minimal pulse distortions, resulting in a more spectrally homogeneous steering of femtosecond pulses.

Outline of the dissertation

This dissertation is divided into four chapters. The first one is devoted to the theoretical background of soliton self-trapping, which is the physical principle allowing steering of femtosecond pulses in DCF. Then, I discuss about the high-order soliton propagation in DCFs. **The first chapter is based on the scientific literature and current state of the art about soliton theory and its application in DCFs. The chapters from second to forth include my original contributions to the study of soliton self-trapping steering in DCFs.** In particular, the second chapter is dedicated to the numerical study of the DCF structure optimization - including the choice of the proper materials - and its fabrication process I was involved in at Ł-IMIF. In the third one, I present the experimental results of ultrafast all-optical switching using the fabricated fiber presented in the previous chapter. The forth and last chapter presents a novel all-optical switching experiment I performed at PI-TUW, which is based on dual wavelength approach. The presentation of the topics has the following structure:

1. **First chapter, *Theoretical background***: The chapter is based on the scientific literature and does not contain my original contribution. In the first chapter of the dissertation, I describe how high-order solitons propagate in optical fibers, introducing the concepts of solitonic oscillations, soliton self-compression and soliton fission. Then, I go into details on the propagation of high-order solitonic pulses in DCFs: here, I present the concept of coupling oscillations and the coupling coefficient dispersion and explain the nonlinearly induced DC asymmetry phenomenon. Afterwards, I have all the elements to describe the theoretical mechanism of self-trapping of high-energy solitonic pulses in DCF. I dedicate space to the key parameters which determine the character of the soliton propagation in DCFs: the soliton number, the soliton compression length and the coupling length.

2. **Second chapter, *Materials and structural optimization***: In the second chapter, I present the properties of the basic glass materials based on the study conducted mainly by J. Cimek and R. Stępień from Ł-IMIF. Then, this chapter contains my original contribution: the optimization phase of the DCF structure and the simulation study of the ultrashort pulse dynamics in such fibers. These are the subsections:

    I. ***Optimization of the DCF materials***: As first step, I present the optimization phase of the DCF structure in terms of choice of the proper materials and structure. I start the analysis from the rheological and optical properties of the two glasses optimized for the DCF fabrication and synthesized at Ł-IMIF: the highly nonlinear lead-bismuth-gallium-silicate PBG-08, for the two cores, and the weakly nonlinear borosilicate UV-710. As mentioned above, this work was conducted by my colleagues from Ł-IMIF.

    II. ***Simulations of the fiber characteristics in the linear regime***: This section contains my original contribution related to the numerical analysis of the fiber propagation characteristics in the linear regime, such as the spectral dependence of the mode profiles, the corresponding effective index and the waveguide losses for each fundamental mode. It includes the calculation of the coupling parameters, which are the most important ones in coupled waveguides systems, and their wavelength dependencies. Furthermore, I present one of my main contributions: the optimization phase of the fiber structure considering some requirements to reach the desired solitonic propagation and efficient switching of femtosecond pulses. A significant part of the thesis will be dedicated to the dependence of the above-mentioned parameters by acting on the structural parameters of the PCF, such as the photonic lattice pitch, diameters of cladding rods, filling factor. The results presented in this section were published on peer-reviewed article *Laser Physics Letters* [6], 17:025102, 2020, and in conference proceedings *2018 20nd International Conference on Transparent Optical Networks (ICTON)* pp. 1–4, 2018 [7, 8].

III. ***Simulations of pulse propagation in the nonlinear regime***: The third section of the chapter contains one of my most important original contribution: the numerical study of ultrafast NLDC performance using the optimized fiber structure. I present an extended numerical model based on the solution of the CGNLSE, incorporating linear and nonlinear effects, such as waveguide and coupling coefficient dispersion, Kerr nonlinearity, self-steepening including its spectral dependence, stimulated Raman contribution, cross-phase modulation effect and waveguide losses. The main contribution relies on the numerical analysis of the nonlinear propagation of picojoule energy femtosecond pulses in order to identify the best switching performance in the input parameter space of 1400 - 1800 nm in terms of excitation wavelengths, and of 75 - 150 fs in terms of pulse width. The simulation outcomes give the basis to prove the first claim of the dissertation. They were also published in peer-reviewed article *Optical Fiber Technology*, 51:48–58, 2019 [9].

IV. ***Fabrication process and choice of the subpreforms***: The thesis proceeds with a brief description of the fabrication process of the DCFs at Ł-IMIF. It is based on the stack-and-draw method. My main contribution presented in this section is the numerical analysis of the real fiber structures including the DC optical asymmetry. A part of the results of this study was published in peer-reviewed article *Optical Fiber Technology*, 63:102514, 2021 [10].

3. **Third chapter, *Experimental results***: The thesis continues with the presentation of the experimental studies I conducted using the new fabricated DCFs.

I. ***Linear experiments at 1560 nm***: First, I present two experiments which I performed in the linear regime of operation. They are devoted to the experimental determination of the coupling length and the attenuation coefficient of the fabricated DCF.

II. ***Experimental results of reversible switching and cut-back method at 1560 nm***: Second, I show the results of the experiments conducted at FUW with a 100 MHz repetition rate Menlo laser operating at 1560 nm. In order to interpret the results and confirm the solitonic character of the switching performance, I report the results of the simulation study performed by dr Viet Hung Nguyen from from Advanced Institute for Science and Technology of Hanoi University of Science and Technology in Vietnam. In addition to performing the experiments, one of my main contribution in this section is the evaluation of the correspondence between the numerical and experimental data. It is important to confirm the role of the self-trapping phenomenon in the investigated propagation regime. The results were presented in peer-reviewed article *Optics Letters*, 45:5221-5224, 2020 [11]. In the following pages, I present my most important contribution to the experimental study at 1560 nm: the fiber length effect of the switching performance and the best results achieved at this wavelength and at the optimized fiber length. The study is shown in my most recent article in *Applied Optics* journal, 60(32):10191-10198, 2021 [12]. The numerical and experimental outcomes from this section should give a verification to the first claim of this dissertation.

III. ***Experimental results at 1700 nm***: I proceed by showing the experimental results conducted with the laser source available at our partner institution PI-TUW: a femtosecond amplifier - optical parametric amplifier (OPA) system with 10 kHz repetition rate and tuneable in the spectral range of 1500 - 1900 nm. The results of the experimental study at 1700 nm is published in the peer-reviewed article *Optics Communications*, 472:126043, 2020 [13]. Even in the case of 1700 nm, my most important contribution is the fiber length effect of the switching performance, as well the best experimental results achieved at this wavelength. Both of them are present in my most recent publication in *Applied Optics* 60(32):10191-10198, 2021 [12]. The outcomes presented in this section should constitute a verification of the second claim of the dissertation, showing the broadband tunability of the switching performance using the optimized DCF.

The combination of experimental and simulation results at both 1560 and 1700 nm provides a stronger verification of the first claim of the dissertation.

4. **Fourth chapter, *Ultrafast all-optical dual wavelength switching in dual-core fibers***: Based on the possibility to achieve the input power and wavelength dependent redistribution of the input optical field between the two output cores of the novel DCF, I introduce the results of the so-called dual wavelength switching experiment. Instead of a single ultrashort pulse, the novel scheme provides two optical pulses, named as *signal* and *control*. Thanks to the physical mechanism of nonlinear balancing of the DC asymmetry, a proper adjustment of the control pulse energy allows the signal pulse to switch the propagation core from the excited to the non-excited one. My main original contributions presented in this chapter are the control pulse energy and the fiber length dependences switching performance of the signal pulses using the optimized DCFs. The results presented in this chapter should rely on the improved DC symmetry of the optimized all-solid DCF should allow the verification of the third claim of the dissertation. They were published in the peer-reviewed article *Journal of Lightwave Technology*, 39(15):5111-5117, 2021 [14].

Introduction

All-optical signal processing is nowadays one of the most interesting research areas in the information technology domain [15]. It involves a large variety of devices in the optical communication technology [16], such as all-optical switches [17], multiplexers [18], de-multiplexers [19] and routers [20], and it can enable digital operations at bit rates above Tbit/s [21, 22]. It represents the physical background of digital optical computers, which are expected to significantly overcome the performance of their electronic counterparts in many aspects [23].

The most frequent digital operations in the optical domain are the arithmetic and logic ones [24–26]; currently, one of the most investigated ones is the all-optical switching [15, 27]. All-optical switches are indispensable for optical buffers [28], wavelength division multiplexed interconnects [29] and data center networks [30]. The physical processes that regulate the operation of all-optical switches - and optical digital devices in general - are mostly nonlinear [31], involving phenomena as Kerr effect [32], inverse Raman scattering [33] and four-wave mixing [34]. One of the elaborated theories for all-optical signal switching is the nonlinear directional coupler (NLDC), which was introduced for the first time in the early 1980s [35]. One of the simplest realization of such concept was in the form of DCFs. They comprise two inherently parallel cores and the interaction between them is easy to control both by nonlinear or phase sensitive excitation of one or both cores.

DCFs are used in various sectors of photonics, with applications in the field of fiber sensing, fiber laser and fiber communication technology. Some examples of DCF-related research achievements of are all-fiber integrated immunosensors [36], flat gain fiber optical parametric amplifier [37] and electrically switchable nanomechanical fiber coupler [38]. Optical fibers are much simpler to fabricate and cascade than other more sophisticated devices for all-optical switching purposes, such as those based on the use of metamaterials [39], ring resonators [40], plasmonic waveguides [41] or nonlinear optical loop mirrors (NOLMs) [42]. Furthermore, all of the other mentioned alternatives have only one single channel and have to be duplicated and outfitted with a proper input signal splitter to work as a cross-switching device, resulting in an increase of their cost and complexity.

Therefore, DCFs, which inherently contain two interaction channels, remain still candidates for all-optical switching in order to realize compact devices at the level of few centimeters. A promising demonstration of ultrafast nonlinear switching was performed using femtosecond pulses in the normal dispersion region of a step-index silica optical fiber coupler [43]. Unfortunately, only moderate switching contrasts were achieved accompanied by significant signal distortions.

In order to prevent signal degradation, Trillo et al. suggested the idea to move to the solitonic regime of operation [44]. Solitons are specific wave packets that, in absence of losses, can be spatially confined due to a balance between nonlinear and dispersive phenomena [45] and keep their shape undistorted along propagation in nonlocal nonlinear media [46]. During the last thirty years, propagation of solitons has been largely investigated numerically in single-core [47–50] and multi-core optical fibers [51–53] due to their resilience to large variations in energy and dispersion.

Moreover, the advent of PCFs in the 90s offered the possibility to engineer the fiber dispersion with higher precision, to boost nonlinearity and also to realize simple multi-core structures [54, 55]. As a consequence, dual- and triple-core PCFs were used as potential all-optical logic gates controlled with femtosecond solitonic pulses [56–58]. In particular, DC PCFs have high application potential for compact, efficient and low-energy switching solutions and straightforward integrability into fiber-based communication systems. A significant amount of theoretical works was dedicated to investigate the soliton-based NLDC possibilities using PCFs: Coelho and coworkers proposed a triple-core PCF with all-optical logic gate functionality [59], the research group of Giessen studied an optofluidic PCF coupler for all-optical switching applications [60], and Sarma modeled the solitonic switching using a highly nonlinear glass PCF [61]. Even though the subject has been intensively studied on the theoretical level, the practical implementation of this concept has been never realized in conventional fiber structures because of the strict requirements imposed on the dispersion, coupling and nonlinear characteristics.

DCFs rely also on the advantage of the self-trapping mechanism of high-order solitons, which is the key condition to establish all-optical switching of femtosecond optical pulses [62]. It has been already demonstrated in the case of multiple optical fiber arrays and permitted the registration of the so-called light bullets [63]. It was accomplished in an hexagonal array of evanescently coupled single-mode fibers: the central fiber was excited by 170 fs pulses at 1550 nm and, at low power input level, the pulse was out-coupled from the central fiber to the surrounding waveguides. Under increase of the input pulse power, the localization of the output field in the central core is improved and a train of considerable compressed pulses ($\approx$ 30 fs) - i.e. light bullets - was detected at the output. Later, triple vortex light bullet formation has been demonstrated by Eilenberger et al. [64]. In the case of a DCF, it is possible to establish self-trapping by a proper design of the properties of the fiber and under slight perturbation of the input pulse energy. In such way, the lower energy pulses are transferred to the non-excited core and trapped there, while the higher energy ones are self-trapped already in the excited core (Fig.1).

The first pioneering experimental work with DC PCFs as solitonic switches was performed by Betlej et al. [1]. Nevertheless, it demonstrated only an equalization between the output energies of the two cores mainly due to uncontrollable multicolor generation, which is inherently present during the nonlinear propagation in PCF. A first time true switching performance using a square-lattice DC PCF made of a multicomponent silicate glass was achieved by Stajanča et al. [5]; however, it was demonstrated in a limited spectral region - i.e. without broadband switching performance - and showed unwanted nonlinear signal deteriorations. To overcome these drawbacks, P. Stajanča and I. Bugár presented a numerical study of a new broadband and efficient switching concept based on controllable self-trapping of higher-order solitons at 1550 nm in a highly nonlinear air-glass DC PCF [2]. The work was followed by an experimental investigation performed by L. Čurilla et al.; nevertheless, the fiber showed unexpected asymmetry effects of the two cores of the structure, which limits the coupling properties of the fiber [3].

The limited amount of experimental demonstrations of solitonic NLDC approach in DCF [3–5], the promising outcomes achieved by my predecessors and the interest in understanding the complex evolution of femtosecond pulses through such fibers motivated me to extensively analyze solitonic steering in a novel DCF. Asides from the asymmetry effects, another crucial challenge to undertake is the control of the soliton fission processes, which are inherently observable during pulse propagation in the anomalous dispersion regime [65]. It causes the soliton pulses to break up into many components, which consequently undergo further nonlinear spectral transformations. The result is a broad and structured output spectrum, whose complexity depends on initial pulse parameters [66, 67]. To limit the asymmetry effect, which was the most crucial drawback of the DC PCF [3], I purpose a DCF which is totally all-solid, made of special multicomponent soft glasses synthesized at Ł-IMIF. To limit the effect of soliton fission, instead, I plan to properly conduct an extensive study of the dispersive, nonlinear and coupling properties of the DCF. Moreover, I target to establish the self-trapping condition using pulses with only few nanojoules energy. The strategies mentioned above could open some perspectives for practical application of DCFs as effective and low-power all-optical switching devices.

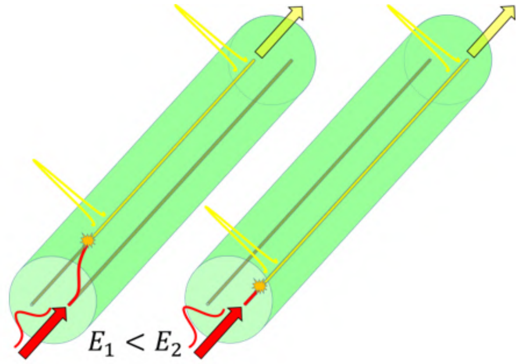

Fig. 1: *Theoretical concept of self-trapped solitonic switching: the high peak powers trap the shortened pulse in the cross or in the bar core in dependence of the input pulse energy. The pulse propagates further in the same core in quasi-stable conditions.*

The aim of this work is to study nonlinear steering of femtosecond laser pulses in the new DCF, focusing on all-optical switching performance of ultrashort pulses. The study is conducted both with experimental and numerical approach:

1. The **numerical part** comprises a numerical model based on CGNLSE, which is a valuable instrument to better understand the underlying optical processes. With this methodology experience and insights, I am able to purpose a more efficient and applicable nonlinear switching concept based on soliton self-trapping. The numerical study includes the basic fiber design optimization and the detailed anal-

ysis of nonlinear switching characteristics in the above-mentioned DCF;

2. The **experimental part** of the dissertation reports the study of multi-wavelength nonlinear switching in the specialty all-solid DCF. I investigate the influence of fiber length, input pulse parameters, structural DC asymmetry on the pulse evolution and switching performance. The study involves the use of different apparatuses and pulsed laser sources in two different institutions: FUW, with technical support of Ł-IMIF, and PI-TUW.

Combining both approaches, I have the ambition to predict and give an experimental evidence of solitonic (more precisely, soliton-like) self-trapping in a sufficiently symmetric DCF. First, this work addresses the soliton theory in the case of coupled discrete waveguides enabling the verification of the high contrast switching performance predicted by the previous numerical simulations. Second, I promise to study the complex propagation of ultrafast femtosecond pulses in such fiber, exploring its spectral, temporal and spatial aspects. Moreover, it provides physical insights about the role of various physical phenomena which characterize pulse propagation in DCFs, such as linear and nonlinear coupling and their dispersion, nonlinear phase modulation and scattering processes. This surely constitutes an useful knowledge towards the demonstration of the theoretical concept of ultrafast soliton switching presented in Fig.1. I rely also on the fiber fabrication background at Ł-IMIF, which has potential to bring further improvement of the desired DC symmetry. In addition, the study I performed could open some interesting perspective towards a practical application of the optimized DCF, in particular for an efficient all-optical switching of femtosecond low-energy pulses. It can eventually find applications in high-speed data routers, time division multiplexing units or optical logic gates.

Contents

CHAPTER 1

Theoretical background

1.1 Introduction to optical solitons: the modulation instability

In the field of nonlinear optics, the word *solitons* refers to specific wave packets that can propagate undistorted over long distances. This property is widely exploited in nonlinear fiber optics, as it finds practical applications in optical signal transfer and its processing. In general, optical solitons can exist both in spatial and temporal domain. However, in the specific case of optical fibers, I consider only *temporal solitons* because the electromagnetic wave is intrinsically confined in the fiber core. Before defining solitons and their properties, I introduce the basic concepts of evolution of optical fields in fibers.

As all electromagnetic phenomena, the evolution of optical fields in fibers is governed by Maxwell's equations. In case of propagation of continuous-wave light in a spatially confined nonlinear media (fiber), the evolution of the wave envelope is governed by the following differential equation in the retarded time frame T [68]:

$$\frac{\partial A}{\partial z} + \frac{\alpha}{2}A + i\frac{\beta_2}{2}\frac{\partial^2 A}{\partial T^2} - \frac{\beta_3}{6}\frac{\partial^3 A}{\partial T^3} = i\gamma\left[|A|^2A + \frac{i}{\omega_0}\frac{\partial}{\partial T}(|A|^2A) - T_R A\frac{\partial |A|^2}{\partial T}\right] \quad (1.1)$$

where A is the electric field amplitude, z the propagation axis and $T = t - z/v_{\mathrm{g}}$ (where t is the time) the time frame of reference moving with the pulse at the group velocity v_{g}. α are the fiber losses, β_2 and β_3 the second- and third-order coefficients of the Taylor expansion of the propagation constant β, respectively, and ω_0 the carrier frequency. γ is the nonlinear parameter (responsible for self-phase modulation) and $T_R = \int_{-\infty}^{+\infty} tR(t)dt$ is the normalized first moment of the nonlinear response function ($R(t)$ the Raman response function). All of these quantities will be discussed in details in the next sections. Eq.(1.1) is referred as the Generalized nonlinear Shrödinger equation (GNLSE) and can be simplified in case of negligible fiber losses and Raman response, and confined continuous wave (CW) propagation along axis z as follows:

$$i\frac{\partial A}{\partial z} = \frac{\beta_2}{2}\frac{\partial^2 A}{\partial T^2} - \gamma|A|^2 A \tag{1.2}$$

This is called the Nonlinear Shrödinger Equation (NLSE). In order to generate solitons inside the fiber, it is necessary to find pulse-like solutions of Eq.(1.2) which have stabilized or a periodic-like evolution along the propagation. This study is part of one of the most investigated theories in the field of nonlinear optics, which is referred as modulation instability (MI).

1.1.1 MI in optical fibers

The phenomenon of MI can be roughly described as the result of the interaction between a strong carrier harmonic wave (at frequency ω) and small sidebands (at $\omega + \Omega$, with Ω frequency of the perturbation) [69, 70]. In the field of optics, the modulation of the steady state takes place due to an interplay of nonlinear and dispersive effects [71, 72]. To the specific case of optical fibers, it causes the CW or quasi-CW radiation to break up into a train of ultrashort pulses [73, 74].

1.1.2 Dispersion phenomena in optical fibers

In general, dispersion is the spreading out of a light pulse in time along propagation through an optical fiber. There are several sources of dispersion in fibers, the most important one include chromatic (sum of material and waveguide dispersion), intermodal and polarization dispersion. Each type of dispersion is discussed in details in this section.

- **Chromatic dispersion**: Chromatic dispersion arises from the fact that the source of radiation is not perfectly monochromatic, i.e. it is characterized by a finite spectral width. It causes the broadening of optical pulses along propagation through optical fibers. It includes two main sources of dispersion: material and waveguide dispersion.

  - **Material dispersion**: It originates from the dependence of the refractive index n of the dielectric medium on the optical wavelength λ. One most common relations for dispersion in glass materials is the Sellmeier equation, which gives a good approximation of $n(\lambda)$ in this form:

    $$n^2(\lambda) = 1 + \sum_{j=1}^{N} \frac{B_j \lambda^2}{\lambda^2 - C_j} \tag{1.3}$$

    B_j and C_j are the Sellmeier coefficients. They are determined empirically by measuring the refractive index in a wide wavelength range and a by fitting the obtained dependence. B_j represents the strength of the j-th absorption resonance and C_j the square of the wavelength the j-th absorption resonance. Therefore, each term of the sum represents an absorption resonance with proper strength and wavelength. Generally, $N = 3$ is sufficient to characterize the glasses in visible and NIR spectral range, thus Eq.(1.3) is used in form:

$$n^2(\lambda) = 1 + \frac{B_1\lambda^2}{\lambda^2 - C_1} + \frac{B_2\lambda^2}{\lambda^2 - C_2} + \frac{B_3\lambda^2}{\lambda^2 - C_3} \tag{1.4}$$

This equation doesn't consider the lattice absorption and temperature effects [75]. However, it is a good approximation of $n(\lambda)$; therefore, it is adopted also by my group for characterization of the refractive index spectral profile of fabricated glasses [76, 77].

It is possible to describe the chromatic dispersion in the frequency domain by introducing the **propagation constant** β. In frequency domain, the input light pulse in the fundamental mode is centered at the frequency ω_0 and each spectral component at ω have a propagation constant $\beta(\omega)$, resulting in the following expression of the electric field:

$$\mathbf{E}(\mathbf{r}, t) = \hat{x}\{F(x, y)A(z, t)e^{i\omega_0 t}e^{-i\beta(\omega)z}\} \tag{1.5}$$

where $F(x, y)$ is the transversal field distribution of the fundamental mode, $A(z, t)$ the envelope function of the signal along z direction in time t.

In other terms, this corresponds to a different **effective refractive index** n_{eff} value for each spectral component, which is defined as

$$n_{\text{eff}}(\omega) = \frac{\lambda}{2\pi}\beta(\omega) \tag{1.6}$$

It means that different spectral components associated with the pulse travel at different speeds given by $c/n_{\text{eff}}(\omega)$, with c the speed of light.

For quasi-monochromatic field with significantly narrow spectral width, it is possible to expand the propagation constant $\beta(\omega)$ near the central frequency ω_0 in a Taylor series:

$$\beta(\omega) = \beta_0 + \beta_1(\omega - \omega_0) + \frac{1}{2}\beta_2(\omega - \omega_0)^2 + \frac{1}{6}\beta_3(\omega - \omega_0)^3 + ... \tag{1.7}$$

where

$$\beta_p = \left(\frac{\partial^p \beta}{\partial \omega^p}\right)\bigg|_{\omega=\omega_0} \quad (p = 0, 1, 2, ...). \tag{1.8}$$

The parameters β_1, β_2 and β_3 are related to the group velocity v_{g}, the refractive index n and the wavelength λ as follows:

$$\beta_1 = \frac{1}{v_{\text{g}}} = \frac{n_{\text{g}}}{c} = \frac{1}{c}\left(n + \omega\frac{dn}{d\omega}\right) \tag{1.9}$$

$$\beta_2 = \frac{1}{c}\left(2\frac{dn}{d\omega} + \omega\frac{d^2 n}{d\omega^2}\right) = -\frac{\lambda^2}{2\pi c}D_{\text{mat}}(\lambda) \tag{1.10}$$

$$\beta_3 = \frac{\lambda^2}{4\pi^2 c^2} S(\lambda) + \frac{\lambda^3}{\pi^2 c^2} D_{\text{mat}}(\lambda) \tag{1.11}$$

where $D_{\text{mat}}(\lambda)$ is the **material dispersion coefficient** and and $S(\lambda)$ the dispersion slope and defined as $S(\lambda) = dD_{\text{mat}}(\lambda)/d\lambda$. $D_{\text{mat}}(\lambda)$ is related to β_1 by the relation

$$D_{\text{mat}}(\lambda) = \frac{d\beta_1}{d\lambda} \approx \frac{\lambda}{c} \frac{d^2 n}{d\lambda^2} \tag{1.12}$$

Therefore, β_1 is the inverse of the group velocity of the optical pulse, while β_2 is the group velocity dispersion (GVD) parameter, which is responsible for pulse broadening. β_3 is the third-order dispersion (TOD) parameter, which is responsible to make the pulse deformations. It introduces a long oscillating tail near the trailing edge of the pulse (if positive) or near the leading edge of the pulse (if negative). Its effect in the pulse propagation is generally negligible with respect to β_2, but it needs to be taken into consideration in case of solitons (see section 1.2.3).

- **Waveguide dispersion**: It arises from the dependence of the group velocity $v_{\text{g}} = d\omega/d\beta$ of the fundamental mode on the guiding properties of the fiber. In particular, it occurs because light travels in both the core and cladding of the fiber with different group velocities. It depends on the wavelength through the V-number, defined as $V = \pi d\sqrt{{n_{\text{co}}}^2 - {n_{\text{cl}}}^2}/\lambda$, where d is the core diameter and n_{co} and n_{cl} the refractive indices of the core and cladding materials, respectively. For V-numbers in the range 1.5 $< V <$ 2.4, the waveguide dispersion coefficient D_{w} can be approximated in this way [78]:

  $$D_{\text{w}}(\lambda) \approxeq -\frac{0.1\lambda}{d^2 \cdot c \cdot n_{\text{cl}}}, \tag{1.13}$$

  Therefore, D_{w} decreases with the wavelength and it is dependent on the geometry of the guiding core.

As a first approximation, the material and waveguide dispersion effects can be simply added, which means that the total chromatic dispersion coefficient $D(\lambda)$ is the sum of the two dispersion coefficients $D_{\text{mat}}(\lambda)$ and $D_{\text{w}}(\lambda)$. One of the main advantages of the chromatic dispersion is that its contribution to the dispersion parameter D (or β_2 as well) mostly depends on fiber-design parameters. This means that there are wide possibilities to properly optimize the structure of the fiber and engineer its dispersion characteristics. Depending on the sign of β_2 parameter, the fiber can exhibit:

- **normal dispersion** ($\beta_2 > 0$): the high-frequency (blue-side) components of the optical pulse travel slower than low-frequency (red-side) ones;
- **anomalous dispersion** ($\beta_2 < 0$): the low-frequency (red-side) components of the optical pulse travel slower than high-frequency (blue-side) ones.

The anomalous dispersion regime is more interesting for the purpose of this dissertation because it allows fibers to support solitons through a mutual interplay between the dispersive and nonlinear effects [79].

- **Intermodal dispersion**: It takes place in multi-mode fibers and originates from the difference in group velocity of the different modes propagating through the fiber. It is not interesting in my study because I am planning to design single-mode fibers, which allow higher bandwidth signals to be sent faster and over longer distances than multimode fibers.
- **Polarization dispersion**: It happens when the fiber structure is not symmetric and homogeneous, i.e. when the refractive index of the core material depends on the direction of the input electric field. Anisotropies can originate from the fabrication process, such as small changes in the glass composition and structural or induced local strains during the drawing phase. Therefore, the propagation constant of the given mode depends on its polarization, leading to different group velocities for fields oriented along the axis of the fiber (X-polarization) or orthogonally to it (Y-polarization). Therefore, the polarization mode dispersion coefficient D_{PMD} depends on the extent of the anisotropy $n_{\text{co}}|_{\text{x}} - n_{\text{co}}|_{\text{y}}$, where $n_{\text{co}}|_{\text{x}}$ and $n_{\text{co}}|_{\text{y}}$ are the refractive index of the core material along X- and Y-polarization dependence. D_{PMD} does not depend on the spectral wavelength of the input source and, in case of my study, can be considered negligible.

Self-Phase Modulation

Self-phase modulation (SPM) is caused by the intensity dependence of the refractive index in a third-order nonlinear optical media. It introduces a nonlinearly-induced phase shift that is responsible for chirping and spectral broadening of optical pulses.

Introducing a pulse with normalized amplitude and shape $U(z, T)$, the solution of Eq. (1.2), in absence of dispersion ($\beta_2 = 0$) and losses ($\alpha = 0$), has an exponential form $U(z, T) = U(z, 0)\exp(i\phi_{\text{NL}})$. $\phi_{\text{NL}} = \gamma P_0 L |U(z, T)|^2$ (where L is the fiber length) is the nonlinear SPM-induced phase shift. The variation of the nonlinear phase in time causes changes in the pulse spectrum because the instantaneous optical frequency is time dependent as well:

$$\delta\omega_{\text{NL}}(t) = -\frac{d\phi_{\text{NL}}}{dt} = -\gamma P_0 L \frac{d}{dt}|U(z, T)|^2 \tag{1.14}$$

$\delta\omega_{\text{NL}}(t)$ is referred in scientific literature as frequency chirp. In order to completely understand Eq.(1.14), it is necessary to define the **nonlinear parameter** γ [80], which is:

$$\gamma = \frac{n_2\omega_0}{cA_{\text{eff}}} = \frac{2\pi}{\lambda}\frac{n_2}{A_{\text{eff}}}, \tag{1.15}$$

where A_{eff} is the **effective mode area**, defined by this equation:

$$A_{\text{eff}} = \frac{\left(\iint_{-\infty}^{\infty} S_z dxdy\right)^2}{\iint S_z^2 dxdy} \tag{1.16}$$

where $S_z = (\mathbf{E} \times \mathbf{H}) \cdot \hat{z}$ is the averaged-in-time component of the Poynting vector along z and $\hat{z}$ the unit vector along the fiber axis [81]. In Kerr-like media, i.e. characterized by an inversion symmetry at the molecular level, the second-order susceptibility $\chi^{(2)}$ is negligible with respect to $\chi^{(3)}$. Therefore, second-harmonic generation and sum-frequency generation phenomena are very weak and the refractive index change is proportional to the intensity of the light I:

$$\tilde{n}(\omega, I) = n(\omega) + n_2 I \tag{1.17}$$

This is known as **nonlinear optical Kerr effect**. n_2 is the **nonlinear refractive index** of the medium: assuming the optical field to be linearly-polarized, it's connected to the component of fourth-rank tensor of the 3-rd order susceptibility of the dielectric media $\chi^{(3)}_{XXXX}$ and to the linear refractive index n by this relation:

$$n_2 = \frac{3}{8n}\mathbb{R}\mathrm{e}(\chi^{(3)}_{XXXX}) \tag{1.18}$$

As noticeable from the expression of ϕ_{NL}, SPM is strongly dependent on the initial pulse shape $U(z, T)$ [82, 83] and on the initial temporal pulse duration [84]. In this work, I am considering pulse profile with a sech^2 shape because they are commonly generated by ultrashort mode-locked lasers [85] and have advantageous properties for soliton generation (they will be discussed in details in section 1.2). They have a temporal intensity profile $I(t)$ described by this function:

$$I(t) = \mathrm{sech}^2 \frac{t}{T_0} \tag{1.19}$$

where T_0 is the pulse duration, and a full width at half-maximum (FWHM) approximately equal to $1.76 \cdot T_0$. The frequency chirp, calculated using Eq. (1.14) is

$$\delta\omega(t) = 2\gamma P_0 \,\mathrm{tgh}\, \frac{t}{T_0} \tag{1.20}$$

with maximum $\delta\omega_{\mathrm{max}} = 2\gamma P_0 \cdot 3^{-3/2}/T_0$ at $t = T_0 \,\mathrm{arctanh}(1/\sqrt{3})$ [82]. The spectral intensity distribution of hyperbolic secant pulses affected by SPM has a periodic constructive/destructive interference pattern [82]. After performing an exact calculation of the optical spectrum by Fourier transformation of ϕ_{NL}, I get the classical shapes of the SPM-associated spectra with high accuracy [86]. They are reported in Fig.1.1 as a function of ϕ_{NL}.

The SPM spectrum is symmetrical and its effect is independent of the sign of the nonlinear coefficient γ, when dispersion is neglected. For values of ϕ_{NL} below $\pi/2$, the chirp has a monotonic temporal variation across the pulse. This causes a broadening of the pulse spectrum with no interference effects (Fig.1.1). For higher values than $\pi/2$, the structure of the spectrum begins to become oscillatory. The increase of the chirp near the pulse center causes the spectrum to broaden. However, the range of frequencies that can interfere becomes larger, thereby leading to the buildup of strong and detrimental oscillations in the pulse wings together with strong side lobes in the resulting spectrum.

It is possible to obtain a **gain spectrum** of the MI. Returning to Eq. (1.2) and introducing a perturbation of the CW steady state $a(z, T)$, in such a way that $A = (\sqrt{P_0} + a)\exp i\phi_{\mathrm{NL}}$, I obtain the form (linearized in a):

$$i\frac{\partial a}{\partial z} = \frac{\beta_2}{2}\frac{\partial^2 a}{\partial T^2} - \gamma P_0(a + a^*) \tag{1.21}$$

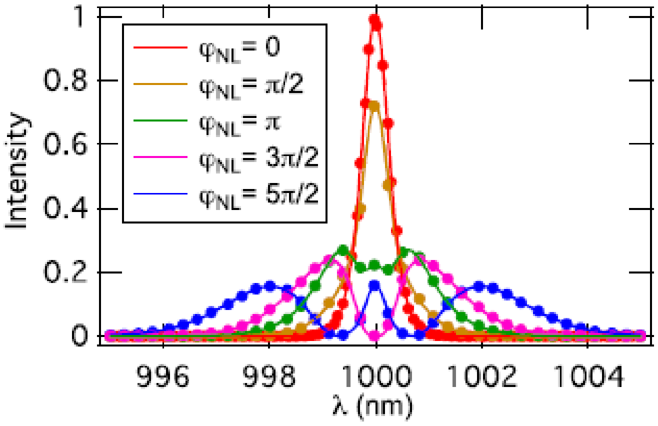

Fig. 1.1: *Calculated intensity spectra of a hyperbolic secant pulse for 1 m fiber length and different values of* ϕ_{NL} [86].

In the spectral domain, Eq.(1.21) has a nontrivial solution when the wave-number K and the frequency of perturbation Ω satisfy the following dispersion relation [68]:

$$K = \pm\frac{1}{2}|\beta_2\Omega|\sqrt{\Omega^2 + \text{sign}(\beta_2)\Omega_C^2} \qquad \Omega_C^2 = \frac{4\gamma P_0}{\beta_2} \tag{1.22}$$

The stability of the steady state depends significantly on the sign of β_2:

1. In the normal dispersion regime ($\beta_2 > 0$), the wave-number K is real for all values of Ω: it corresponds to mere oscillations around the unperturbed solution;
2. In the anomalous dispersion regime ($\beta_2 < 0$): K is imaginary for $|\Omega| < \Omega_C$. The perturbation grows exponentially with z: the CW solution is unstable and it's modulated into a train of pulses. This phenomenon is referred as **modulation instability** [69, 87].

For standard single-mode fibers operating in the near-infrared region (1550 nm) and in case of lossless medium, the gain spectrum $G(\Omega)$ assumes the form [88]:

$$G(\Omega) = 1 + \frac{\sinh^2\left[2\gamma P_0 L\sqrt{\left(\frac{\Omega}{\Omega_c}\right)^2\left(1-\left(\frac{\Omega}{\Omega_c}\right)^2\right)}\right]}{2\left(\frac{\Omega}{\Omega_c}\right)^2\left(1-\left(\frac{\Omega}{\Omega_c}\right)^2\right)} \qquad \Omega_c = \sqrt{\frac{4\gamma P_0}{|\beta_2|}} \tag{1.23}$$

where $\Omega = \omega - \omega_0$ is the detuning around the pump frequency ω_0, and has a peak value G_{max} of:

$$G_{\text{max}} = g(\Omega_{\text{max}}) = 1 + 2\sinh^2(\gamma P_0 L) \qquad \Omega_{\text{max}} = \pm\Omega_c\sqrt{2} \tag{1.24}$$

The gain spectrum at the pump frequency ($\Omega = 0$) has a quadratic dependence on the peak power and it is symmetric with respect to $\Omega = 0$. Its width is very sensitive to the dispersion parameter β_2, while its peak G_{max} is independent on GVD parameter β_2 and increases with the input power P_0. Therefore, the MI manifests itself as a pair of sideband components around the carrier wave component [89]. In the time domain, SPM breaks up the otherwise uniform CW wavefront and generates a train of finely localized pulses [89].

The picture changes in case of pulse propagation. The numerical study of Boscolo et al. shows that, if pulses have temporal durations below 30 ps, SPM acts in combination with dispersive phenomena [84]. As mentioned before, GVD is responsible for pulse broadening. At the same, depending on whether the pulse propagates in normal or anomalous fiber dispersion region, the spectral transformations generated by SPM are responsible for temporal stretching or compression of the pulse. Then, if the anomalous dispersion is targeted, it is possible to compensate broadening (by GVD) and compression (by SPM) and consequently generate an unbroadened pulse with sufficient stability along propagation. This is referred as soliton. In conclusion, the mutual interplay between GVD and SPM in the anomalous dispersion region is the basis of formation of temporal solitons.

1.2 Soliton propagation in optical fibers

If the MI occurs in the anomalous GVD regime ($\beta_2 < 0$) of optical fibers, the solution of NLSE equation in Eq.(1.2) has a specific pulse-like profile, which doesn't change - or follows a periodic evolution pattern - along the fiber length. This solution is known as **optical soliton**.

Solitons play an important part in the dynamics of the one-dimensional NLSE. They constitute the stable and asymptotic state of the field in physical systems in which nonlocality of the nonlinear interaction plays an important role [45]. It has been identified and studied in various physical systems, such as fluids [90], nematic liquid crystals [91] plasma [92] and relativistic fluids [93], and nonlinear optics [94–98].

Two kinds of solitons can be distinguished:

- **Spatial solitons**: They can be generated in Kerr-like media with weakly nonlocal optical response [99]. A refractive index change Δn induced by a beam with intensity $I(x, z)$ (x and z are the transverse and propagation spatial coordinates) can be represented in form

  $$\Delta n(I) = s\left(I + \chi\frac{\partial^2 I}{\partial x^2}\right) \qquad \chi = \frac{1}{2}\int_{-\infty}^{\infty} x^2 R(x)dx \tag{1.25}$$

  where $s = \pm 1$ in case of focusing or defocusing nonlinearity and χ is a small positive parameter indicating the degree of nonlocality. $R(x)$ is the response function of the nonlocal medium: its width with respect to the one of the intensity profile $I(x, z)$ determines the degree of nonlocality (Fig.1.2a). In case of weak nonlocality in (case (2) in Fig.1.2a), which is the most interesting one in my discussion, the width of $R(x)$ is finite, but still negligible with respect to the width of the intensity $I(x, z)$.

  It has been shown theoretically that the weak nonlocal contribution arrests the catastrophic collapse of self-focusing of high power optical beams in a self-focusing

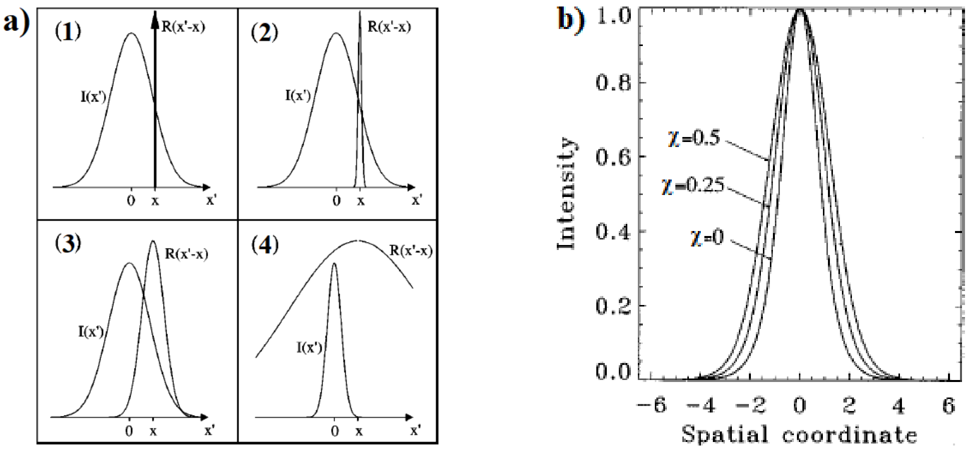

Fig. 1.2: *Different degrees of nonlocality, depending on the relative widths of the intensity profile $I(x)$ and response function $R(x)$: (1) local, (2) weakly nonlocal, (3) general and (4) strongly nonlocal response* [99]. *(b) Intensity profiles of bright solitons with normalized amplitudes $u_0^2 = 1$ for different degrees of non-locality χ* [100].

medium. This leads to the formation of stable two-dimensional solitons [101]. Integrating the paraxial wave equation describing the propagation of a 1D beam in weakly nonlocal Kerr-like self-focusing medium ($s = 1$, which means $\Delta n > 0$) in [100], the stationary bright soliton profile assumes this form (implicit equation):

$$\pm\, x = \frac{1}{u_0} \operatorname{arctanh}\left(\frac{\sigma}{u_0}\right) + \sqrt{4\chi}\, \operatorname{arc\,tg}(\sqrt{4\chi}\sigma) \tag{1.26}$$

where u_0 is the profile peak value at the center $x = 0$ and $\sigma^2 = (u_0^2 - u^2)/(1 + 4\chi u^2)$. In the limit of $\chi = 0$, the profile of the soliton is the most common hyperbolic secant one $u(x) = u_0 \operatorname{sech}(u_0 x)$. The intensity profile of the solution in Eq.(1.26) broadens monotonically by increasing the value of the non-locality parameter χ (Fig.1.2b) [100].

In summary, the Kerr effect in a self-focusing medium (with $n_2 > 0$, which means $\gamma > 0$) causes the pulse to narrow along propagation. If the focusing nonlinear and the diffractive linear effects are perfectly balanced, the field creates its own waveguide structure while propagating and, at the same time, it's the mode of the waveguide itself (**self-induced waveguide**) [102]. This means that the field evolves without changing its shape (if the media is lossless). This diffusion-like model applies to plasma physics [103] and nonlinear optics [100].

- **Temporal solitons**: They can be formed in media where the electromagnetic field is intrinsically confined, for example in optical fibers. They were predicted in a single-mode fiber by Hasegawa and Tappert [104], and observed experimentally for the first time by Mollenhauer et al. [105]. As already explained in section 1.1.2, a self-focusing medium (with $n_2 > 0$) experiences an increase on its effective refractive index, which is proportional to the intensity of the incident light (Eq.(1.17)). Along the propagation, the pulse accumulates a phase shift $\phi(t)$ equal to

$$\phi(t) = \omega_0 t - kz = \omega_0 t - k_0 z[n + n_2 I(t)] \tag{1.27}$$

where ω_0 is the carrier frequency, $\kappa_0 = \omega_0/c$ (with c the speed of light) is the wave number at ω_0 and $n = n(\omega_0)$. The accumulated phase shift is equal to

$$\Delta\omega = \frac{\partial\phi}{\partial t} - \omega_0 = -\frac{n_2 n}{k_0^2}\omega_0^2 z \frac{dI(t)}{dt} \tag{1.28}$$

From Eq.(1.28), it follows that the lower-frequency components of the pulse ($\Delta\omega < 0$) develop near its front, where $dI(t)/dt > 0$, while higher frequencies ($\Delta\omega > 0$) develop close to the back of the pulse, where $dI(t)/dt < 0$ [106]. The trend of phase shift presented in Eq.(1.28) is opposite to the one caused by anomalous GVD (when $\beta_2 < 0$) presented in section 1.1.2. It means that it is possible to compensate the nonlinear and dispersive effects: dispersion effect tends to let the high-frequency components propagate faster, while the nonlinear Kerr effect slows them down. This phase shift compensation allows the pulse to keep its shape unchanged while propagating: this is called temporal soliton. It has been demonstrated that the profile of temporal solitons is similar to Eq.(1.26) obtained for spatial solitons: in the limit of confined and stationary solution, it results in the hyperbolic secant one $u(t) = u_0 \operatorname{sech}(u_0 t)$ [107]. Temporal solitons find many application in telecommunications systems [108, 109], as well as all-optical switching using DCFs [1, 2].

1.2.1 Fundamental and high-order temporal solitons

As explained so far, temporal solitons can be generated in Kerr-like media ($n_2 > 0$, which means $\gamma > 0$) in the anomalous dispersion regime ($\beta_2 < 0$). The Kerr effect introduces a SPM that changes the refractive index proportionally to the intensity. If the medium is self-focusing, the nonlinear and the dispersive linear effects are perfectly balanced and the field propagates without changing its shape (if the media is lossless).

In order to prove this statement mathematically, it is useful to go back to Eq.(1.2) once again and normalize it introducing three dimensionless variables:

$$U = \frac{A}{\sqrt{P_0}} \qquad \xi = \frac{z}{L_\mathrm{D}} \qquad \tau = \frac{T}{T_0} \tag{1.29}$$

where P_0 is the peak power, T_0 the pulse width. Therefore, Eq.(1.2) assumes the following form:

$$i\frac{\partial U}{\partial \xi} = \frac{\operatorname{sign}\beta_2}{2}\frac{\partial^2 U}{\partial \tau^2} - N^2|U|^2 U \tag{1.30}$$

The parameter N is called **soliton number** and it's defined in this way:

$$N^2 = \frac{L_\mathrm{D}}{L_\mathrm{NL}} = \frac{\gamma P_0 T_0^2}{|\beta_2|} \tag{1.31}$$

where $L_\mathrm{D} = T_0^2/|\beta_2|$ (introduced already in Eq.(1.29) and $L_\mathrm{NL} = (\gamma P_0)^{-1}$ are the dispersion and nonlinear length, respectively. They provide the length scale where the dispersive or the nonlinear effect become predominant in the pulse evolution. Introducing $u = NU$ in Eq.(1.30), I obtain the standard form of the NLSE:

$$i\frac{\partial u}{\partial \xi} + \frac{1}{2}\frac{\partial^2 u}{\partial \tau^2} + |u|^2 u = 0 \tag{1.32}$$

Solving Eq.(1.32) with the inverse scattering method [68], three different scenarios can be identified in dependence of integer values of N:

- $N \ll 1$: It means that $L_\mathrm{D} \ll L_\mathrm{NL}$: the field is affected by the linear/diffraction effect much earlier than the nonlinear effect. This means that no stable soliton is generated and the pulse is just dispersion-shaped without being effected by any nonlinear behavior. It is not interesting for my purpose;
- $N = 1$: The dispersion (GVD) and nonlinear effects (SPM) are in perfect balance. A soliton is generated because the shape of the pulse doesn't change along propagation. This is referred as the **fundamental soliton**. Choosing the proper frequency, position and initial phase, the form of the fundamental soliton (with normalized amplitude) is the hyperbolic secant one:

  $$u(\xi, \tau) = \mathrm{sech}(\tau)\exp(i\xi/2), \tag{1.33}$$

  where η is the amplitude of the soliton. As already mentioned in the previous section, if the medium is lossless, the pulse propagates undistorted without changes in shape for arbitrarily long distances. The required peak power to support fundamental solitons in optical fibers is $P_0 = |\beta_2|/(\gamma T_0^2)$;
- $N > 1$: The dispersion and nonlinear effects are in mutual interplay between each other: initially, SPM dominates, but GVD soon contributes to pulse compression. Such cooperation allows the pulse to follow a period pattern in ξ, with reestablishment of the original shape after a period $\xi_0 = \pi/2$. This is known as **high-order soliton**, which is characterized by a **soliton period** defined in this way:

  $$z_0 = \frac{\pi}{2} L_\mathrm{D} = \frac{\pi T_0^2}{2|\beta_2|} \tag{1.34}$$

  Closed-form expressions for high-order solitons have been derived only for $N = 2$ and $N = 3$ [110]. A general expression of the hyperbolic secant pulse profile as a function of the soliton number N is

  $$A(o, t) = N\sqrt{P_0}\,\mathrm{sech}\left(\frac{t}{T_0}\right). \tag{1.35}$$

  with T_0 as the pulse duration. The soliton has an energy $E = 2N^2 P_0 T_0 = N^2 E_\mathrm{sol}$, where $E_\mathrm{sol} = 2P_0 T_0$ is the energy of the fundamental soliton.

  Pulse evolution of a second and third-order soliton over one period z_0 in a lossless medium is shown in Fig.1.3. For a second-order soliton (Fig.1.3a), at the distance of half-period $z_0/2$, the pulse gets its maximum compression with the peak power increases by a factor around 4; the latter half of period, the pulse recovered to its original shape. For a third-order soliton (Fig.1.3b), the pulse first contracts itself, then it splits into two distinguished peaks at $z_0/2$ and than recovers back to the original shape after a period z_0.

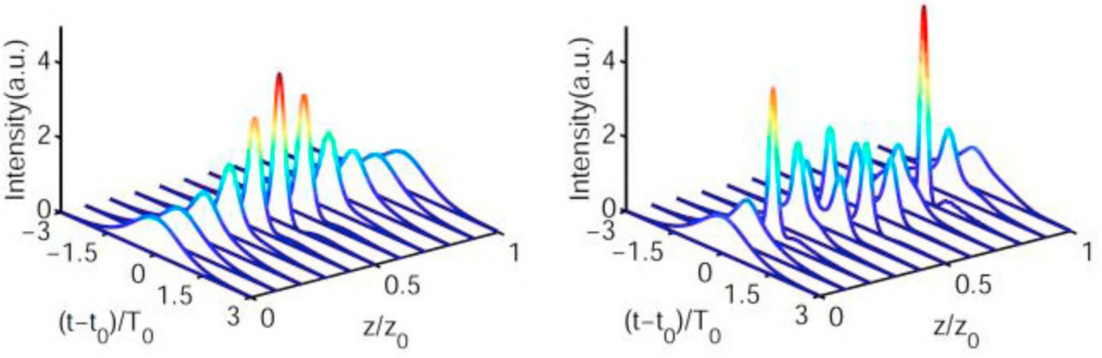

(a) (b)

Fig. 1.3: *Pulse evolution for the cases (a) $N = 2$ and (b) $N = 3$* [111].

One interesting feature to notice is that the soliton temporal width scales inversely with the amplitude η. This inverse relationship between amplitude and width has many advantages. It allows strong **temporal pulse compression** (and subsequently spectral broadening), with many applications in nonlinear optics [66, 111–113]. Its relevance in my discussion will be explained in the next sections.

1.2.2 Effect of attenuation

In general, optical signals which are propagating through a medium are subjected to attenuation. It the reduction of the transmitted optical field with respect to the input power. The most common expression of attenuation is the Beer-Lambert law:

$$P_{\mathrm{T}}(L) = P_0 \exp(-\alpha L), \tag{1.36}$$

where P_0 is the signal input power, P_{T} the output transmitted one and α the **attenuation coefficient**. It is usually expressed in dB/km and retrieved empirically by measuring the power ratio P_{T}/P_0, considering a fiber with length L in this way: $\alpha_{\mathrm{dB}} = -10/L \log(P_{\mathrm{T}}/P_0)$. It takes into account all the possible sources of losses; the most important contributions are:

- **Material absorption**: The materials which constitute the core and cladding of fibers are slightly absorbing, causing a diffraction of the input beam. Primary sources of material absorption are
  - **Atomic or molecular vibrations**: It is caused by the interaction between the incident electromagnetic wave and the atoms/molecules of the glass material, which converts the energy of the wave into bond or lattice vibrations. It mostly occurs in the NIR (e.g. beyond 1600 nm for SiO_2 glass fibers [78]) or mid-infrared (eg. at 4500 nm for chalcogenide glass fibers [114]) spectral regions.

  - **Electronic transitions**: They are caused by the excitation of the electrons of the materials from the valence band to the conduction band. It is strong in the short ultraviolet wavelength range ($\lambda < 600$ nm), with a long tail extended into the longer wavelength. Its effect is negligible in the range 800-1700 nm range [78]. It contribution is expressed by the attenuation coefficient α_{E}.

  It can be described mathematically in polar coordinate by the complex refractive index $n_{\mathrm{I}}(r)$, where r is the radius of material with cylindrical shape. Therefore, the refractive index of the medium can be written as $n(r) = n_0(r) + in_{\mathrm{I}}(r)$, where $n_0(r)$ is the real part of the refractive index and i the imaginary unit. The absorption coefficient per unit length due to material absorption $\alpha_{\mathrm{A}}(r)$ can be written as:

$$\alpha_{\mathrm{A}}(r) = \frac{4\pi}{\lambda} n_{\mathrm{I}}(r) \tag{1.37}$$

  As both the core and the cladding materials are constituted of materials with slight absorption properties, their contributions on $\alpha_{\mathrm{A}}(r)$ can be summed together (in dB/km): $\alpha_{\mathrm{A}}(r) = \alpha_{\mathrm{A}}(r)|_{\mathrm{co}} + \alpha_{\mathrm{A}}(r)|_{\mathrm{cl}}$, where $\alpha_{\mathrm{A}}(r)|_{\mathrm{co}}$ and $\alpha_{\mathrm{A}}(r)|_{\mathrm{cl}}$ are the attenuation coefficients of the core and cladding materials, respectively.

- **Rayleigh scattering**: It is caused by density fluctuations inside the material, which causes local fluctuations of the refractive index. In glass materials, it is caused by crystallized local domains, which alter the chemical composition of the glass among several bond lengths [115]. The Rayleigh scatterers on an initially on-axis pulse redistribute the beam power among all bound-ray directions and distort the pulse through ray dispersion. Simultaneously, the power is lost from the pulse by scattering into radiation. The Rayleigh power loss is significant at shorter wavelengths. Its contribution to losses is expressed by the attenuation coefficient α_{R}, which is strongly wavelength dependent ($\propto 1/\lambda^4$).

The loss term is taken into account in the GNLSE (Eq.(1.1)) through the Beer's loss coefficient α, which is the sum (in dB/km) of the attenuation coefficients described before, α_{A} and α_{R}. The impact of the loss can be characterized by the characteristic loss length $L\alpha = 1/\alpha$. As long as I am using fibers with lengths of few cm-mm, the loss contribution is weak (i.e. $L\alpha \gg L_{\mathrm{D}}, L_{\mathrm{NL}}$), the equilibrium of dispersive and nonlinear effects that characterizes the soliton is only mildly perturbed. In this situation, the soliton can rearrange its shape: its peak power droops slightly and its width increases accordingly [112, 116].

1.2.3 Effect of high-order terms

High-order solitons are generally less stable than the fundamental ones and can break up into its fundamental components or other wave features under the influence of various phenomena. The most common ones are higher-order dispersion (especially TOD), Raman scattering, self-steepening, two-photon absorption and pulse chirp perturbation. This soliton breakup is referred as **soliton fission**, which is essential for supercontinuum generation in PCFs [66]. The fission process takes place at a distance z_{comp}, where the maximal soliton compression is achieved (**soliton compression length**). For soliton numbers $N > 10$, it can be approximated as follows [2]:

$$z_{\text{comp}} = \left(\frac{0.32}{N} + \frac{1.1}{N^2} z_0\right) \tag{1.38}$$

As a matter of this, the nonlinear propagation scenario of high-order solitons can be divided into three distinguishable phases:

1. Initial phase, with temporal compression/spectral broadening;
2. Soliton fission into their fundamental components;
3. Final phase, with individual propagation of the generated fundamental components.

All the physical phenomena listed above have a predominant role during one phase of propagation and are responsible, for example, of the red-shift of the soliton components or the generation of dispersive waves. In order to clarify their contribution to the pulse propagation through optical fiber, each of the phenomena will be briefly described in the following subsections.

High-order dispersion terms

In section 1.1.1, I explained that the dispersion curve can be written as a Taylor expansion around the carrier frequency ω_0 according to Eq.(1.7) and (1.8). GNLSE in Eq.(1.1) reports on the left side both the β_2 and β_3 terms, which are responsible for GVD and TOD, respectively. It is possible to introduce another term in the GNLSE, which takes into account the effect of the forth-order dispersion (FOD) and it's proportional to β_4. I have already discussed about GVD, now I describe the effect of TOD and FOD. The effect of high-order dispersion terms (characterized by β_p with $p \geq 5$) is no further discussed because it is generally negligible with respect to GVD and it is not correlated to any observable physical phenomena.

From Eq.(1.11), it is possible to notice that β_3 is proportional to the first derivative of the dispersion curve $S(\lambda) = dD(\lambda)/d\lambda$. Therefore, if the optical pulses propagate relatively far from the zero-dispersion wavelength (ZDW) - i.e. where the dispersion curve $D(\lambda)$ is less steep - the TOD effects can be treated as a small perturbation. It acts only of the spectral peak position of the soliton and not of its amplitude, frequency and phase. The peak q changes according to this equation [68]:

$$\frac{dq}{d\xi} = -(\omega - \omega_0) + \frac{\beta_3}{6|\beta_2|T_0}\eta^2 \tag{1.39}$$

where the term $\omega - \omega_0$ represents the frequency shift from the carrier ω_0. In physical terms, TOD induces a delay in the solitons and, in general, is negligible for picosecond pulses when β_2 is relatively higher than zero and for distances $\xi > 100$ [117].

In case of $\beta_3 < \beta_2$ (approximately by one order of magnitude), TOD affects the leading and the falling edges of the soliton. The pulses becomes asymmetric, with the trailing part containing a weakly decaying dispersive wave. For $\beta_3 \approx \beta_2$, the soliton can loose its stability and propagate with a complex chaotic dynamic [118].

As TOD $\propto dD(\lambda)/d\lambda$, the effect of the TOD can be minimized with a proper fiber dispersion engineering and choice of the carrier frequency, which should be sufficiently far from the ZDW [119].

The effect of FOD is the emission of a Cherenkov radiation by the soliton at the frequencies $\omega_{\text{rad,FOD}} = \pm 1/\sqrt{2\epsilon}$, where $\epsilon = \beta_4/(24|\beta_2|t_0^2)$ [120]. These radiations have lower intensity than the main soliton one and cause a decay of the soliton energy with an exponential law on ϵ [121]. For pulses exceeding 100 fs and in proximity of the ZDW, the effect of FOD is weaker than TOD [120]. Moreover, the Cherenkov radiations emitted by FOD are generally very stable because they can rely on the soliton MI balance over many soliton periods, which suppresses their self-frequency shift [121].

Radiation from High-order solitons

It has been shown that, if the soliton number N in Eq.(1.31) has a non-integer value, the solution of GNLSE is in the form of a soliton plus a non-solitonic remainder, which propagates as a linear (purely dispersive) wave. This is referred as **soliton radiation** [109, 122]. The first study on it was conducted by Zakharov and Shabat [123]. Radiation waves are subjected to dispersive broadening, which means that their energy is dispersed away from the soliton. After a soliton period z_0 determined by Eq.(1.34), the soliton itself emerges. Until that happens, the different phase evolution of soliton and radiation creates a beat note, visible as a slowly-decaying beat pattern (Fig.1.4a) [124]. If N is integer, the soliton follows a period pattern (with period z_0 independently on N) (Fig.1.4b).

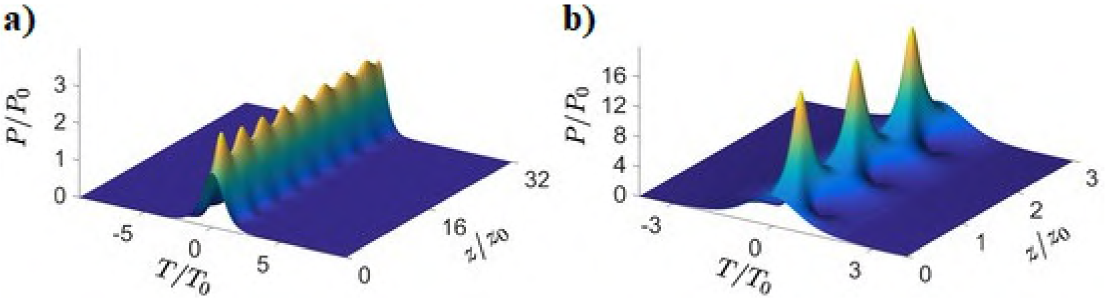

Fig. 1.4: *(a) Evolution of a soliton with number $N = 1.2$: a slowly decaying beat with radiation causes the soliton to emerge gradually. (b) Evolution of a soliton with $N = 2$: the soliton period is perfectly recognizable.* [124].

The energy of the soliton radiation reaches its maximum value of $E_{\text{rad}} = E_{\text{sol}}/4$ [124]. However, Satsuma and Yajima verified mathematically that the energy transfer between soliton and radiation wave is conservative [125]. It means that, in case of soliton perturbed only by radiation waves - i.e. with non-integer N - can readjust its shape after every period z_0. The periodic transfer of energy between the soliton and the radiation wave is advantageous for the design of optical fibers cascaded systems for efficient soliton compression purposes [126].

Stimulated Raman scattering

The Stimulated Raman Scattering (SRS) leads to a redistribution of spectral power to the advantage of the low-frequency slope of the pulse spectrum. It is caused by the scattering of a photon to a lower-frequency photon by one of the molecules of the medium, which make transition to a higher-energy vibrational state. The evidence of SRS is given by the growth of frequency-shifted radiations called Stokes waves, which is described by the following equation [68]:

$$\frac{dI_S}{dz} = -g_R I_P I_S \tag{1.40}$$

where I_S is the Stokes intensity, I_P the pump intensity and g_R the Raman-gain coefficient, which is related to the imaginary part of the third-order susceptibility. Its spectral $g_R(\Omega)$ (with Ω as the pump-Stokes waves frequency shift) characterizes the SRS and depends generally on the composition of the fiber core material.

A first study of the Raman gain in silica-core fibers was performed by R. H. Stolen et al. [127]. It showed that the spectral center of mass of a pulse is shifted to longer wavelengths (in [127], from 532 nm to 972 nm - first-Stokes peak generation). Then, Gordon calculated that the Raman frequency shift scales with the inverse fourth power of the pulse width: $d\nu/dz = 0.0436/\tau^4$ [THz/km], where ν is the frequency displacement in THz [128].

In the case of hyperbolic secant pulses propagating in a medium with anomalous dispersion ($\beta_2 < 0$), which is the case of my interest, the propagation has a peculiar dynamics [129]. First, the pulse is subjected to both GVD and SPM effects and undergoes self-compression, forming an intense narrow peak. After that, the pulse continues to be compressed, but **red-shifted Stokes wings** starts to appear in the spectrum. Then, part of the broadened spectrum fall in the region of SRS. Therefore, the pump pulse forms a new intense pulse at the Stokes frequency, which cuts the trailing tail of the pump pulse itself. By increasing the pump power, the SRS appears earlier and the Stokes pulse can acquire more energy till the limit of when it has a comparable frequency to the pump one (limit of pump-Stokes resonance).

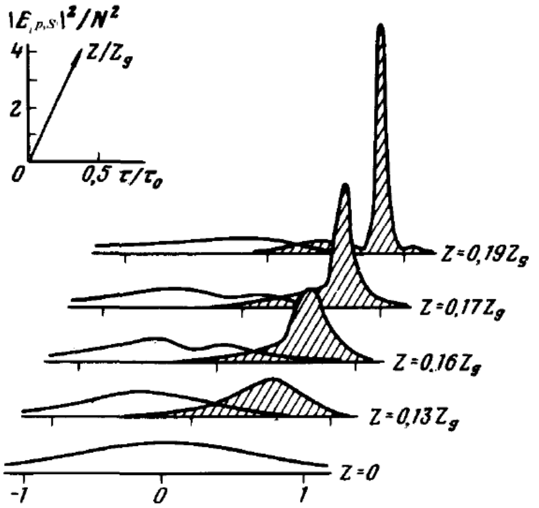

Fig. 1.5: *Stokes pulses generated by SRS in the field of an hyperbolic secant pulse with* $N = 5$. [129].

Fig.1.5 reports the Stokes pulses generated by SRS in the field of an hyperbolic secant pulse with intensity $I(0,\tau) = N^2 \operatorname{sech}^2(\tau/\tau_0)$ (with τ_0 initial length of the pump pulse) with $N = 5$ [129]. The pulse evolution has the dynamics described in the previous paragraph. In fact, considering $Z_g = \tau_0^2/(\partial^2 k/\partial\omega^2)$, the pulses have a group velocity difference of $\Delta v = Z_g|1/v_s - 1/v_p/|\tau_0$ and follow these propagation steps:

1. Transfer of energy between the pump and stimulated-Raman pulse ($z \approx 0.13Z_g$);
2. Generation of a symmetric stimulated-Raman pulse ($z \approx 0.17Z_g$);
3. Isolation of the non-soliton components ($z \approx 0.19Z_g$).

The SRS effect is taken into account in the GNLSE. The term expressing it is shown on the right-end side of Eq.(1.1) in a simplified version, which contains the normalized first moment of the nonlinear response function T_R. It is calculated by integrating the Raman response $R(t)$ in this way: $T_R = \int_{-\infty}^{+\infty} tR(t)dt$. Generally, for silica glass, $R(t)$ has the form

$$R(t) = (1 - f_R)\delta(t) = f_R h_R(t), \tag{1.41}$$

where f_R defines the relative contribution of SRS to the nonlinear refractive index n_2 at the central frequency ω_0, $h_R(t)$ is the medium **Raman response function** in time domain and $\delta(t)$ is the delta function. The first term in Eq.(1.41) describes the instantaneous Kerr response, while the second term represents the delayed Raman response of the medium. The Raman response of the medium $h_R(t)$ is typically modeled as a single Lorentzian line centered at the corresponding optical phonon frequency in the frequency domain. It is expressed as a decaying sine function he time domain:

$$h_R(t) = \frac{\tau_1^2 + \tau_2^2}{(\tau_1\tau_2)^2} \exp\left(- \frac{t}{\tau_2}\right) \sin\left(\frac{t}{\tau_1}\right) \tag{1.42}$$

where $1/\tau_1$ is the frequency of the emitted phonon and $1/\tau_2$ characterizes the bandwidth of the modeled Lorentzian line [131]. This model is valid for pulses being not longer than ≈ 100 fs. More accurate models were purposed by Mamyshev and Chernikov [132] and by Lin and Agrawal [133].

An estimation of the evolution of the Raman-induced frequency shift (RIFS) within the propagation distance z for hyperbolic secant solitons was calculated by Santhanam and Agrawal [130]. In the case of no losses, no chirp and no other high-order effects, the shift $\Omega_R(z)$ evolves in this way:

$$\Omega(z) = -\frac{8T_R|\beta_2|z}{15\tau^4} \tag{1.43}$$

The expression is in accordance with the first calculations of Gordon et al. [128]. Fig.1.6 show the RIFS and pulse widths

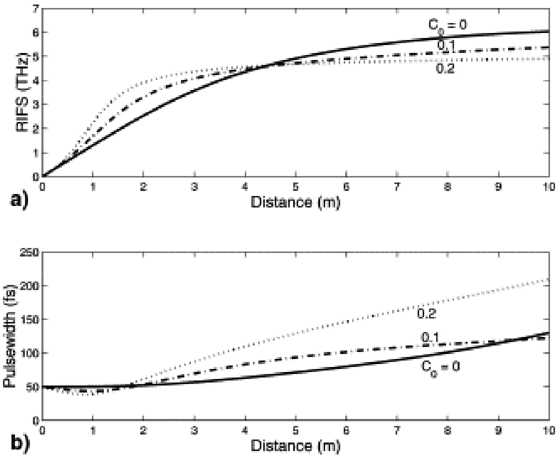

Fig. 1.6: *Evolution of (a) RIFS and (b) pulse width when* sech*-shaped pulses with* $\lambda = 1550$ *nm and* $T_0 = 50$ *fs propagate inside a 10-m-long fiber exhibiting anomalous dispersion (*$D = 4$ *ps/km/nm). The input chirp parameter* C_0 *is in the range* $0 - 0.2$ *for the three curves* [130].

as a function of the distance z in a 10-m-long fiber exhibiting an anomalous dispersion $D = 4$ ps/km/nm. The hyperbolic secant input solitons have a wavelength of $\lambda = 1550$ nm and temporal width $T_0 = 50$ fs. Also $\alpha = 0.2$ dB/km and $\beta_3 = 0.1$ ps^3/km. The solid curve represents the case of standard solitons, while the other curves report the case of chirped pulses (model in [130]).

In the unchirped case, the pulse width is initially maintained, but begins to increase after 2 m because of the RIFS and TOD effects. The magnitude of RIFS becomes comparable to the spectral width of the pulse (about 2 THz) at a distance of 2 m: Ω_R increases linearly initially up to that distance of 2 m and saturates as the pulse width increases. A relatively small chirp affects the RIFS considerably, as visible from the other curves in Fig.1.6.

In conclusion, RIFS resulting from SRS is a general phenomenon that occurs for pulses (including hyperbolic secant ones) propagating in anomalous dispersion regime. It becomes quite large in the case of ultrashort pulses because it depends on the local pulse width as τ^{-4} and varies considerably with the initial pulse chirp. Therefore, RIFS can be very large for solitons and can become even comparable or larger than the spectral width of the pulse up to saturation (soliton broadening).

Self-steepening

The self-steepening (SST) term results from the intensity dependence of the group velocity and leads to an asymmetry in the pulse shape [134–136]. It can produce shifts in spectral and temporal positions even in the absence of the Raman term [137].

In case of $\beta_2 = \beta_3 = 0$ and including the term responsible for SST, Eq.(1.30) assumes the form

$$\frac{\partial U}{\partial \xi} = iN^2 \left[|U|^2 U + is \frac{\partial U}{\partial \tau} |U|^2 U \right] \tag{1.44}$$

where $s = \omega_0 / T_0$ is the parameter that governs the SST effect.

From Fig.1.7 (in case of $s = 0.3$ and $N = 1$), it can be seen that, by increasing the value of ξ (normalized distance, as in Eq.(1.29)) the pulse becomes asymmetric, with its peak shifting towards the trailing edge. Therefore, in the absence of GVD effects, SST can create an optical shock on the trailing edge of the pulse. This is due to the intensity dependence of the group velocity such that the peak moves at a lower speed than the wings. For hyperbolic secant pulses, the distance z_s at which the shock is formed is given by $z_s \approx 0.43 L_{\mathrm{NL}}/s$ [68].

For an hyperbolic secant pulse with $N = 1$, the GVD reduce drastically the effect of SST and causes the smoothing of the trailing edge [138]. The intensity of the pulse peaks remains more or less constant during the propagation, but the pulse center is changed due to SS. In case of $N \geq 2$ and $N = 3$ (Fig.1.8b), the pulse envelope becomes asymmetric and splits to several sub-pulses during the propagation, which means that they are subjected to soliton fission. Therefore, SST affects the spectral broadening induced by SPM, causing **spectral asymmetry**: the red-shifted components are more intense than the blue-shifted ones. Fig.1.8 reports the propagation of an hyperbolic secant pulse over the distance $\xi = 50$ for $s = 0.3$ and (a) $N = 2$ and (b) $N = 3$.

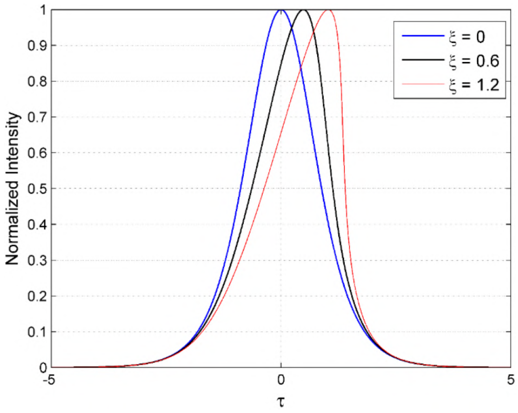

Fig. 1.7: *Influence of self-steepening and self phase modulation effect on the propagation characteristic of hyperbolic secant pulses* [138].

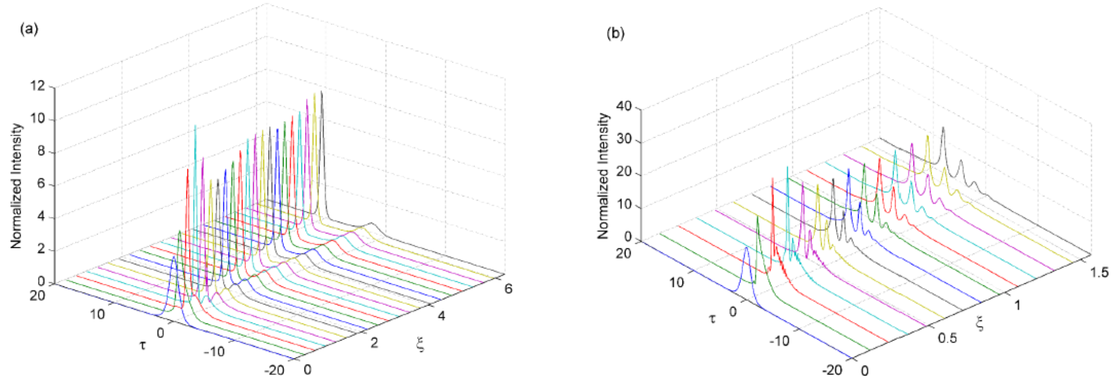

Fig. 1.8: *Propagation of the hyperbolic secant input pulse with (a)* $N = 2$ *and (b)* $N = 3$ [138].

Blue-shifted dispersive waves generation

The generation of dispersive waves (DWs) is a common optical phenomenon that occurs when high-power pulses are propagating in optical fibers with non-negligible high-order dispersion [139–141]. It has been observed in the case of both normal [142, 143] - red-shifted DWs (R-DW) - and anomalous dispersion regime [144, 145] - blue-shifted DWs (B-DW) - and it has been exploited for supercontinuum generation in microstructured optical fibers [146, 147] and soliton microcomb generation [148]. One of the most important contributions to the generation of DWs is the **cascaded four-wave mixing** (CFWM) phenomenon [141, 145]. It can be explained as a consequence of a small detuning $\delta\omega$ of the pump from the ZDW (i.e. in high TOD regime). If the fiber exhibits anomalous dispersion, a soliton is generated at frequency $\delta\omega$; in order to respect the phase-matching condition, a dispersive wave with a detuned frequency $-2\delta\omega$ from the ZDW will propagate in the normal dispersion regime in phase with the soliton (blue-shifted DW). A schematic of the CFWM principle is reported in Fig.1.9. The coherent transfer of energy between the pump and the dispersive wave is known in literature as spectral recoil [149, 150]. The peak conversion of the cascade always occurs at the detuned frequency Ω_{DW} from the pump one

$$\Omega_{\mathrm{DW}} = -3\frac{\beta_2(\omega_0)}{\beta_3(\omega_0)} \tag{1.45}$$

where $\beta_2(\omega_0)$ and $\beta_3(\omega_0)$ are the GVD and TOD coefficients evaluated at the pump frequency ω_0 [142, 151].

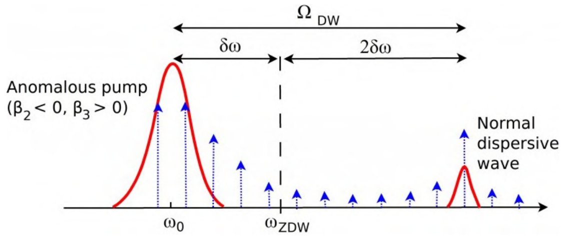

Fig. 1.9: *Principle of nonlinear cascaded four wave mixing: the power is transferred from an anomalous pump to a dispersive wave in the normal dispersion regime.*

I will concentrate on the case of B-DW because it's more interesting in the context of soliton propagation in optical fibers. In addition to CFWM, the are many other physical phenomena that cause the formation of DWs among soliton, which are rather complicated and out of my discussion. Here I slightly describe the most important ones:

- **TOD and Cherenkov radiation generation**: The Cherenkov radiation is the resonant radiation of the solitons emerging in the region of the anomalous GVD, which overlap spectrally with the normal GVD region [152, 153]. This overlap creates suitable conditions for energy transfer from the soliton to a resonant DW, which has a specific frequency and wave number at the intersection of the dispersion characteristics of the soliton and linear waves [121, 154].

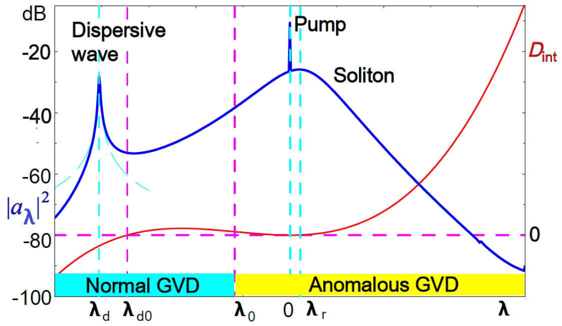

Fig. 1.10: *Schematic image of the dispersion law and associated soliton and dispersive wave dynamics. $D_{int} = \beta_1(\lambda)$. λ_{d0} is the ZDW, λ_r is soliton spectral peak, λ_d is the dispersive wave wavelength. Pump wavelength corresponds to $\lambda = 0$ [152].*

  The intensity of the Cherenkov peaks (equal to $2\beta_3/3\pi^2\sqrt{(}\beta_2)$ [152]), for a given detuning between the solitons and their resonances, is several orders of magnitude less than the intensity of the DWs generated by CFWM [145];

- **Cross-Phase Modulation (XPM)**: XPM interaction between the soliton and the blue dispersive wave results in an enhancement of the bandwidth of the continuum towards the blue wavelengths due to the sign of the group velocity mismatch between the soliton and the dispersive wave [155].

- **Intrapulse Raman Scattering and soliton deceleration**: It has been shown that the B-DW in the normal dispersion region can be trapped by the potential barrier presented by the decelerating soliton in the anomalous dispersion region and then the two pulses co-propagate along the fiber [141,147,156]. The DWs generated by both of these mechanisms initially have group velocities smaller than those of the solitons. However, the solitons are continuously decelerated and the DWs catch up with and start to interact with the solitons. This interaction leads to emission of new frequencies at shorter wavelengths.

In general, the impact of DWs in soliton propagation and supercontinuum generation as well is rather negligible, even if the pump is sufficiently close to the ZDW [150]. In addition, Dudley et al. predicted by numerical simulations that the energy transfer to the DWs is significantly reduced by SRS [73]. When SRS is taken into account, the soliton frequency shift increases up to longer wavelength due to the self-frequency shift and the amplitude of DWs is reduced.

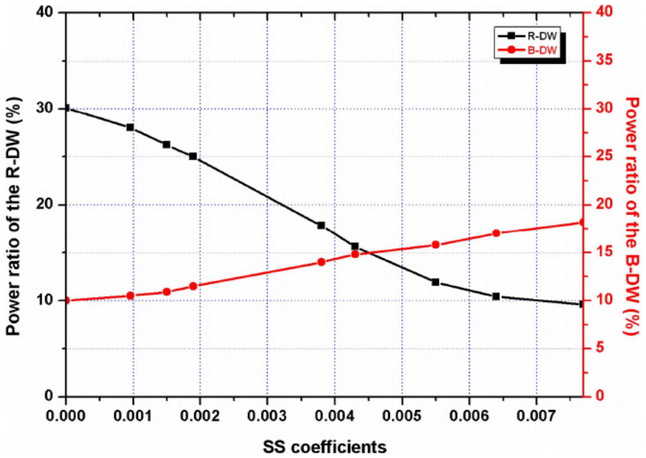

Fig. 1.11: *Power ratio of the R-DW (square-symbol line) and B-DW (circus-symbol line) intensity are as a function of SST coefficients.* [157].

Even SST contributes to decrease the effect of DWs during the pulse propagation. Fig.1.11 illustrates the power ratio of the B-DW and R-DW to the total output power as a function of SST coefficient s (see Eq.(1.44)) [157]. While the intensity of R-DW is significantly affected by SST in a wide range of values, with a considerable fall in the percentage of their power ratio, the B-DW intensity changes just slightly, with a slow growth in the percentage of B-DW ratio. This indicates that SST effect leads to an energy redistribution between the soliton components and the DWs.

In conclusion, good strategies to reduce the effect of DWs are not only the proper choice of the pump wavelength, but even the minimization of the TOD effect. As already mentioned, this can be done by a proper dispersion engineering of the fiber structure, which will be the topic of the next chapter of this dissertation.

Other nonlinear effects

- **Two photon absorption**: It is a specific type of inelastic nonlinear effect and describes the simultaneous absorption of two photons that occurs normally only if the photon energy is equal or higher than the half bandgap energy of the material. It has been shown that this phenomenon perturbs the propagation of higher-order solitons [158] and affect operation of certain nonlinear devices, e.g. Kerr-based optical regenerators [159] or nonlinear directional coupler based switching devices [160, 161]. Its contribution is significant for waveguides with low nonlinear refractive index n_2 and high optical intensities [162]. As my designed DCF includes a glass material with high n_2 (20 times higher than silica one) and energies in the nanojoule range, the effect is not included in my model of the GNLSE.

- **Spontaneous Raman scattering**: Spontaneous Raman scattering processes are generated by independent oscillations (vibrations and rotations) of the atoms in molecules. It is much slower than Kerr effect because it involves atoms nuclei rather than electrons (as for Kerr) [163]. It is responsible of the generation of Stokes and anti-Stokes spectral peaks, at higher and lower wavelengths than the pump one, respectively (Fig.1.12). It can be exploited for making distributed sensors for strain and temperature profiles [164,165]. It has an impact on the counting probability in quantum key distribution systems based on optical fibers [166].

- **Brillouin scattering**: It is similar to spontaneous Raman effect, but it includes the vibration of whole structure of atoms, which produces sonic waves. The oscillations due to Brillouin scattering are much slower than Raman ones and generate sonic phonons at higher/lower frequencies than the Raman Stokes/anti-Stokes peak ones (Fig.1.12). The process is too slow to influence propagation of femtosecond pulses relevant for this work. Anyway, it is disadvantageous with ultrahigh-speed femtosecond soliton compression exceeding 40 GHz [167].

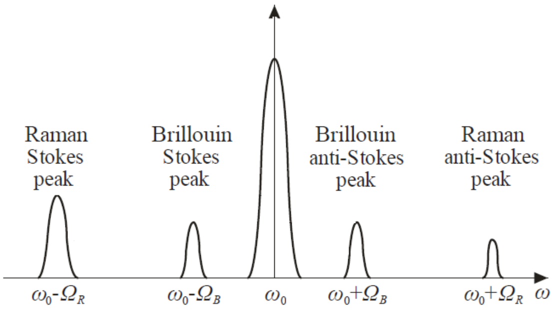

Fig. 1.12: *Spectral shifts caused by Raman scattering vibrations at* Ω_R *and Brillouin scattering vibrations at* Ω_B *[168].*

- **Pulse chirp perturbations**: If a soliton pulse with a strong, symmetric chirp is injected into a lowly anomalous dispersion optical fiber can undergo an irreversible pulse breakup. In this case, a number of fundamental solitons are symmetrically ejected from the pulse, with the tallest solitons moving faster than the smaller ones and each one subjected to TOD and SRS with different strength [169]. This phenomenon can occur over hundreds of meters of fiber and can be caused by many perturbations, such as filtering, soliton amplification and perturbation by superimposed control pulses [170].

Optical phenomenon	Effect on soliton propagation	
GVD ($\beta_2 < 0$)	Self-compression	
SPM	Spectral broadening	
TOD	Pulse delay, dispersive waves	Soliton fission
SST	Pulse asymmetry, optical shockes	
SRS	Soliton frequency shift	
Losses	Power attenuation	
Spontaneous Raman scattering	Spontaneous Raman Stokes/anti-Stokes peaks	
Brillouin scattering	Brillouin Stokes/anti-Stokes peaks	
Pulse chirp perturbations	Perturbation, extra soliton peaks	

Table 1.1: *Optical phenomena and related effect on soliton propagation in optical fibers.*

1.2.4 Resume on soliton propagation in fibers and GNLSE

In light of what has been described so far, there are both linear and nonlinear phenomena that contribute to propagation of ultrashort pulses through optical fibers. Most of them have been already taken into account inside the GNLSE reported at the beginning of this chapter (Eq.1.1). It is time to propose it again and underline the terms corresponding to each of the most important phenomena described so far:

$$\begin{aligned}\frac{\partial A}{\partial z} + \underbrace{\frac{\alpha}{2}A}_{\text{Losses}} + \underbrace{i\frac{\beta_2}{2}\frac{\partial^2 A}{\partial T^2}}_{\text{GVD}} - \underbrace{\frac{\beta_3}{6}\frac{\partial^3 A}{\partial T^3}}_{\text{TOD}} &= \underbrace{i\gamma|A|^2 A}_{\text{SPM}} \\ &\underbrace{-\gamma\frac{i}{\omega_0}\frac{\partial}{\partial T}(|A|^2 A)}_{\text{SS}} - \underbrace{i\gamma T_R A\frac{\partial |A|^2}{\partial T}}_{\text{SRS}}\end{aligned} \tag{1.46}$$

Table 1.1 reports the optical phenomena that occur in optical fibers and their relative contribution in the case of soliton propagation. The combination of anomalous GVD and SPM is responsible for soliton generation and stability along propagation. Losses, TOD, SST and especially SRS contribute to soliton perturbations and soliton fission. The rest of the phenomena have a negligible impact on solitons; therefore, their effect is not taken into account in the GNLSE.

As the solutions of GNLSE is rather complicated and could be time-consuming, many versions of GNLSE have been successfully formulated in order to simulate numerically the nonlinear pulse propagation simulations in optical fibers [132, 171–173]. One of the most general and advantageous forms has been derived by Blow and Wood [131]:

$$\begin{aligned}\frac{\partial A(z,T)}{\partial z} + \frac{\alpha(\omega_0)}{2}A(z,t) - \sum_{p\geq 2}\frac{i^{p+1}}{p!}\beta_p(\omega_0)\frac{\partial^p A(z,T)}{\partial T^p} &= \\ i\gamma(\omega_0)\left(1 + i\tau_{\text{shk}}\frac{\partial}{\partial T}\right)\left[A(z,t)\int_{-\infty}^{+\infty} R(T') \times |A(z,T-T')|^2 dT'\right]&.\end{aligned} \tag{1.47}$$

It is a slowly-varying-envelope approximation of the general form in Eq.(1.1) and can sufficiently model the wave-packet evolution of field down to a single-cycle pulse

[174]. On the left hand side of Eq.(1.47), the attenuation $\alpha(\omega_0)$ and GVD $\beta_p(\omega_0)$, $(p \geq 2)$ coefficients are present. The right hand side of shows the nonlinear effects, including SST and SRS. The medium nonlinear response function $R(T')$ includes both instantaneous Kerr and delayed Raman contribution. The Raman relative contribution f_R and response function h_R Eq.(1.41) are usually determined experimentally for the material used for the fiber. The time derivative term on the right hand side of Eq.(1.47) models the SST in another form of Eq.(1.1): it is defined through the optical shock formation time τ_{shk}, which is usually derived as an approximation to γ first-order derivative in this way:

$$\tau_{\text{shk}} = \frac{1}{\omega_0} + \frac{\partial}{\partial\omega}\left[\ln\left(\frac{1}{n_{\text{eff}}(\omega)A_{\text{eff}}(\omega)}\right)\right]_{\omega=\omega_0} \tag{1.48}$$

where n_{eff} is the fiber effective refractive index calculated following Eq.(1.6), n_{eff} is the fiber effective refractive index calculated following Eq.(1.16) and ω_0 the pulse central frequency [175]. The inclusion of the term in Eq.(1.48) allows to model the wave packet envelope evolution down to pulse durations as short as one carrier oscillation cycle [174].

Instead of the time-domain formulation, an equivalent version in the spectral domain has been formulated and adopted in many studies as well [155, 172, 176]. Its physical interpretation is not straightforward and the nonlinear processes are quite difficult treat in this way. Nevertheless, its easier and faster to compute, as the frequency dependence of effects such as losses or dispersion can be incorporated more directly there. In fact, the separate solving of linear and nonlinear terms in frequency and time domain, respectively, is the basis of well-known split-step Fourier method [68]. This method is rather advantageous and it is presented in details in Appendix A.

1.3 High-order soliton propagation in dual-core optical fibers

DCFs are optical fibers which consist of two cores parallel to each other throughout their length. The cores are designed to be close enough to allow the evanescent fields, which inherently propagate outside the core, to overlap in the cladding region. This leads to a transfer of optical power between the cores under suitable conditions. For this advantageous property, DCFs have been currently studied as potential all-optical switching devices due to their relatively simple structure, well-consolidated fabrication process and promising integration inside optical networks [54, 55]. DCFs are one of the simplest realization of the NLDC approach [177]. I introduce this concept in the next section.

1.3.1 The nonlinear directional coupler

NLDCs are 4-port (2-input 2-output ports) devices that allow for intensity-controlled all-optical switching of optical signals between the two output ports. Theoretical studies related to them were performed for the first time in 1982 by Jensen and Maier [178]. From then on, many implementations of the NLDC have been purposed in the scientific literature, such as the plasmonic [179], semiconductor [180] or photonic crystal [181, 182], the asymmetric [183, 184], the graphene-coated nanowires [185] or the liquid crystal approach [186]. The most interesting solutions in my discussion are the fiber-based ones, for example the active (doped) [187, 188] or fiber Bragg grating-assisted NLDCs [189, 190]. It has other - rather less popular - applications than all-optical switching, such as active lasers [191] or optical gratings [192] and enabling the generation of entangled photons [193].

The study of all-optical switching in such types of NLDCs can be performed with two different approaches: the **self-switching** and the **control/signal switching**. In the first case, the signal pathway is controlled by the intensity of the transported signal itself. In the other case, the redirection of a low-power signal is controlled by another control pulse with higher power. I explore both alternatives in the next chapters; however, in this section I limit my discussion to self-switching operation in a simple symmetric NLDC, which the basis for the implementation of solitonic steering in DCFs.

In the most general and simple form, NLDCs are made of two nonlinear optical waveguides placed in close proximity. As observable in the schematic of Fig.1.13, the coupling properties between the waveguides are controlled by the power of the input radiation with two alternative scenarios:

1. At low power (red line in Fig.1.13), the light coupled into one waveguides is transferred to the other waveguide at the coupling length (linear coupling).
2. At relatively high power (blue line in Fig.1.13), the optical nonlinearities introduces a phase mismatch in the light field, which leads to a decoupling of the waveguides.

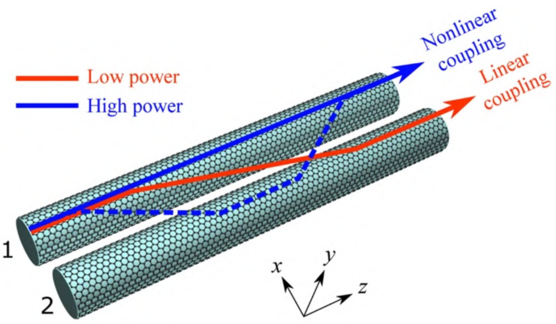

Fig. 1.13: *NLDC principle: the linear and the nonlinear propagation scenarios are evidenced by a red and blue line, respectively [185].*

DCFs represent one of the possible implementations of the NLDC for all-optical switching purposes. In fact, in their easiest form, they are made of two parallel cores (characterized by a refractive index n_{co}) incorporated into a cladding layer (with refractive index $n_{cl} < n_{co}$). An example of DCF schematic can be found in Fig.1 in the introduction section (page IX). In that figure, the green and the gray colors represent the materials with n_{cl} and n_{co}, respectively. The basic principle of controlled-intensity switching is exactly the same as described above, considering the fiber cores instead of the two parallel waveguides. As for the basic NLDC, two approaches can be used to describe the optical properties of DCFs [194]:

1. The theory based on the so-called **supermodes**: they are the eigenmodes of whole DCF structure and, by definition, their intensity distribution doesn't change during the propagation;

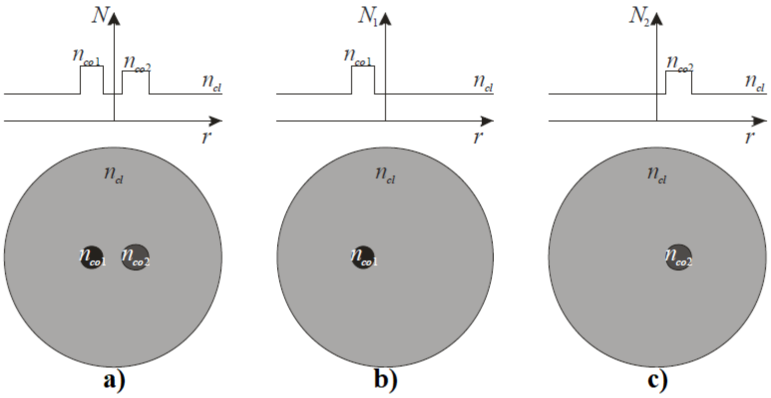

Fig. 1.14: *Refractive index profile of the DCF structure: (a) combined $n_1(x,y) \cup n_2(x,y)$, (b) $n_1(x,y)$ and (c) $n_2(x,y)$ [168].*

2. The **coupled-mode theory**: it rather more intuitive because it's based on mutual two-core interaction, which is easier to understand physically. It is based on assumption that fields propagate in each core separately and their interaction is defined by coupling coefficients.

The two approaches are complementary between each other, as they give different information on the same phenomenon. I discuss them separately in the next sections.

Coupling mode theory

Coupled-mode theory (CMT) is an approximation of Maxwell's equations and it's more intuitive description because the coupling characteristics of DC structure are defined directly on the basis of coupling coefficients [195–197]. The energy transfer between two cores is governed by a pair of coupled-mode equations (CME) [198]. I discuss only the case of the fundamental mode, which propagate faster than the higher-order ones and typically has the best in-coupling efficiency (IE), the lowest losses and the highest contribution to nonlinear effects.

Under the weekly guiding approximation [199], CME can be obtained solving Helmholtz equation for light with central frequency ω_0 propagating along the fiber z-axis:

$$\Delta\tilde{\mathbf{E}}(\mathbf{r},\omega_0) + n^2(x,y)k_0^2\tilde{\mathbf{E}}(\mathbf{r},\omega_0) = 0 \tag{1.49}$$

where $k_0 = \omega/c$ (c speed of light) is the light vacuum wave number and $\tilde{\mathbf{E}}(\mathbf{r},\omega_0)$ is the Fourier transform of the electric field $\mathbf{E}(\mathbf{r},t)$ [194]. As shown in Fig.1.14, the refractive index n of the DCF in x-y plane is considered real (no absorption) and has value of $n_{\mathrm{co_m}}$ (with $m = 1,2$ the individual fiber cores) in the region occupied by the two cores and n_{cl} elsewhere. The CMT approximation is based on an assumption that the electric field $\tilde{\mathbf{E}}(\mathbf{r},\omega_0)$ can be decomposed into two separate parts for individual cores and the approximate solution of Eq.(1.49) results to be

$$\tilde{\mathbf{E}}(\mathbf{r},\omega_0) \approx \hat{\mathbf{e}}[\tilde{A}_1(z,\omega_0)F_1(x,y) + \tilde{A}_2(z,\omega_0)F_2(x,y)]\exp(i\tilde{\beta}z). \tag{1.50}$$

$\tilde{\beta}$ is the common propagation constant at ω_0, $\tilde{A}_m$ the amplitude of the electromagnetic field in the m-th core and $\hat{\mathbf{e}}$ the polarization direction of the optical field, which is assumed to remain unchanged during propagation. $F_m(x,y)$ denotes the spatial distribution of fundamental mode of the m-th core and must satisfy the following relation:

$$\frac{\partial^2 F_m}{\partial x^2} + \frac{\partial^2 F_m}{\partial y^2} + [n_m^2(x,y)k_0^2 - \bar{\beta_m}^2]F_m = 0 \tag{1.51}$$

where $\bar{\beta}_m$ is the propagation constant of the fundamental mode in the m-th core. The refractive index profile $n_m(x,y) = n_{\text{cl}}$ everywhere in the cross-sectional x-y plane except of the region occupied by the m-th core, where it takes the value n_{co_m}. Assuming that the mode spatial distributions are normalized such that $\int_{-\infty}^{\infty} |F_m(x,y)|^2 dxdy = 1$ it is possible to derive from Eq.(1.50) and (1.51) a pair of frequency-domain CME, which describe how $\tilde{A_m}$ evolves along the propagation direction:

$$\frac{d\tilde{A}_1}{dz} = i(\beta^{(1)} + \Delta\beta_{\text{NL}}{}^{(1)} - \beta)\tilde{A}_1 + i\kappa_{12}\tilde{A}_2 \tag{1.52}$$

$$\frac{d\tilde{A}_2}{dz} = i(\beta^{(2)} + \Delta\beta_{\text{NL}}{}^{(2)} - \beta)\tilde{A}_2 + i\kappa_{21}\tilde{A}_1 \tag{1.53}$$

k_{mp} is the coupling coefficient, defined as

$$k_{mp} = \frac{k_0^2}{2\hat{\beta}} \iint_{-\infty}^{\infty} (n^2 - n_p^2) F_m * F_p dxdy \qquad (p, m = 1, 2; p \neq m) \tag{1.54}$$

and it characterizes the mutual coupling of the cores, i.e., the energy transfer from the p-th to the m-th core. The nonlinear contribution to propagation constant in the m-th core has this expression:

$$\Delta\beta_m{}^{\text{NL}} = \frac{k_0^2}{2\beta} \iint_{-\infty}^{\infty} (n^2 - n_L^2) F_m * F_p dxdy \tag{1.55}$$

where n_L is the linear part of n. In general, both $\bar{\beta_m}$ and k_{mp} depend on frequency.

The obtained coupled-mode Eq.(1.52) and Eq.(1.53) incorporate both linear and nonlinear effects and take into account the asymmetry of the DC structure. The general CME can be solved only numerically. In the simplest case of low-power monochromatic CW excitation, CME Eq.(1.52) and Eq.(1.53) can be considerably simplified. By expanding the coupling coefficients $k_{mp}(\omega)$ and propagation constants $\beta_m(\omega)$ in a Taylor series around the carrier frequency ω_0 (with a similar procedure to Eq.1.7) as

$$\beta_m(\omega) = \beta_{0_m} + \beta_{1_m}(\omega - \omega_0) + \frac{1}{2}\beta_{2_m}(\omega - \omega_0)^2 + o((\omega - \omega_0)^3) \tag{1.56}$$

$$\kappa_{mp}(\omega) = \kappa_{0_{mp}} + \kappa_{01_{mp}}(\omega - \omega_0) + \frac{1}{2}\kappa_{2_{mp}}(\omega - \omega_0)^2 + o((\omega - \omega_0)^3), \tag{1.57}$$

I can arrange such quantities through $\bar{\beta}_a$ and δ_a (with a the order of the Taylor expansion coefficients), which define the guiding properties of the DC structure:

$$\bar{\beta}_a = \frac{1}{2}(\beta_{0_1} + \beta_{0_2}) \tag{1.58}$$

$$\delta_a = \frac{1}{2}(\beta_{0_1} - \beta_{0_2}) \tag{1.59}$$

Coefficients $\bar{\beta}_a$ are the Taylor expansion coefficients representing the propagation constant $\bar{\beta}$ of the whole DC structure. Coefficients δ_a are the measure of **asymmetry** between the cores. In the CW regime or quasi CW regime, both the dispersion and nonlinear effects can be neglected because the wave can be sufficiently characterized by central frequency ω_0. Therefore, the CME can be simplified to the following form

$$\frac{d\tilde{A}_1}{dz} = ik_{0_{12}}\tilde{A}_2 + i\delta_a\tilde{A}_1 \tag{1.60}$$

$$\frac{d\tilde{A}_2}{dz} = ik_{0_{21}}\tilde{A}_1 + i\delta_a\tilde{A}_2 \tag{1.61}$$

Eq.(1.60) can be solved by differentiating it and then substituting expression of $d\tilde{A}_2/dz$ in Eq.(1.61) on the right side, leading to

$$\frac{d^2\tilde{A}_1}{dz^2} + k_e^2\tilde{A}_1 = 0, \tag{1.62}$$

The same equation can be found for $\tilde{A}_2$. **Effective coupling coefficient** k_e is defined as

$$k_e = \sqrt{k_{0_{12}} + k_{0_{21}} + \delta_a^2} \tag{1.63}$$

With the boundary conditions $\tilde{A}_1(0) = \tilde{A_{10}}$ and $\tilde{A}_2(0) = \tilde{A_{20}}$, Eq.(1.60) and Eq.(1.61) have the following solutions:

$$\tilde{A}_1(z) = \left\{\tilde{A_{10}}\left[\cos(k_e z) + i\frac{\delta_0}{k_e}\sin(k_e z)\right] + i\tilde{A_{20}}\frac{k_{0_2}}{k_e}\sin(k_e z)\right\}\exp(i\bar{\beta}_0 z) \tag{1.64}$$

$$\tilde{A}_2(z) = \left\{\tilde{A_{20}}\left[\cos(k_e z) + i\frac{\delta_0}{k_e}\sin(k_e z)\right] + i\tilde{A_{10}}\frac{k_{0_1}}{k_e}\sin(k_e z)\right\}\exp(i\bar{\beta}_0 z) \tag{1.65}$$

Solutions of CME in Eq.(1.64) and Eq.(1.65) show that the transfer of the radiation between the two cores is periodic with half-period $k_e z = \pi/2$. The length where the maximum of energy is transferred to the other core is called **coupling length** (CL) L_c and is defined as

$$L_\mathrm{c} = \frac{\pi}{2k_e} \tag{1.66}$$

After defining the initial powers $P_{10} = |\tilde{A_{10}}|^2$ and $P_{20} = |\tilde{A_{20}}|^2$, I can calculate the power exchange between the cores:

$$P_1(z) = P_{10}\left[\cos^2(k_e z) + i\left|\frac{\delta_0}{k_e}\right|^2\sin^2(k_e z)\right] + P_{20}\left|\frac{k_{0_2}}{k_e}\right|^2 k_e\sin^2(k_e z) \tag{1.67}$$

$$P_2(z) = P_{10}\left|\frac{k_{0_1}}{k_e}\right|^2 k_e\sin^2(k_e z) + P_{20}\left[\cos^2(k_e z) + i\left|\frac{\delta_0}{k_e}\right|^2\sin^2(k_e z)\right] \tag{1.68}$$

Eq.(1.67) and Eq.(1.68) do not follow the energy conservation because some extra power is present in each core due to the evanescent mode field from the other core [4, 200]. This is the base for so called cross-talk in telecommunication systems.

If I consider the case of single-core excitation, which corresponds to impose $\tilde{A_{10}} = A_0$ and $\tilde{A_{20}} = 0$, the solutions of CME in Eq.(1.64) and Eq.(1.65) assume this form

$$\tilde{A}_1(z) = A_0\left[\cos(k_e z) + i\frac{\delta_0}{k_e}\sin(k_e z)\right] \tag{1.69}$$

$$\tilde{A}_2(z) = A_0\frac{ik_{0_1}}{k_e}\sin(k_e z) \tag{1.70}$$

Even in the case of single-core excitation, the radiation is periodically transferred between the two cores with a half-period equal to the CL L_c. However, Eq.(1.69) and Eq.(1.70) show that there is still an inefficiency of coupling due to the asymmetry of cores δ_0. This leads to a partial energy coupling between the cores, which means that not all the energy is transferred to the other core. The power transfer to the other core follows a periodic pattern, with a maximum at distances such that $ke_z = m\pi/2$, where $(m = 1, 2, ...)$. The CL $L_\mathrm{c} = \pi/(2k_e)$ is the shortest distance at which maximum power is transferred for the first time to the other core. Therefore, the power at the output of the two cores depends on the length of the fiber L and on the powers injected at the two input ends.

If the cores are perfectly symmetric ($\delta_0 = 0$) and are characterized by the same coupling coefficients ($k_{0_1} = k_{0_2} = k_e$) and in case of single-core excitation ($P_{10} = P_0, P_{20} = 0$), Eq.(1.67) and Eq.(1.68) assume the simplified form

$$P_1(z) = P_0\cos^2(k_e z) \tag{1.71}$$

$$P_2(z) = P_0\sin^2(k_e z) \tag{1.72}$$

with a clearly periodic exchange of energy between the cores. Only in this case, if the fiber length is $L = L_\mathrm{c}/2$, the power is equally divided between the cores.

1.3.2 Supermodes theory

Supermodes are the eigenmodes of the total DC (or multi-core) structure and propagate without changing their spatial distribution [201, 202]. Generally, the ratio between the energy in-coupling efficiencies of the two cores depends on the excitation adjustment at the input end. However, if the modes are excited in such way that the back-and-forth energy transfers from one core to the other with the same behavior, then there would be no energy exchange at all. This, from the CMT point of view, can be seen as a special DC excitation case when the energy transfer rates between individual cores cancel each other out and the amplitudes $\tilde{A}_{1,2}$ don't change along the direction of propagation z. Then, according to CME in Eq.(1.69) and Eq.(1.70) and neglecting the nonlinear contribution, $\tilde{A}_1$ and $\tilde{A}_2$ become z-independent if this condition on the DC excitation ratio f is satisfied

$$f = \frac{\tilde{A}_2}{\tilde{A}_1} = \frac{\beta - \bar{\beta}_1}{k_{12}} = \frac{k_{21}}{\beta - \bar{\beta}_2} \tag{1.73}$$

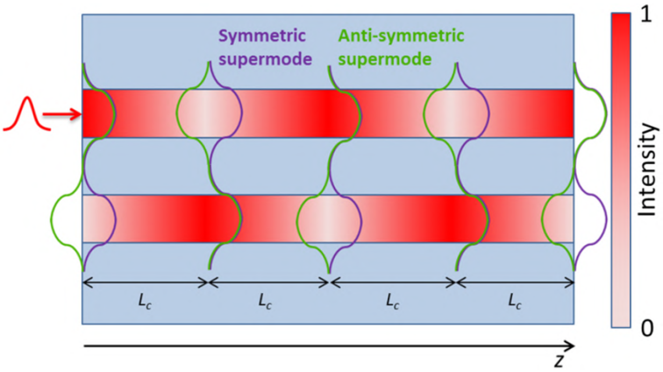

Fig. 1.15: *Description of inter-core energy transfer via intermodal interference of the supermodes propagating along the DC structure [168].*

Since the common propagation constant β satisfies a quadratic equation, I find two values of β, which I call β_S and β_A

$$\beta_{S,A} = \frac{1}{2}(\bar{\beta}_1 + \bar{\beta}_2) \pm k_e \tag{1.74}$$

The spatial distribution of the two eigenmodes with propagation constants β_S and β_A and corresponding excitation ratios f_S and f_A is given by

$$F_{S,A}(x,y) = (1 + f_{S,A}^2)^{-1/2}[F_1(x,y) + f_{S,A}F_2(x,y)] \tag{1.75}$$

where $f_{S,A}$ is obtained from Eq.(1.73) with $\beta = \beta_{S,A}$. $F_1(x,y)$ and $F_2(x,y)$ constitute the symmetric and anti-symmetric supermodes of the DC structure, respectively, with eigenvalues $\beta_{S,A}$. For symmetric DC structures, the two fundamental supermodes have an identical intensity distribution ($f_{S,A} = \pm 1$), but different phase distribution between the cores. The phase is the same in both cores in the case of symmetric supermode (even combination of $F_1(x,y)$ and $F_2(x,y)$) and opposite for anti-symmetric one (odd combination of $F_1(x,y)$ and $F_2(x,y)$). When the input conditions are such that an eigenmode of the coupler is excited, no power transfer occurs between the two cores. On the other hand, in the case of fiber excitation that does not correspond to DC eigenmode, both supermodes are excited simultaneously and exhibit a relative phase difference on propagation $\psi(z) = (\beta_S - \beta_A)z$. Consequently, the inter-core energy transfer can be seen as a result of mutual interference of the supermodes at given point along the fiber (Fig.1.15). L_c can be expressed in terms of beat length between the supermodes with this form:

$$L_c = \frac{\pi}{|\beta_S - \beta_A|} = \frac{\pi}{2\sqrt{k_{0_{12}}k_{0_{21}} + \delta_0^2}} = \frac{\pi}{2k_e} \tag{1.76}$$

Even if it has been neglected in the description of the theory, it has to be mentioned that the coupling characteristics of the DCF are polarization dependent because the effective refractive index of individual cores is affected by the presence of the opposite core [203]. As a consequence of this anisotropy, it is possible to determine the CL by the polarization of the light (polarization L_c). The impact of light polarization decreases with increasing the separation between the cores. Nonetheless, the cores must be close enough in order to support the coupling between the cores. Thus, the polarization dependence of CL of DCFs is advantageous for practical applications as polarization splitters [204, 205]. In my numerical studies, the issue is addressed in a semi-vectorial manner by evaluating the fiber guiding properties for two orthogonal polarizations: one along and one perpendicular to the inter-core axis, which I call **horizontal X-polarization** and **vertical Y-polarization**, respectively. As I consider propagation distances/fiber lengths in the order of tens of mm, the cross-polarization effects are not taken into account and the polarization is assumed not to change during the propagation.

1.3.3 Nonlinearly induced dual-core asymmetry

The theoretical discussion purposed above was limited to the CW regime. However, switching of CW radiation is not practical because the fiber can be damaged due to the high CW powers required for the switching operation. In practice, short optical pulses with high peak powers are used. Despite of this, the previous theory is still applicable for optical fibers exhibiting negligible GVD, losses and high-order terms effects. This corresponds to have a dispersion length L_D (used in Eq.(1.31)) much longer than the fiber length L. This is know as the **quasi-CW regime** [194]. For a symmetrical coupler in quasi-CW regime, the CME in the time domain can be derived from Eq.(1.52) and Eq.(1.53) and have this form

$$\frac{dA_1}{dz} = ikA_2 + i\gamma(|A_1|^2 + \sigma|A_2|^2)A_1 \tag{1.77}$$

$$\frac{dA_2}{dz} = ikA_1 + i\gamma(|A_2|^2 + \sigma|A_1|^2)A_2 \tag{1.78}$$

where $k = k_{12} = k_{21}$ and σ is the inter-core cross-phase modulation coefficient.

Cross-Phase Modulation

XPM is another nonlinear phenomenon that perturbs the soliton propagation through optical fibers. I have already shown its contribution to the propagation of high-order solitons in fibers in section 1.2.3, where I discussed about the generation of B-DW. Moreover, XPM has been observed in the case of birefringent fibers [206], in optical logic gates [111] or even in single-core fibers [207], when a pair of pulses co-propagate through the same core. In DCF symmetric couplers, it is caused by the mutual Kerr-like interaction between two fields propagating through the two cores: the high intensity field propagating through one core modifies the effective refractive index of that core, which can affect the phase of the field propagating in the other core [208]. The effect is amplified in case of asymmetric couplers, where the difference between the effective refractive indexes increases. In general terms, XPM contributes to SPM with an additional phase shift contribution [68]. The combination of both phenomena give rise to a total phase shift as follows:

$$\Delta\phi_\mathrm{NL} = \phi_1 - \phi_2 = \gamma L(1-\sigma)(P_1 - P_2) \tag{1.79}$$

where γ is the nonlinear parameter, L the fiber length and σ the XPM one; $P_{1,2}$ are the input powers for first and second cores, respectively. σ can be calculated numerically from the overlap integrals of the respective core fields. As both polarization and Kerr birefringence are quite negligible in DCFs, σ has a small value [209].

Nonlinear switching of CW and quasi-CW optical beams

Combing back to the quasi-CW model, Eq.(1.77) and Eq.(1.77) can be solved analytically. An important role is played by the critical power $P_C = 4k/[\gamma(1-\sigma)]$, which represents the power threshold at which half of the input power is switched nonlinearly from one core to the other in quasi-CW operation regime. Fig.1.16 shows the comparison between the theoretical CW (solid line) and quasi-CW (dashed line) switching performance. The trend of the solid curve is depending on the ratio P_0/P_C, where P_0 is the input power, and four regions of operation can be identified:

- $P_0/P_C \ll 1$ (**cross state**): The power is completely transfer to the second core.
- $P_0/P_C < 1$: The power is periodically transferred between the two cores. The CL L_c, which is strongly dependent on k, starts to increase as P_0 approaches P_C. At $P_0 = P_C$, L_c becomes infinite and half of the power is transmitted to the second core;
- $P_0/P_C > 1$: The power is transferred to the second core, but with lower percentage than 50%;
- $P_0/P_C \gg 1$ (**bar state**): Negligible (or, to the infinite limit, no) energy is transferred to the second core.

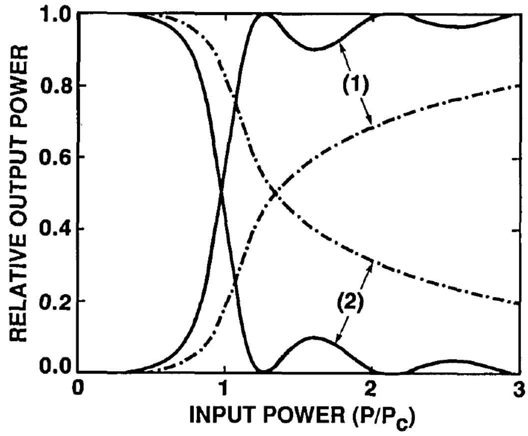

Fig. 1.16: *Nonlinear switching of CW beams in a fiber coupler with $kL = \pi/2$ as a function of the input power in CW case (solid curve) and quasi-CW case (dashed curve). Number 1 and 2 indicate the curves of the non-excited and excited core, respectively* [194].

Thus, a switching of an optical beam can be established in dependence of its input power. Moreover, I can observe that the optical physical mechanism that allows the switching is totally nonlinear because it is mostly governed by the dispersive-induced bistability imposed by SPM (through parameter γ). As a result, even a symmetric fiber coupler (with identical linear propagation constants for both cores) can behave like an asymmetric one because of phase-shift introduced by the nonlinear effects. This is the principle of **nonlinearly-induced DC asymmetry** [210]. In the limit case of large CW input powers, the SPM-induced detuning (phase shift) is so large that the input beam remains confined to the same core it was initially launched.

Nevertheless, the situation changes for short optical pulses (quasi CW-state). I can see from dashed line in Fig.1.16 that the switching induced by SPM phase shift is not only more gradual, but incomplete, even for high values of the ratio P_0/P_C and in absence of GVD phenomena. Some experimental studies were performed in order to demonstrate nonlinear switching of short pulses (80-100 ns) in DCF couplers [43, 211, 212]. One of the most successful and pioneering is the one conduced by Friberg et al. with 100 fs, 620 nm pulses in 5 mm long Ge-doped DC fiber [43]. Nonetheless, the efficiency of the switching was not sufficient for a possible applicability of the fiber and switched pulses suffered of significant distortions (inset of Fig.1.17a). The efficiency was improved in a later experiment conduced by Wiener et al. utilizing square-shaped fs pulses to avoid the pulse breakup Fig.1.17b [213]. Nevertheless, this approach is rather complicated because it involves a relatively complex pulse-shaping procedure, which, for ultrashort pulses, may lead to severe forms of dispersive distortion of the steep edges [214].

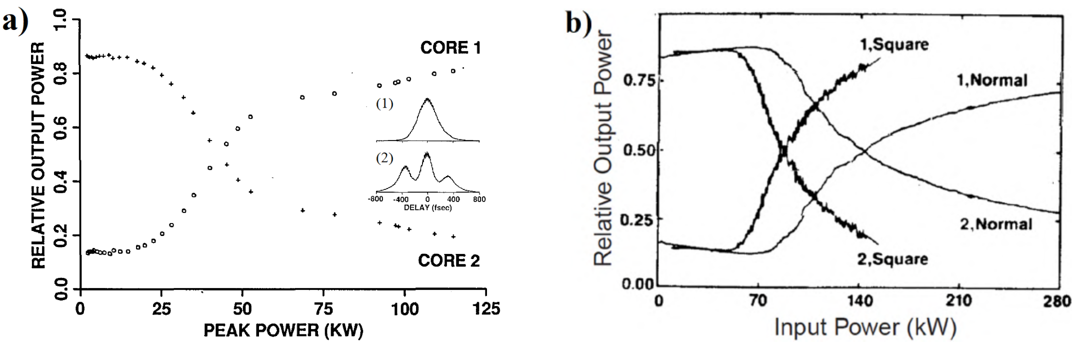

Fig. 1.17: *(a) Fractional output power from 5-mm DCF NLDC in case of 100 fs input pulses. As insets the output autocorrelation traces from (1) first and (2) second guide, where distortion is visible. (b) Comparison of experimentally measured NLDC performance with 90 fs Gaussian-like pulses (normal) and 540 fs square-shaped pulses (square)* [43].

Nonlinear switching of ultrashort pulses

In order to overcome pulse break-up and dispersive distortions, an alternative could be the use of soliton-like pulses at the input of the fiber [215]. As explained in section 1.2.1, a fundamental soliton can be generated in a fiber exhibiting anomalous dispersion and has an uniform phase distribution across the whole propagation. Solitons are rather advantageous for both phase and power-controlled switching because they show a similar behavior as the one predicted in case of CW radiation [44, 63, 197, 216]. In other words, their stability is responsible for their natural tendency to couple and switch avoiding the issue of incomplete switching and pulse breakup from the coupling process.

The solution of CME considering soliton pulses cannot be calculated analytically and can only be solved by means of perturbative or purely numerical methods [217, 218]. In the case of single-core excitation, I impose this input condition: $A_l(t, z = 0) = A_0 \operatorname{sech}(t/T_0)$, $A_2(t, z = 0) = 0$, where A_0 is the pulse peak amplitude and T_0

the pulse width. The behavior is identical to the one described for CW input beams case: whenever A_0 is smaller than a certain critical amplitude, the input pulse oscillates back and forth between the two cores, with a relatively small distortions; for input amplitudes higher than the critical one, the soliton transfer between the cores is inhibited.

Fig.1.18a presents the fraction of energy transmitted in the input channel as a function of the input peak power (in units of the CW critical power $P_\mathrm{C} = a_0^2/4k$) in case of $k = \pi/2$ and $T_0 = 1/\sqrt{2\pi}$. k and T_0 were chosen in this way in order to equalize the CW critical power to the fundamental soliton peak power. As seen in the graph, in the normal dispersion regime ($\beta_2 > 0$) the CW switching doesn't take place; on the opposite side, for the anomalous dispersion case ($\beta_2 < 0$), the switching characteristic is similar to the one of the CW beam case in Fig.1.16, apart from an increase of the switching power. The same characteristic is maintained even if the nonlinear response is non-instantaneous, which means characterized by a relaxation time τ (Fig.1.18b). Even when $\tau \approx T_0$, the switching is still quite efficient, with the drawback of higher switching powers required.

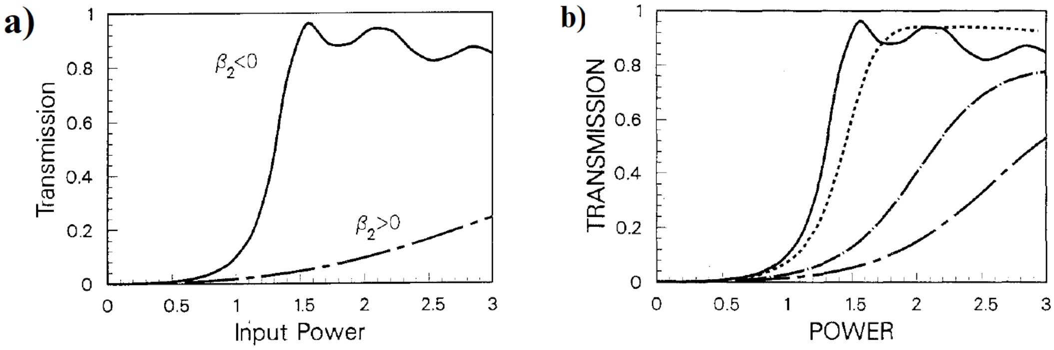

Fig. 1.18: *(a) Transmitted energy characteristic of a NLDC of length L_c vs. input peak power (in units of the CW critical power), in the normal ($\beta_2 > 0$) and anomalous ($\beta_2 < 0$) dispersion regime. (b) Soliton switching in a NLDC of length L_c as a function of the relaxation time τ: $\tau = 0$ (solid), 0.1 (dots), 0.3 (dot-dashes), 0.5 (short-long dashes).* [217].

1.3.4 Coupled generalized nonlinear Schrödinger equations

In order to model completely the ultrafast NLDC performance in DCFs including the linear and nonlinear perturbations, the most widely used method is based on the Coupled generalized nonlinear Schrödinger equations (CGNLSE). They are the results of the combination of GNLSE (Eq.(1.1)) and the CME in Eq.(1.52 and (1.53)), which were introduced in sections 1.2.4 and 1.3.1, respectively, and can be derived both in case of normal and anomalous dispersion regime. They can be found in various particular forms throughout the scientific literature: for example the time - or frequency - domain formulations, the absolute or normalized ones and many more. Including the optical losses terms and rearranging Eq.(1.52 and (1.53)), CME become

$$\frac{d\tilde{A}_1}{dz} + \frac{\alpha^{(1)}}{2}\tilde{A}_1 - i(\beta^{(1)} - \beta)\tilde{A}_1 - i\kappa_{12}\tilde{A}_2 = i\Delta\beta_{\mathrm{NL}}{}^{(1)}\tilde{A}_1 \tag{1.80}$$

$$\frac{d\tilde{A}_2}{dz} + \underbrace{\frac{\alpha^{(2)}}{2}\tilde{A}_2}_{\text{Losses}} - \underbrace{i(\beta^{(2)} - \beta)\tilde{A}_2}_{\text{Linear propagation}} - \underbrace{i\kappa_{21}\tilde{A}_1}_{\text{Optical coupling}} = \underbrace{i\Delta\beta_{\text{NL}}{}^{(2)}\tilde{A}_2}_{\text{Nonlinear term}} \tag{1.81}$$

I approximate the common propagation constant β in terms of individual single-core elements at the second term of the Taylor series using Eq.(1.7). After replacing $(\omega - \omega_0)$ by a time derivative in the inverse Fourier transformation and expanding the nonlinear term, the CGNLSE takes the form in the retarded frame T (same as the one introduced in the GNLSE in Eq.(1.1))

$$\begin{aligned}\frac{\partial A_1}{\partial z} &= i\delta_0 A_1 - \delta_1 \frac{\partial A_1}{\partial T} - \frac{1}{2}\sum_{o\geq 0}\frac{i^o}{o!}\alpha_0^{(1)}\frac{\partial^o A_1}{\partial T^o} + \sum_{p\geq 2}\frac{i^{p+1}}{p!}\beta_p^{(1)}\frac{\partial^p A_1}{\partial T^p} + \\ &+ \sum_{q\geq 0}\frac{i^{q+1}}{q!}k_q^{(12)}\frac{\partial^q A_2}{\partial T^q} + i\gamma^{(1)}A_1\Bigg[\sigma^{(1)}|A_2|^2 + \left(1 + i\tau_{\text{shk}}{}^{(1)}\frac{\partial}{\partial T}\right) \\ &\int_{-\infty}^{\infty} R(T') * |A_1(z, T - T')|^2 dT'\Bigg]\end{aligned} \tag{1.82}$$

$$\begin{aligned}\frac{\partial A_2}{\partial z} &= -i\delta_0 A_2 + \delta_1 \frac{\partial A_2}{\partial T} - \frac{1}{2}\sum_{o\geq 0}\frac{i^o}{o!}\alpha_0^{(2)}\frac{\partial^o A_2}{\partial T^o} + \sum_{p\geq 2}\frac{i^{p+1}}{p!}\beta_p^{(2)}\frac{\partial^p A_2}{\partial T^p} + \\ &+ \sum_{q\geq 0}\frac{i^{q+1}}{q!}k_q^{(21)}\frac{\partial^q A_1}{\partial T^q} + i\gamma^{(2)}A_2\Bigg[\sigma^{(2)}|A_1|^2 + \left(1 + i\tau_{\text{shk}}{}^{(2)}\frac{\partial}{\partial T}\right) \\ &\int_{-\infty}^{\infty} R(T') * |A_2(z, T - T')|^2 dT'\Bigg]\end{aligned} \tag{1.83}$$

The first two terms with $\delta_0 = (\beta_0^{(1)} - \beta_0^{(2)})/2$ and $\delta_0 = (\beta_0^{(1)} - \beta_0^{(2)})/2$ are associated to the phase and group velocity differences between the cores, respectively. They characterize the asymmetry of the DC structure. Next three terms are the linear operators describing attenuation, dispersion and coupling processes, respectively, expressed through the Taylor expansion coefficients

$$\alpha_r^{(m)} = \left(\frac{d^r \alpha^{(m)}}{d\omega^r}\right)_{\omega=\omega_0} \qquad (r \geq 0) \tag{1.84}$$

$$\beta_s^{(m)} = \left(\frac{d^s \beta^{(m)}}{d\omega^s}\right)_{\omega=\omega_0} \qquad (s \geq 2) \tag{1.85}$$

$$k_v^{(m,3-m)} = \left(\frac{d^v k^{(m)}}{d\omega^v}\right)_{\omega=\omega_0} \qquad (v \geq 0) \tag{1.86}$$

for attenuation, dispersion and coupling in the m-th core, respectively. My formulation includes the whole spectral dispersion character of these linear processes. The nonlinear parameter of m-th core $\gamma^{(m)}$ is defined in Eq.(1.15). The optical shock wave timescale $\tau_{\text{shk}}{}^{(m)}$ takes into account the nonlinear SST nonlinearity dispersion effect (from Eq.(1.48)), R is the nonlinear response function of the medium (Eq.(1.41)) and $\sigma^{(m)}$ is the XPM coefficient, which is calculated using the overlap integral between the field intensity profiles of the individual cores [119, 219].

1.3.5 Impact of higher-order effects on ultrashort pulse switching performance

The impact of higher-order perturbing effects on ultrashort pulse switching performance has been studied using the CGNLSE [98, 220–222]. One of the key parameters of the NLDC operation has been derived by Wang and Wang: it is the dimensionless ratio between the soliton period and the CL, z_0/L_c, which is equivalent to the multiplication of the coupling parameter and the dispersion length kL_D [221, 223]. Depending on it magnitude, three distinctive regions of operation can be identified (see Fig.1.19 left):

1. $z_0/L_\mathrm{c} \leq 1$: When the input power is small, the energy is coupled from the excited waveguide to the other; in the opposite case, when the input power is sufficiently higher than the critical one, the energy doesn't transfer to the opposite core. Hence, an all-optical switching can be implemented in an NLDC;
2. $z_0/L_\mathrm{c} > 50$: The energy transfer efficiency curves become very close to that of the CW in Fig.1, especially if $z_0/L_\mathrm{c} > 200$. Both the pulse coupling and CW coupling can be performed in the NLDC.
3. $1 < z_0/L_\mathrm{c} \leq 50$: NLDC performance are still possible, but the pulses generally suffer from pulse compression and serious distortions.

Fig.1.19a shows also that the switching power is strongly dependent on z_0/L_c, and it reduces with an increase of the ratio. In addition, it can be seen from Fig.1.19a panel (1) that it is possible to implement a pulse width selective switch even in the normal dispersion regime ($\beta_2 > 0$) if $z_0/L_\mathrm{c} \geq 200$ [221].

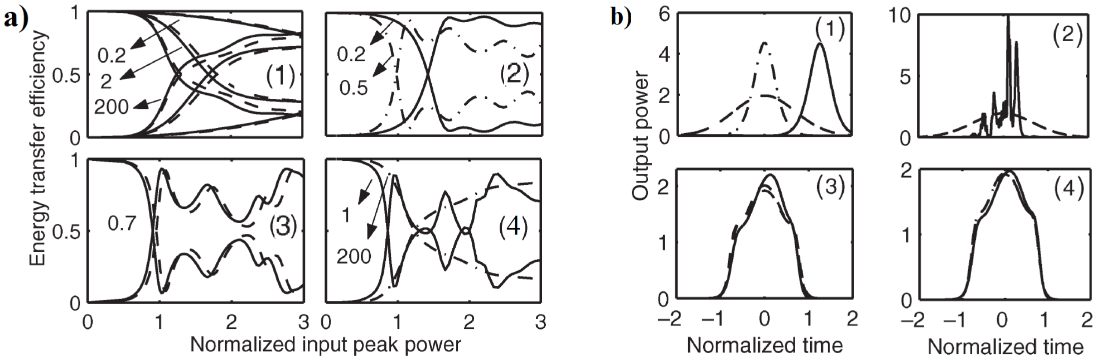

Fig. 1.19: *(a) Influence of the input pulse shapes and z_0/L_c on the power transmission coefficient in an NLDC with (1) $\beta_2 > 0$ and (2-4) $\beta_2 < 0$. (b) Temporal profiles of the switched pulses in the anomalous dispersion regime in case of single-core excitation with L_c-long NLDC by Gaussian pulse with $P_0 = 2P_C$ for z_0/L_c ratios equal to (1) 0.5 (2) 20 (3) 200 and (4) 1000. The dotted curves in (1) and (2) show the excitation pulse. The dashed-dotted lines in (1), (3) and (4) and the solid lines in all the panels show pulse profile when the higher-order effects are neglected and included, respectively* [221].

Fig.1.19b reports the temporal profile of the output pulse from the launching waveguide in an NLDC with anomalous dispersion for increasing values of z_0/L_c. In case of inclusion of the higher-order effects (solid lines), it can be seen that, for low z_0/L_c values, a considerably narrower and delayed pulse is obtained. This is associated with soliton formation and its self-frequency shift. In the intermediate region of $z_0/L_\mathrm{c} \approx 10$, the output pulse is heavily distorted and broken-up.

Another prediction from the same authors is that the pulse evolution along the NLDC doesn't have evident differences in dependence of the input pulse shape [223]. Fig.1.20a reports the spatial evolution of soliton and Gaussian pulse along a NLDC with $k = 1$. In both cases, the NLDC performance can be predicted and both Gaussian pulse and soliton experience pulse broadening. Nevertheless, the NLDC performance is sensitive to the input pulse width.

Fig.1.20b reports the NLDC switching characteristics in the three operational regimes described so far. It is from a second study conducted by Wang and Wang [223]. The curves for $z_0/L_\mathrm{c} = 100$ case are comparable to the ones for the quasi-CW regime in Fig.1. If the NLDC has a ratio $z_0/L_\mathrm{c} < 1$, the NLDC performance are achievable and reasonably good, but the value should not be too small in order to prevent pulse broadening. In the intermediate ratio region, the characteristics have a complex profile, leading to lower switching efficiency and multiple inter-core events due to soliton fission. In addition, the switching energy is dependent on $z_0/L_\mathrm{c} < 1$ ratio and not constant as predicted by previous analytical studies [223].

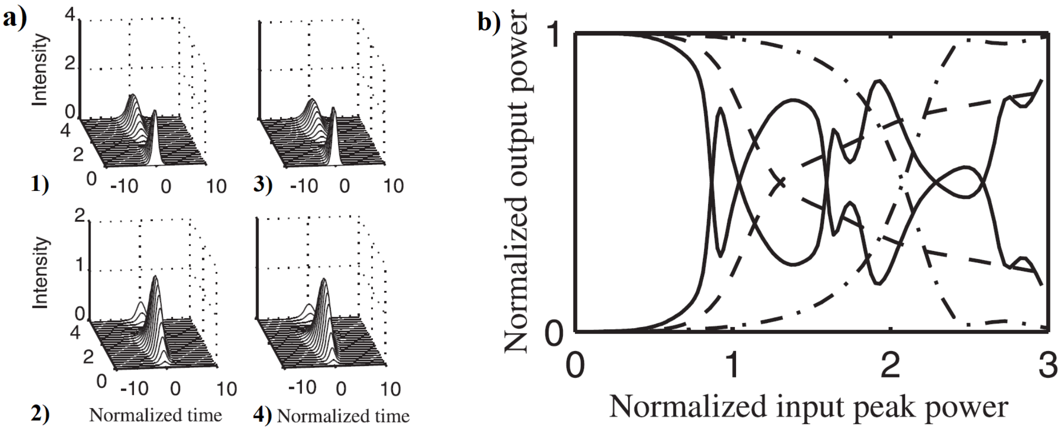

Fig. 1.20: *(a) Spatial evolution of a (a,b) hyperbolic secant and (c,d) Gaussian pulse along a NLDC with $k = 1$. First and second column correspond to first and second core, respectively. (b) Normalized output power from the individual ports of a L_c-long NLDC excited by hyperbolic secant pulses as a function of the input peak power for z_0/L_c ratio of 0.1 (dash-dotted line), 2.1 (solid line) and 200 (dashed line).* [223].

Soliton fission

The advantages of optical solitons for nonlinear switching purposes have been investigated on a theoretical basis since 1988, when the first study of solitonic switching in DC NLDC was presented by Trillo et al. in 1988 [44]. Even so, the practical relevance of this studies was rather limited because most of them relied adopted simplified numerical models neglecting higher-order perturbing effects [35, 95, 188]. Only from the second half of the 90s, the higher-order effects have been included in the numerical models. Especially for ultafast femtosecond pulses, the effects of TOD, intrapulse Raman scattering and SST can be quite significant [224, 225].

In the previous section, I analyzed the NLDC performance in the case of fundamental solitons ($N = 1$). Practically speaking, fundamental solitons are quite hard to be observed experimentally: if I impose N to be unitary in Eq.(1.31), I have some strict limitations on both the input power P_0 and the pulse width T_0, which have to be rather small and difficult to control. In addition, the effect of high-order terms is quite significant, which can compromise their stability. Therefore, I need to discuss more about high-order solitons (with $N > 1$) and study their propagation including the high-order effects, such as high-order dispersion, SRS, SST and dispersive waves generation.

As known from section 1.2.1, high-order solitons are characterized by a periodic pattern of propagation, with a period z_0. This is caused by a combination of GVD and SPM. SPM is responsible for chirping and spectral broadening of the pulse and it is strongly dependent on the shape of the pulse: it is negative on the leading edge of pulse and positive on the trailing edge, but it doesn't distort the pulse in the time domain. On the other side, anomalous GVD ($\beta_2 < 0$) causes the positive shorter wavelength components of the pulse to travel faster than the negative one. Thus, the trailing edge of the pulse will catch up with its leading edge due to the combined affect of the nonlinear chirp and negative dispersion. This phenomenon is called **pulse self-compression** [129, 226, 227].

An estimation of the propagation distance at which pulse compression takes place (I call it z_{comp}) was purposed by Chen and Kelly and have this expression [200]:

$$z_{\text{comp}} = \sqrt{\frac{t}{|\beta_2|\gamma\partial|A(z,t)|^2/\partial t}}\Bigg|_{t\to 0}, \tag{1.87}$$

where $A(z,t)$ is the pulse envelope. For the case of hyperbolic secant pulses $A(z,t) = A_0\,\mathrm{sech}(t/T_0)$, it can be approximated as follows:

$$z_{\text{comp}} \approx \frac{T_0}{A_0}\sqrt{\frac{1}{2|\beta_2|\gamma}} = \frac{\sqrt{2}}{\pi}\frac{z_0}{N} \tag{1.88}$$

This last equation shows that the pulse compression is expected to take place at shorter distances by increasing the soliton order. Similar expressions can be obtained for Gaussian pulses. However, for large N, the hyperbolic secant pulses are slightly more effective in self-compressing than the Gaussian ones [200].

Unfortunately, the propagation of high-order solitons is quite unstable due to the action of other high-order perturbations, such as the SRS, SST and DWs generation. Chan and Liu predicted that the pulse compression (and the periodic pulse recover too) is ruined especially by the effect of SRS and - even more - by TOD [228]. The trend of the compression factor F_{SC} - i.e. the ratio between the widths of the original and compressed soliton - as a function of the soliton number N is reported in Fig.1.21a. There, four curves are present, which correspond to the cases: (1) ideal ($\approx 2N$), (2) only SRS (i.e. $\beta_3 = 0$), (3) only TOD (i.e. $\beta_3 \neq 0$) and (4) combined SRS and TOD. For $N = 15$, TOD causes the highest degradation of F_{SC} than the other two cases, which decreases of more than 76% from the ideal case (Fig.1.21, line 1), much higher than the 25% caused by SRS (line 2). The combination of both TOD and SRS causes a degradation of F_{SC} of more than 80%.

Therefore, the outcomes of this study suggest that, if TOD is sufficiently low, the fission of optical solitons is mostly induced by the SRS. If I look at results of the

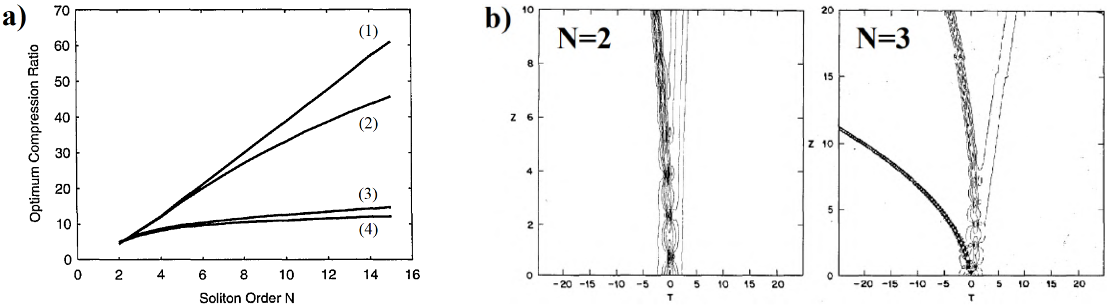

Fig. 1.21: *(a) Optimum compression ratio as a function of soliton order in (1) ideal, (2) only SRS, (3) only TOD, (4) TOD and SRS cases* [228]. *(b) Temporal evolution of hyperbolic secant soliton propagation in a glass fiber with (left)* $N = 2$ *(propagation distance* $z = 10$*), (right)* $N = 3$ *(*$z = 20$*)* [65].

simulations conducted by Tai et al. in Fig.1.21b (left for the case $N = 2$, right for $N = 3$) in case of no TOD effect, I observe that the pulse is not recovering the period pattern along the propagation and the pulse splits into some sub-fundamental soliton components [65]. Each resultant pulse of the breakup is constituted by a combination of more fundamental solitons, whose number is equal to the soliton order N of the input incident pulse. This is phenomenon is referred as **soliton fission** [107]. For example, in Fig.1.21b (left), fission produces a separation of the trajectories of the two soliton components: the fundamental soliton one with the largest amplitude (dark line) and shorter width than the original one ($\tau < 0$) and the lower-amplitude one (white line), with longer width ($\tau > 0$) in order to obey, at first approximation, to the momentum conservation law [65].

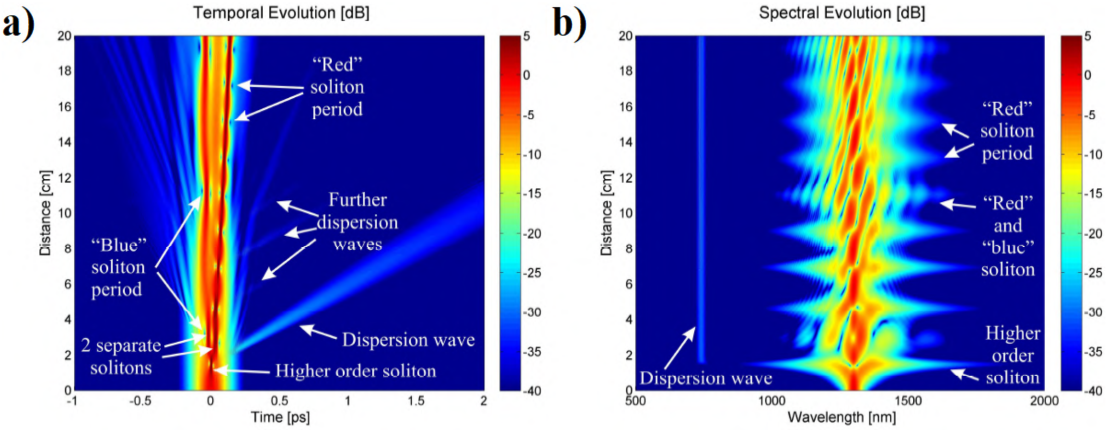

Fig. 1.22: *E*
xample of propagation of a $N \approx 3$-order soliton in the excited core of a PBG-01 glass DC PCF. Fission and dispersive wave generation phenomena are observable in (a) temporal and (b) spectral domain [168].

Simulations of propagation of high-order solitons in DC PCF made of multicomponent silicate soft glass PBG-01 were performed by M. Koyš [168]. The results are shown in Fig.1.22, where a 3-order soliton is propagating in the excited core of a 200 mm PBG-01 DC PCF and including all the high-order terms. The fission is taking place at about 28 mm, after which the three fundamental components propagate separately without combining again. In addition, blue dispersive waves are generated at 740 nm (see the spectrum in Fig.1.22b): they have much lower energy than the original soliton and propagate with a slower group velocity. The two main fundamental components of the soliton (intensive red colors in Fig.1.22a) can be distinguished between *blue* and *red* one, which have faster and slower group velocity than the original high-order soliton, respectively. Each separate soliton has its own CL (15 mm for the *red* and 81 cm for the *blue* one). Further dispersion waves are generated by *red* soliton at the beginning of the propagation and causes subsequent energy loss for the *red* soliton. Due to partial spectral overlap and interference observable in the spectral representation in Fig.1.22b, the spectral components of the two separate solitons are not easy to distinguish.

In conclusion, the propagation scenario explained in the previous paragraph is rather complicated and completely different from the ideal periodic one. This is a logic consequence to say that soliton fission and dispersive wave generation, which inevitably compromise the switching performance of the fiber coupler [229, 230]. The soliton splits into many fundamental components, which have their own peak power, width and group velocity/frequency peak and - consequently - coupling efficiency. At the same time, the change of input pulse energy affects the onset of soliton fission, number, spectral content and relative intensity of the individual solitonic components generated in the fission. Therefore, in order to avoid excessive losses and splitting phenomena, the switching performance of the coupler should be optimized by acting on the fiber length and on the pulse energy as well.

Intermodal/CL dispersion

Another nonlinear effect that leads to pulse breakup in DCF is the intermodal dispersion (IMD), i.e. the dispersion of coupling coefficient. Its influence on NLDC performance has been analyzed both numerically [224, 231] and experimentally [225]. For fundamental soliton, increasing IMD was shown to degrade the switching characteristics due to the soliton splitting [231].

IMD is a phenomenon that arises from the fact that a fiber-based NLDC is inherently a bimodal structure supporting two fundamental supermodes, i.e. the symmetric and the anti-symmetric supermodes. In order to characterize the phenomenon in a complete way, I can still use the two approaches for the description of the NLDC principle presented in section 1.3.1: the supermodes theory and the CMT. The first describes IMD as the group-delay difference between the two supermodes. On the other hand, the second one explains it as the frequency dependence of the coupling coefficient (dispersion of k).

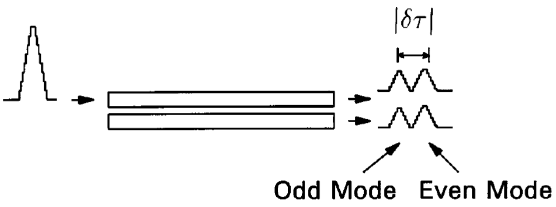

Fig. 1.23: *Principle of intermodal dispersion.* [224]

If the group delays of the two supermodes of the DCF are different, the optical pulses carried by the two supermodes exhibit a walk off along the propagation [224]. This walk-off effect results in two separate pulses at the output of each core, which correspond to the two fundamental modes of the DCF. Therefore, the beating between the two supermodes vanished because of they have no possibility to interfere. To allow the DCF to work as a switching device, the fields of the two orthogonal modes must overlap in time, which means that the duration of the optical pulse should be longer than the group-delay difference between the two modes. The group delay difference of the two supermodes propagating along a unit-length DCF are given by $\tau_{\pm} = 1/c \cdot d\beta_{\pm}/d\bar{k} = dk/d\omega$, where c is the speed of light, $\bar{k}$ the wave number and k the coupling coefficient. Therefore, the group-delay difference per unit length is given by

$$\delta\tau = \frac{2}{c}\frac{d\beta_{\pm}}{d\bar{k}} = 2\frac{dk}{d\omega} \tag{1.89}$$

To ensure that the coupler works effectively, the length of the coupler must be sufficiently short in order to neglect the IMD effects. A suggestion purposed by Chiang is to have at least the input pulse width $T_0 > 10|\delta\tau|L$, where L is the fiber length [224].

In order to get the measure of IMD, optical pulses of initial power P_{in} were launched through one core of the coupler and the power P_{out} is calculated after a propagation distance L_{c} for different values of the IMD coefficient K_1. It is defined as

$$K_1 = \frac{k_1 T_0}{|\beta_2|} \tag{1.90}$$

where $k_1 = \partial k_{\text{e}}/\partial\omega$ calculated at $\omega = \omega_0$ [231]. Droulias et al. identified three region of IMD depending on the value of K_1:

- **Low IMD** ($K_1 = 0 - 0.3$): the switching is not affected; the transfer between the cores still occurs because the balancing dispersion and nonlinearity is strong enough to keep the soliton stable;
- **Moderate IMD** ($K_1 = 0.3 - 1.3$): IMD effect is comparable to the combination of dispersion and nonlinearity and deteriorates the switching due to severe and quick pulse distortions;
- **High IMD** ($K_1 = 1.3 - 5$): IMD is so strong that the pulse splits into its two supermodes, which propagate with walk off. The propagation profiles of the two supermodes for this case are reported in [231].

From Eq.(1.89), I can notice that the coupling coefficient k is wavelength-dependent. Therefore, Eq.1.76 has to be updated considering the supermodes dispersion:

$$L_{\text{c}}(\omega) = \frac{\pi}{|\beta_S(\omega) - \beta_A(\omega)|} \tag{1.91}$$

Therefore, even L_{c} is dependent on the pulse wavelength (or frequency). Chiang calculated that the CL is strongly decreasing by elongating the wavelength, with an exponential-like trend [232]. The representation of L_{c} as function of the wavelength is known as the **CL characteristic curve** [2,222,233]. An example is reported in Fig.1.24.

Moreover, the coupling coefficient also depends on the symmetry properties between the structure of the two core. Due to a small structural asymmetry of the fiber, which is unavoidable during the fabrication process of the fiber, the two cores exhibit a mismatch of the propagation constants, i.e. a difference of the effective refractive indices n_{eff}. For this reason, the two cores can be distinguished as *slow* and *fast*, with propagation constants β_s and $\beta_f < \beta_s$, respectively. When the fast core is excited, a

Kerr-induced phase shift decreases the mismatch between the cores, causing an elimination of the DC asymmetry. On the opposite side, when exciting the slow core, the Kerr effect increases the asymmetry between the cores and the coupling between the cores is further weakened. I will discuss this issue in the next chapter, when describing the optical properties of the fabricated DCFs.

In conclusion, the coupling period of the separate pulses is dependent on their spectral content and partly on their intensity. The spectral content influences the pulse propagation due to the spectral dependence of L_c. Therefore, the switching properties of the NLDC depends also on the choice of the input central wavelength. Nevertheless, knowing the dependence of the CL with respect to the wavelength, the switching performance becomes controllable by the fiber length and pulse energy. As a result, the switching can occur at the desired wavelength by the pulse energy control for a given fiber length. This is quite advantageous for the design of a wavelength-tuneable nonlinear switch.

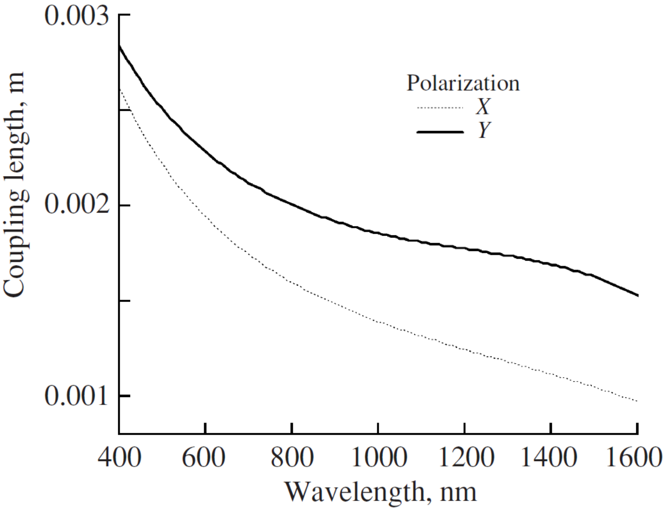

Fig. 1.24: *Example of CL characteristics for the case of DC PCF.* [233]

1.4 Nonlinearly-induced steering of femtosecond pulses in dual-core fibers

In the last sections, I showed that solitons in DCFs are affected not only by intrinsic linear and nonlinear optical phenomena, but also by coupling inefficiencies (section 1.3.5). All of these effects set some limitations regarding the energy, the wavelength, the shape and other properties of the input pulses. Even more, they are dependent also on the structure of the DCF, which has to be properly designed not only to support solitons, but also to allow the establishment of the switching performance. Nevertheless, solitons represent the best candidates for optical couplers due to their potential to maintain their shape in significantly nonlinear and dispersive media [227]. In addition, their advantageous propagation features in the ultrafast regime can be exploited for all-optical data processing tasks [234], as well for all-optical switching. The possibility to switch femtosecond pulses at Tb/s rates has potential to bring breakthrough to the optical communication systems [235]. However, up to now, just small number of attempts for experimental demonstration of solitonic all-optical switching in DCFs were reported and were rather unsuccessful [1,3].

The theoretical scenario supporting the switching performance of ultrafast optical pulses relies on the concept of **nonlinear self-trapping of high-order solitons**. The schematic of the concept is depicted in Fig.1.25b in comparison to the weak nonlinear propagation regime of DCFs reported in in Fig.1.25a.

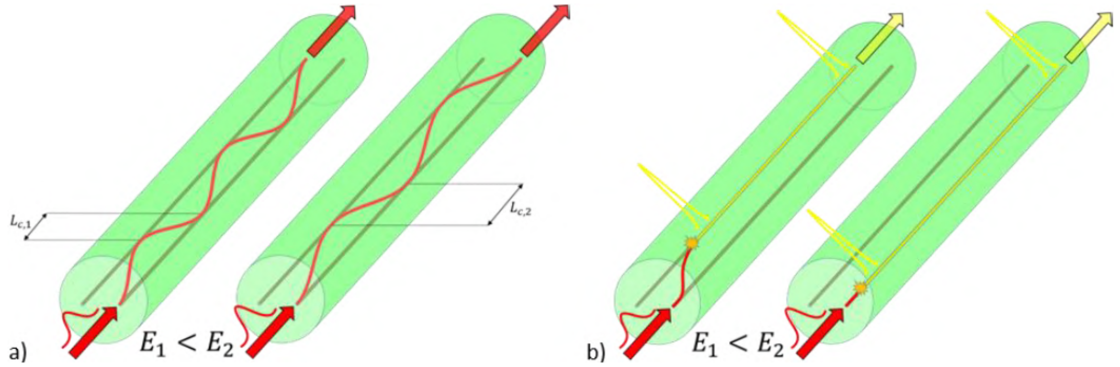

Fig. 1.25: *(a) Solitonic propagation through a DCF in weak nonlinear regime: the radiation in-coupled into one of the cores oscillates between the two cores with CL L_c, whose value is power dependent. (b) Theoretical concept of self-trapped solitonic switching: after the pulse compression phase, the pulse is trapped in the non-excited or in the excited core depending on its input energy. Then, it propagates further in the core where it is trapped in quasi-stable conditions.*

In the weak nonlinear case, the soliton period $z_0 \gg L_\mathrm{c}$; it means that coupling dominates over nonlinearity and the pulse oscillates between the two cores with a period equal to L_c (Fig.1.25a). In his theoretical study conducted using a hypothetical lead silicate PCF, Sarma et al. predicted that the weak nonlinear regime supports the best switching performance of ultrafast picosecond pulses in fiber-based NLDC [61]. The curves in Fig.1.26 reveal that the power transmission between the cores is more effective (close to 97%) for the weak nonlinear case (solid curve) and it takes place at lower values of the input energies.

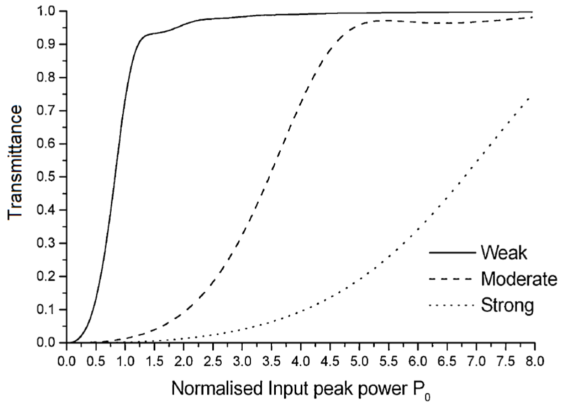

Fig. 1.26: *Transmission coefficient of excited core as a function of the normalized input peak power for 10 ps width soliton in case of weak (solid curve), moderate (dashed curve), and strong (dotted curve) coupling regime* [61].

In conclusion, the period of pulse oscillation between the cores depends not only on its wavelength (IMD, section 1.3.5), but also on its input energy. Considering once again Fig.1.25a, it can be seen that, for $E_1 < E_2$ (low energy case), the corresponding CL is shorter than the one at E_2 (high energy case). In this regime of operation, therefore, it is hard to determine the core at which the pulse is irradiated at the output because L_c is very sensitive to the pulse characteristics.

By a proper design of the properties of the DCF and a proper set of the pulse parameters, it is possible to work beyond the weak nonlinear regime (Fig.1.25a) and establish self-trapping of high order solitons in exchangeable manner (Fig.1.25b). In such way, the propagation of the pulse is localized only in one core of the fiber depending on its input energy. In the optimal case, the lower energy pulses (with energy E_1) are transferred to the non-excited core after half of CL period and then immediately localized there, while the higher energy ones (with energy $E_2 > E_1$) are localized already in the excited core. After that, the pulse propagates undistorted till the fiber end. This mechanism exploits both the high-order soliton self-compression effect (mostly caused by SPM), combined with the nonlinearly induced DC asymmetry effect. Therefore, it is possible to establish a **bistable-state operation** of the DCF, whose threshold is the energy of the input pulses. In case of low input energy pulses (but sufficient to generate solitons) and single-core excitation, the pulse can be coupled to the opposite (non-exited) core, where is then compressed and localized there. On the contrary, in case of sufficiently high-energies, the nonlinear mechanisms cause a fast compression of the pulse; therefore, the coupling to the other core is prevented and the pulse propagates through the excited core only.

1.4.1 Self-trapping and steering of ultrafast solitons

I now focus on the concept of self-trapping of high-order ultrafast solitons. It has been demonstrated using nonlinear optical media [236, 237] and multiple fiber arrays [238]. Generally speaking, a self-tapped optical wave packet is a stable and localized mode of a waveguide array that originate from the balance between the nonlinearity and the linear coupling [62]. Self-confinement can be achieved both for spatial and temporal solitons. In case of spatial ones, it can be established when the dispersive and nonlinear effect are perfectly balanced [239]. In fact, as explained in section 1.2, in a medium with weakly nonlocal response the field creates its own waveguide structure while propagating and, at the same time, it's the mode of the waveguide itself. Therefore, depending on both the input beam energy and the optical properties of the beam, it is possible to steer the trajectory of the beam in order it to follow a specific path along the propagation. This possibility has quite interesting applications in the field of optics communication, in particular it is advantageous for the design of optical logic gates [240] or multi-array optical multiplexers [241].

In case of temporal solitons propagating through "fixed" fibers, Jensen et al. estimate that the critical power to induce self-trapping is the one required to generate 2π Kerr-induced phase shift on the propagation distance of one L_c [178]. This condition translates into a requirement for the pulse input power P_0 [242]:

$$P_0 = \frac{|\beta_2|}{2\gamma T_0}. \tag{1.92}$$

If solitary waves are highly localized at the same time both in the spatial and temporal domain, spatiotemporal solitons or light bullets can be formed [46, 243]. These form of self-trapped solitons was observed in inhomogeneous nonlinear media [244], as well as in multi-core waveguides [43]. The first experimental demonstration of light bullets was presented by Minardi et al. in a hexagonal array of evanescently coupled single-mode fibers [63]. Exiting the central fiber at 170 fs pulses at 1550 nm, it was observed that the localization of the output field in the central core is dependent on the input pulse power. At low power input levels, the high coupling caused the pulse to be diffracted from the central fiber to the surrounding waveguides. On the opposite side, when the input pulse power was increased, the coupling ceased to exist and a train of approximately 30 fs compressed pulses was generated and observed at the output port. The short lifetime of the light bullets was mainly limited by perturbations caused by SRS and SST. Solitary waves were observed in the form of vortex light bullets in an experiment conducted by Eilenberger er al. in a similar hexagonal array structure [64].

1.4.2 Controllable solitonic self-trapping in DCFs

DCFs constitute a simplified version of the multi-core array and allow easier interpretation and optimization of the self-trapping mechanism. The key aspect of my approach is the possibility of energy-controlled self-trapping of the pulse in the both individual cores of the fiber. Selective soliton self-trapping opens a way for the demonstration of highly efficient soliton switching, with higher application potential than the multi-core solution demonstrated earlier.

In the previous section, I pointed out that the key parameters to establish self-trapping are the initial propagation phase of the beam and its input energy, which both are responsible for temporal compression and spectral broadening. Combining Eq.(1.38) with Eq.(1.31), one can recognize that the initial compression distance z_{comp}, at which the maximal temporal compression and spectral bandwidth is reached, decreases with increasing input pulse energy. At the same time, pulse compression increases the pulse peak power, which consequently decreases the coupling efficiency. This interplay between temporal compression and coupling can lead, under suitable conditions, to selective soliton self-trapping in one of the fiber cores.

The main idea to achieve switching based on soliton self-trapping using DCFs is that, under a lower energy pulse excitation, the maximal pulse compression should take place at z_{comp} that is slightly longer than L_{c}. In this way, the pulse is trapped in the non-excited core. Upon sufficiently higher input pulse energy, z_{comp} decreases below L_{c} and the maximal compression point is reached already in the excited core. This causes a coupling inhibition and the pulse propagates in the excited core nearly undistorted (Fig.1.25). The fiber length should be at the level of L_{c} in order to avoid higher perturbations along the propagation (especially soliton fission and pulse breakup).

The compression process depends on both fiber and pulse parameters. An empirical expression for z_{comp} was introduced before in Eq.(1.38). Thus, the self-trapping of solitons take place if the following requirement is satisfied:

$$z_{\text{comp}} \approx L_{\text{c}} \tag{1.93}$$

By inserting Eq.(1.31) and Eq.(1.34) for soliton number N and soliton period z_0, respectively, into the equation for z_{comp} (1.38), the compression length can be estimated in terms of input pulse and fiber parameters according to this equation [6]:

$$z_{\text{comp}} \approx 0.32 \frac{\pi T_0}{2\sqrt{\gamma P_0 |\beta_2|}} + 1.1 \frac{\pi}{2\gamma P_0} \tag{1.94}$$

Therefore, the optimization of z_{comp} depends on the choice of suitable pulse (through power P_0 and temporal width T_0) or fiber characteristics (through the nonlinear parameter γ or GVD parameter $\beta_2 < 0$). For a fiber with given coupling and dispersion characteristics, pulse parameters needs to be optimized to fulfill Eq.(1.94). Alternatively, if the operation with certain excitation pulse characteristics is desired, a suitable fiber needs to be designed to support switchable self-trapping. It has been reported that, to reach a strong pulse compression at a simultaneous short distance, N has to be rather high (more than 10) [47]. This can be obtained by utilizing high power input pulses or strongly nonlinear fibers with high n_2.

In his doctoral dissertation, P. Stajanča purposed a theoretical analysis of the ratio between the soliton period and the CL z_0/L_c influence on the soliton self-trapping switching performance. This is based on the fact that the relative strength of solitonic and coupling processes is crucial to predict a switching performance in DCFs. From another perspective, the ratio takes into account that the increase of the soliton number N causes a decrease of the soliton compression length z_comp (Eq.(1.38). As an example, Fig.1.27 reports the simulation results of the CGNLSE in Eq.(1.82) and (1.83) - neglecting losses and SST effects - for different values of the ratio z_0/L_c and of the soliton number N, in the temporal domain along a propagation length of $10L_\mathrm{c}$ [245] of an hypotetical PCF fiber made of PBG-08 (optimized by Stajanča himself and I. Bugár and presented in [2]) excited with a 1550 nm, 100 fs hyperbolic secant pulse. Two cases of the ratio z_0/L_c are considered: 0.25 and 2, with increasing N in the range 1-2.8. It is possible to distinguish two propagation scenarios:

- $z_0/L_\mathrm{c} = 0.25$ (Fig.1.27a): At $N = 1$ (first row), the pulse has still an oscillating behavior, with the central high-intensity part with a constant temporal width along propagation, which indicates linear coupling. For $N \geq 1.2$, self-trapping in the excited core is predicted. For $N = 1.2$, the temporal profile is slightly broadened and its peak power drops below its initial value along propagation, indicating that the coupling-related broadening dominates over solitonic compression; for $N > 1.2$, the nonlinearity boots the solitonic compression over the coupling: the pulse maintains its peak power, its temporal width decreases, and propagates predominantly in the excited core. However, the value of z_0/L_c is too low to predict soliton self-trapping also in the non-excited core.
- $z_0/L_\mathrm{c} = 2$ (Fig.1.27a): The propagation scenario is more complex and it's influenced by the switching operation. For $N = 2.6$, the pulse, after a propagation length of $0.4L_\mathrm{c}$, is maximally compressed. As the condition for self-trapping in Eq.(1.93) is satisfied, the soliton is well confined (self-trapped) in the non-excited core. For just a small increase of N to 2.7, the self-trapped soliton is confined in the excited core. This exchange of the high-order soliton between the cores is actually a switching performance of ultrafast pulses using DCF. Increasing N to 2.8, the pulse is out-coupled from the excited core and trapped in the non-excited one. The back-and-forth exchange of the cores performed by high-order soliton is referred as a **reversible switching mechanism**. It opens some possibilities for switching of self-trapped solitons also in the opposite directions, from excited to non-excited core.

In my dissertation, I purpose another method to investigate the switching performance of self-trapped solitons, which is based on the ratio between the soliton compression length and the CL: $z_\mathrm{comp}/L_\mathrm{c}$. This parameter considers also the pulse peak

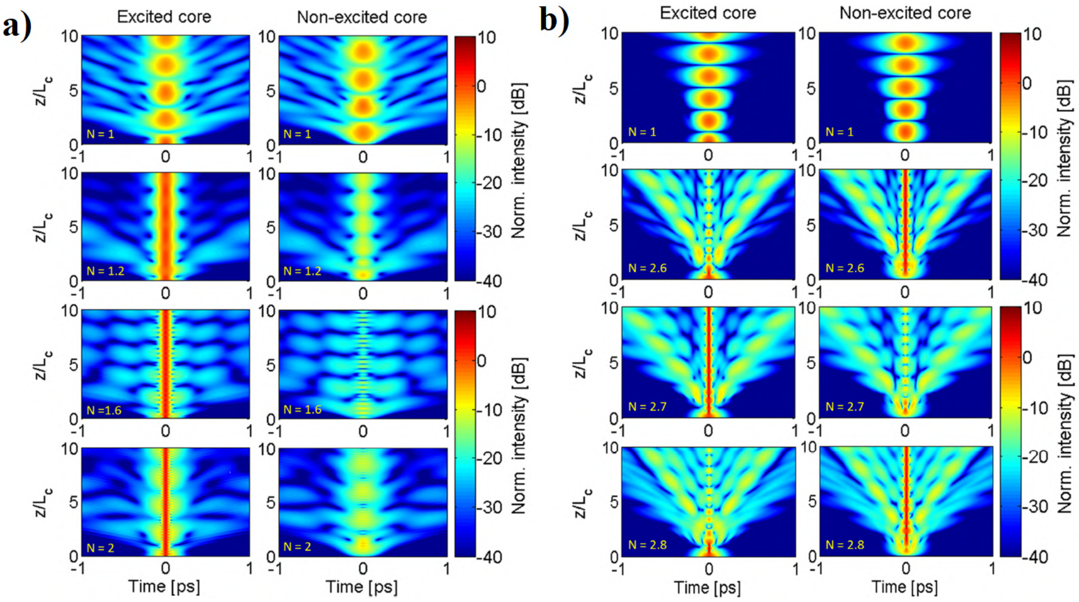

Fig. 1.27: *Simulated DC temporal evolution of 100 fs pulse at 1550 nm with different N values along $10L_c$ propagation distance in a DCF with (a) $z_0/L_c = 0.25$ and (b) $z_0/L_c = 2$* [245].

power: in fact, z_0 does not depend on the pulse peak power (Eq.(1.34), while z_{comp} gradually decreases from the soliton period z_0 by increasing it (Eq.(1.38)). The study of $z_{\mathrm{comp}}/L_{\mathrm{c}}$ is, therefore, more complete than the one purposed by Stajanča because it is estimates the necessary power to establish the switching performance of self-trapped solitons, the condition to establish self-trapping, and also the fiber length at which it takes place. This information is advantageous to investigate in details the concept depicted in Fig.1.25: when z_{comp} is tuned by the pulse energy slightly above L_{c}, the high-order soliton is compressed immediately after its transfer to the non-excited core. On the contrary, when the pulse energy is sufficiently high, z_{comp} is shortened and the soliton is already compressed in the excited core. Therefore, the key condition of the self-trapped solitonic switching concept is to achieve comparable CL and soliton compression length. The complete analysis based on this parameter is reported in the next chapter of the dissertation.

1.5 New perspectives: the microstructured all-solid soft glass DCF

Even if many theoretical articles about different aspects of solitonic switching performance in DC waveguides have been published [44, 246–248], only a very limited number of experimental works on this topic could be found in the scientific literature [3–5]. The main reason relies on the very strict requirement on dispersion, coupling and nonlinear characteristics of the suitable DC structure and on the high powers necessary to achieve the desired switching performance. In terms of lowering the switching powers, many materials with n_2 higher than silica have been utilized to increase the NLDC nonlinearity. These include dye-doped [249] and poly-conjugated [250] polymers or GeS$_2$-based chalcohalide glass [251].

The advent of the PCF technology at the end of the 90s offered also the possibility to improve the design of basic NLDC guiding characteristics and boosting the nonlinearity. The main advantage of PCF consists of the possibility to vary the basic structural parameters of DC silica PCF microstructure in order to reach the desired dispersive and coupling characteristics [251, 252]. In addition, the fabrication process of PCF is, up to now, well-consolidated and offers the possibility to utilize soft glasses with high level of nonlinearity [253].

An interesting theoretical study of Sarma showed the possibility of soliton switching on mW power level in a highly nonlinear DC PCF with lead silicate glass [61]. The first experimental realization of nonlinear switching in PCF-based NLDC was performed by Betlej et al. for femtosecond pulses in the telecommunication C-band, using a DC PCF [1]. In the frame of that study, pulses centered at 1550 nm and with 120 fs of duration were launched into one fiber core. Unfortunately, only an intensity equalization between the two output channels was achieved by applying tens of nanojoule pulse energies. Their outcome has also a positive aspect because it required only 9 mm fiber length. On the other hand, significant spectral deformations were registered during the switching process, which prevented to achieve an applicable performance in the studied conditions.

Later on, Lorenc et al. performed a series of studies on the analysis of ultrafast nonlinear propagation in a specialty square-lattice DC PCF [254]. The possibility of polarization-controlled redirection of dispersive wave between the fiber cores was demonstrated by Bugár et al. [233]. The soliton switching performance in a DC PCF was predicted for the first time by Koyš et al. [4]. Then, Stajanča et al. demonstrated a switching performance in the C-band using a soft-glass PCF with a similar level of Kerr nonlinearity. It exhibited 20 nJ and 50 nJ switching energies and 100 fs pulses [5]. However, this achievement was not obtained under the C-band excitation as Betlej's study, but only at the longer wavelength as 1650 nm. Beside the spectrally limited switching performance at 1560 nm, the rest of the nonlinearly broadened spectra expressed a different behavior, which prevented to demonstrate a broadband switching.

In order to improve the achieved performance, Stajanča and Bugár chose a new fiber material with a 20 times higher nonlinear index of refraction n_2 with respect to the standard silica glass [2]. The NLDC concept using highly nonlinear glass was investigated theoretically by optimizing the structure of a DC PCF and a controllable self-trapping of high-order solitons was predicted using sub-nanojoule switching energies and high-contrast switching possibilities above 30 dB in the C-band, never demonstrated before in the case of fiber based NLDC. However, so far there was no successful experimental realization of such a scenario. The last experimental work using highly nonlinear soft-glass PCF (Fig.1.28a) was presented by Čurilla et al. [3]. In this case, the coupling efficiency between the cores was unfortunately not high enough and only small part of the excitation radiation was observed in the non-excited core, as presented in Fig.1.28. The motivation of this drawback is the low level of initial structural symmetry of the two PCF cores, which compromised the coupling efficiency.

Motivated by the not promising outcomes presented by Čurilla, in this dissertation I present a strategy that has the chance to improve the level of DC symmetry required for solitonic switching purposes: the all-solid PCF approach. The cores and cladding are made of two distinct soft glasses with advantageous optical properties and combinable during the standard PCF fabrication process. Moreover, both glasses have been synthesized and characterized in-house at my institution, Ł-IMIF. The opportunity to work at

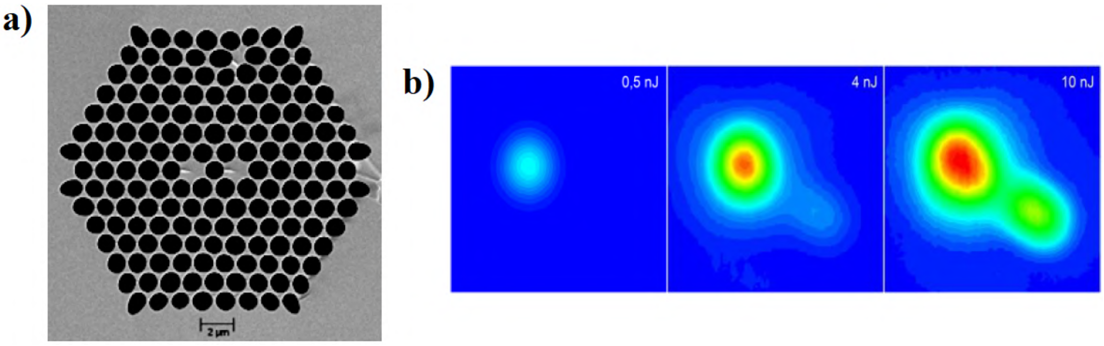

Fig. 1.28: *(a) Scanning electron microscope image of the cross-section of the asymmetric DC PCF with air holes. (b) Intensity distributions at the output facet of a 10 mm PCF in case of excitation by Y-polarized 1600 nm pulses at 0.5 nJ, 4 nJ and 10 nJ excitation pulse energies* [3].

Ł-IMIF gave me the possibility to optimize the fiber structure after an extensive simulation study and also to be involved in the fabrication process of the optimized fiber using the facilities available there. Moreover, I had the possibility to perform both extensive nonlinear simulation study and experiments at FUW and PI-TUW using the fabricated DCFs. The combination of both works would constitute a solid base to prove the theses that I listed at the beginning of this dissertation (section *Objectives and claims*) and also to demonstrate an efficient self-trapping of ultrafast solitons using DCFs.

In conclusion, in the following chapters of this dissertation I present my work related to DCFs optimized and fabricated at Ł-IMIF and tested at FUW and PI-TUW, respectively. I start with describing the design and optimization methods of the DCF, including the choice of the proper materials and of the parameters of the fiber structure, such as cores diameter, distance between the cores, photonic lattice pitch, etc. Then, I continue with describing the experimental results obtained both at FUW and PI-TUW, which constitute the most important verification of the self-trapping phenomenon. Then, I discuss about the potential application of the optimized DCF for all-optical switching, in particular the dual-wavelength experiment, which has some interesting purposes in the field of optics communications. In the next chapter I begin with the description of the material and structure optimization of the DCF.

CHAPTER 2

Materials and structural optimization

In this chapter, I discuss about the systematic optimization process of an all-solid DCF made of two glasses with high contrast of the refractive indices. It is presented in peer-reviewed articles *Optical Fiber Technology*, 51:48–58, 2019 and *Laser Physics Letters*, 17:025102, 2020 [6, 9]. The process started considering an all-solid PCF with micro-structured photonic cladding.

First, I introduce the glass materials used for the cores and cladding and their optical properties. Then, I report one of my original contribution to the study: the optimization of the basic linear spectral characteristics of the DCFs. The most important goal is to achieve a proper anomalous dispersion profile in the near-infrared spectral region, with particular attention to the telecom C-band. A section is dedicated to my second contribution to the study. It is related to the investigation of the self-trapped soliton switching in different types of DCFs: air-glass PCF, all-solid PCF and all-solid DCF with homogeneous cladding. I discuss the dependence of the switching performance on the excitation wavelength considering the optimized DCF using the simple cladding approach. Then, I present the best results for the optimized fiber under properly chosen excitation conditions and compare them with the ones obtained for the air-glass DC PCF [2]. I investigate the key conditions in terms of maximal SC (MSC) parameter and suggest a realistic fiber structure from the point of view of both technology and promising switching performance.

At the end, I describe the fabrication process of the optimized DCF, which is based on the stack-and-draw method, and my original contribution related to the analysis of the optical properties of the fabricated DCFs from the point of view of DC symmetry. The second one was presented in the peer-reviewed article *Optical Fiber Technology*, 63:102514, 2021 [10].

2.1 Motivation for the choice of the all-solid approach

In the first chapter, I discussed about the concept of NLDC in the form of DCFs. I showed that it is possible to nonlinearly control the coupling between the cores by applying intensive fields and establish switching from one core to the other one [44]. The concept works well in the CW regime, but it has some limitations for optical signal processing applications. Therefore, it is possible to address Tb/s data transmission rates by moving to the ultrafast nonlinear regime and use sub-picosecond pulse sequence as input source. Unfortunately, ultrashort pulses suffer with significant perturbations caused by the dispersion, coupling or nonlinearity [43]. Fortunately, it is possible to benefit from the solitonic propagation principles both in the time and spatial domains. The soliton propagation regime can preserve the pulse shape in the time domain [87] and it can maintain exchangeable asymmetric DC field distribution in the spatial domain under specific excitation conditions [177].

With this motivations, I purposed and showed the concept of self-trapped solitonic switching in Fig.1.25. It combines the advantages of the high-order soliton self-compression with the nonlinearly induced DC asymmetry [2]. In this way, it is possible to establish a bistable condition of DCF operation, where the pulse is confined and propagates through one specific core in dependence of its input intensity: the lower energy pulse in the non-excited core, while the higher energy pulse in the excited core.

The concept has been introduced first theoretically by optimizing the structure of a DC PCF. It was made of a highly nonlinear glass, which was predicted to support controllable self-trapping of high-order solitons in its cores [2]. In the frame of this study, the numerical results predicted sub-nanojoule switching energies and high switching contrasts above 30 dB in the C-band. Unfortunately, the experimental demonstration was rather unsuccessful because of insufficient DC symmetry [3]. As I have pointed out in section 1.3.3, this limits the coupling efficiency between the cores and prevents to establish of the advantageous nonlinearly-induced DC asymmetry, which constitutes the basis of the controlled switching of self-trapped solitons [210, 247]. It is possible to overcome this limitation by taking advantage of the all-solid PCF technology, which avoids air holes in the fiber structure, with potentially higher levels of the structural symmetry.

All-solid PCFs have more advantages than the classic air-hole PCFs because of their stability during the drawing process. The photonic structures of all-solid PCFs are not exposed to fluctuation of air pressure during fabrication. This prevents the formation of initial structure defects. Then, the possibility of thermally match the two glasses enables new possibilities of dispersion engineering, which enhance application potential of the fiber [255]. It is a matured fabrication method and has already brought several new achievements in the case of single-core optical fibers [77, 256]. All-solid PCF technology has been reported by other authors as well, mainly in the area of fiber laser development [257]. The substitution of the air holes in the fiber structure with low index glass rods undoubtedly improves the integrability potential of such waveguides into standard fiber communication systems. Moreover, a DC all-solid PCF has already been manufactured and used for a switchable multi-wavelength fiber laser [258]. With these motivations, I performed an optimization of the all-solid DCF fiber structure for all-optical switching purposes.

2.2 Optimization of the DCF materials

I begin with the choice of the two glass materials for the cores and the low-index inclusions of the all-solid PCF. In order to obtain the maximum difference in refractive index values of glasses, I consider two types of oxide glasses fabricated in-house at Ł-IMIF. As a high refractive index glass I used the lead-bismuth-gallium-silicate glass labeled as **PBG-08**. This glass is characterized by good rheological properties and refractive index of 1.945 at 1500 nm [76]. It has been already used also in the case of the air-glass DC PCF structure [2, 3].

In order to maintain the required drawing properties for the all-solid PCFs development, the difference in the temperature-viscosity curves of PBG-08 and the complementary glass should not exceed 50°C. In addition, the thermal expansion coefficient of the two glasses should be similar. These requirements needs to be fulfilled because the stack and draw technique used for PCFs fabrication involves multiple thermal processes to reduce the diameter of the fiber structure. Therefore, the high difference in viscosity or the temperature stress during the cooling phase can cause the formation of cracks.

To have similar rheological properties and thermal expansion coefficient to PBG-08, a borosilicate glass from the SiO_2-B_2O_3-Al_2O_3-Li_2O-Na_2O-K_2O system was chosen: the **UV-710** glass.

Thermal expansion coefficient, transformation temperature and dilatometric softening point were obtained by BAHR Thermoanalyse GmbH DIL801 dilatometer [77, 259]. Dilatometric measurements showed the difference of linear coefficients of thermal expansion equal to $3.9 \cdot 10^{-7}$ K^{-1}.

In order to see if the glasses are suitable for simultaneous drawing process, their viscosity η was obtained as a function of temperature. Both glasses must have a comparable viscosity which is sufficiently low to allow the fiber to be drawn out without formation of cracks, but high enough that the glass does not automatically succumb to the force of gravity. The viscosity of the glasses was estimated by the most common method in the glass industry and fiber optic technologies. It involves the Leitz heating microscope and consists with observation of the changes in the shape, typically cubic, of the sample during its heating [260]. The temperatures of the transitions, corresponding to certain values of viscosity (given in Poise) are recorded:

1. Ovalization temperature ($\log \eta = 9$): when the original cubic sample loses the edge clarity during heating;
2. Sphere creation temperature T_k ($\log \eta = 6$): during further heating the sample takes the shape of a sphere due to the cohesion forces;
3. Hemisphere creation temperature ($\log \eta = 4$): the sample decreases its viscosity and the cohesive forces weaken, the sample takes the shape of a hemisphere;
4. Spreading temperature ($\log \eta = 2$): the sample melts completely.

A comparison of changes in viscosity for different types of glasses is shown in Fig.2.1. The viscosities of the selected glasses are close to each other in optimal region for fiber fabrication ($6.6 \leq \log \eta \leq 9$, green region in Fig.2.1b). The temperature differences between the ovalization and sphere formation ones do not exceed 40°C,

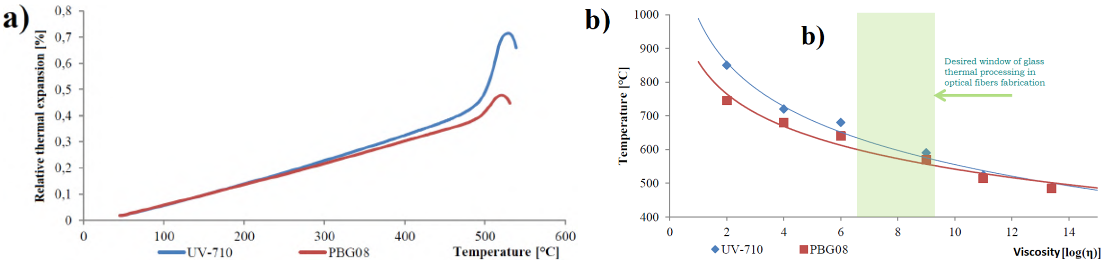

Fig. 2.1: *(a) Dilatometric and (b) viscosity curves for PBG-08 and UV-710 glasses* [77].

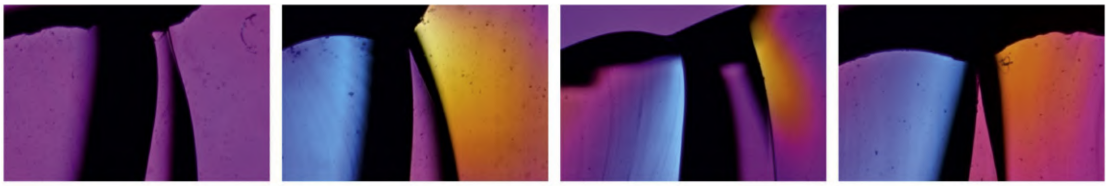

UV-706 $\Delta\alpha_{20}^{300} = 2.4\cdot10^{-6}/K$

UV-709 $\Delta\alpha_{20}^{300} = -1.2\cdot10^{-6}/K$

UV-710 $\Delta\alpha_{20}^{300} = 3.9\cdot10^{-6}/K$

UV-711 $\Delta\alpha_{20}^{300} = 0.8\cdot10^{-6}/K$

Fig. 2.2: *Polariscope images showing stress induced by the difference in thermal expansion coefficient between the corresponding borosilicate glass and PBG-08 ($\Delta\alpha_{20}^{300}$)* [77].

which means that the glasses are suitable for joint processes for the fabrication of the optical fiber structures. Fig.2.1a and Fig.2.1b show the dilatometric and glass viscosity curves, respectively. Thermal measurements show that the selected UV-710 glass meets the criteria for matching the PBG-08 lead-bismuth gallium silicate glass.

As a verification of the conformity of the expansion coefficients of the developed pair of glasses, a test of joining two glasses, the so-called sandwich, was performed by Cimek et al. [77]. It consists in the thermal connection of the plates from different glasses into a uniform block and, after relaxation, the mechanical stress is checked by a polarizing microscope. In the frame of the test, a thin glass plate of PBG-08 is placed between two plates of different types of borosilicate glass. During the annealing process at the sphere temperature, the UV-710 glass coats the PGB-08 glass, creating an arrangement similar to core-cladding structure of the fiber. The image from the polarizing microscope is shown in Fig.2.2. If the values of the linear coefficient of thermal expansion do not differ by more than the value of 5%, the glass will not crack and a block is obtained. Then, after cutting it into slices, the block can be analyzed under a polarizing microscope. The colors observed in the cross-section of the layered structure indicate the existence of stresses between the glasses. The polaroscopic photos in Fig.2.2 show that the best match of thermal expansion coefficients in combination with PBG-08 glass is with the UV-706 glass. In combination with UV-710 and UV-711 glasses, the stresses are acceptably small, as well.

Even though the UV-706 glass does not show any stresses in combination with the PBG-08 glass, the UV-710 glass was selected for further research, as it was the only glass which did not crystallize. In fact, the material showed no traces of crystallization even after 4 hours of heating at $T_k + 10°\text{C} = 690°\text{C}$, and met the assumed thermal parameters. This because the boron and lithium oxide contents, which tends to decrease the glass viscosity and its susceptibility to crystallization, is well compensated by the

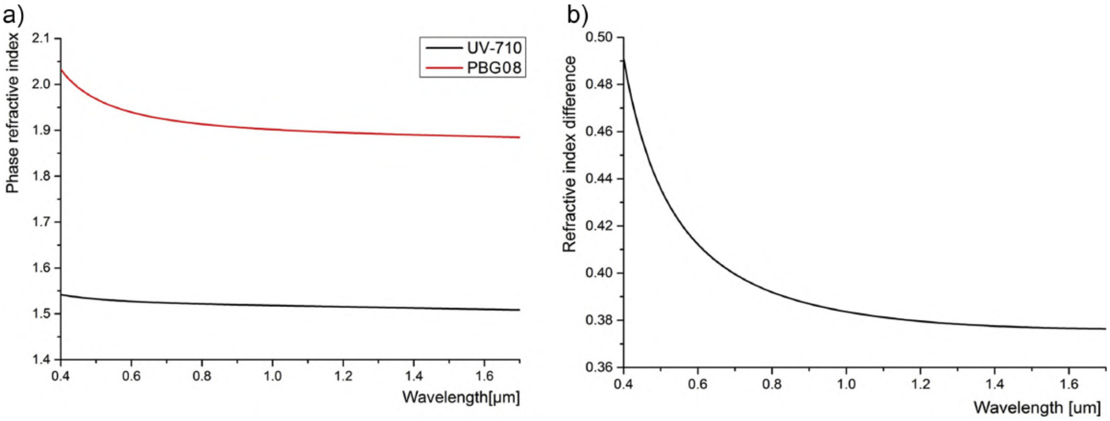

Fig. 2.3: *(a) Material dispersion of PBG-08 and UV-710 glasses, (b) Difference of their refractive indexes* [77].

content of silicon and aluminum oxide, which increases the viscosity of the glass.

The measurements of the material dispersion in the range of 400 - 1700 nm was made using the Michelson interferometer [261, 262]. With this method, it is possible to determine the group refractive index N of the material, because of the broad spectral analysis. It is equal to

$$N(\lambda) = n(\lambda) - \lambda \frac{\partial n(\lambda)}{\partial \lambda} \tag{2.1}$$

Using this equation, known as the Sellmeier equation, it is possible to retrieve the refractive index as a function of the wavelength from interferometric measurements. By fitting the first derivative of Eq.(2.1), it is possible to determine the Sellmeier coefficients B_i and C_i $(i = 1, 2, 3)$, which are used to calculate the phase refractive index n. The expression has been already introduced in Eq.(1.4).

The measurement of the refractive indices was carried in the range of 400 - 1700 nm wavelengths (Fig.2.3a). The refractive index at 1500 nm wavelength are 1.945 and 1.523 for PBG-08 and UV-710 glass, respectively. This means that the two glasses mentioned above show a contrast of the refractive indices of around 0.422 at 1500 nm. As reported in Fig.2.3b, the refractive index difference tends to decrease when wavelengths increase, but is approximately equal to 0.4 over a wide spectral range.

Both glasses have very good transmission (higher than 75%) in the window from 600 to 2650 nm for a 2-mm glass layer (Fig.2.4). It was measured with the spectrophotometric approach [77]. Measured transmission shows that borosilicate glass UV-710 has shifted spectral window to the shorter wavelengths comparing to PBG-08 glass and its transmittance is higher in general.

The obtained values of nonlinear refractive indices n_2 for PBG-08 and UV-710 are $4.3{\cdot}10^{-19}$ m^2/W and $0.93{\cdot}10^{-19}$ m^2/W, respectively. They were measured with the z-scan method [263]. Therefore, PBG-08 glass shows an almost 20 times higher values of n_2 than silica [264] and more than 4 times higher than UV-710, which makes it suitable for the design of NLDC in the form of DCFs and to establish sufficient anomalous dispersion.

In conclusion, Table 2.1 shows the composition of both PBG-08 and UV-710, together with their thermal and optical properties. The glass are thermally matched due

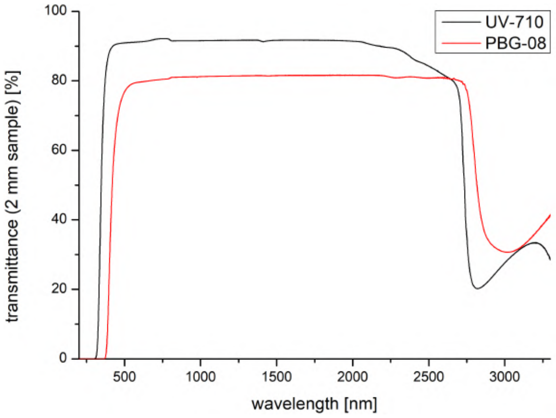

Fig. 2.4: *Transmission window of the selected glasses UV-710 (black curve) and PBG-08 (red curve).* [77]

to comparable thermal expansion coefficients and characteristic temperatures, The main achievements of the material optimization can be summarized as follows:

1. Low thermal stress due to small difference in thermal expansion coefficient ($3.9 \cdot 10^{-6}\ \mathrm{K}^{-1}$) between the two glasses, resulting in sufficient thermal stability;
2. Thermally matched glasses, suitable for the stack and draw fiber fabrication due to the ovalization temperatures in the range 610-690°C and resistance to crystallization;
3. No air pressure fluctuations: due to all-solid approach, the fiber has more homogeneous structure with respect to the air-glass case;
4. High transmission window between 600 and 2650 nm;
5. High refractive index constant difference (0.422 at 1500 nm) enabling to ensure significant anomalous dispersion.

2.3 Optimization of the fiber characteristics in the linear regime

After choosing the pair of the soft glasses, the DCF was optimized from the point of view of the structural parameters. As explained in the first chapter, the condition for establishing soliton self-trapping is the balance between the soliton compression length z_{comp} and the coupling length L_{c}. I recap here the expressions:

$$z_{\mathrm{comp}} = \left(\frac{0.32}{N} + \frac{1.1}{N^2}\right) z_0 \approx L_{\mathrm{c}} \qquad z_0 = \frac{\pi T_0^2}{2|\beta_2|} \qquad N = T_0\sqrt{\frac{\gamma P_0}{|\beta_2|}} \tag{2.2}$$

In order to design a DCF suitable for ultrafast all-optical solitonic switching application, I considered the following requirements:

1. **Maximized anomalous dispersion** in the wavelength region of 1400 - 1800 nm, with particular attention to the **C-band (1530 - 1565 nm)**, to allow a stable propagation of solitons and to keep their order N (Eq.(1.31)) at a moderate level;

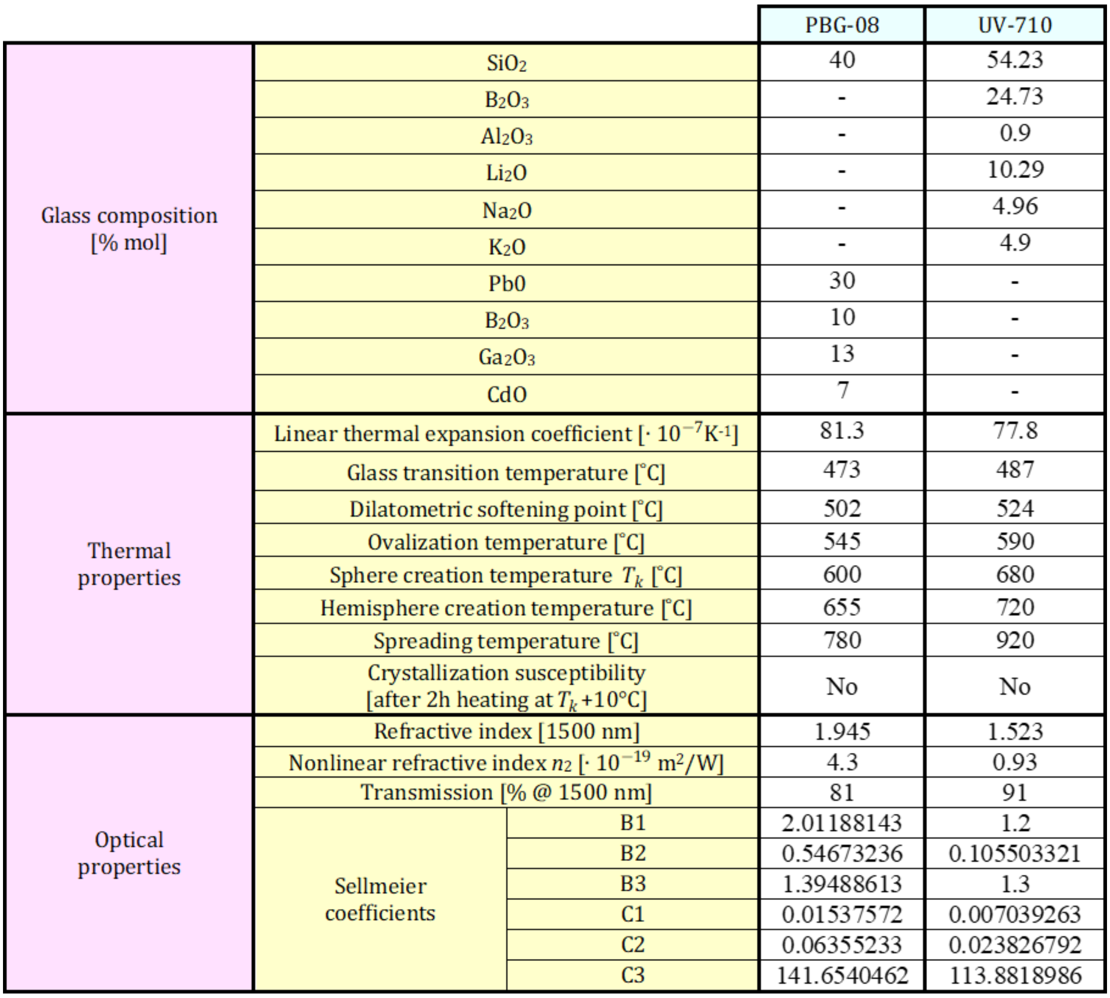

			PBG-08	UV-710
Glass composition [% mol]	SiO_2		40	54.23
	B_2O_3		-	24.73
	Al_2O_3		-	0.9
	Li_2O		-	10.29
	Na_2O		-	4.96
	K_2O		-	4.9
	PbO		30	-
	B_2O_3		10	-
	Ga_2O_3		13	-
	CdO		7	-
Thermal properties	Linear thermal expansion coefficient $[\cdot 10^{-7} K^{-1}]$		81.3	77.8
	Glass transition temperature [°C]		473	487
	Dilatometric softening point [°C]		502	524
	Ovalization temperature [°C]		545	590
	Sphere creation temperature T_k [°C]		600	680
	Hemisphere creation temperature [°C]		655	720
	Spreading temperature [°C]		780	920
	Crystallization susceptibility [after 2h heating at T_k+10°C]		No	No
Optical properties	Refractive index [1500 nm]		1.945	1.523
	Nonlinear refractive index n_2 $[\cdot 10^{-19}\ m^2/W]$		4.3	0.93
	Transmission [% @ 1500 nm]		81	91
	Sellmeier coefficients	B1	2.01188143	1.2
		B2	0.54673236	0.105503321
		B3	1.39488613	1.3
		C1	0.01537572	0.007039263
		C2	0.06355233	0.023826792
		C3	141.6540462	113.8818986

Table 2.1: *Resume of the composition, thermal and optical properties of PBG-08 and UV-710 glasses* [265].

2. Sufficient **nonlinearity for picojoule pulse energies** at pulse duration level of 100 fs. With this choice, simple ultrafast fibre oscillators can be used for the future experimental realization. This also prevents the damage of the fiber input facet during the experiments and limits the energy losses caused by fission processes;

3. **CL of few millimeters/centimeters**, to allow the self-trapping at very short fiber lengths. It represents a good compromise between the compactness and easy handling aspects;

4. **Minimization of TOD effect**, ensured by as flat as possible dispersion curve in the spectral range of interest, in order to eliminate the dispersive wave generation and other perturbing high-order effects.

At the beginning, I considered a **periodic hexagonal lattice** formed by hexagonal low-index UV-710 glass rods (Fig.2.5). The structure was characterized by a uniform period (or pitch, Λ) of the hexagons. The two high-index PBG-08 cores (violet color) are localized beside the central rod of the photonic structure and they are separated from each other by one low-index rod. The gaps between the UV-710 rods (yellow color) are filled by the high index glass; therefore, the structure is all-solid without any air filled areas.

The first condition of the list can be achieved by choosing the diameter of the cores in the range 1-2 µm and considering pulses with energy of about 100 pJ and width of 100 fs. In this way, it is possible to keep the soliton number below 5, even with a moderate level of anomalous dispersion below 100 ps/nm/km [2]. The second condition has already been addressed by choosing the highly nonlinear glass PBG-08, which has a 20-times higher n_2 than fused silica, for the two cores. There is a trade-off between the dispersion and the nonlinearity aspects because a larger mode area supports higher anomalous dispersion, while a smaller one higher nonlinear coefficient n_2. At the same time, the CL increases with increasing the overall structural dimensions and needs to be kept at the mm-cm level to preserve the device compactness.

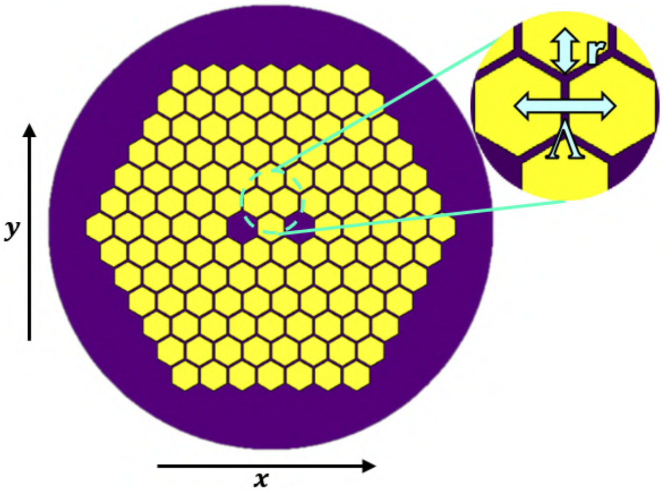

Fig. 2.5: *Scheme of the DC all-solid PCF fiber structure with photonic lattice made of hexagonal UV-710 rods (yellow color). The two cores, the bridges between the low-index glass rods and the outer cladding are made of high-index PBG-08 glass (violet color). In the inset, the parameters of the photonic lattice: the pitch* Λ *and the radius* r.

First, the structure was studied from the point of view of the propagation characteristics in the linear regime. I used the commercial Mode Solution software from Lumerical to calculate the spectral dependencies related to the fundamental modes, the effective refractive index and the waveguide losses for each fundamental mode. It is important to remind that, in the case of DCFs, the fundamental modes are actually a set of four fundamental supermodes (symmetric and anti-symmetric with both X- and Y-polarization directions) instead of two orthogonally-polarized fundamental modes in the case of single core fibers. Moreover, as I have already pointed out in section 1.3.2, the linear optical characteristics in the studied range of structural parameters and wavelengths are very similar for the both main polarization directions. Therefore, in the following pages, I will focus only on the X-polarized field, which is parallel with the connecting line of the two cores.

I acquired all the relevant quantities - like the effective mode area, dispersion, coupling coefficient, losses - in the spectral window between 300 and 4100 nm, which sufficiently covers the spectral region of interest. The identification of the modes and the dispersion characteristics calculation was initially performed for an artificial single core structure, which was obtained by placing with a low-index glass rod into one of the cores. In the second step, I considered the more complex DC structure to determine the coupling characteristics between the single core modes based on the overlap integrals [68]. This dependence, together with the ones calculated with the single core fiber, constitutes the input for the nonlinear simulation code, which is based on the solution of the CGNLSE.

The optimization of the structure started with the high anomalous dispersion requirement. It was satisfied by analyzing the wavelength dependence of the chromatic dispersion parameter $D(\lambda)$ (introduced in section 1.1.2) - or simply the dispersion profiles - of the single-core fiber under a systematic change of the r at constant lattice pitch Λ or by increasing Λ at constant r. r (evidenced in Fig.2.5) is the radius of the circumscribed circle around the hexagonal rod; for simplicity, I will call it **radius** of the hexagonal rods. Different values of Λ and Λ/r were explored in the range 1.2-1.8 µm and 2-3, respectively.

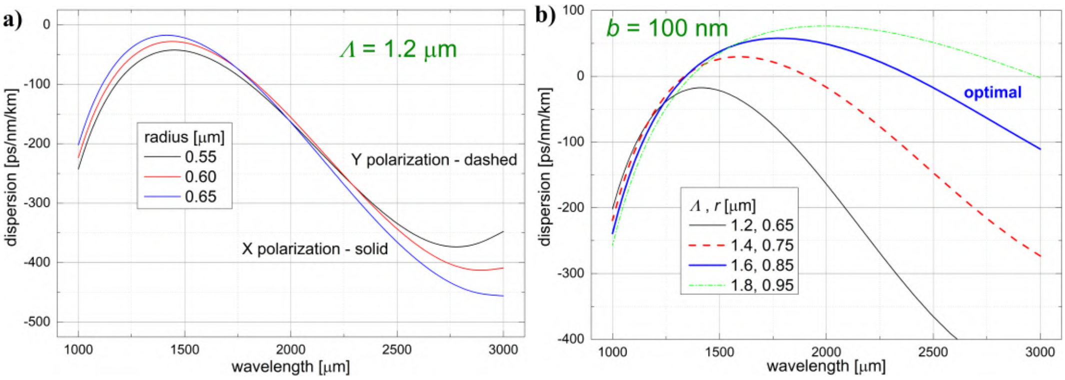

Fig. 2.6: *(a) Dispersion profile of the single core fundamental modes in the case of an all-solid PCF structure with 1.2 µm pitch for different lengths of rod radius r. (b) Dispersion profiles of the single core fundamental mode for different structure pitches Λ and maintaining the bridges length between the rods b constant at 100 nm.*

Fig.2.6a presents the single core dispersion profiles for a structure with constant lattice pitch at value $\Lambda = 1.2$ µm and different dimensions of the hexagonal low index rods radius [7]. This pitch value is the same of the air-glass DC PCF one designed by Stajanča et al. [2]. In the case of all curves in Fig.2.6a, the dispersion parameter decreases rapidly by increasing the wavelength from 1500 to 2500 nm, with a maximum in the range 1300 - 1400 nm and a minimum between 2700 - 3000 nm. However, no anomalous dispersion has been predicted in the whole spectral range. A different situation was achieved in the case of the air-glass PCF, where a peak of 250 ps/km/nm anomalous dispersion was predicted [2]. The main reason is that the contrast of the refractive indices of the all-solid PCF (about 0.4 at 1500 nm) is significantly lower than in the case of the previous air-glass PCF, which was at the level of 0.9. In addition, the flat region of the dispersion curve (lowest TOD) in Fig.2.6a is the in the spectral region of 1400 - 1450 nm, which is beyond the C-band. This outcome motivated us to move forward to larger pitch values, with corresponding higher percentage of the low-index glass rods in the photonic lattice (filling factor, FF). This strategy allows to reduce the effects of TOD in the C-band (flatter dispersion curve in that spectral region) and has a positive effect on the dispersion as well. According to Fig.2.6a, by the increasing radius (and the FF as well), the dispersion curve shifts closer to the anomalous region (positive values in the graph), which is my target area. The case of lattice pitch $\Lambda = 1.2$ µm and rod radius $r = 0.65$ µm value is the limit of the fiber fabrication process, because the PBG-08 bridges between the low-index UV-710 rods is only 100 nm.

Fig.2.6b shows the single core dispersion profiles at the sequential 0.2 µm increase of the pitch Λ and 0.1 µm one of the radius [7]. This strategy focuses on the structure pitch effect at slight increase of the FF, keeping the bridge width at 100 nm. Considering this structural parameters, the dispersion profiles of the X- and Y-polarized modes cannot be distinguished in the spectral region of interest; therefore, I present only the X-polarization curve for each combination of parameters. The simultaneous increase of the lattice pitch and the rod radius cause an enhancement of the FF. This has a positive effect on the dispersion profiles, which at this time reach the anomalous dispersion region. Moreover, the dispersion profile for the case of $\Lambda = 1.8$ µm (green dashed-dotted curve in Fig.2.6b) is in the anomalous dispersion region for a wide spectral range between 1.3 and 3 µm and it is quite flat in the spectral window 1500 - 1700 nm. Another improvement of the increasing pitch value is the shift of the zero dispersion wavelength towards the mid-infrared region, reaching about 3000 nm at the maximal considered pitch value. Nevertheless, the anomalous dispersion at 1550 nm already decreases with increasing pitch between 1.6 and 1.8 µm. Furthermore, the dispersion profile for 1.8 µm pitch is already steeper in proximity of the C-band than the one for 1.6 µm.

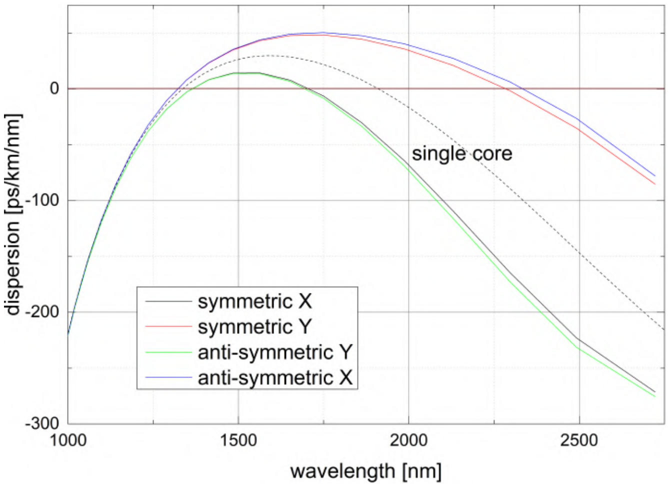

Fig. 2.7: *Dispersion profiles of the 4 fundamental supermodes for an all-solid PCF structure with 1.4 µm pitch and r =0.75 µm radius. The orange dashed line represents the dispersion profile of the single-core fiber with the same structural parameters.*

Fig.2.7 presents the dispersion profile of the 4 fundamental supermodes for the PCF structure with parameters $\Lambda = 1.4$ µm, $r = 0.75$ µm together with the single core dispersion curve for the same pitch and radius dimensions and X-polarization [8]. It can be seen that, at the short wavelength side, the dispersion profile of the supermodes overlap with the single core ones, while the single-core dispersion curve spans between the symmetric and the anti-symmetric modes dispersion curve in the long wavelength range, considering the same polarization direction. In the spectral region 1500 - 1700 nm, the symmetric X curve shows a flatter profile than the case with the longest pitch $\Lambda/r = 1.8$ µm$/0.65$ in Fig.2.6b. However, the dispersion is almost two times lower at 1550 nm and can be insufficient to allow the soliton generation. Therefore, I selected the combination of parameters as $\Lambda = 1.6$ µm$/r = 0.85$ µm, which seems to be more suitable for my application. It ensures lower TOD and at the same time a higher value of anomalous dispersion in the C-band than the case with pitch $\Lambda = 1.4$ µm (Fig.2.6b).

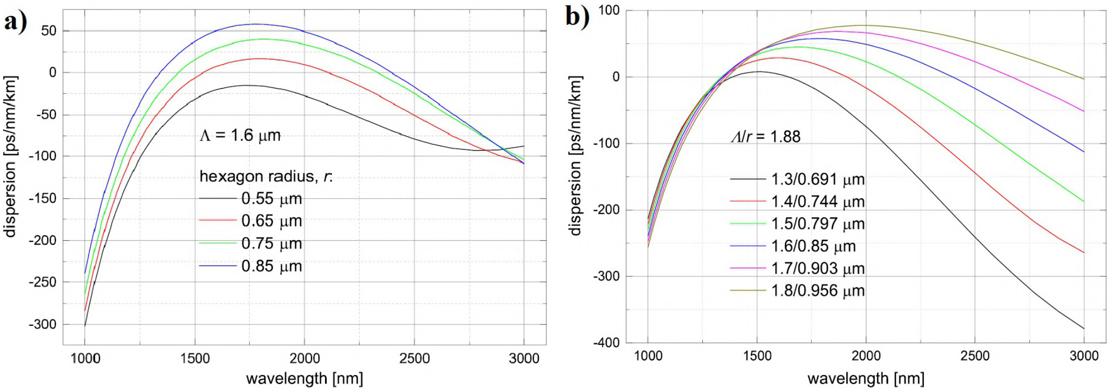

Fig. 2.8: *Dispersion profiles of the hexagonal type single-core all-solid PCF fiber (a) at constant pitch* Λ *of 1.6 μm and changing hexagon radius* r *and (b) at constant fill factor* $\Lambda/r = 1.88$.

Fig.2.8a presents the single-core dispersion curves of the analyzed structures with constant pitch of 1.6 μm and changing the rod radius r in the range 0.55 - 0.85 μm (step 0.1 μm) [9]. The results reveal that the lower is the ratio Λ/r of the structure, the higher is the anomalous dispersion in the mid-infrared region. However, in the case of 0.85 μm rod radius, the bridges length b is maintained constant at 100 nm, which is the limit from the point of view of technological feasibility. Therefore, in the next step I fixed the ratio Λ/r at this maximal value of 1.88 and I analyzed the effect of the structural period at the maximum possible FF. The results are shown in Fig.2.8b. By increasing the structural period, the anomalous dispersion increases and the dispersion maxima monotonically shift towards the mid-infrared region. Then, it is well observable in the C-band spectral region that the dispersion is very similar comparing the curves for the case of structural pitches of 1.6 and 1.8 μm, with slight increase of the TOD measure with increasing Λ. It is disadvantageous from the point of view of ultrafast pulse propagation.

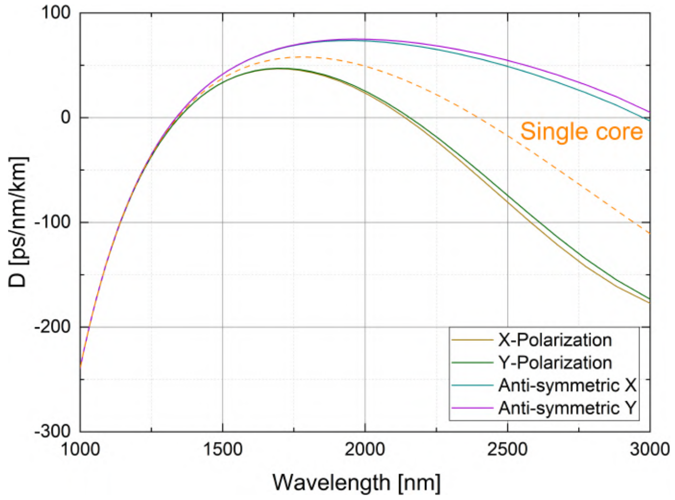

Fig. 2.9: *Dispersion profiles of the 4 fundamental supermodes for an all-solid PCF structure with pitch* $\Lambda = 1.6$ *μm and radius* $r = 0.85$ *μm. The orange dashed line represents the dispersion profile of the single-core fiber with the same structural parameters.*

Fig.2.9 shows the dispersion profiles of the 4 fundamental supermodes - two po-

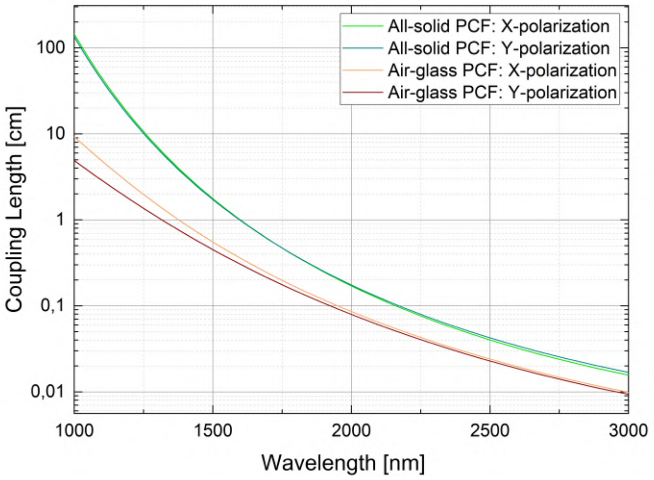

Fig. 2.10: *CL spectral characteristics of the all-solid PCF structure with parameters* Λ/r *=1.6 µm/0.85 µm and the air-glass PCF* [2] *for both orthogonal polarizations.*

larizations directions (horizontal X and vertical Y) and two DC states (symmetric and anti-symmetric) - for the all-solid PCF structure with pitch $\Lambda = 1.6$ µm and radius $r = 0.85$ µm. As for the case of $\Lambda/r = 1.4$ µm$/0.65$ µm in Fig.2.7, the single core dispersion curves are identical to the supermodes curves at short wavelengths, while, in the longer wavelength region, they are situated between the symmetric and the anti-symmetric curves. Nevertheless, the highest values of anomalous dispersion remain far below the level of 180 ps/nm/km reached in the case of the air-glass PCF structure [2]. In particular, at 1500 nm the anomalous dispersion is 42 ps/km/nm (X-polarization), which is 4 times lower than the estimated value of 165 ps/km/nm for the air-glass PCF [2].

In order to identify the influence of the fiber structural parameters on the coupling performance, I simulated the CL characteristics in the same spectral region 1000 - 3000 nm. It was calculated according to Eq.(1.76) using the values of the propagation constants for the symmetric and anti-symmetric supermodes calculated with Lumerical software ($\beta_S(\omega)$ and $\beta_A(\omega)$, respectively). Fig.2.10 reports the L_c spectral characteristics of the DC PCF structure with Λ/r =1.6 µm$/0.85$ µm for both orthogonal polarizations. As matter of comparison, the graph also includes L_c of the air-glass DC PCF from [2]. The optimized all-solid DC PCF shows a similar CL characteristics as the one for the optimized air-glass structure [2]. However, the exact value of the CL at 1500 nm (X-polarization) is more than three times higher (17 mm vs 4.5 mm).

In order to evaluate whether the self-trapped switching concept is satisfied, it is necessary to consider once again the key importance condition of balance between the soliton compression distance z_comp and L_c. I have already purposed an estimation of z_comp in terms of fiber and pulse parameters in Eq.1.94. From that equation, it can be seen that a decrease of the GVD parameter β_2 causes an elongation of the compression length of a factor $\sqrt{\beta_2}$. Therefore, in the case of Λ/r =1.4 µm$/0.75$ µm, the decrease of the dispersion by a factor of 4 than the one of the air-glass PCF (as evaluated in the last paragraph) causes about two times longer soliton compression distance. In the case of air-glass PCF, the self-trapped solitonic switching was predicted for 100 fs pulse width and at above 150 pJ of the pulse energy, resulting in a soliton compression distance at the level of 2 - 3 mm. This value is close to the CL at 1500 nm, which means that the structure was supposed to support the switching concept. Even in the case of the optimized DC PCF, the balance between z_{comp} and L_c is better satisfied (both around 12 mm), considering the same pulse parameters (100 fs, 150 pJ). On the other hand, the simultaneous reduction of the anomalous dispersion and the elongation of the soliton compression distance are responsible for an increase of the duration of the compressed pulse (Eq.1.88), which influences the nonlinear interaction between the cores [200]. Moreover, if the lattice pitch is increased from 1.6 to 1.8 µm, L_c - and z_{comp} as well - increase due to the lower nonlinear interaction.

In conclusion, the structural parameter combination Λ/r of 1.6 µm/0.85 µm was chosen as optimal from the point of view of both anomalous dispersion and reasonably short coupling/compression lengths. The FF of the DC PCF with these structural parameters is approximately 94%. According to the numerical analysis (Fig.2.10), the selected structure has 12 mm CL at 1550 nm (central wavelength of the C-band), which is more than 3 times longer than the air-glass PCF at the same wavelength (3.7 mm) [2]. The main reason of the L_c elongation is the larger structural pitch, which was only 1.2 µm in the case of the air-glass PCF. Moreover, the measure of the anomalous dispersion decreased about 4 times because the all-solid structure has lower refractive index contrast than the air-glass one in the C-band (0.422 vs 0.945 at 1500 nm, respectively).

As a consequence of the significant change of the linear propagation characteristics with respect to the air-glass DC PCF structure, it is not possible to fulfill the self-trapping condition to have comparable CL and soliton compression distance at the same excitation parameters (wavelength, pulse width, pulse energy). Therefore, the excitation wavelength and pulse width should be optimized once again. As L_c decreases rapidly with the wavelength, a good strategy to achieve similar CL values to increase the pulse central wavelength from 1550 nm to 1700 nm. The same procedure was carried out for the air-glass PCF too [3]. Moreover, according to Eq.1.31, the impact of the decreased measure of the anomalous dispersion can be compensated by decreasing the pulse width. This strategy keeps the soliton order at the same level of the air glass PCF one. Nevertheless, it is important to remember that the optimized all-solid structure has a longer pitch than the air-glass PCF, which translates into larger effective mode area. According to Eq.(1.15), the increase of A_{eff} causes a decrease of the nonlinear parameter γ, limiting the switching performance of the new all-solid PCF. Considering these differences, it is possible to achieve the same soliton number (about 4) at the same pulse energy lev-

Fig. 2.11: *Scheme of the all-solid DCF structure with homogeneous cladding without glass bridges between the UV-710 rods (100% FF). The two cores and the low-index microrods have the same diameter of 1.85 µm. The distance between the cores, indicated by the arrow, is 3.2 µm.*

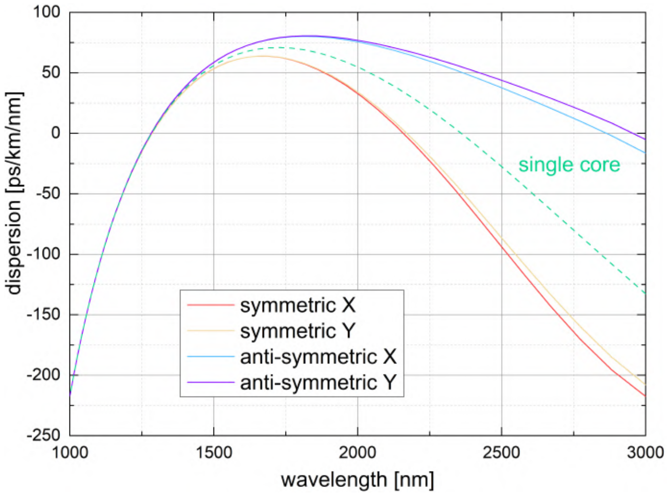

Fig. 2.12: *Dispersion profiles the all-solid DCF with simple cladding with 1.6 µm lattice pitch and with hexagonal core shape of 1.85 µm outer diameter. The green dashed line represents the dispersion profile of the single-core fiber with the same structural parameters.*

els (around 120 pJ) as for the air-glass PCF case by slightly reducing the pulse width. Thus, according to Eq.(1.38), the combination of excitation pulse parameters of 1700 nm, 70 fs and 120 pJ results in the soliton compression distance of 3.5 mm according to equation. This is equal to the value calculated in the case of the air-glass PCF structure under excitation by 1550 nm, 100 fs, 120 pJ pulses. In this way, the condition $z_{\text{comp}} \approx L_{\text{c}}$ is satisfied in both cases.

Motivated by the monotonic increase of the anomalous dispersion in Fig.2.8, I then maximized the FF of the all-solid DCF in order to improve its linear properties. Therefore, I exchanged the PCF structure with a simple PCF one with homogeneous low-index glass cladding. It avoids the PBG-08 glass bridges between the UV-710 glass hexagonal rods and keeps the optimized 1.6 µm pitch (Fig.2.11). With this new approach, the two cores and the low-index microrods have the same outer diameter of 1.85 µm, reaching a FF of 100%. Moreover, the fabrication process of this fiber, which includes the preform stacking and drawing phases, is considerably simplified.

Fig.2.12 reports the dispersion curves of the fundamental modes of the single-core (green dashed line) and PCF high index contrast all-solid fiber (solid lines). The single-core dispersion curve has two zero dispersion points at 1280 nm and 2360 nm and the anomalous dispersion value is above 50 ps/nm/km in the region 1500 - 2000 nm. The dispersion maximum is at 1730 nm, with only moderate TOD effect in the C-band. An improvement of the dispersion profile is predicted in comparison to the optimized PCF both in terms of anomalous dispersion value and TOD elimination. Due to the predicted large effective single-core fundamental mode area of about 1.7 µm^2 in the C-band and a core diameter of 1.9 µm, this structure can eventually have good levels of nonlinearity and high IE (which becomes worse for effective mode areas lower than 1 µm^2).

As for the case of Λ/r = 1.4 µm/0.75 µm in Fig.2.7, the single core dispersion curves are identical to the supermodes curves at short wavelengths, while, at in the longer wavelength region, they are situated between the symmetric and the anti-symmetric curves, depending on their polarization direction. Higher values of anomalous dispersion in the 1400 - 1800 nm spectral range were reached with respect to the optimized PCF structure (Fig.2.8). Nevertheless, the highest values of anomalous dispersion remain far below the level of 200 ps/nm/km reached in the case of the air-glass PCF structure [2]. In particular, at 1500 nm the anomalous dispersion is 42 ps/km/nm (X-polarization), which is 5 times lower than the estimated value of 200 ps/km/nm for the air-glass PCF.

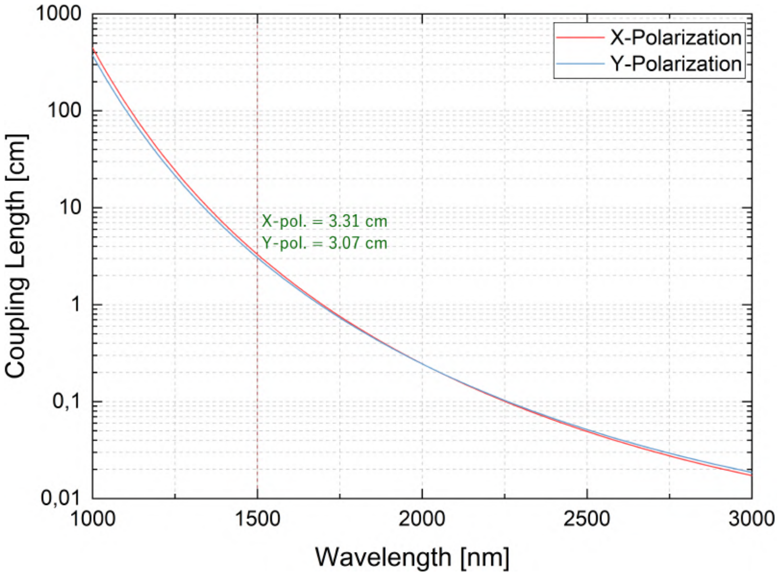

Fig. 2.13: *Numerically calculated CL spectral characteristics for fundamental X- and Y-polarized modes of the optimized all-solid DCF with homogeneous cladding.*

Fig.2.13 reports the CL characteristics of both orthogonal polarizations calculated using Eq.(1.91). Even for L_c, the polarization dependence is relatively weak. The simple PCF structure has a longer CL than the optimized PCF, with a value of 24 mm at 1550 nm. It is about 6 times longer than the air-glass PCF PCF fiber [2]. On the other hands, this elongation relaxes the requirements on the pulse energy, because the soliton compression length increases with decreasing energy (peak power), as it can be seen from Eq.(1.94).

For a matter of comparison, the single-core dispersion profiles of the three studied structures (air-glass PCF, all-solid PCF and all-solid simple DCF) are reported in the same graph in Fig.2.14a [6]. It can be seen there that the difference of the anomalous dispersion measures between the two PCF structures is significant. The anomalous dispersion range is nearly two times broader in the case of the air-glass PCF (green curve) and its value is 4 times larger than the all-solid one (black curve), not only in the C-band, but also at the dispersion maxima. On the other hand, the both profiles have the dispersion maxima in the same area of 1750 - 1800 nm. Anyway, the strategy of maximizing the FF to 100% (no high-index bridges between the rods) is advantageous from the dispersion point of view (red curve): its value increases by 50% in the C-band region and its peak slightly shifts to shorter wavelengths, to about 1700 nm. The higher measure of anomalous dispersion is advantageous from point of view of solitonic propagation and also the reduction of the TOD effects (smoother curve in the C-band). The only drawback of the homogeneous cladding is the reduced coupling, resulting in

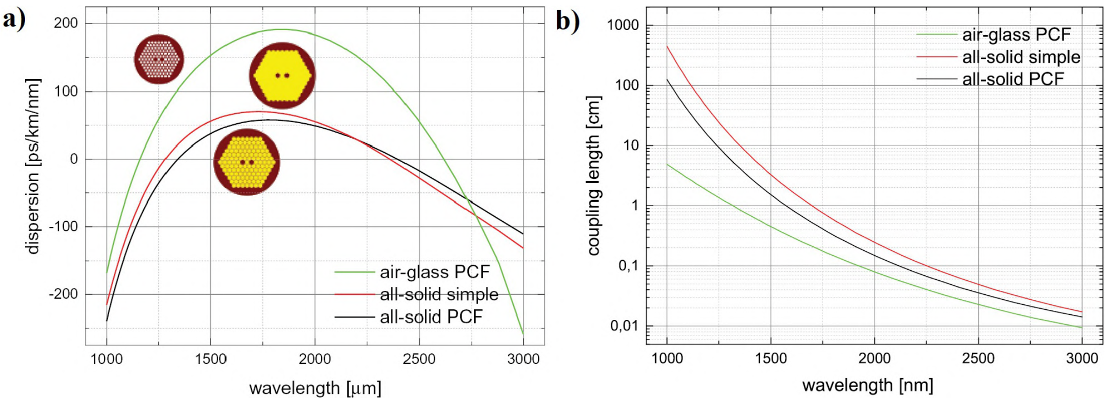

Fig. 2.14: *(a) Dispersion profiles of the single-core fibers (air-glass PCF, all-solid PCF with* $\Lambda/r = 1.6$ *µm/*0.85 *µm) with the corresponding picture of the fiber cross-sections; (b)* L_c *characteristics (right) in the case of the three optimized structures.*

about two times longer CL to be 24 mm at 1550 nm (Fig.2.14b), which is not situated in the sub-cm range as the air-glass PCF (2.7 mm - green curve). However, the CL characteristic is strongly dependent on the wavelength and decreases rapidly with its elongation for all the three DCF alternatives. Therefore, one strategy to reach a similar L_c for the all-solid structure and the air-glass one could be increasing the wavelength from 1550 nm to 1700 nm. For this reason, I can expect that, at 1700 nm, the switching performance of the all-solid structure would be comparable with the ones of the to the air-glass structure at 1550 nm.

Thus, from Fig.2.14, the modeled air-glass PCF structure is still predicted to be the best from the point of view of all-optical switching because of its smoother CL dependence on the wavelength, i.e. robustness against alterations of the excitation wavelength. However, the experimental demonstration of such scenario has been never verified because the coupling efficiency between the cores of the fabricated air-glass PCF was unfortunately not sufficient [3]. Therefore, the all-solid structure with homogeneous cladding looks like a good alternative to it because of its sufficient anomalous dispersion measure in the region 1400 - 1800 nm and minimized TOD (flat dispersion curve) especially in the C-band. For the X polarized single core mode, the dispersion parameter is $D = 62$ ps/nm/km and the effective mode area $A_\text{eff} = 1.72$ µm^2 at 1550 nm.

The last remained point of requirements listed at the beginning of this section is the sufficient nonlinearity at pico-joule pulse energies. For further considerations, I set hyperbolic secant pulses with 100 fs width in order to create the same excitation conditions used for the air-glass PCF case [2]. I estimate the range of pulse energy which supports the self-trapped solitonic switching, which means when the condition $L_\text{c} \approx z_\text{comp}$ is satisfied. Therefore, the in-coupled pulse peak power P_0 for pulses with input energy E_0 and its time duration in terms of full width at half-maximum T_FWHM is

$$P_0 = \frac{0.88 \cdot E_0 \cdot k_\text{in}}{T_\text{FWHM}} \tag{2.3}$$

The factor 0.88 is a conversion factor between average energy and peak power for hyperbolic secant pulses and k_in is the in-coupling efficiency (IE). In order to estimate the pulse energy before the in-coupling, I will consider a $k_{\text{in}} = 32\%$, which corresponds to the measured value in the case of the air-glass PCF [266]. E_0 was calculated using Eq.(1.94). It resulted in a value of 41 pJ considering $z_{\text{comp}} = 24$ mm (from Fig.2.13), which is in accordance with the desired requirement. It constitutes a significant improvement with respect to the energy levels predicted for the air-glass PCF, which, in the case of best switching performance, were in the range 300 - 400 pJ energies before the in-coupling optics. Hence, a stable soliton self-trapping is predicted at approximately 10 times lower input energies for the all-solid DCF. Nevertheless, this estimated value have to be verified in the context of nonlinear propagation of ultrafast pulses. It will be the topic of the next section, where I present the outcomes of the CGNLSE for all the three cases of investigated DCF structures.

2.4 Simulations of ultrafast pulse propagation in the nonlinear regime

The identified single core and the coupling spectral characteristics are used to solve the CGNLSE numerically. The equations have the form like Eq.1.82 and 1.83 and include effects like coupling coefficient dispersion, SST nonlinearity and its spectral dependence, SRS contribution, XPM effect and waveguide losses. The general form of the GNLSE has been already introduced in section 1.2.4 in Eq.(1.47) and includes the instantaneous Kerr and delayed Raman response functions material nonlinear response function [131]. Both of them have been determined experimentally for the highly nonlinear PBG-08 core glass and are combined together into the material nonlinear response function $R(T')$ [263].

The couple of equations was solved numerically with the **split-step Fourier method** applying 40000 steps. This value has been already optimized during the previous air-glass PCF study [2]. After every 200 steps of calculations, the field arrays were saved and then used to generate the output propagation maps; therefore, the whole propagation distance is divided into 200 points. For example, if the fiber is 100 mm long, it is possible to determine the optimal switching length with a precision of 0.5 mm. This approach represents a good compromise between the calculation time and the resolution of the propagation distance. During the numerical simulations, I used sech^2 input pulses with a power envelope expressed by the equation

$$P(t) = \frac{0.88 E_0 k_{\text{in}}}{T_{\text{FWHM}}} \operatorname{sech}^2\left(\frac{t}{T_0}\right) \tag{2.4}$$

where $T_0 = T_{\text{FWHM}}/1.763$ is the pulse width in terms of its full width at half-maximum, E_0 is the input energy and k_{in} is the IE. I performed a systematic simulation study of the CGNLSE solutions by changing T_{FWHM} between 75 fs and 150 fs and the excitation wavelength between 1400 nm and 1800 nm, covering most of the NIR optical communication bands. The split-step Fourier method employed for the nonlinear simulations is described in **Appendix 4.4** at the end of the dissertation.

2.4.1 Representation of the results

During the numerical calculation of the CGNLSE solutions, it is possible to switch many physical effects on and off by setting the value of the corresponding coefficients equal to zero or to realistic nonzero values. In particular, I can switch on or off the individual terms like: optical losses, SRS, XPM and spectral dependence of the optical shock-wave formation (SST). To evaluate the effect of these specific terms, I performed two series of simulations: 1. all aforementioned terms switched off, while keeping GVD, TOD and SST terms on, and 2. all the terms switched on. All the mentioned effects have not shown a strong influence on the pulse propagation both in time and spectral domain. Moreover, the soliton self-trapping mechanism is not affected by the mentioned extensions of the basic CGNLSE. Anyway, I decided to keep all the terms switched on during the whole extensive simulation work because their inclusion doesn't elongate the calculation time too much. Their effect starts to be non-negligible when I want to estimate the switching energies with a precision at the level of 1 pJ. I neglected only the loss term because their effect is limited in targeted range of fiber lengths below 100 mm. I also neglected the polarization effect on the dispersion, which is rather weak as presented in Fig.2.14, and on the CL characteristics in Fig.2.13. Therefore, I considered only X-polarized input pulses.

I performed series of nonlinear simulations based on the presented model for X polarized light at excitation wavelengths in range of 1400 - 1800 nm with 100 nm step and at pulse widths in the range of 75 - 150 fs with 25 fs step. At every combination of wavelength and pulse width, the numerical code generates two pairs of propagation maps (in the retarded time frame representation), one in the spectral and one in the time domain, for excited and non-excited core. In order to explore the influence of the input pulse energy, I increased it from 20 to 400 pJ with 5 pJ step. The goal of the nonlinear simulation study was to identify the lowest energies at which the soliton self-trapping mechanism occurs in the non-excited and in the excited core. After identifying these two energy levels, I reduced the step to 1 pJ and performed the simulations once again around the two mentioned pulse energies. This procedure was combined with the calculation of the switching contrast (SC) between these levels and along the whole propagation distance in order to find its optimal value. Thus, the final results were the two energy levels and the propagation distance which ensure the highest Switching contrast (SC).

As an example of typical outcomes of the nonlinear simulations, Fig.2.15 report the propagation maps in time and spectral domain for the non-excited core of 40 mm all-solid DC PCF with Λ/r = 1.4 µm/0.75 µm. The excitation X-polarized pulse parameters are $\lambda = 1700$ nm, $T_{\text{FWHM}} = 100$ fs and input energy $E_{\text{in}} = 2$ nJ. Please notice that the energy value reported here - as well as in the propagation maps I am presenting in the next pages - is considered before the in-coupling, i.e. without the in-coupling efficiency k_{in}. The 2D spatial-time pulse intensity evolution is depicted in a logarithmic color scale in dB units and it's normalized to the input peak intensity. The time scale in Fig.2.15a is normalized with respect to the input pulse group velocity; therefore, the velocity in the retarded frame is set to 0 in the X axis. The pulse components which propagate faster than the group velocities are plotted in the half-right part of the graph (t >0); on the opposite side, slower pulse components are reported in the half-left side of the graph (t <0). Both maps reveal all the linear and nonlinear processes that affect the pulse propagation in DCF I described so far. First, the pulse shows a linear periodic behavior between the cores (alternations between red and light-blue colors), with a period equal to the CL to be to 2.3 mm. At about 12 mm, the pulse is compressed in time, reaching higher intensity than the input one (dark-red color situated above the 0 dB

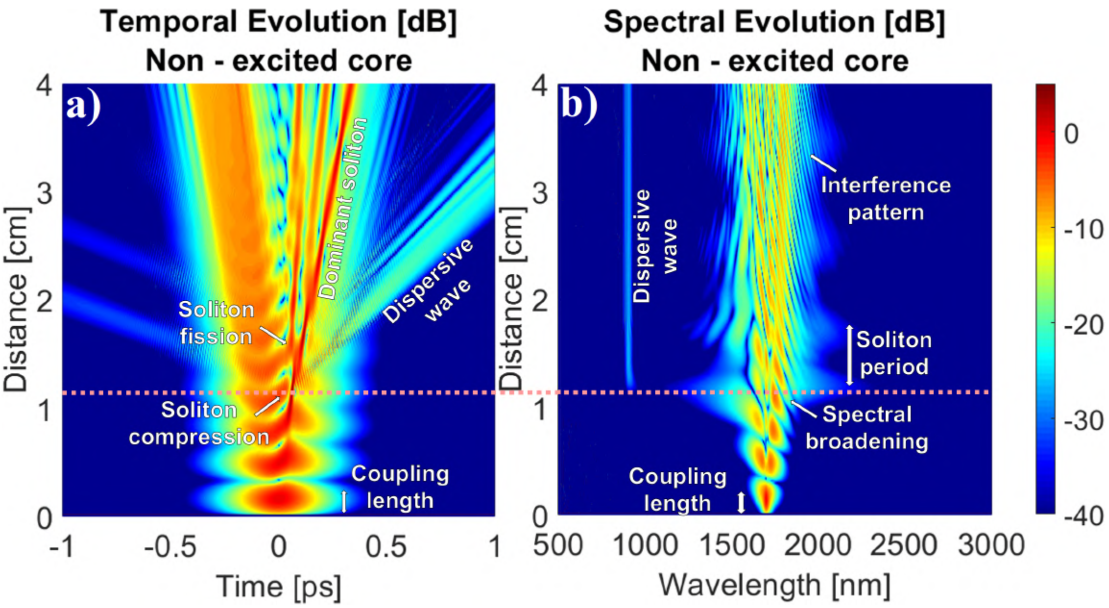

Fig. 2.15: *Example of propagation maps in (a) time domain (retarded time frame representation) and (b) spectral domain, considering X-polarized hyperbolic secant input pulses with* $\lambda = 1700$ *nm,* $T_0 =$ *100 fs and energy* $E_{in} = 2$ *nJ. The fiber was an all-solid PCF with* $\Lambda/r = 1.4$ *µm/0.75 µm.*

level) and a solitonic peak feature is generated. In the spectral domain, it corresponds to spectral broadening in the range 1250 - 2250 nm. Afterwards, at about 15 mm, the effect of high-order terms (in particular TOD, SRS and SST) starts to be significant due to pulse shortening and high intensities generated in the fiber. This causes pulse splitting into 3 fundamental soliton components determined by the soliton number N (soliton fission). At the same length, lower intensity dispersive waves are generated at shorter wavelengths (at about 1000 nm, as seen in Fig.2.15b). They are recognizable by the smooth straight lines extending towards the positive half of the time domain map (Fig.2.15a). The 3 fundamental solitons (dominant one in red color) propagate mostly independently with some interference pattern till the fiber end at 40 mm. In Fig.2.15b, it is possible to notice a signature of the soliton period z_0 of about 7 mm; however, it is strongly affected by the soliton fission process.

2.4.2 Switching performance of the all-solid PCF

I start my nonlinear simulation analysis with the air-glass PCF structure. A switching of self-trapped solitons performance has been already predicted by Stajanča et al. under excitation by hyperbolic secant pulses at 1550 nm and pulse width 100 fs [2]. The input in-coupled energy levels were identified to be 129 (self-trapping in the non-excited core) and 141 pJ (self-trapping in the excited one). The self-trapping condition of $z_{\text{comp}} \approx L_c$ was respected because the 3.5 mm soliton compression distance was almost balanced with the 3.7 mm CL. I performed the nonlinear simulations considering the same fiber and excitation conditions of 1700 nm, 70 fs. Fig.2.16 reports the 4 propagation maps for the excited (left column) and non-excited (right column) core for two levels of input pulse energies: at 231 pJ (top row) and 241 pJ (bottom row) of the input pulse energy. The propagation distance is in both cases 15 mm, which means that the simulation step has an approximately 0.4 µm resolution.

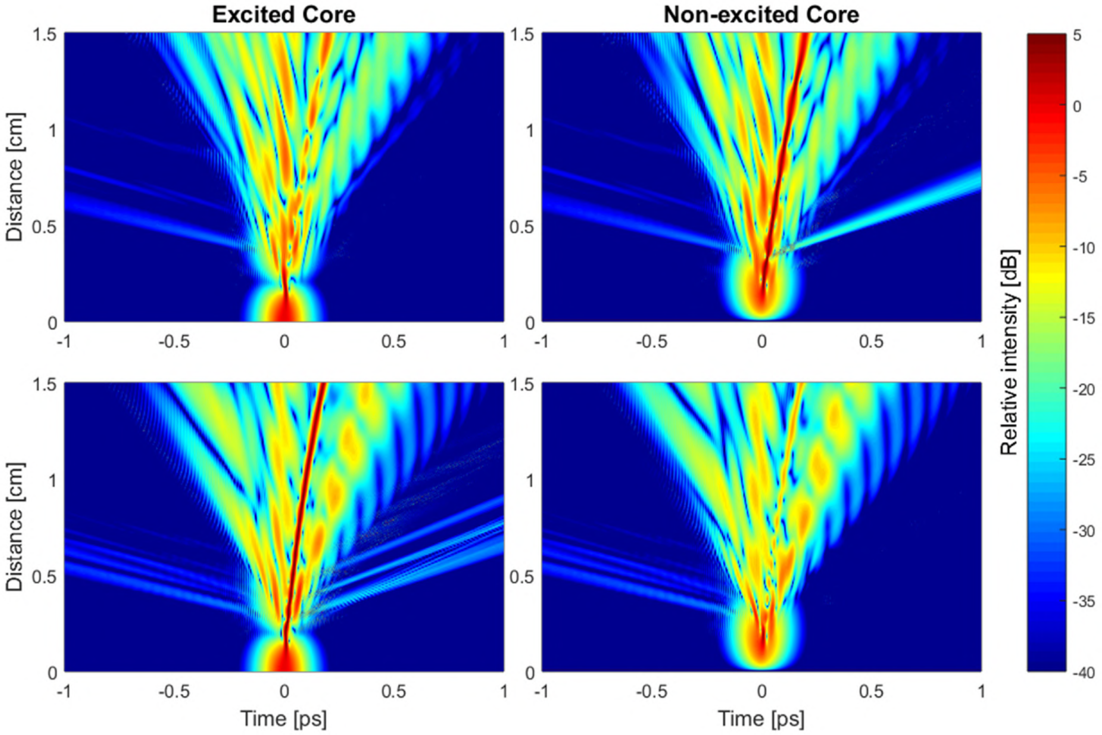

Fig. 2.16: *Self-trapped soliton switching performance considering air-glass DC PCF with* $\Lambda/r = 1.3$ *µm/*1 *µm. under excitation by 1700 nm, 70 fs pulses. Time domain evolution of the field intensity in the excited (left) and non-excited (right) core at 231 pJ (top) and 241 pJ (bottom) pulse energies.*

Even though the wavelength and pulse width were changed, the switching performance is convincing and comparable to the previous study of the optimized air-glass PCF [2]: at the lower energy, the high-intensity components (dark red color in the maps) are located in the non excited core, while they are dominant in the excited one at higher energy. This is the desired switching scenario based on self-trapped solitons scenario I depicted in Fig.1.18. The clear soliton self-trapping effect has been achieved in the case of the both switching energies and it's preserved through the whole propagation distance. In order to evaluate the switching performance quantitatively, the propagation maps were integrated line by line and the spatial evolution of the field energy was tracked in each of the 4 maps. For each discretized propagation distance step z_i, I calculate the **extinction ratio** $ER(E_{\text{in}}, z_i)$. It is defined as the ratio between the integrated field energies in the excited (E_{ex}) and non-excited ($E_{\text{non-ex}}$) core at specific z_i ($1 \leq i \leq 40000$) and applied input energy E_{in} It is calculated in dB units according to the following equation:

$$ER(E_{1,2}, z_i) = 10 \log \left[\frac{E_{\text{ex}}(E_{1,2}, z_i)}{E_{\text{non-ex}}(E_{1,2}, z_i)} \right] \tag{2.5}$$

where E_1, E_2 are the lower and higher switching energies. Finally, I can estimate the efficiency of the switching performance by calculating the **integral energy switching contrast** $SC_{\text{E}}(z_i)$, which is the subtraction between the *ER*s at the two energy levels

$$SC_{\mathrm{E}}(z_i) = ER(E_1, z_i) - ER(E_2, z_i) \tag{2.6}$$

Thus, the goal of the nonlinear simulation phase is to maximize the parameter $SC_{\mathrm{E}}(z_i)$ in terms of energies and propagation distance. I call **switching length** L_{s} the propagation distance at which the maximum of $SC_{\mathrm{E}}(z_i)$ is predicted. According to the simulation results in Fig.2.16, $SC_{\mathrm{E}}(z_i)$ was calculated to be 13.4 dB at $L_{\mathrm{s}} = 7$ mm.

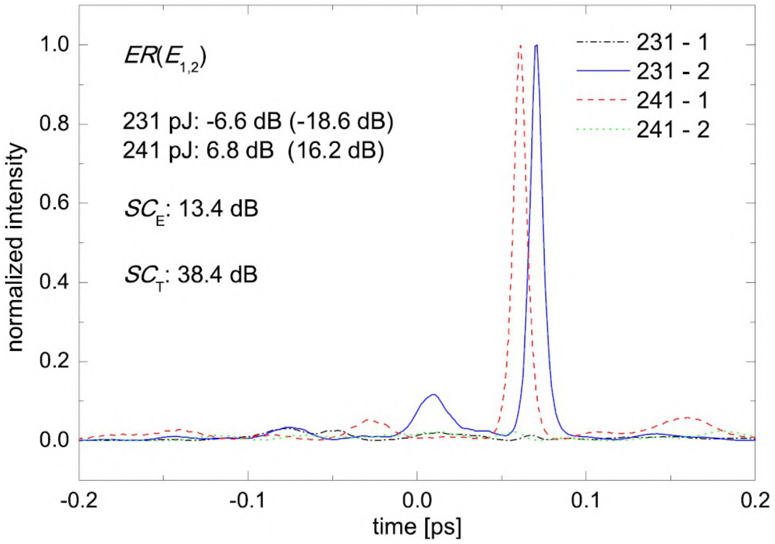

Fig. 2.17: *Time dependence of the field intensity envelope at the switching length in the both cores and at the both switching energies. Air-glass PCF excited with 1700 nm, 70 fs pulses.*

Fig.2.17 depicts the temporal envelopes of field intensity at the switching length L_{s} taken from the 4 propagation maps in Fig.2.16 at linear intensity scale. The curves are normalized separately for the both input energies in order to have the peak intensities in the dominant core at the same level of 1 (tags: - 1, excited core; - 2, non-excited core). The maximum of $SC_{\mathrm{E}}(z_i)$ was calculated to be 13.4 dB, which is higher than the 11.8 dB for the excitation case 1550 nm, 100 fs [2]; then, L_{s} is 7 mm, shorter than 11 mm in [2]. Despite of the change of the excitation parameters, the soliton number was preserved to be 4. Nevertheless, the soliton compression distance z_{comp} is halved (2 mm instead of 4 mm) and it's in balance with the shortened $L_{\mathrm{c}} = 2$ mm. Unfortunately, the change of excitation parameters causes the increase of the switching energies of about 100 pJ. The improved switching performance are a consequence of the higher value of anomalous dispersion and lower TOD at 1700 nm than at 1550 nm (green curve in Fig.2.14).

It is possible to evaluate the SC with a different method, which consists in considering the field energy only in the time window of the short self-trapped solitonic pulses. This evaluation approach is also appropriate from the application point of view, where the switched pulses will interact with timely synchronized short optical signals. In this case, the low intensity side pulses do not interact with the main switched pulse and their effect on the nonlinear switching is negligible. Therefore, the time envelopes $I(t)$ of the both main solitons at the lowest and highest switching energies were fitted with sech^2 function in the corresponding time window and core where they have their maxima. The resulted curves $F_{1,2}(t)$ were used to calculate the integral

$$E_j^i = \int F_j(t) I_j^i(t) dt \tag{2.7}$$

where i, j = 1,2 indicate the core and the energy level, respectively. Then, the *ER*s were calculated using the four values of the temporally localized energy and according to Eq.2.5. The temporally localized switching contrast SC_T are obtained with the new values of *ER* and using Eq.2.6. The calculation for the case in Fig.2.16 resulted in $SC_\mathrm{T} =$ 36.2 dB. This value is more than 20 dB higher than SC_E and it originates from the localized temporal intensity distributions in the excited and non-excited cores. In the case of the both switching energies, most of the field intensity in the non-dominant cores is beyond the time window of the main soliton. In conclusion, the air-glass PCF structure is a promising candidate for all-optical switching due to its high values of SC_E and SC_T, and its robustness against perturbations of the excitation wavelength and pulse width.

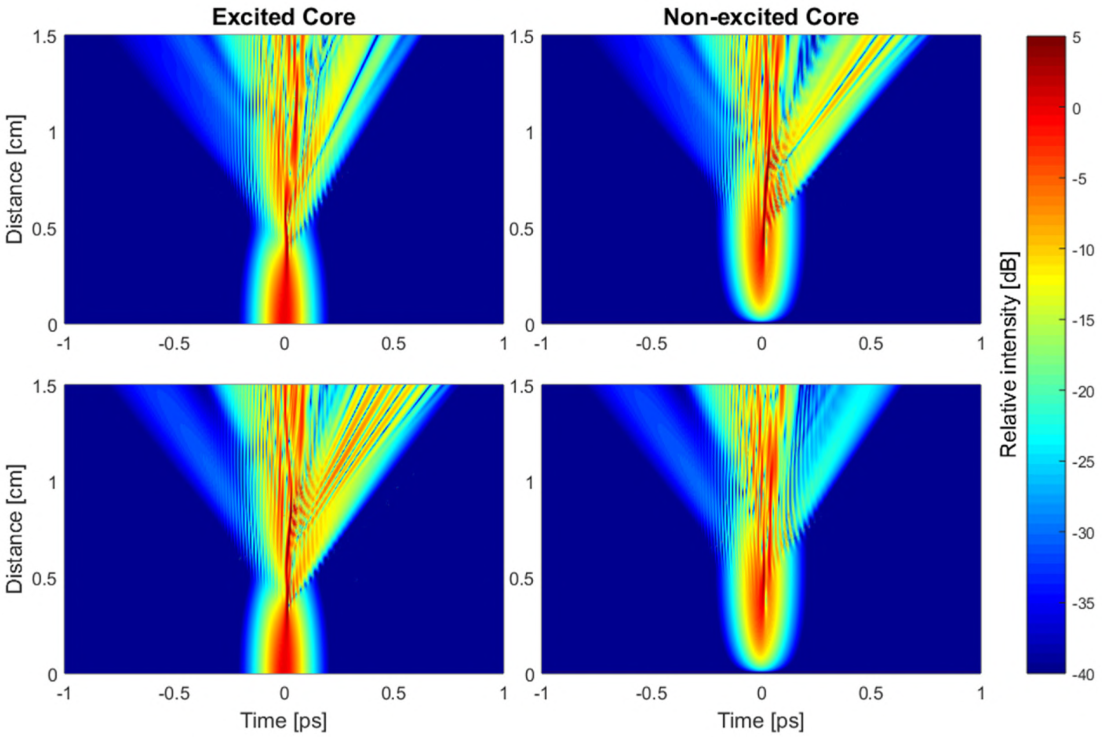

Fig. 2.18: *Best found switching performance considering optimized all-solid PCF structure under excitation by 1700 nm, 70 fs pulses. Time domain evolution of the field intensity in the excited (left) and non-excited (right) core at 129 pJ (top) and 141 pJ (bottom) pulse energies.*

It would be advantageous to ensure similar performance in the case of the all-solid approach. Hence, I performed the nonlinear simulation with the optimized PCF structure with Λ/r = 1.6 µm/0.85 µm and considering the same excitation condition as before (1700 nm, 70 fs). Fig.2.18 reports the four propagation maps (left side - excited core; right side - non-excited core) at the excitation energies of 129 pJ (top) and at 141 pJ (bottom). A promising switching performance together with the self-trapping mechanism is predicted in the range 5 - 10 mm of propagation distance. Unfortunately, the self-trapping process is not maintained beyond 10 mm due to the strong dispersive wave generation process. This phenomenon is recognizable by the smooth straight lines extending towards the positive half of the time domain map. Moreover, the all-solid PCF has lower level of anomalous dispersion and higher TOD than the air-glass PCF structure at 1700 nm (Fig.2.14). All these effect, combined also with the strong compression and nonlinear behavior, does not support an effective self-trapping. After 10 mm of propagation distance, the soliton fission process occurs and the multiple solitonic features (represented by red colored lines) redistribute themselves between the cores by linear coupling oscillations. Nevertheless, after the soliton compression distance of 4 mm, a high intensity (dark red) stable line (compressed soliton) occurs in the non-excited core at the lower excitation energy (top row) with peak at 8 mm. In contrast, at higher excitation energy (bottom row) and at the same propagation distance, the line occurs in the excited core with only weaker field intensities in the non-excited core.

Fig.2.19 depicts the temporal envelopes of field intensity at the switching length $L_\mathrm{s} = 8$ mm extracted from the 4 propagation maps in Fig.2.18. The calculated value of SC_E at L_s is 7.1 dB, much lower than the 13.4 dB calculated for the air-glass PCF at the same excitation conditions. The value is too low for application perspectives, when simple detectors with time integration character are used for the electro-optical conversion of the switched signal [267]. On the contrary, the obtained temporally localized SC in the time window of the highest intensity pulse is about 2 dB higher than the previous case, with a value of 36.2 dB. Thus, the best-found switching performance in the case of the all-solid PCF promises the attainability of an effective all-optical switching device with the new technological approach. On the other hand, the structure needs to be optimized more in order to support an effective soliton self-trapping.

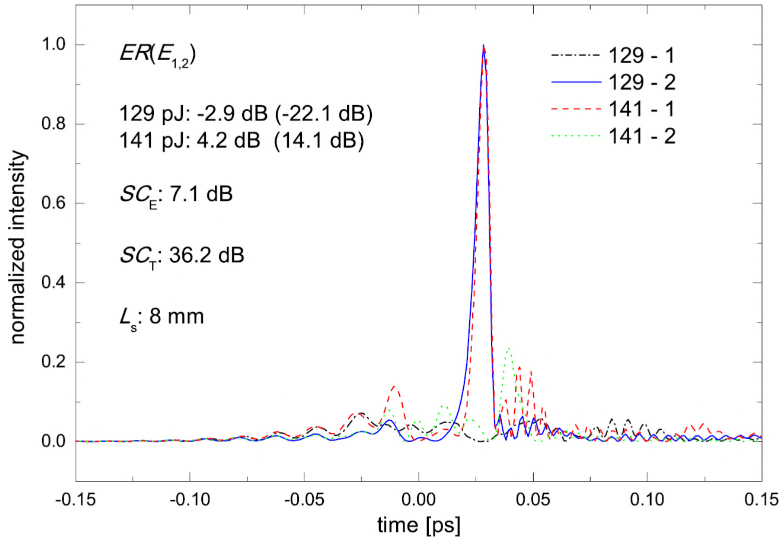

Fig. 2.19: *Time dependence of the field intensity envelope at the switching length (8 mm) in the both cores and at the both switching energies. All-solid DC PCF excited by 1700 nm, 70 fs pulses.*

Switching performance of the all-solid DCF with homogeneous cladding

Fig.2.20 reports the pulse envelopes in the case of the homogeneous cladding all-solid one and pitch $\Lambda = 1.6$ μm (structure depicted in Fig.2.12). At the same excitation conditions (1700 nm, 70 fs), the new structure supports SCs at the level of 12.1 dB regarding the integral energy and 32.5 dB regarding the temporally localized one. The switching length was elongated from 7 mm to 16 mm due to the longer CL in the case of simple all-solid DCF (Fig.2.14). Nevertheless, the requirement of $L_c \approx z_{comp}$ is satisfied at longer soliton compression distances, requiring lower pulse energies - and consequently lower soliton orders - to establish the self-trapping. Therefore, the switching energies in the case of the new structure are only 67 and 73 pJ, i.e. 3 times lower than in the case air-glass PCF at the same excitation parameters. They are already in the sub-100 pJ range of the in-coupled energy, which is an important progress from the application point of view.

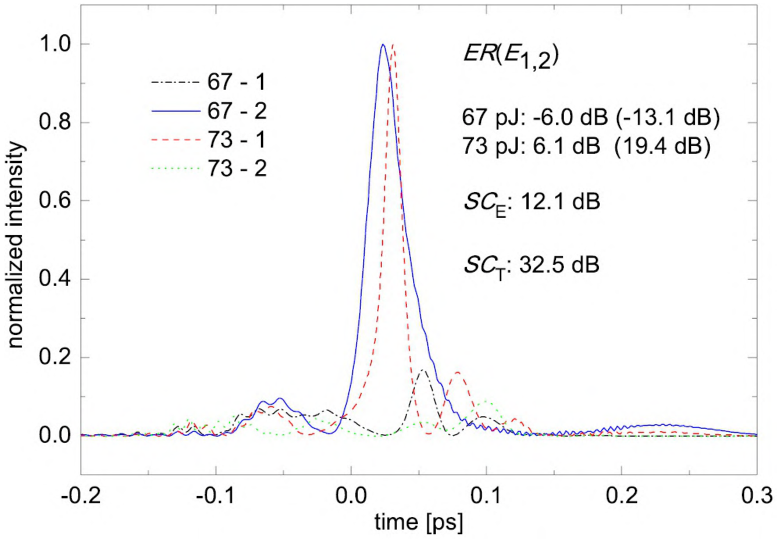

Fig. 2.20: *Time dependence of the field intensity envelope at the switching length in the both cores and at the both switching energies. All-solid homogeneous cladding DCF excited by 1700 nm, 70 fs pulses.*

To allow a comparison between the new air-glass PCF and the all-solid DC structure, I investigated the switching performance under the same excitation condition as in work [2], i.e. 1550 nm, 100 fs pulses [9]. In this case, the soliton compression length z_{comp} was calculated to be 20 mm, according to Eq.(1.38). Fig.2.21 shows the spectral propagation maps for two input energies of 100 (first row) and 112 pJ (second row)and both fiber cores (left and right columns). The propagation length was fixed to 100 mm in order to monitor the field evolution far beyond the soliton compression point. A switching performance has been predicted: at 100 pJ, the soliton is self-trapped in the non-excited core, while the same behavior occurs in the excited core at 112 pJ. The unbalanced field distribution in the cores can be noticed in both sets of maps. At 100 pJ (top row), the initial excitation in the excited core (left) is transferred to the non-excited one (right) after a propagation distance of 24 mm, which is equal to the CL (Fig.2.13). However, at the same length, the spectrum is significantly broadened in the non-excited core, i.e. soliton compression occurs; then, the highest intensities are maintained in the non-excited core even beyond 30 mm, while the excited core spectrum remains narrow, and no significant transfer of energy back to the excited core has been predicted. At 112 pJ energy level (bottom row), spectral broadening takes place in the excited core at around 23 mm and the dominance is maintained in the same core till 100 mm. The soli-

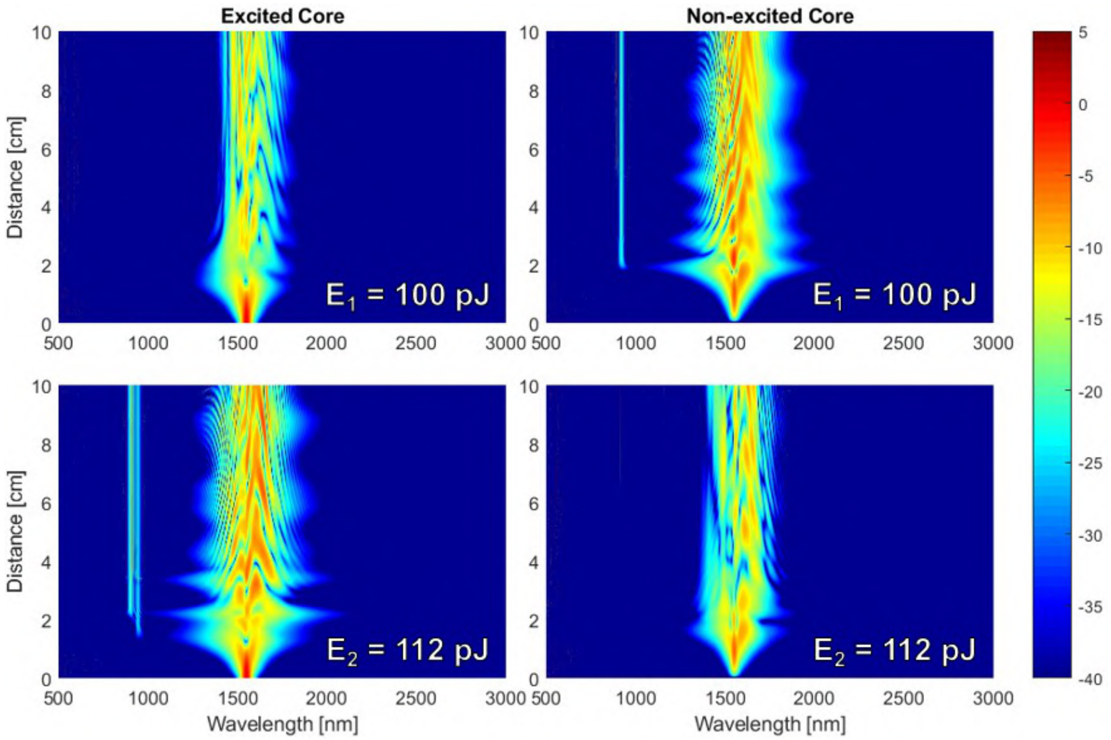

Fig. 2.21: *Spectral domain evolution of the field intensity in the excited (left) and non-excited (right) core at 100 pJ (top) and 112 pJ (bottom) pulse energies, under excitation with X polarized, 100 fs, 1550 nm. All-solid DCF with homogeneous cladding.*

ton period and the dispersive wave features are noticeable by the periodic oscillation of the spectral width with vanishing character. The sharp blue-shifted spectral features are predicted in the normal dispersion region at around 900 nm. In conclusion, the soliton-like pulse continues to propagate predominantly in the core where the soliton compression occurs. This is a typical signature of the soliton self-trapping mechanism with quasi-bistable character, determined by the input pulse energy.

The corresponding retarded time frame intensity propagation maps (Fig.2.22) show the soliton self-trapping mechanism in a more straightforward way. In the case of 100 pJ, the high-order soliton is transferred from the excited to the non-excited core at about 20 mm and it's immediately compressed there. After that, the back transfer to the excited core is only partial due to high peak powers generated by the compression mechanism. At 100 pJ (bottom row), the high-order soliton is compressed at around 10 mm (shorter than L_c), with small transfer to the non-excited core, and it is trapped in the excited core without any exceptions up to the end of the propagation distance. The linear coupling process has been prevented because, according to Eq.(1.38), z_{comp} is 15 mm for 112 pJ, which is shorter than the estimated 24 mm CL.

At the end of the previous section, I estimated that minimum energy required for the self-trapping, i.e. for the exact balance between the compression length and CL, is 41 pJ (before the in-coupling). However, the simulation results in Fig.2.21 and Fig.2.22 revealed that shorter compression lengths are necessary to establish the switching performance based on self-trapped solitonic propagation. According to Eq.1.94, a shorter z_{comp} requires a higher pulse energy than the estimated one. Moreover, the initial energy

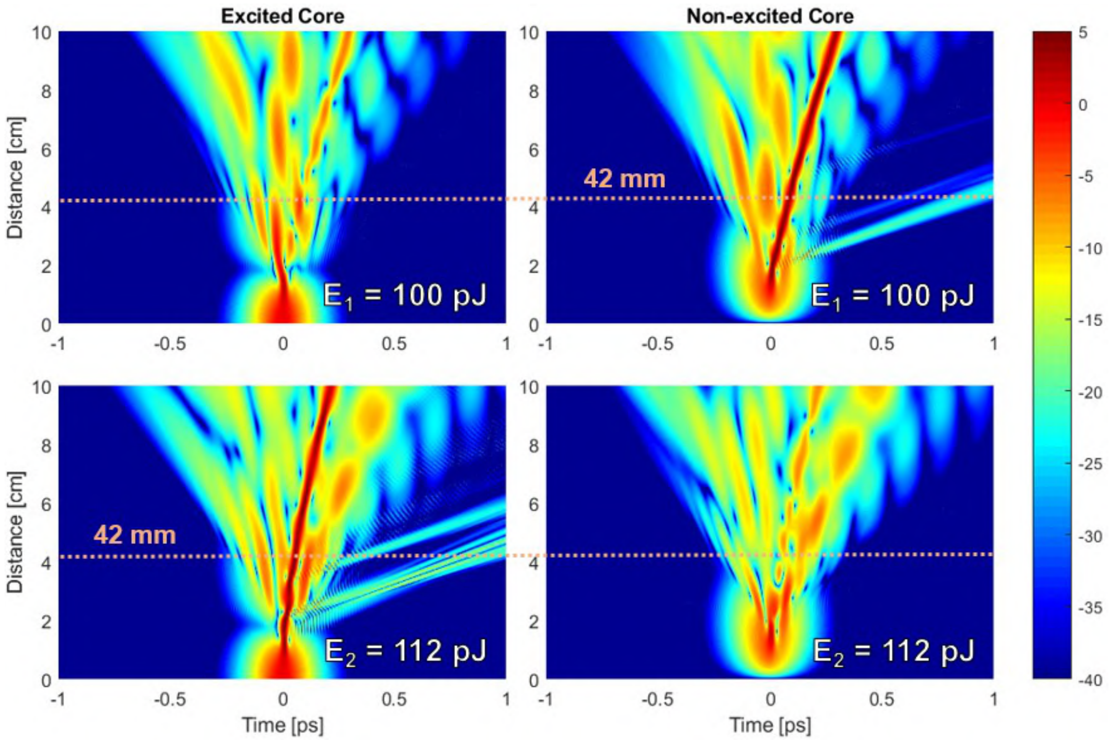

Fig. 2.22: *Time domain evolution of the field intensity in the excited (left) and non-excited (right) core at 100 pJ (top) and 112 pJ (bottom) pulse energies, under excitation with X polarized, 100 fs, 1550 nm. All-solid DCF with homogeneous cladding.*

transfer between the two cores slows down the compression process, which means that an additional increase of the energy is required to induce a compression length at the level of 24 mm. Thus, the value of 41 pJ for the input pulse energy is underestimated. In fact, it is important to notice that this value is evaluated before the in-coupling, i.e. without into account the IE of the fiber, which was considered as 32% as for the air-glass PCF [2]. Therefore, the minimum in-fiber energy to allow self-trapping is about 13 pJ. Moreover, the minimum value of 100 pJ from the simulation results corresponds to an in-fiber pulse energy of only 32 pJ, which is more than 3 times lower than the one identified for the air-glass PCF [2].

At the identified optimal switching length L_s of 42 mm, the *ER*s are -4.7 dB (negative, non-excited core dominance) for 100 pJ and 7.7 dB (positive, excited core dominance). The switching performance is asymmetric with 3 dB higher absolute *ER* at the higher pulse energy in comparison to the lower one. The SC_E is then 12.4 dB, which is approximately at the same level of one estimated for the air-glass PCF [2]. Fig.2.23 reports the temporal evolution of the pulse envelopes at L_s extracted from the four propagation maps in Fig.2.22. The self-trapped soliton in the non-excited core has longer duration and is delayed with respect to the excited core one. Even though, the energy of both envelopes is located in the time window of 100 fs, bearing some potential applications for data processing rates above 1 Tb/s. SC_T is calculated to be 34.8 dB. The presented switching performance is promising, because it predicts better contrasts than in the case of the air-glass PCF structure [2]. Even though the nonlinear coefficient γ and the effective mode area (of the fundamental mode) A_eff of the air-glass and all-solid

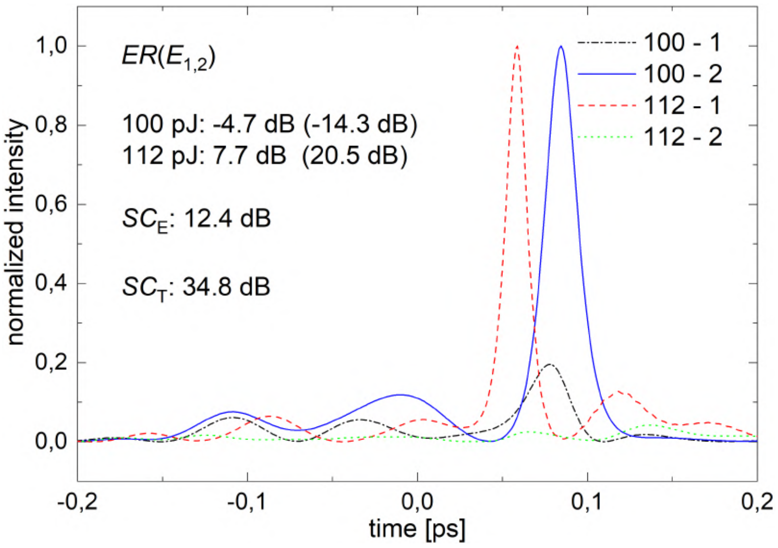

Fig. 2.23: *Time dependence of the field intensity envelope at the switching length in the both cores and at the both switching energies. All-solid homogeneous cladding DCF excited by 1550 nm, 100 fs pulses. SC of 12.4 dB.*

fiber are quite close to each other, the all-solid DCF with simple cladding has a much simpler manufacturing process and potentially promises a higher level of DC symmetry, which was not established in the case of the air-glass structure [3]. On the other hand, the simple DC all-glass structure has 3 times lower anomalous dispersion and 6 times longer L_c in the C-band. The increase of the wavelength λ causes an increase of the anomalous dispersion and at the same time a dramatic decrease of the CL (Fig.2.13 and 2.12). The strong predicted dependence of the switching performance on λ and its asymmetric character at 1550 nm motivate us to proceed further with the numerical analysis, looking for the best combination of excitation wavelength, pulse width and propagation distance.

2.4.3 Systematic nonlinear simulation analysis

I investigated the switching performance in the spectral range 1400 - 1800 nm to evaluate the excitation wavelength effects on the switching parameters. Then, I performed the same study, but related to the pulse width effect in the range 75 - 150 fs, which is achievable experimentally. I analyzed the switching performance for different combinations of excitation wavelengths λ and pulse widths T_0 and compared to the case presented in the previous section (1550 nm, 100 fs).

Excitation wavelength, λ [nm]	1400	1500	1600	1700	1800
Switching energies, $E_{1,2}$ [pJ]	17, 22	53, 65	107, 115	215, 232	422, 435
Soliton number, N	1.9, 2.2	2.4, 2.7	2.8, 2.9	3.4, 3.6	4.3, 4.4
Switching contrast, SC_E [dB]	12.5	**17.2**	16.1	12.4	7.2
Switching length, L_s [mm]	62	43	41	32	32

Table 2.2: *Switching parameters for different excitation wavelengths at fixed pulse width of 75 fs and at minimal switching energy levels for which the self-trapping of high-order solitons is induced in the non-excited (first value) and in the non-excited core (second value).*

Table 2.2 presents the switching parameters for different wavelengths at fixed pulse width of 75 fs: the switching energies $E_{1,2}(\lambda)$, the soliton number N, the switching contrast $SC_{\mathrm{E}}(E_{1,2}(\lambda))$ and the switching length L_{s}. By increasing the wavelength, the couple of switching energies increases monotonically, while the switching length has an opposite trend. The latter is manly caused by the decrease of the CL with λ (see Fig.2.13). Consequently, according to Eq.(1.94), the soliton compression length z_{comp} should also decrease in order to balance the CL and satisfy the self-trapping condition. The dispersion and the nonlinear parameter, which appear in Eq.(1.94) as well, have a weak dependence with λ. Thus, at increasing wavelength, the only possibility to decrease z_{comp} at fixed pulse width is to increase the peak power - e.g. pulse energy - (see again Eq.(1.94)). This assumption is in good agreement with the switching energies trend in Table 2.2. From this analysis, the optimal wavelength is 1500 nm at 75 fs pulse width, with an integral SC at the level of 17 dB. According to Eq.(1.31), the optimal soliton number supporting the self-trapped solitonic switching is in the range of 2 - 3. The results Table 2.2 point out that the switching of self-trapped solitons can be reached in a wider range regarding the input pulse energies (about 20 - 450 pJ) and fiber length (about 30 - 60 mm). On the other hand, the optimal SC requires an appropriate of soliton number: N should be high enough to allow an efficient self-trapping (i.e. pulse compression with sufficient peak powers) and low enough to minimize the soliton fission process, which can prevent an efficient propagation of fundamental solitons in the fiber cores.

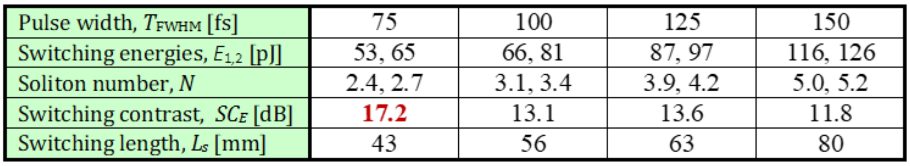

Pulse width, T_{FWHM} [fs]	75	100	125	150
Switching energies, $E_{1,2}$ [pJ]	53, 65	66, 81	87, 97	116, 126
Soliton number, N	2.4, 2.7	3.1, 3.4	3.9, 4.2	5.0, 5.2
Switching contrast, SC_E [dB]	**17.2**	13.1	13.6	11.8
Switching length, L_s [mm]	43	56	63	80

Table 2.3: *Switching parameters for different pulse widths at fixed wavelength of 1500 nm and at minimal switching energy levels for which the self-trapping of high-order solitons is induced in the non-excited (first value) and in the non-excited core (second value).*

Afterwards, I maintain the excitation wavelength λ fixed and I analyzed the pulse width dependence of the switching performance. Table 2.3 presents the values of the switching parameters in the case of constant $\lambda = 1500$ nm and changing pulse width in the range 75 - 150 fs, with a 25 fs step. The switching energies $E_{1,2}(\lambda)$, the soliton number N and the switching length L_{s} increase monotonically with T_{FWHM}. The integral SC SC_{E}, instead, generally decreases with increasing the pulse width, with the highest value of 17.2 dB at the shortest 75 fs T_{FWHM}. The only deviation from this trend is the slight increase of the SC at 125 fs pulse width. The reason of the monotonic increase of the switching length is the elongation of z_{comp}. According to Eq.(1.94), z_{comp} is directly proportional to T_0, which is the only changing parameter in the frame of this study. Therefore, the increase of the compression length cause the SC to decrease: as the CL L_{c} remains constant due to the unchanged wavelength and z_{comp} is getting longer, the self-trapping requirement $z_{\mathrm{comp}} \approx L_{\mathrm{c}}$ is not totally satisfied and the SC slightly decrease. The same evaluation can be done in the case of wavelength dependence study, because pulses with longer widths than 75 fs cause rather a reduction of the SC. I did not consider shorter widths than that, because my goal is to establish the switching performance using laser pulses from commercially available cheap Er-based mode-locked oscillators. Furthermore, the broadband character of shorter pulses would be a disadvantage from the point of view of the dispersion.

The most important outcome of the two above presented studies is the optimal level of the soliton number to be between 2 and 3, which ensures the best SC of 17.2 dB in both cases. Second, I can observe that the bistable switching process is very sensitive to all the linear and nonlinear propagation parameters. In particular, the increase of the excitation wavelength has a strong impact on the switching energies, which can increase of about 20 times between 1400 and 1800 nm. Moreover, the small deviations from the general trends are a natural effect of the soliton self-trapping process, which has a threshold character and experience sudden switching between cores.

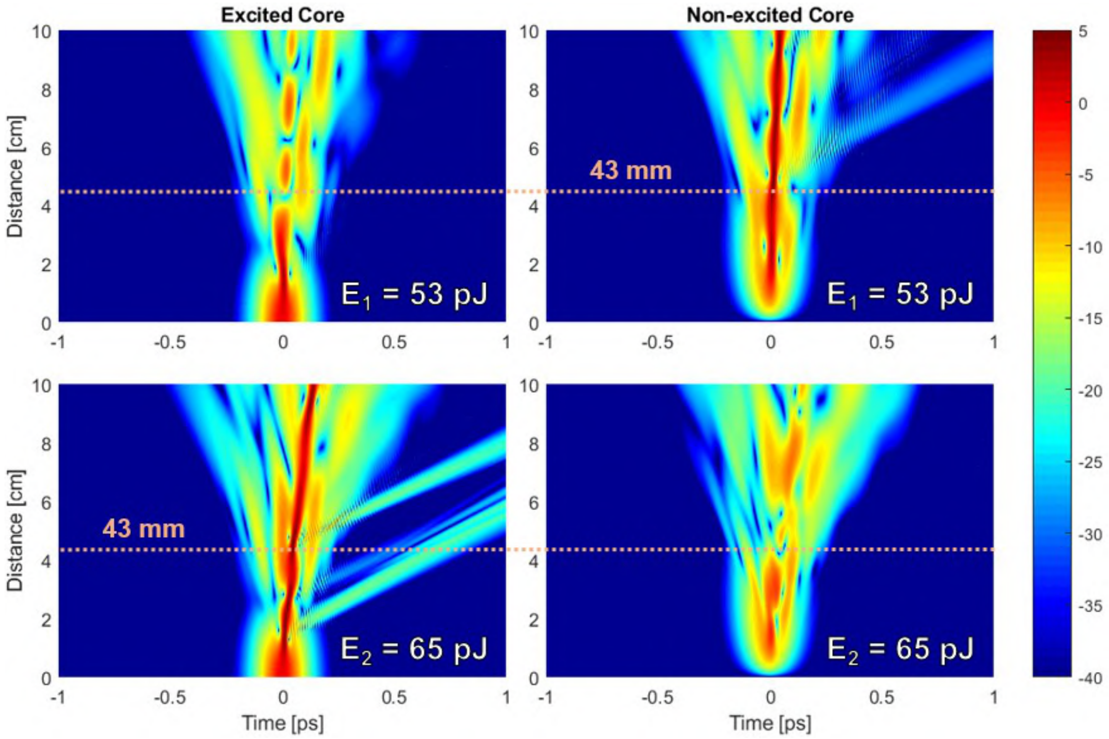

Fig. 2.24: *Time domain evolution of the field intensity in the excited (left) and non-excited (right) core at 53 pJ (top) and 65 pJ (bottom) pulse energies, under excitation with X polarized, 75 fs, 1500 nm in case of the best switching performance. All-solid DCF with homogeneous cladding.*

In conclusion, the combination **1500 nm, 75 fs** with a soliton number of 2.5 (in average) results to be the best overcome from the point of view of SC in the chosen excitation parameter ranges. Fig.2.24 reports the temporal propagation maps corresponding to this specific case. Comparing them to the results obtained for combination 1550 nm, 100 fs in Fig.2.22, I can see that the propagation character is less complex due to negligible soliton fission, which is one of the advantage of the relatively low soliton number. The combination 1500 nm, 75 fs ensures higher SCs because of the higher energy concentration in the fundamental dominant soliton (the dark red line in the maps). In addition, the switching length L_s is comparable in the both presented case (42 mm and 43 mm, respectively). This is another confirmation of the trends showed in Tables 2.2 and 2.3: shorter wavelengths cause an elongation of L_s, while shorter pulse widths have the opposite trends, reaching an optimum at 1500 nm and 75 fs, respectively.

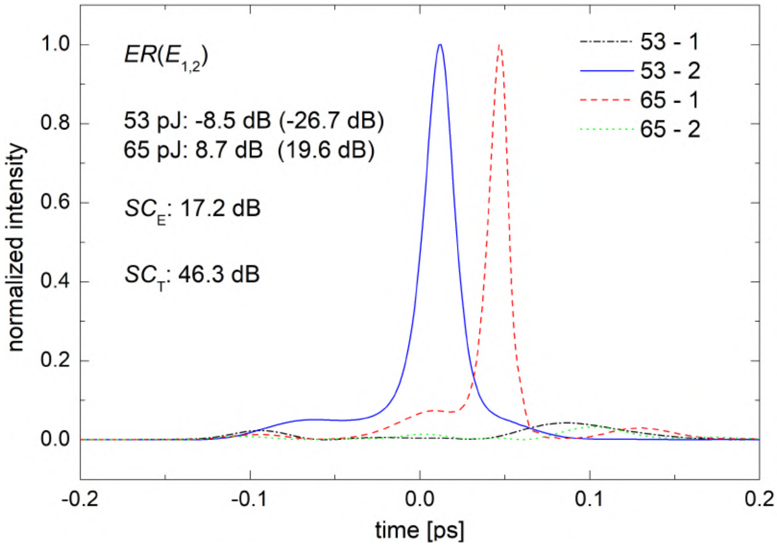

Fig. 2.25: *Time dependence of the normalized field intensity envelopes at the switching length in the both cores and at the both switching energies in the case of the best switching performance. 43 mm all-solid homogeneous cladding DCF excited by 1500 nm, 75 fs pulses. SC of 17.2 dB.*

Fig.2.25 shows the temporal intensity envelopes in the best switching performance case at the identified optimal L_s of 43 mm. The input pulse energy E_1 and E_2 are 53 pJ and 65 pJ, respectively. Even in this case, there is a similar temporal delay between the dominant pulses in the two different cores, as for the one presented in Fig.2.23. The integral energy SC SC_E increased from value 12.4 dB (1550 nm, 100 fs) to value 17.2 dB. Above all, the switching performance in the best switching performance case is symmetric because it expresses the same level of DC ER at the both energies (-8.5 at 53 pJ vs. 8.7 dB at 63 pJ). The temporally localized SC SC_T increased significantly, from 34.8 dB to 46.3 dB.

Table 2.4 reports the compared values of the switching parameters from the air-glass DC PCF structure study [2] and the optimized simple DCF one. I report the in-coupled switching energies instead of the input ones in order to compare the two cases. For both I considered the experimentally determined 32% IE in the case of the DC PCF fiber used in the experiments [3], even if the value for the all-solid structure should be much higher [13]. In general, the excitation parameters are very similar in the both cases, but the dispersion and CL differ significantly. The 3-times lower anomalous dispersion and almost 10 times longer L_c lead to a structure with relatively weak coupling and switching lengths only at the level of more than 40 mm. However, from the point of view of all the other parameters, the all-solid DCF approach offers important advantages. The switching energies are 6 times lower and even the soliton number is lower, enabling a strong self-trapping after the soliton compression. These improvements relies on the simultaneous elongation of L_c and corresponding L_s, which causes the decrease of the switching energies at the level of 20 pJ (clearly in the sub-100 pJ range). The combination of these improvements permit to enhance both the integral and the temporally localized SC by a factor of 30% in comparison to the air-glass PCF case. Furthermore, the all-solid DCF has more application potentials than the alternative air-glass structure due to its simple cladding, without the photonic lattice structure, and high integrability into the standard communication systems based on optical fibers. It means that it is possible to use simple fiber oscillators without any amplification stage to allow the soliton self-switching in DCFs. In fact, the optimal wavelength is close to the central one of the C-band and the pulse width is comparable to the typical values obtained using standard commercially available Er-doped fiber oscillators.

	λ [nm]	T_0 [fs]	D [ps/nm/km]	$E_{1,2}$ [pJ]	N	z_{comp} [mm]	L_c [mm]	L_s [mm]	SC_E [dB]	SC_T [dB]
Air-glass PCF	1550	100	169	115, 124	4.1, 4.3	3.4, 3.2	3.7	10.3	11.8	34.8
All-solid simple	1500	75	56.1	17, 21	2.4, 2.7	13.7, 11.7	33	43	17.2	46.3

Table 2.4: *Comparison of the switching parameters in the case of earlier studied air-glass DC PCF structure and in the case of simple all-solid DCF structure. The new structure supports the switching performance at the optimal soliton number and it enables higher SCs at simultaneous lower switching energy requirement.*

Moving the discussion to the spectral domain, Fig.2.26 shows the wavelength dependence of (a) pulse envelopes and (b) DC *ER* in the range 1375 - 1625 nm for the best switching performance case: all-solid simple DCF, 1500 nm - 75 fs excitation, L_s =43 mm in the wavelength range 1375 - 1625 nm. The spectral profiles in Fig.2.26a are normalized to 1 for each of the two switching energies, while the intensity relation between the two cores in Fig.2.26b is preserved in the case of the both energies. An output nonlinear spectral broadening with a bandwidth beyond 200 nm was predicted. It expresses **broadband and uniform character** of the self-trapped soliton switching concept. The dominance of the non-excited and excited core is maintained in the whole spectral range (except in a very narrow window at around 1600 nm) considering 17 and 21 pJ pulse energies, respectively. The value SC (difference between the two depicted *ER* curves) exceeds the level of 10 dB for most of wavelengths with an average value of approximately 20 dB. Moreover, three exceptional SC peaks of 39 dB, 39 dB and 30 dB can be found at wavelengths 1420 nm, 1480 nm and 1515 nm, respectively. This could open some perspectives of the studied novel switching concept for spectrally resolved multichannel applications. All of the new predicted SC and SE values are even much higher than the best ones achieved experimentally by Stajanča et al., i.e. 15 dB of SC and switching energies of 20 and 50 nJ before the in-coupling optics [5]. In conclusion, the numerical study presented here show that a switching performance is potentially achievable and the previous experimental results can eventually be improved using a relatively easy-to-fabricate all-solid DCF.

From the point of view of potential experimental realization, it is necessary to investigate if the presented best switching performance is robust against the fluctuations of the input pulse energy (peak power) and of the structural dimensions of the fiber. I performed the nonlinear simulations considering the same optimized all-solid DCF structure and the optimal excitation parameters of 1500 nm, 75 fs and exploiting the values of the optimal switching energies (53 pJ, 65 pJ) under a fluctuation at the level of $\pm 5\%$ close to the optimal ones. The results are presented in Table 2.5. The extensive study revealed that the upper energy level is very **robust against fluctuations** of the pulse energy: it means that the energy pairs 53 pJ, 68 pJ or 53 pJ, 62 pJ result in a high

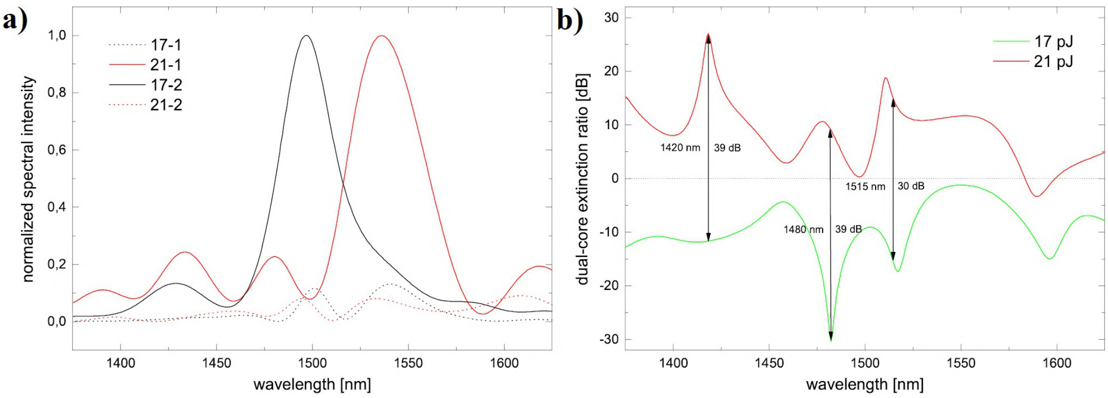

Fig. 2.26: *Wavelength dependence of (a) field intensity envelope at the switching length of 43 mm in the both cores and at the both switching energies, and (b) DC ER of the spectral intensities. Homogeneous cladding high index contrast DCF excited by 1500 nm, 75 fs pulses.*

contrast switching performance at the level of 17 dB, very close to the optimum one. The soliton remains to be strongly trapped in the bar core in the whole energy range of 62 - 68 pJ. The lower energy level is also robust because the soliton is still strongly trapped in the non-excited core in the energy range of 47 - 53 pJ. Even the combination of 50 pJ and high energy levels between 62 pJ and 68 pJ results SCs at the level of 17 dB, but the optimal switching length L_s is elongated to 58 mm. For the lowest considered value of 47 pJ, the SCs decrease significantly below 13 dB at switching lengths in the range of 55 - 60 mm.

Switching energies, $E_{1,2}$ [pJ]	47, 62	47, 65	47, 68	50, 62	50, 65	50, 68	53, 62	53, 65	53, 68
Switching contrast [dB]	12.4	12.8	13.2	16.3	16.7	16.8	16.6	17.2	17
Switching length [mm]	60.0	56.7	55.7	58.2	58.3	57.7	44.8	43.0	43.8

Table 2.5: *Effect of input energy fluctuation at level of* $\pm 5\%$ *on the SC and switching length in the conditions of the best-found switching performance.*

Fortunately, the standard femtosecond Er-doped mode-locked fiber oscillators I used in the experimental phase exhibit an amplitude RMS noise at the level of 0.5%. Therefore, the fluctuations of the input peak power will not compromise the optimal switching performance described so far. The problem of the structural dimensions fluctuations along the fiber axis is even less crucial. In fact, the predicted optimal fiber length is rather short, at the level of only 40 mm. Furthermore, it is possible to monitor the diameter of the soft glass fibers during the fabrication process with a precision at the level of 1%, which causes only negligible changes of linear and nonlinear properties of the fiber.

2.5 Fabrication process of the all-solid DCFs

I was involved in the fabrication of the optimized all-solid DCF at Ł-IMIF in Warsaw. At this institute, I used the **stack-&-draw** technique, which is well-consolidated for the fabrication of multicore and microstructured optical fibers and has more than 30 years of history in the institution [253]. The stack-&-draw technique essentially means to pile up together rods of two or more glasses into a macrostructure called preform. Then, this preform is fed into a high-temperature furnace in order to scale down its diameter up to few millimeters. The control of the core diameter is performed by monitoring the overall diameter of the fiber varying the temperature of the furnace (typically in the range 600 - 800°C) or by the seeding and pulling speed. They are the speed at which the preform is fed through the furnace and extruded from it, respectively.

The stack-&-draw process (schematized in Fig.2.28) can be summarized in this list:

1. **Preparation of rods** for the fiber preform: from a heavy glass matrix (example in Fig.2.27a for PBG-08), many glass rods of both UV-710 and PBG-08 are drawn down from a fiber tower (Fig.2.27b) in order to reach a diameter size between 1 and 2 mm;

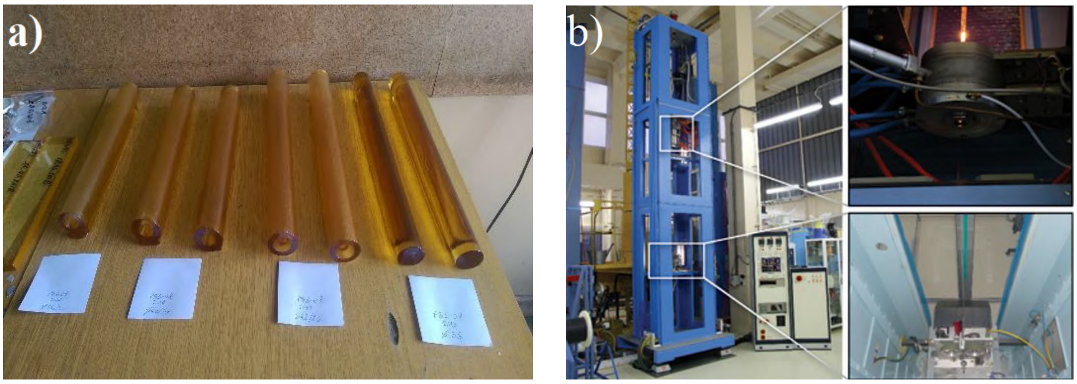

Fig. 2.27: *(a) Heavy glass matrices of PBG-08 with different diameter and weight fabricated at Ł-IMIF. (b) Drawing tower facility at Ł-IMIF (left), including a high-temperature furnace for glass melting (top right) and various fiber fabrication units (bottom right).*

2. **Preform stacking**: The rods are assembled by hand into a designed fiber subpreform that contains approximately 100 individual rods. In the central line, the subpreform has two PBG-08 rods, which represent the two cores of the fiber, inside a hexagonal shaped matrix of UV-710 rods. Then, the stacked subpreform, with a total diameter of 50 mm, is surrounded by small PBG-08 rods in order to form the outer cladding with circular shape. At the end, the whole structure is placed into a PBG-08 glass tube;

3. **Subpreform drawing**: The subpreform is drawn down to a 1 mm diameter with the same drawing tower in Fig.2.27b. During the drawing phase, a series of subpreform samples with a length of around 30 cm is collected;

4. **Subpreform analysis**: The scanned electronic microscope (SEM) image of each subpreform sample cross-section is acquired using the Auriga ZEISS microscope available at Ł-IMIF. Then, the images are processed numerically to identify the optimal subpreform for the final drawing phase. More details of this method will be provided later;

5. **Final fiber drawing**: The selected optimal subpreform is placed again into a PBG-08 tube; then, it is drawn down once again to get the desired fiber diameter (in my case, at the level of 110 μm) and fill the small remaining air gaps between its rods.

In section 1.3.4, I pointed out that the coupling properties of the DCF and the principle of soliton self-trapping rely on the symmetry of the DC structure. This means that the switching performance of the DCF is strongly dependent on the cores shape and overall fiber structure symmetry, i.e. on the fiber fabrication process. Therefore, the DC symmetry had been checked several times at each phases of fabrication.

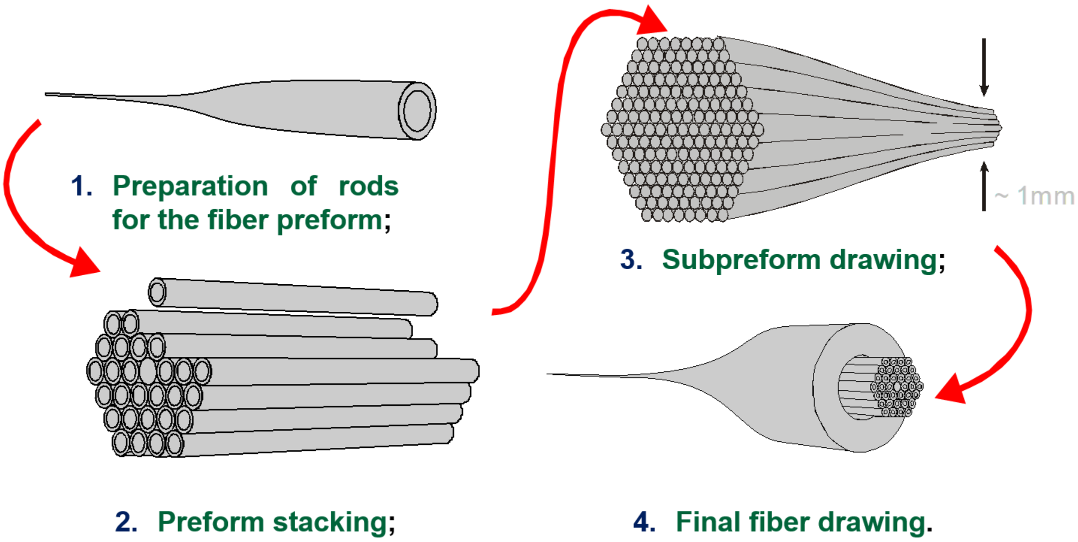

Fig. 2.28: *Scheme of stack-&-draw fabrication process typical for PCFs manufactured at Ł-IMIF. The same method was adopted for fabrication of the optimized DCFs.*

At the beginning, during the stacking of the initial preform, all the PBG-08 glass rods were checked individually and their diameter measured along the length using a caliber with 10 µm resolution. Then, a couple of rods with equal diameter and its stable value which show both a constant diameter along their length wase selected as the two cores. The rest of the PBG-08 rods were used for the outer cladding of the DCF. After the stacking, a series of subpreforms was drawn down with a drawing tower under monitoring the drawing speed and the temperature of the furnace. The diameter of the subpreforms was measured using a microscope after each sample. I manufactured a few 20 - 30 cm long subpreforms with the diameter of about 1.6 mm. The subsequent phase of the fabrication is indeed the most crucial: the identification of the best subpreform for the final fiber drawing.

2.5.1 Analysis of the subpreforms and final fabrication of DCFs

The study of the subpreforms structure was performed with the help of a Matlab code, which analyzes the SEM pictures of the subpreforms cross-sections. Fig.2.29 shows an example of cross-section picture of a DCF subpreform sample with a magnification of (a) 46x, (b) 132x, (c) 500x. The subpreform has a total diameter of 1.6 mm. The SEM images show that the core borders do not form the optimal hexagonal shape as expected from the numerical simulations (Fig.2.11), but they are deformed towards a star-like shape. This deformation took place because the UV-710 glass for the cladding is harder than the PBG-08 glass for the cores. Therefore, the original curvature of the cladding rods is preserved more. All the most important parameters, such as fiber diameter, cores/cladding structure lengths and cores diameters and distance are evidenced in Fig.2.29 (a), (b), (c) respectively. The cores have an average diameter of 67 µm and a core distance of 106 µm. Fig.2.29d reports the SEM picture of the cores (magnification 500x) and the inscribed circumferences, which show the deviation from the original cylindrical shape of the rods.

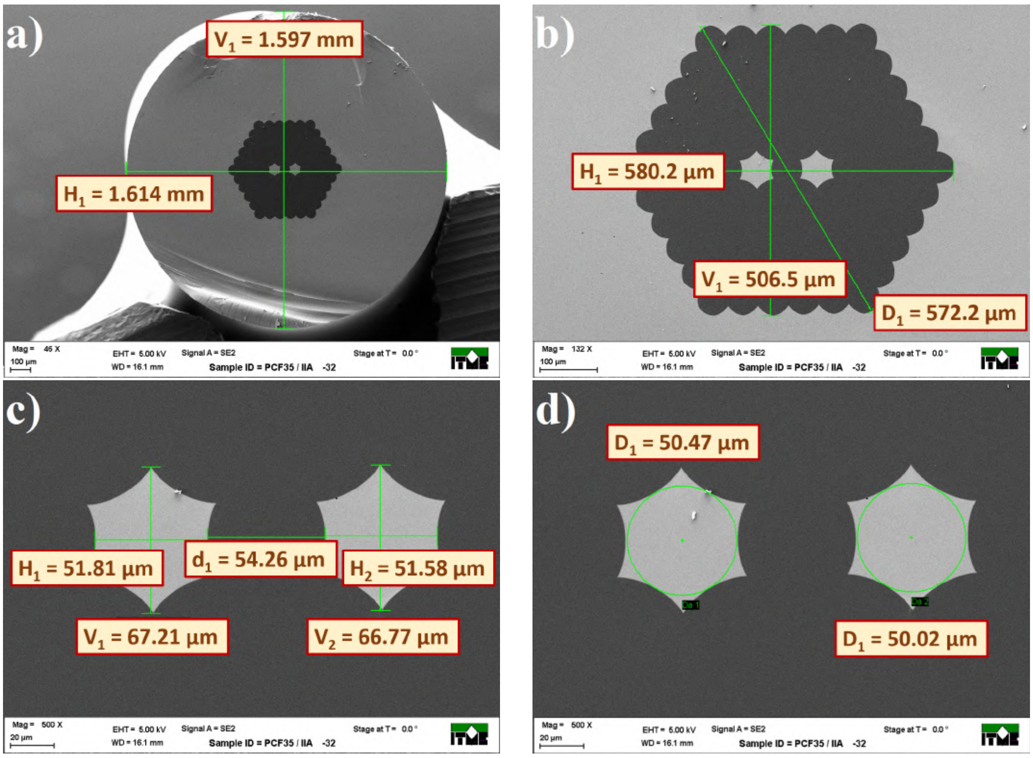

Fig. 2.29: *Example of SEM images of the cross-section of the all-solid DCF subpreform with 6 rings around the central rod at three different magnifications: (a) 46x, (b) 132x, (c) 500x (with measured core distance and main core dimensions) (d) 500x (with inscribed circumferences diameters).*

The SEM subpreform images with the highest magnification were processed numerically in order to retrieve the boundaries between PBG-08 and UV-710 glass. This process is called **segmentation** and allows to retrieve the core shapes and identify their geometrical parameters in an easier way. Fig.2.30 reports an example of the outcome of such operation performed on Fig.2.29d. To study the DC symmetry, which is the goal of this study, the core shapes were studied in terms of **diagonals** and **core area differences** between the cores. For each core, the Matlab code first identifies the position of the 6 vertices of both hexagonal cores (red diamonds in Fig.2.30). Then, it calculates the length of the 3 diagonals crossing the center of gravity for both hexagons: $D_{1,\mathrm{j}}$, $D_{2,\mathrm{j}}$ and $D_{3,\mathrm{j}}$, with $j = l, r$ corresponding to left and right core, respectively. They were selected in Fig.2.30 and give a more intuitive representation of the symmetry deviation of the core shapes. At the end, the difference (in percentage) between left and right core diagonals was calculated separately as follows

$$D_{\kappa,\mathrm{diff}} = \left| 1 - \frac{D_{\kappa,\mathrm{l}}}{D_{\kappa,\mathrm{r}}} \right| \cdot 100 \tag{2.8}$$

where $\kappa = 1, 2, 3$ indicates the corresponding diagonal in Fig.2.30. To have an over-

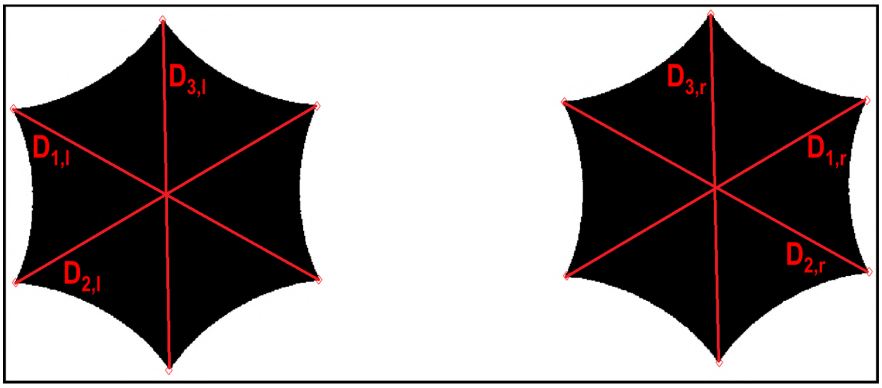

Fig. 2.30: *SEM image of the DCF with the highest magnification after segmentation process of Fig.2.29d. The vertices of the hexagons and the diagonals* $D_{k,l}$ *and* $D_{k,r} (k = 1, 2, 3)$ *measured during the subpreform analysis are evidenced with red dots and red lines, respectively.*

all view of the diagonal deviations between left and right core, the 3 calculated deviations were then averaged to get the value D_{av}, which gives an indicative value of the DC structural asymmetry.

Another approach for the study of the DC shape is the difference between the two cores area. This method implies Fig.2.30 once again and it's simply performed by counting the number of black pixels on the left and right half of the figure A_l (left) and A_r (right core), respectively. Then, the percentage difference is calculated by a similar expression as Eq.(2.8):

$$A_{\text{diff}} = \left| 1 - \frac{A_l}{A_r} \right| \cdot 100 \tag{2.9}$$

As for D_{av}, the values of A_{diff} calculated from the processed SEM images which corresponded to the same subpreform were averaged too in order to get $A_{\text{diff,av}}$. Even if it is an added value to the geometry analysis of the cores, the calculations of the area difference is sometimes misleading: it doesn't take into account the position of the vertices of the hexagonal cores, but just on the surface occupancy of the cores. This is not a proper approach because it can happen that the two cores have the same area, but significant different hexagonal shapes, which compromises the coupling efficiency. Therefore, I paid more attention on the diagonal difference investigation, which actually gives more information about the vertices position and shape spread of the two cores.

To improve the DC symmetry and to match better the advantageous numerical simulation results under assumption of a totally symmetric structure, I fabricated another subpreform. It consists of an hexagonal structure with 6 rings around the central rod and it incorporates **5 DC waveguides** which are separate between each other in such a way that the interaction between them is negligible. Fig.2.31a presents the final subpreform structure after the two-glass rods stacking phase: *orange* and *white rods* are made of PBG-08 and UV-710 glass, respectively. With this new approach, the probability of to get better symmetry structure will increase and can help statistically to get better DC structure. It is rather advantageous from the fabrication point of view because it allows not to repeat many times the preform preparation - fiber drawing sequence. In fact, the time for the subpreform fabrication is rather comparable to the one of the previous DCF subpreform in Fig.2.29 because the stack-&-draw method described before is unchanged. Thus, I manufactured a few 20 cm subpreforms with a diameter of about 1.6 mm and then I acquired the SEM images of each of them. An example of them is reported in Fig.2.31b, which shows the new multiple DC pair subpreform with a magnification of 118x and structural diameter of 685 µm.

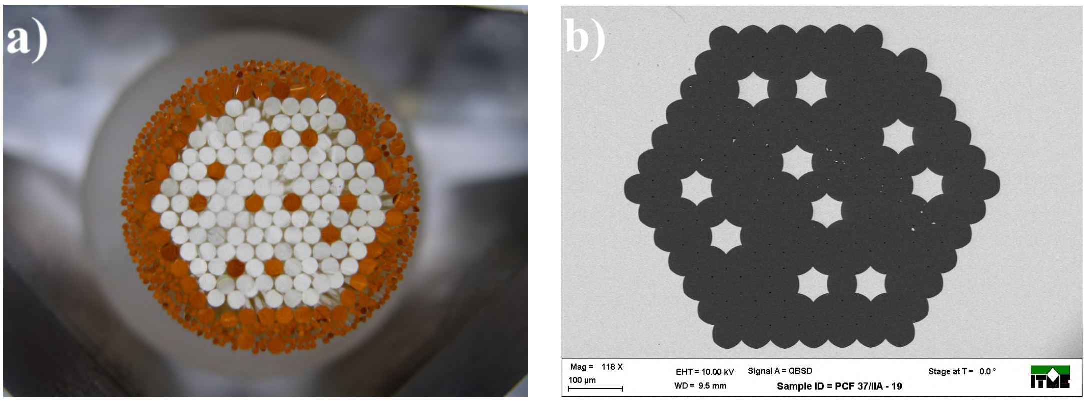

Fig. 2.31: *(a) Picture of the subpreform cross-section of the new multiple-pair DCF after stacking process conducted at Ł-IMIF. (b) Scanned SEM of the final subpreform of the multiple-pair DCF the same diameter (magnification 118x). The diameter of the cladding is at the level of 685 µm.*

The final fibers were drawn with the help of a 30 m drawing tower available at Ł-IMIF. The goal was to reach the optimal core distance of 3.2 µm predicted by the numerical simulations (section 2.4). In order to do so, it is possible to control the temperature of the furnace, the seeding speed of the original subpreform and the pulling speed of the final fiber during the last fabrication step. The temperature of the furnace was set in the range of 800-820°C, which is slightly above the spreading temperature of the PBG-08 glass and below the one of UV-710 (Table 2.1). This allows the subpreform to be melted down while keeping the UV-710 cladding structure stable and more controllable during the drawing. The seeding speed was kept mostly constant to 1 mm/min to allow the homogeneous glass melting. The only changing parameter is the pulling speed of the fiber, which can be accelerated or decelerated to decrease or increase the fiber diameter, respectively. The drawing parameters during the fabrication of the DCF with 5 DC waveguides is reported in Table 2.6.

Sample	Furnace temperature [°C]	Seeding speed [mm/min]	Pulling speed [m/min]	Estimated fiber diameter range [µm]	Estimated D_{cl} [µm]
1	820	0.8	0.9	140-150	24-25
2	805	0.8	1	145-155	
3	805	1	1.2	140-145	22-23
4	810	1	3.9	135-140	
5	810	1	1.5	130-145	20-21
6	810	1	1.65	115-120	
7	810	1	1.8	120-125	18-19
8	810	1	1.9	115-120	

Table 2.6: *Set of drawing parameters of the final all-solid DCF with 5 DC waveguides. The estimated fiber and cladding (D_{cl}) diameters are reported on the right side of the table.*

The general approach while drawing the optimized DCFs is to fabricate more samples, starting from longer diameter than the optimal one. Then, the pulling speed is decreased step by step to reach and overcome the predicted optimal diameter in the range of about ±10% with respect to that value. During the fiber drawing, the diameter is checked regularly with the help of a microscope. Due to the limited resolution of this instrument, it is possible to have only a rough estimation of the fiber diameter and of the cladding structure D_{cl}. Table 2.6 reports the results of these measurements for the fabricated 8 DCF samples. The drawing phase started from DCFs with a fiber with estimated cladding diameter of 24 - 25 μm (longer than the optimal) and ended after 8 samples, which have 18 - 19 μm cladding diameter (shorter than optimal). The best correspondance with optimal diameter of 20.8 μm (1.6 μm times 13 elements on the diagonal) identified in the study of the fiber structure optimization was established in the case of samples 5 and 6.

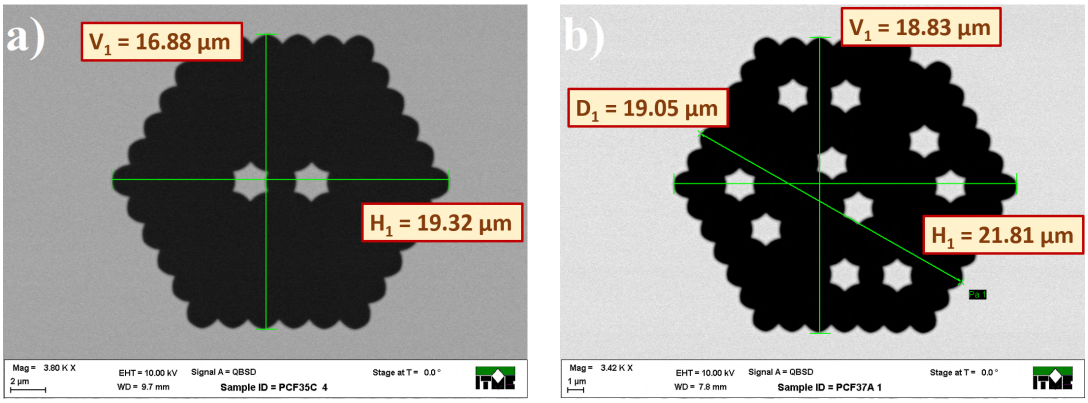

Fig. 2.32: *Example of SEM images of the final fabricated DCFs with optimal DC symmetry: (a) all-solid DCF with simple cladding; (b) all-solid DCF with 5 incorporated DC elements.* D_{cl} *of the fibers are 19.3 μm, corresponding to 3.5 μm and 3.4 μm, respectively. Both fibers have longer core distance than the optimal one (3.3 μm).*

After fabrication, SEM images of each sample were acquired once again to verify the symmetry of the DC structure and the core distance, which are the most important parameters in my study. An example of SEM for two final fiber samples are shown in Fig.2.32a (simple DCF) and Fig.2.32b (DCF with multiple DC elements, with evidenced D_{cl}). At the end, I analyzed all 5 DC waveguides with the same method presented above and finally selected the central one to be analyzed in the experimental phase due to its higher level of DC symmetry.

2.5.2 Technological methods and study of the DC optical asymmetry

In conclusion, a series of fiber samples from two different preforms with optimal DC symmetry ($D_{\mathrm{diff}}{}^{\mathrm{av}}$, $A_{\mathrm{diff}}{}^{\mathrm{av}} < 0.5\%$) was fabricated: 1) all-solid DCF with two hexagonal star-shaped cores and homogenous photonic cladding; 2) a preform containing 5 DC units non-interacting between each other, with one extra cladding ring of UV-710 glass rods. I performed the study of more fiber samples with different diameters at the thorough excitation of the both fiber cores. However, in the following pages, I present only the experimental outcomes in the case of two different samples with optimized fiber length: one from the first generation and one from the second generation, respectively. They allow comparison between two generations of fibers and a deeper inside on the physical mechanisms regulating the solitonic all-optical switching. The geometrical parameters of the two final fibers, i.e. number of glass rings, cladding diameters and core distance, are reported in Table 2.7. The first fiber had slightly smaller cores distance than the optimal one (3.2 µm) identified during the numerical simulations study (see section 2.3) [6, 9]. On the contrary, the second fiber has a larger cladding diameter than the first fiber due to the extra ring of rods added during the stacking phase. Moreover, the central DC pair of the second fiber had a larger distance between the cores (3.3 µm), but improved DC structural symmetry than the first generation one, thanks to the better structural control during the drawing phase of fabrication.

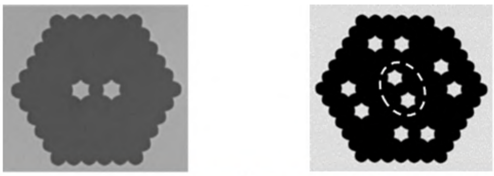

	First generation DCF	Second generation DCF (Central pair)
Number of rings	5	6
Cladding diameter [µm]	17.4	21.3
Core distance [µm]	3.1	3.3

Table 2.7: *Geometrical parameters and corresponding scanning electron microscope cross-section picture of the two samples of DCF used in the experimental phase. The analyzed DC pair in the second generation DCF is evidenced by a dashed ellipse.*

In the second step, I calculated the overlap integrals between the two cores in order to determine the coupling coefficient between the two cores [268]. Fig.2.33 reports the CL characteristics of the two fibers with cross-section as in Table 2.7. The curves are compared with the one of the hypothetical symmetric all-solid DCF structure (also shown in Fig.2.13). The CL characteristics of the first and second generation fiber differ significantly from the one of the hypothetical structure. At 1500 nm they are 1.8 and 2 mm, respectively, more than an order of magnitude shorter than the 33 mm of the hypothetical one. At 1700 nm they are 1.5, 1.6 and 9 mm, respectively. The graph in Fig.2.33 shows then that the coupling properties of the fabricated DCFs are very sensitive to the structural asymmetry between the cores. This property is referred as **DC structural asymmetry**. Moreover, the second generation DCF shows a longer CL than the first generation one in the range 1000 - 1700 nm, indicating that the DC asymmetry in the second generation fiber was reduced using the improved fabrication technology.

Moreover, as I explained in section 1.3.5, the two cores exhibit also a mismatch of the propagation constants because of the fiber structural asymmetry. This effect of is referred as **DC optical asymmetry** [10]. Due to the mismatch, the two cores exhibit a difference of the effective refractive indices n_{eff} and can be distinguished as **slow** and **fast core**, with effective refractive index $n^{\mathrm{s}}_{\mathrm{eff}}$ and $n^{\mathrm{f}}_{\mathrm{eff}} < n^{\mathrm{s}}_{\mathrm{eff}}$, respectively. When the fast core is excited, a Kerr-induced phase shift decreases the propagation constants mismatch between the cores, causing a decrease of the DC asymmetry. On the contrary, in case of slow core excitation, the asymmetry between the cores is further increased by the Kerr nonlinearity, which weakens the coupling between the cores. Table 2.8 reports the basic optical properties of the individual cores of the both studied DCFs [10].

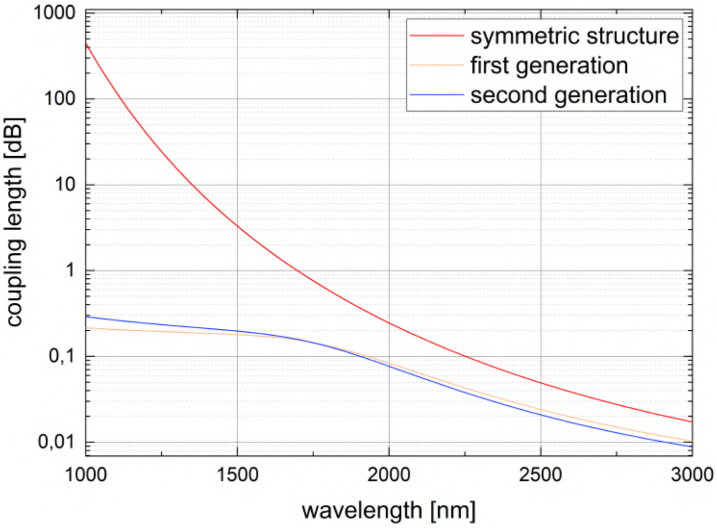

Fig. 2.33: *Coupling length characteristics (X-polarization) of the first and second generation DCF, compared with the one of the hypothetical symmetric all-solid DCF with homogeneous coupling (Fig.2.11).*

They are calculated using the Lumerical optical solver at the wavelength of 1560 nm, considering two orthogonal polarization directions. The X- and Y-polarization indicate the parallel and perpendicular direction of field oscillation, respectively, in relation to the connection line of the two cores. It can be seen that the polarization birefringence $\delta_\mathrm{p} = n_\mathrm{eff}^\mathrm{X} - n_\mathrm{eff}^\mathrm{Y}$ (where $n_\mathrm{eff}^\mathrm{X}$ and $n_\mathrm{eff}^\mathrm{Y}$ are the effective refractive indices in case of X- and Y-polarization, respectively, for the same core) is lower than the asymmetry effect $\delta_\mathrm{p} = n_\mathrm{eff}^\mathrm{s} - n_\mathrm{eff}^\mathrm{f}$ (considering for the same polarization); therefore, I will not consider it later.

	First generation DCF				Second generation DCF			
	X-Polarization		Y-Polarization		X-Polarization		Y-Polarization	
@ 1560 nm	Fast core	Slow core	Fast core	Slow core	Fast core	Slow core	Fast core	Slow core
n_{eff}	1.79911	1.79935	1.79902	1.79924	1.80735	1.80749	1.80734	1.80746
$\beta \cdot 10^{-3}$ [1/mm]	7.24624	7.24721	7.24588	7.24677	7.27943	7.27999	7.27939	7.27988

Table 2.8: *Basic optical properties of the two studied generation of DCFs at the wavelength of 1560 nm considering two orthogonal polarization directions. The second generation DCF exhibits a lower difference of effective refractive indices between the fast and slow cores, which is an evidence of improved optical symmetry with respect to the first generation one.*

In terms of DC asymmetry, the DCF from the second generation exhibits lower δ_a than the first one at both polarizations, with minimum value of $1.2 \cdot 10^{-4}$ for Y-polarization, which confirms the improvement of the DC symmetry in the case of the second generation fiber. Additionally, this sample shows a lower polarization birefringence too. However, a structural DC asymmetry is still present because the propagation constants between fast and slow cores still exhibit a slight difference. The identified level of asymmetry intends me to expect two different scenarios under separate excitation of the slow and fast fiber cores in the case of the both studied fibers.

2.6 Conclusions

In this chapter of the thesis, I investigated the capability of soft glass high index contrast DCF for all-optical steering of ultrafast pulses. I studied a novel switching concept based on soliton self-trapping in the case of three different alternatives of DCF structures. The optimization of the soft glass materials resulted in the pair of lead silicate PBG-08 / borosilicate UV-710 glasses for the cores and photonic cladding, respectively. They are thermally matched and have high contrast of the refractive index at the level of 0.4 in the near infrared [77]. The nonlinear numerical simulations of sech^2 sub-nJ pulses propagation at different excitation wavelengths (1400 - 1800 nm) and at different pulse widths (75 - 150 fs) predicted that the optimized high index contrast all-solid PCF did not support better switching performance than the air-glass PCF. Therefore, in a following step, I chose a simple DCF structure with homogeneous cladding to be considered in the framework of nonlinear propagation simulations and switching performance analysis [9]. The optimization of the excitation wavelength and pulse width resulted in even lower switching energies at simultaneous improvement of the switching contrasts at combination of 1500 nm and 75 fs, where the optimal level of soliton number in range of 2 - 3 was identified. The optimal condition for self-trapped solitonic switching was reached using of 1500 nm, 75 fs hyperbolic secant pulses at 43 mm fiber length, requiring only in-coupled pulse energies at the level of 20 pJ. It resulted in SCs of 17.2 dB and 46.3 dB in the case of integral and temporally localized field energies, respectively. The character of the switching performance in the spectral domain is broadband and uniform, with SCs exceeding 30 dB at three different wavelengths relevant to optical communication technology (inside E-, S- and C-band).

Despite the proper control of the drawing parameters during the fabrication process (furnace temperature, seeding and pulling speed in Table 2.6), the final DCFs from the first and second generations exhibit a 1 µm shorter and a 1 µm longer distance between the cores than the 3.2 µm optimal one estimated by the numerical simulations (Table 2.7). More importantly, the fibers from both generations still show a residual effect of the DC asymmetry. Even if the subpreforms for the final drawing was chosen is such a way that the estimated diagonal and area deviations between the cores are below only 0.5%, the DC asymmetry significantly influence the coupling and optical properties of the fibers. For both fiber generations, the CL at 1500 nm is more than one order of magnitude shorter than the optimal one. It means that, in order to satisfy the self-trapping condition in Eq.(1.93) and consequently shorten the soliton compression length z_{comp}, the power of the input pulse should increase. Moreover, another effect of the DC asymmetry is that, in both DCF generations, the two cores can be still distinguished between fast and slow one, with smaller and higher effective refractive indices n_{eff}, respectively (Table 2.8).

To estimate the energy of the input pulse required for the establishment of the self-trapping condition, I combine Eq.(1.93) with the equation of the soliton compression length z_{comp} as a function of the input pulse and fiber parameters in Eq.(1.94), and the expression of the in-coupled peak power P_0 in Eq.(2.3). I ended up with the following equation:

$$L_{\mathrm{c}} \approx 0.32\frac{1.763\pi \cdot T_0^{3/2}}{2\sqrt{0.88 \cdot \gamma E_{\mathrm{st}} k_{\mathrm{in}} |\beta_2|}} + 1.1\frac{\pi T_0}{\gamma k_{\mathrm{in}} E_{\mathrm{st}}}. \tag{2.10}$$

E_{st} is the energy required to achieve the soliton self-trapping condition, i.e. $L_{\mathrm{c}} \approx z_{\mathrm{comp}}$. L_{c}, γ, and β_2 are calculated for the first and second generation DCFs; T_0 is 100 and 75 fs, respectively, as the ones in the case of the optimal switching performances presented in Table 3.1. Substituting all the mentioned values in Eq.(2.10), the estimated values of E_{st} are 3.9 and 10 nJ for the first and second generation DCFs, respectively. These values are more than two orders of magnitude higher than the predicted switching energies. It means that, even if the DC symmetry has generally improved with respect to the one of the air-glass PCF [3] and the difference between the effective refractive indices of slow and fast core is rather small, with maximum of $2.4 \cdot 10^{-5}$ for the first generation DCF, X-polarization (Table 2.8), the DC asymmetry has a significant influence on the optical properties of the fabricated all-solid DCFs. It means that, during the experimental study of the fiber, not only I need to increase the energy of the input radiation in order to achieve the desired self-trapping condition, but also I expect two different scenarios under separate excitation of the slow and fast fiber cores in the case of the both studied fibers.

The experimental verification of ultrafast soliton switching using the fabricated DCFs with structural and optical parameters reported in Table 2.7 and Table 2.8 is the topic of the next chapter.

CHAPTER 3

Experimental results

In the third chapter of the thesis, I present the experimental results of ultrafast nonlinear propagation study in the optimized and fabricated DCFs. I used the fibers from the two generations of DCF which were presented in section 2.5.2: 1) the all-solid DCF with homogeneous cladding (first generation DCF, with cross-section as in Fig.2.29) and 2) the DCF containing 5 DC units (second generation DCF, with cross-section in Fig.2.32a), with improved DC asymmetry (Table 2.8). They are also presented in the peer-reviewed article *Optical Fiber Technology*, 63:102514, 2021 [10].

The goal of this chapter is to show the progress in the experimental demonstration of efficient nonlinear self-switching of femtosecond pulses in solitonic propagation regime using DCFs. The background of this progress is the improvement of the DC symmetry due to the all-solid approach, combining PBG-08 and UV-710 glasses with 0.4 of refractive indices difference, and the more accurate fabrication technology, which was described in details in the previous chapter.

My first original contribution presented in this chapter is the analysis of the linear characteristics of the fabricated DCFs. I present the results of the experiments which have the scope to determine the coupling length L_c and the attenuation coefficient α at 1560 nm (central wavelength of the C-band). The experiment enabled the simultaneous determination of the in-coupling efficiency (IE) of the DCFs.

In the second section, I present my original contribution to the experimental study of ultrafast solitonic switching in the C-band using the second generation DCF. It is published in the peer-reviewed article *Optics Letters*, 45:5221-5224, 2020 [11]. The experimental findings are supported by numerical simulations performed by my colleague Viet Hung Nguyen. It involved a simplified model than the one presented in section 2.4 and experimentally relevant parameters to solve the CGNLSE. The last part of the section is dedicated to one of my main original contribution to the study of DCFs:

the investigation of the fiber length effect on the switching performance. It is performed by sequentially cutting the second generation DCF with 2 - 5 mm steps. It is presented in the peer-reviewed article in *Applied Optics*, 60(32):10191-10198, 2021 [12]. The results presented in this section constitute a strong proof of the successful improvement of switching performance than previous attempts [3, 5] and are sufficient to verify the first claim of the dissertation.

The following section of this chapter is dedicated to the experiments I conducted at longer excitation wavelength, more specifically at 1700 nm (limit of the optical communication U-band). It is the topic of the peer-reviewed article *Optics Communications*, 472:126043, 2020 [13]. I present the results of solitonic all-optical switching using the first generation DCF, which did not allow to record any switching performance in the C-band. Then, I complete the discussion by showing one of my main original contributions: the fiber length effect of the switching performance at 1700 nm using the first generation of DCFs. The interpretation of the results at the end of the discussion allow me to say that the shown propagation scenario at 1700 nm has solitonic character, giving a strong proof of the second claim of the dissertation.

At the end of the chapter, I present the optimal results of the switching performance at the excitation wavelengths of 1700 nm and 1560 nm, using the DCFs from the first and second generations, respectively. They are included in the peer-reviewed article *Applied Optics*, 60(32):10191-10198, 2021 [12]. My main original contribution in this section is the influence of the asymmetry on the switching performance, which allows comparison between the experimental outcomes and on the effect of the excitation wavelength. The fiber length effect and the optimal experimental results at both wavelengths constitute a strong proof of the first claim of the dissertation.

3.1 Linear experiments at 1560 nm

The first step of the experimental analysis is the determination of the DCF characteristics in the linear regime of operation, i.e. applying low input light intensities. The two experiments that I am going to present in the following pages have the objective to **determine** the **CL** and the **attenuation coefficient** of the fabricated DCF. In both of them, I used the multiple DC pair presented in section 2.5.2, with the same structure as in Fig.2.32 and 3.3 μm distance between the cores.

The first experiment was performed by coupling the radiation into one core of the DCF in the linear regime originating from a laser diode at the wavelength of 1550 nm. The fiber was sequentially cut from 61 mm to 49 mm with a 2 mm step and we investigated how the in-coupled energy oscillates between the two cores. The second one involved the same laser diode source at 1550 nm; it was performed by coupling the light into one single core and measuring the power irradiated from the output of the fiber. In that case, the fiber was cut from 1 m up to 10 cm length, with a step 10 cm. The starting length is significantly longer than the ones predicted during the simulation phase and used during the nonlinear experiments; therefore, the results of this experiment constitute a good approximation of the attenuation coefficient.

3.1.1 CL determination experiment

I have already introduced the concept of CL in section 1.3.2. It represents the shortest fiber length at which the pulse is transferred from the excited to the non-excited core in the linear regime of operation. In this condition, the input radiation experiences periodic oscillations between the two cores, characterized by $L_\mathrm{c} = \pi/(\beta_S - \beta_A)$, where β_S and β_A are the propagation constants of symmetric and anti-symmetric supermodes of the fiber, respectively. In other words, the pulse oscillates between cores sinusoidally, with a period equal to L_c. I have already presented the simulated CL characteristics for the optimized all-solid DCF with hypothetical symmetrical structure in Fig.2.13. In this case, L_c is predicted to be approximately 22 mm at 1560 nm for horizontally X-polarized radiation (Fig.2.13). In this section, I present the experiment, which aims to identify the CL at 1550 nm and verify the simulation predictions.

Fig.3.1 shows a photo of the experimental setup used for the experiment. The source is a fiber-coupled laser diode with 1550 nm central wavelength and 1.5 mW peak power (not present in the image). Then, the light was directed through a Glan polarizer. This strategy was used to set the horizontal polarization of the input radiation and minimize scattering of the transmitted extraordinary polarization component of the incident light field. The in-coupling and out-coupling of the radiation was managed by two 40x microscope objectives mounted on two identical 3D positioning stages with a submicrometer precision for separate excitation of a single fiber core and for imaging the output facet of the DCF onto an infrared camera chip (AST CamIR^{1550}), respectively. As the orientation of the cores is determined by the positioning of the DCF on the holder, I first identified the angle of the two core axis from the camera image; then, I set the polarizer at the same angle to allow the input field to oscillate towards this axis. The measurement started with a DCF from the second generation (right-end column of Table 2.7) with core distance of 3.3 µm and length of 61 mm. First, I coupled the input radiation inside one single core of the central DC waveguide of the fiber. The recorded camera image at this length is on the left-end side of Fig.3.2. Afterwards, I sequentially performed a cut of the fiber every 2 - 3 mm and recorded the camera images at every step. Fig.3.2 reports the complete series of camera images from 61 mm to 49 mm. I observe that the light, which is initially confined in the top core at 61 mm, is slightly transferred to the bottom core, reaching an extreme at 54 mm of length, where the max-

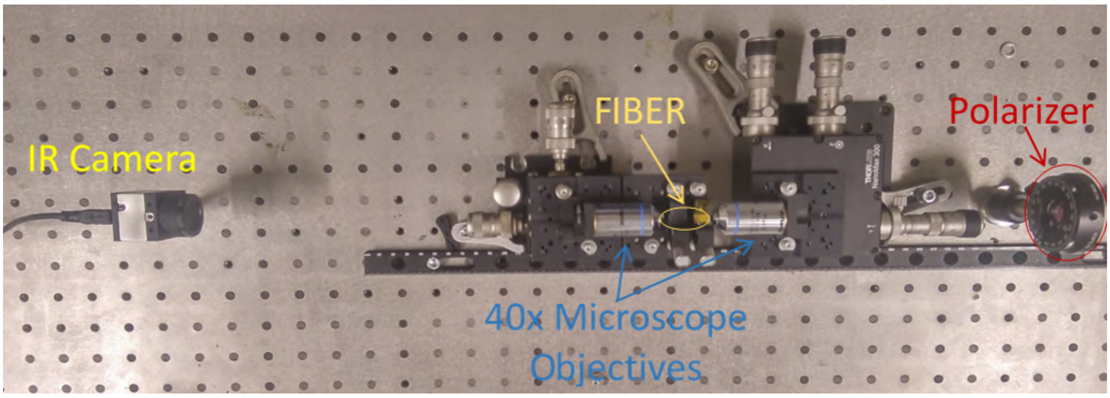

Fig. 3.1: *Photo of the experimental setup used for the determination of the coupling length L_c in the linear propagation regime.*

imal bottom core illumination is reached. In the next two steps, the original top core dominance is restored. Therefore, the results in Fig.3.2 indicate an oscillation period of the coupled radiation (i.e. CL) of 7 mm.

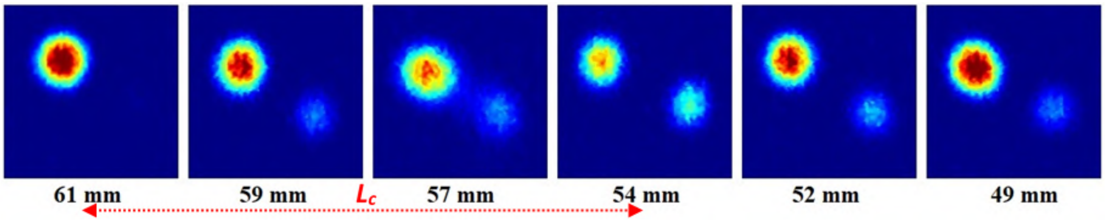

Fig. 3.2: *Infrared camera images of the output of the DCF with increasing length under single-core excitation at 1550 nm. A CL of 7 mm (between 61 and 54 mm) is identified.*

3.1.2 Attenuation measurement

The second experiment in the linear regime of operation aimed to retrieve the attenuation coefficient α of the DCF. As for the previous experiment, the fiber was the second generation DCF with 3.3 µm core distance. The experimental setup is rather similar to the one in Fig.3.1, but with some extra precautions. The laser source at 1550 nm was set at its maximum output power of 4 mW; the Glan polarizer and the in-coupling and out-coupling micro-objectives were kept in the same position as the previous setup. Moreover, I put an iris aperture between the output micro-objective and the infrared camera chip to restrict the output radiation from one core only and cut out the one from the second core. At the same distance of the camera chip, I measure the output radiation from one single core only with a power sensor connected to a power meter. The sensor was a germanium photodiode with optical power range of 50 nW - 40 mW in the spectral window 700 - 1800 nm. The experimental setup is depicted in Fig.3.3.

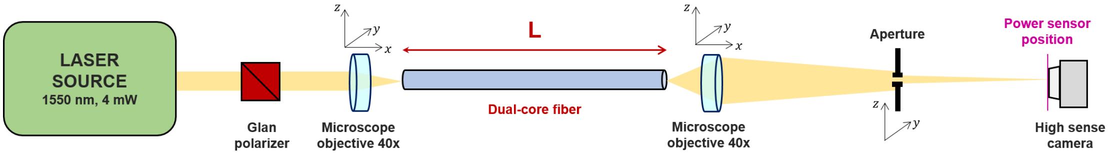

Fig. 3.3: *Schematic of the experimental setup used for the measurement of the attenuation coefficient α and the IE.*

The measurement started from 1 m length; then, the fiber was cut with a 10 cm step up to the final length of 10 cm. At each length, I coupled the light into one core, I oriented the iris aperture (monitoring with the camera) in order to cut the radiation from the second core and finally measure the output power from the selected core. I repeated this operation twice for both core excitation. Fig.3.4 presents the fiber length dependence of the measured output power (in dB scale) from (a) top and (b) bottom core, separately. The orange line results from fitting using the linear regression method. The characteristics of this line determine the most important measured quantities: the attenuation coefficient and the power of the input radiation which is coupled inside the fiber. The first one is the slope of the fitted curve, which indicate the rate at which the light loosing its intensity while propagating through the fiber (in dB/m). The second one is the value of the intercept of the curve with the vertical axis. From this value, I can retrieve the measure of the input radiation which is in-coupled into the guided fiber mode, i.e. the **in-coupling efficiency**.

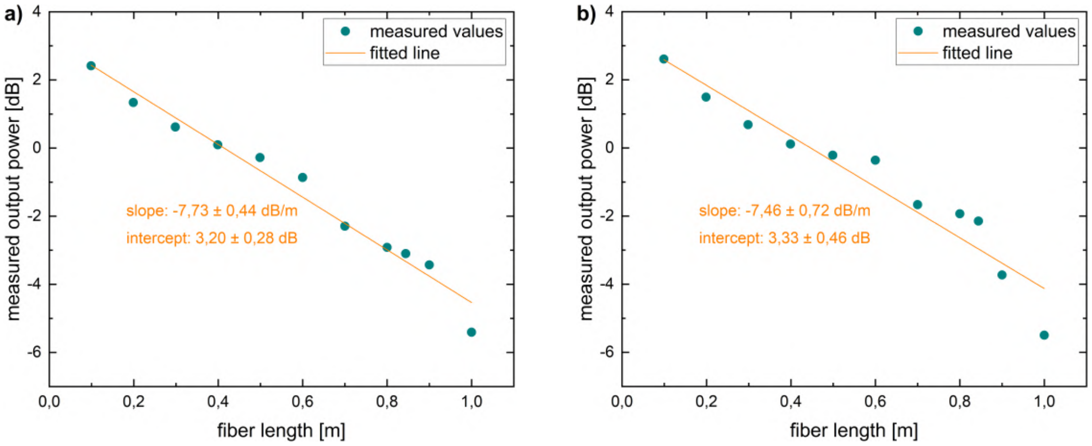

Fig. 3.4: *Fiber length dependence of the measured power at the output of a DCF (in dB scale) in the case of (a) top and (b) bottom core excitation. The input radiation had 1550 nm central wavelength and 4 mW peak power. The retrieved fitting curve of the measured data (blue dots) and its characteristics are depicted in orange color.*

In the case of top core excitation (Fig.3.4a), the attenuation coefficient α (i.e. slope of the line) resulted in value of approximately -7.7 dB/m, while the intercept is 3.2 dB, corresponding - in linear scale - to an in-coupled power of around 2.1 mW. Considering the power of the laser source of 4 mW, this corresponds to an IE of 52%. For the bottom core excitation, the slope is -7.5 dB/m and the in-coupled power is 2.15 mW (3.3 dB), which indicates an IE of approximately 54%. Taking into account the fluctuation of the values (written as insets in both graphs in Fig.3.4), I estimated the average values of the attenuation coefficient and in-coupling coefficient to be 8 dB/m and 50%, respectively. The value of the attenuation coefficient is significantly lower than 30 dB/m reported in the case of the previously used air-glass DC PCF [3]. Moreover, the IE of the all-solid DCF is higher than the air-glass PCF, which was at the level of 32% [3].

3.2 Experimental observation of ultrafast solitonic switching in DCF at 1560 nm

In the nowadays information technology domain, the optical data transfer and processing is mainly on in the C-band (1530 - 1565 nm) [269–271]. Its central wavelength of 1550 nm is the most diffused one in the data transport systems based on optical fibers, because of absorption loss minima at this wavelength [272,273]. The ultrafast solitonic switching performance in DCFs operating in the C-band has been predicted since the 1980s [43,44], but up to now has not been reached any promising and applicable experimental demonstration. In fact, in the face of many published theoretical articles on this topic, only a limited number of experimental works can be found in the scientific literature [4,5]. In the most successful scenario reached by Betlej et al. [1] using a silica made DC DCF, the switched pulse is only partially transferred between the core and still suffers from significant spectral deformations, preventing to achieve an applicable performance in the studied conditions. Moreover, the power requirements were relatively high ($\approx$100 kW). The last attempt was performed by Čurilla et al. using a DC PCF [3]. Nevertheless, the high level of the DC asymmetry allowed to achieve the switching performance only in a very narrow spectral area (with 3 nm spectral window). Therefore, motivated by the theoretical outcomes presented in the previous chapter and relying on the matured fabrication technology of soft glass fibers at my institution (Ł-IMIF), the fiber with the glass pair PBG-08 (cores)/UV-710 (cladding) and optimized structural parameters was finally fabricated. From the study of the switching performance in terms of excitation wavelength of the input femtosecond pulses between 1500 and 1800 nm [9], I showed that the optimal excitation wavelength for solitonic all-optical switching purposes is close to the C-band central one (1500 nm) [6, 9]. Moreover, the new DCF design developed by me was predicted to support broadband anomalous dispersion, which is necessary for ultrafast solitonic propagation, and better preservation of the DC symmetry during the drawing process.

This section of the chapter is dedicated to the study of ultrafast solitonic switching in the C-band using the two generations of high index contrast DCFs presented in the previous chapter: the all-solid DCF with simple cladding (first generation) and the one with multiple DC units with improved DC asymmetry (second generation), respectively. Afterwards, I report the results outcomes of the dedicated numerical simulations of the pulse dynamics in nonlinear DCFs. The numerical model is based on the CGNLSE and is rather similar to the one presented in section 2.4. The correspondence between the numerical and experimental data in the case of the second generation of DCF unveils both the soliton-based and the reversible characters of the switching performance using ultrashort pulses in the C-band.

3.2.1 Experimental methods and all-optical switching results

To demonstrate the switching performance in the optical communication C-band, I used the experimental setup depicted in Fig.3.5. A Menlo C-fiber amplified oscillator generating 3.6 nJ pulses at 1560 nm wavelength with pulse width of 75 fs at the repetition rate of 100 MHz was used as a source of the excitation pulses [274]. In order to explore the switching potential of the DCF, the pulses were directed through two half-wave plates with a Glan-Taylor polarizer placed in between. The first half-wave plate and the polarizer allow the fine attenuation of the pulse energy, while the second half-wave plate set the polarization of the pulses before launching them into the fiber. I managed the in-coupling and out-coupling of the radiation by 40x microscope objectives mounted on two identical 3D positioning stages having a sub-micrometer precision. The first objective enabled separate excitation of a single selected fiber core; the second one imaged the output facet of the DCF onto a phosphor-coated CCD infrared camera with sensitivity peaks in the C-band (AST CamIR^{1550}), or alternatively to the end facet of multimode collecting fiber attached to an optical spectrum analyzer (Yokogawa).

I collected several series of camera images in order to show the dependence of the switching performance on the input pulse energy. For each generation of studied fibers, I investigate the switching performance in more samples under the thorough excitation of both fiber cores. However, I present here only two series, which represent the best outcomes separately from the first (at 30 mm) and second (at 38 mm) generation DCFs.

Fig.3.6a presents the SEM image of the cross-section of the second generation DCF

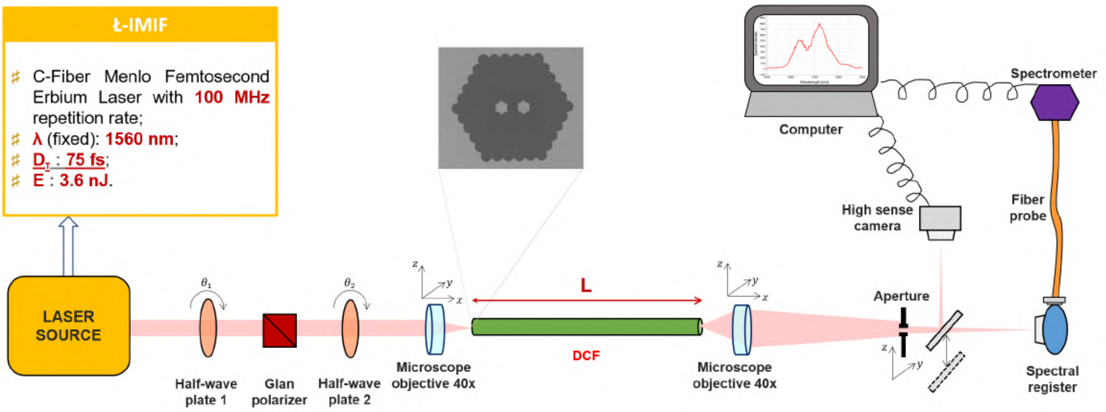

Fig. 3.5: *Experimental setup for the investigation of nonlinear switching in DCFs using the femtosecond Menlo C-fiber laser source operating at 1560 nm.*

containing 5 DC waveguides. The distance is 3.3 µm, which is slightly larger than the optimal one (3.2 μm), predicted by the numerical simulations in section 2.3. In the right-end column of 2.8, where its optical parameters are reported, I observed that the fiber expresses a DC optical asymmetry $\delta \approx 0.5 \cdot 10^{-6}$ m^{-1} at 1560 nm [10]. The larger separation between the cores leads to a longer CL. The fast (bottom) core of the central DC unit was excited by 1560 nm, 75 fs pulses. Fig.3.6b presents a series of camera images at 45 mm fiber length under increasing the input pulse energy in the range of 0.05 - 0.25 nJ, considering an IE of 50% [12]. No evident switching was observed at any of the considered pulse energies: the majority of the pulse energy remained confined in the excited core, with only nearly equalized transfer to the non-excited one in the case of 0.25 nJ.

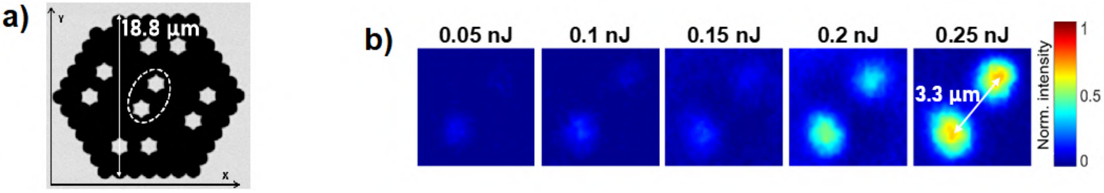

Fig. 3.6: *(a) SEM image of the cross-section of the DCF with lower level of asymmetry. The studied DC unit is marked by a dashed ellipse. (b) Infrared camera images of the output of the 51 mm DCF at different energies of 1560 nm, 75 fs input pulses. The core distance to be 3.3 µm is indicated by a white arrow.*

To evaluate the switching performance in the form of *ER* (see section 2.4.1), I processed the obtained camera images numerically. I divided the pictures into two areas along the symmetry axis between the two cores; then, I integrated the recorded intensities separately across the both areas. I used the obtained relative energy values for each separate core, $E_{\text{bottom}}(E_{\text{in}})$ and $E_{\text{top}}(E_{\text{in}})$ (where E_{in} is the input pulse energy), to calculate the DC *ER* in dB scale. It is expressed in a similar way as Eq.(2.5):

$$ER(E_{\text{in}}) = 10 \log \left[\frac{E_{\text{bottom}}(E_{\text{in}})}{E_{\text{top}}(E_{\text{in}})} \right] \tag{3.1}$$

The values of $ER(E_{\text{in}})$ are positive in the case of bottom core and negative in the case of top core dominance, respectively. The values of the SC are finally calculated by subtracting the two extreme positive and negative values of the $ER(E_{\text{in}})$ series.

Unfortunately, in the case presented in Fig.3.6b I obtained only positive values of $ER(E_{\text{in}})$ because no dominance exchange between the cores has been observed. For the same reason, it is not possible to evaluate a SC, but instead an additional parameter: the minimal *ER* (MER). It is reached in the case of maximum energy transfer from the fast (bottom) to the slow (top) core. At all of the energy levels reported in Fig.3.6b, the values of *ER* are positive, which indicates a bottom (fast) core dominance; the MER of 0.6 dB was calculated at input energy of 0.25 nJ, which approximately indicates an equal distribution of the energy between the cores at the output of the DCF. Therefore, this outcome cannot be properly identified as a switching performance; however, it is just a promising outcome which motivated me to proceed with the examination of the fiber sample with the cut-back method. Moreover, this pulse energies reported in Fig.3.6 are still higher by a factor of 5 than predicted by the corresponding numerical simulations performed on similar but totally symmetrical structure and presented in section 2.4.3.

3.3 Reversible ultrafast soliton switching at 1560 nm

In this section, I report more advanced experimental results achieved in the C-band (at 1560 nm) and using the second generation sample of strongly nonlinear high-index-contrast DCFs. The experimental findings are supported by numerical simulations. They were performed using a simplified model with respect to the one presented in section 2.4 and including the experimentally relevant parameters.

3.3.1 Experimental results

The first observation of effective switching performance with exchange of the dominant core was recorded for the first time at 43 mm fiber length. I used the setup depicted in Fig3.5 and I recorded a series of images and spectra at each level of the input pulse energies. Fig.3.7 presents a sequence of camera images recorded with increasing energy of the input pulse in the range 150-700 pJ in case of left core excitation. I observed for the first time a switching performance with forth and back character: 1) energy transfer from excited to non-excited core between 500 and 600 pJ energy levels; 2) transfer back to the excited core at 700 pJ. More interesting is the switching performance under excitation of the right core (Fig.3.8), as the forth-and-back performance was recorded at lower input energies than the left core excitation one: 1) first transfer at levels 100 - 150 pJ and 2) back transfer at 150 - 200 pJ, respectively. The results in Fig.3.7 and Fig.3.8 constitute the first observation of reversible ultrafast switching of femtosecond pulses in the C-band using a DCF. This means that the switching performance takes place independently on the initial core excitation.

The spectrally-resolved *ER*, labeled as $ER(\lambda, E_{\text{in}})$, was calculated using two spectra $S_{\text{bottom}}(\lambda, E_{\text{in}})$ and $S_{\text{top}}(\lambda, E_{\text{in}})$, recorded separately for both cores under identical experimental conditions as mentioned on Fig.3.8 according to the following expression:

$$ER(\lambda, E_{\text{in}}) = 10 \log \left[\frac{S_{\text{bottom}}(\lambda, E_{\text{in}})}{S_{\text{top}}(\lambda, E_{\text{in}})} \right]. \tag{3.2}$$

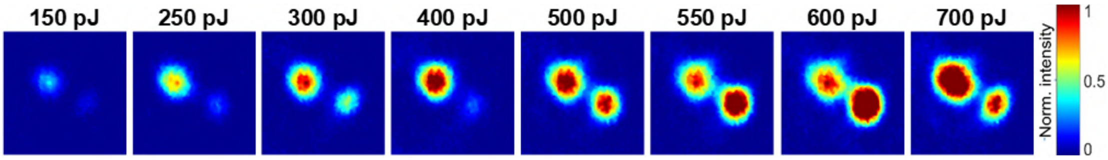

Fig. 3.7: *Infrared camera images of the output of the 43 mm multiple pair DCF (Fig.3.6a) under increasing energies of 1560 nm, 75 fs input pulses in the range 150 - 700 pJ, in the case of top core excitation.*

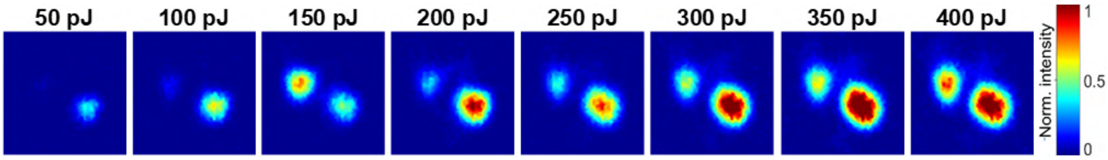

Fig. 3.8: *Infrared camera images of the output of the 43 mm multiple pair DCF (Fig.3.6a) under increasing energies of 1560 nm, 75 fs input pulses in the range 50 - 400 pJ, in the case of bottom core excitation.*

Fig.3.9 reports the dependence of $ER(\lambda, E_{\text{in}})$, measured in dB, on the input pulse energy, E_{in}, in the case of bottom core excitation (same as Fig.3.8). It reveals the spectral details of the complex switching behavior, which is in correspondence with the camera images: at first, $ER(\lambda)$ decreases with the increase of the input energy in the range of 50 - 150 pJ (first energy transfer) and increases in the range of 150 - 250 pJ (back energy transfer). The spectral results indicate that the recorded switching scenario has a solitonic character. In fact, only moderate spectral broadening takes place and the switching is spectrally homogeneous in the considered spectral range (1450 - 1650 nm): the forth-and-back switching scenario taking place was recorded almost in the whole spectral range, in particular in the window 1475 - 1575 nm. Thus, the demonstrated switching performance supports the redirection of the energy between the two cores in a reversible way.

3.3.2 Theoretical insight

The new simulation work was performed by dr Viet Hung Nguyen from Advanced Institute for Science and Technology of Hanoi University of Science and Technology in Vietnam. The model used by him is based on the system of two linearly-coupled NLSEs (LCNLSE). This system was widely used, also in the context of the spontaneous symmetry breaking of solitons in couplers [184, 275, 276]. It is a simplified version of the one presented in section 2.3 because it does not include secondary-order effects, such as SRS, SST and TOD. However, the results do not differ in terms of predicted switching performance, except for a factor of scaling between the experimental and theoretical energy values, as I have $E_{\text{exp}} \approx 1.25 \cdot E_{\text{theor}}$. Lastly, losses, which were identified to be only 8 dB/m (section 3.1.2), were not included in the theoretical model presented above, because their effect in the pulse propagation is negligible.

Considering the amplitudes of electromagnetic waves in the two cores $\Psi_{1,2}(t, z)$, LCNLSE can be written in this form:

$$i\partial_z \Psi_1 = -(1/2)\beta_2 \partial_t^2 \Psi_1 - \gamma |\Psi_1|^2 \Psi_1 - \kappa \Psi_2, \tag{3.3}$$

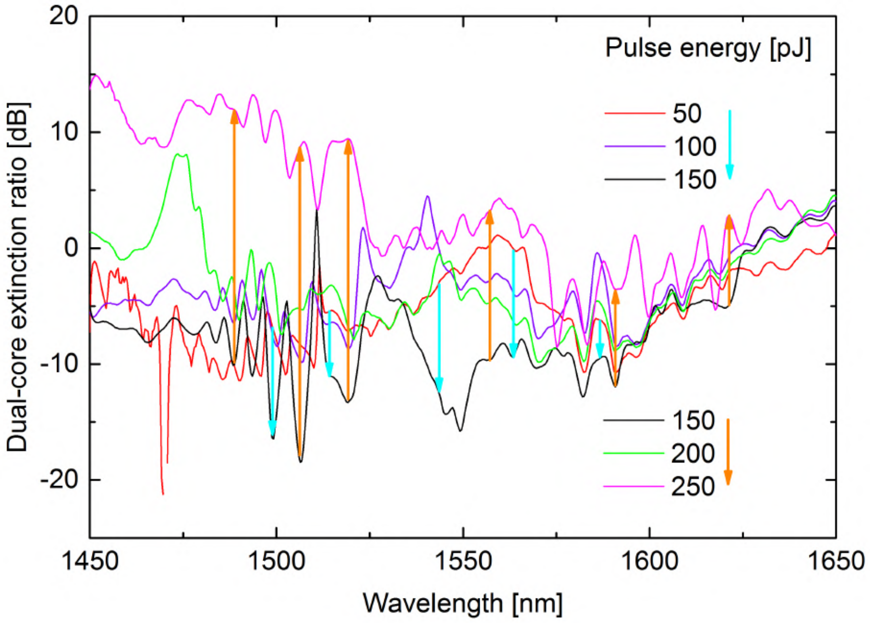

Fig. 3.9: *Spectrally-resolved $ER(\lambda, E_{in})$ originating from the output intensities in the two cores, measured for different values of the input energy. Light blue and orange arrows represent the forth-and-back step of the switching performance, respectively, and they are always directed towards the increasing E_{in}.*

$$i\partial_z\Psi_2 = -(1/2)\beta_2\partial_t^2\Psi_2 - \gamma|\Psi_2|^2\Psi_2 - \kappa\Psi_1, \tag{3.4}$$

with z and t the propagation distance and time, β_2, γ and κ the group-velocity dispersion, Kerr nonlinearity, and inter-core coupling, respectively. Eq.(3.3) and Eq.(3.4) can be rescaled by setting $t = \sqrt{\beta_2/\kappa\tau} \equiv t_0\tau$, $z = \zeta/\kappa$, $\Psi_{1,2} = \sqrt{\kappa/\gamma}A_{1,2}$. In case of left core excitation, the input pulses were launched at $z = 0$ into one fiber core and set with the soliton-like form: $A_l(0,\tau) = a\,\mathrm{sech}(\eta\tau)$, where a is the independent amplitude and $\eta = 1.76t_0/t_{\mathrm{FWHM}}$ the inverse width [125]. $A_r(0,\tau) = 0$ are for left (l) and right (r) core, respectively.

The numerical simulations were performed in the same parameter range of the experiments, considering a 43 mm fiber. To support my colleague, I contribute to retrieve the necessary parameters for the numerical simulations. To do that, I acquired the fiber cross-section by processing the SEM images of the DCF (as the ones in Fig.2.32) used during the experiments. I calculated all the relevant parameters - i.e. the effective refractive index (Eq.(1.6)), the propagation constants β_0, β_1 and β_2 (Eq.(1.7)), the coupling coefficient (Eq.(1.63)) the losses - in the spectral window between 300 and 4100 nm with the commercial Mode Solution software, sufficiently covering the transmission windows of both glasses [77]. An additional input characteristic was the experimentally determined nonlinear Kerr coefficient $4.3 \cdot 10^{-19}$ m^2/W), which is necessary to the nonlinear parameter γ (Eq.(1.15)). First, I performed both the mode identification and the dispersion characteristics calculation for an artificial single core structure. They were obtained by replacing one of the cores with the low refractive index UV-710 glass used for the cladding. Then, I considered the total DC structure and I calculated the coupling coefficient between the two cores based on the overlap integrals [194].

The excitation wavelength was 1560 nm, the propagation constants $\beta_1 = 6.56\cdot10^{-9}$ s/m, $\beta_2 =$ -$7.73\cdot10^{-26}$ s^2/m, the nonlinear parameter $\gamma = 0.4$ W^{-1}m^{-1}, and the coupling coefficient $\kappa = 75$ m^{-1}, as reported in [263]. Then, the propagation unit is $z_0 = 1/\kappa \approx$ 13 mm, the time unit is $t_0 \approx 32$ fs, with $t_{\mathrm{FWHM}} \approx 75$ fs and $\eta = 0.78$. In the scaled units, the CL $L_c = \pi$ (from Eq.(1.76) approximately fits the length of the sample, which is $\approx$ 3. Therefore, the fiber is suitable for the implementation of the switching. The scaled amplitude a was related to the pulse energy (in physical units) in this way:

$$E = (\kappa/\gamma)\,\tau_0 \int_{-\infty}^{+\infty} |A_1(0,\tau)|^2 t_0 d\tau \approx 1.14a^2\kappa t_{\mathrm{FWHM}}/\gamma, \tag{3.5}$$

where a is the scaled amplitude. The energy considered in the experiment is $E \approx 30a^2$ pJ.

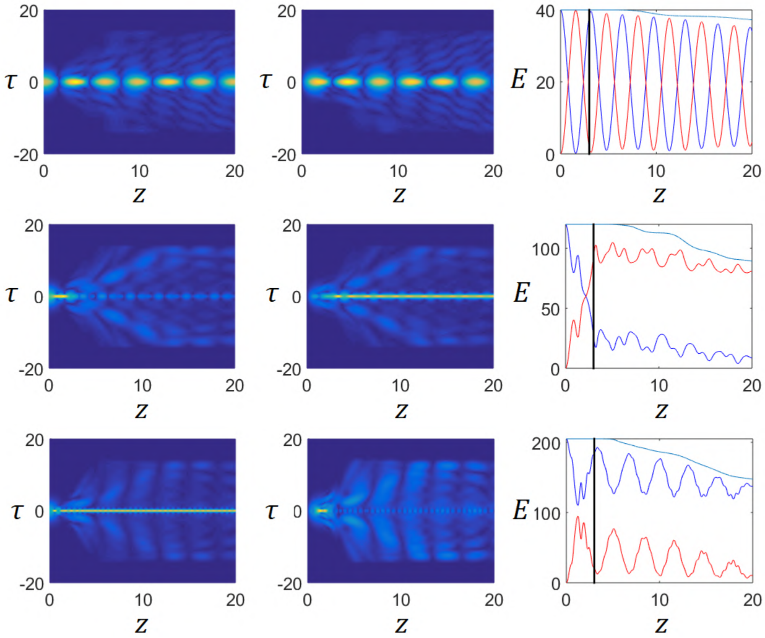

Fig. 3.10: *Dynamics of the switching between cores, obtained by plotting the solutions of Eq.(3.3) and Eq.(3.4), for three values of the rescaled input amplitude* $a = 1.15, 2.0, 2.6$ *(from top to bottom), and a fixed inverse width,* $\eta = 0.78$. *The spatial-temporal patterns of the powers in the excited and non-excited core,* $|A_{1,2}(z,\tau)|^2$, *are reported in the first and second column, respectively. The blue and red curves in the third column show the energy in each core (together with the total energy in the cyan curve) along the propagation distance. The first, second and third row panels are related to the three identified dynamical regimes: 1) periodic oscillations between cores; 2) self-trapping in the non-excited core; 3) self trapping in the excited core. The vertical line at* $z = 3$ *corresponds to the length of the fiber used in the experiment.*

Fig.3.10 shows the propagation dynamics in the excited (first column) and non-excited core (second column), respectively, in the case of non-zero coupling coefficient κ. For the smallest amplitude of $a = 1.15$, i.e. low level of nonlinearity, I still observe quasi-harmonic oscillations of the energy between the cores. If the rescaled amplitude is increased to $a = 2.0$, a quasi-soliton is generated and the nonlinearity acts to switch it from the excited (left) to the non-excited (right) core, where finally gets trapped. At even larger input amplitude $a = 2.6$, the nonlinearity is so strong that the soliton is immediately trapped in the excited core. In all of the three cases, an emission of small-amplitude radiation waves from the pulse takes place in each core, mostly at the initial phase of propagation. As explained in section 1.2.3, radiation waves oscillate periodically between the cores and their amplitude increases with a; they can be identified as light blue periodic patterns in Fig.3.10 [122]. The third column of Fig.3.10 reports the graphs of the energy dynamics along z in the excited core (blue curve) and non-excited core (red curve). The total energy is plotted with a cyan curve. The graph in the first row shows the periodic inter-core oscillation regime in case of low level of nonlinearity, while the ones in the second and third row (higher nonlinearity) represent the cases of self-trapping in the excited and non-excited core, respectively.

The vertical line at $z = 3$ indicates the length of the fiber corresponding to the experiment. The theoretical results at $z = 3$ are an indication of the complex switching performance observed in the camera images in Fig.3.7 and Fig.3.8 and in the spectral graph in Fig.3.9. At low values of a, the initial pulse keeps oscillating between the cores (linear regime of operation). Then, the self-trapping occurs only if the quasi-soliton acquires a sufficiently high peak intensity. The forth-and-back switching persist after several periods due to the interplay between the breathing of the deformed soliton and the inter-core oscillations. The slow decay of the total energy (cyan line) is caused by the radiation loss. It was emulated during the simulations by installing absorbers at edges of the time-integration domain.

To summarize the comparison between the numerical and experimental results presented above, I note that the three values of the pulse's amplitude in Eq.(3.3) and Eq.(3.4), $a = 1.15$, 2, and 2.6, which give rise to the three different outcomes of the transmission through the DCF, presented in Fig. 3.10 and Fig.3.8 (quasi-linear oscillations, self-trapping in the non-excited core, and retention in the excited one), correspond, in physical units, to incident-pulse energies 40, 120 and 205 pJ, respectively. The numerical results obtained for this set of values of the energy correspond to the experimental results observed for energies 50, 150 and 250 pJ. They differ from their theoretical counterparts by only a constant factor, ≈ 1.25. The reason of this discrepancy is that the second-order nonlinear effects, such as TOD, SRS and SST, which start to be significant for sub-100 fs pulses, were not taken into consideration in the simplified model described above.

In conclusion, the results may be summarized as a well-defined reversible soliton switching effect, controlled by the monotonous increase of the pulse's energy. Such a sub-nanojoule high-contrast switching protocol may find applications to the design of all-optical signal-processing setups.

3.3.3 Fiber length effect at 1560 nm

I studied the fiber length effect in the range 51 - 33 mm by back-cutting the fiber with 2-5 mm steps [12]. Fig.3.11 shows the dependences of the MER values on the fiber length L. At shorter fiber lengths than 45 mm, negative values of $ER(E_{\text{in}})$ were observed, which means that a dominance exchange between fast and slow core took place. Consequently, I could calculate the corresponding values of MSC, which gives information about the switching performance. The excitation conditions and the pulse energy ranges were kept the same as in the case of full lengths of the fibers (51 mm). Beside MER and MSC, the number of switching steps (SSs) was evaluated in order to complete the description of the switching performance. SS is obtained by analyzing the images of the output fiber facet and indicates how many times the dominance between the two cores is exchanged in the same interval of pulse energies E_{in}. Analyzing the table in (Fig.3.11), the switching performance was not observed (SS = 0) for the fiber lengths between 51 and 48 mm. The extreme MER of -5.1 dB was obtained in the case of 35 mm fiber length. The highest MSC of 20.1 dB was identified at the same fiber length at pulse energies 0.38 and 1.18 nJ (IE = 50%); however, it exhibited only one SS.

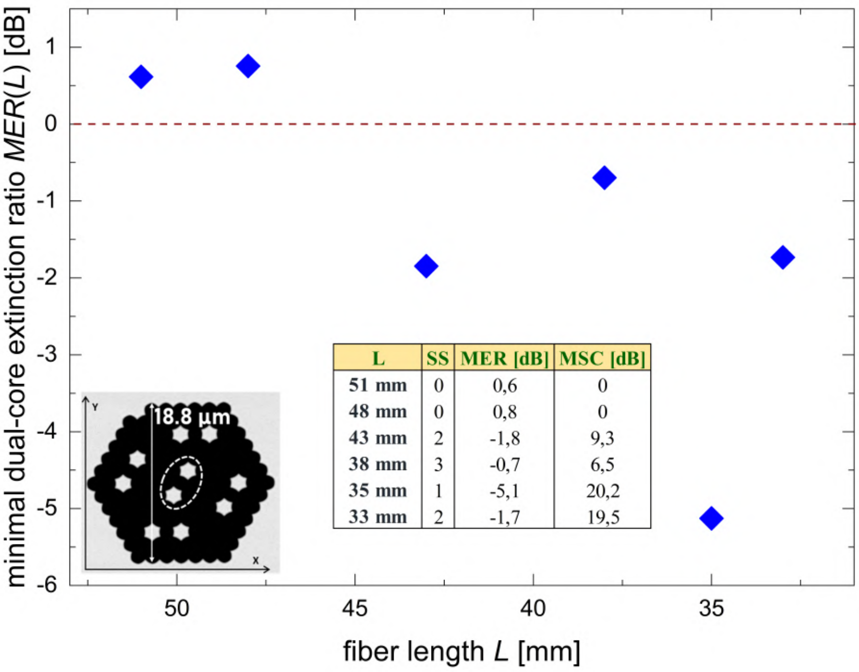

L	SS	MER [dB]	MSC [dB]
51 mm	0	0,6	0
48 mm	0	0,8	0
43 mm	2	-1,8	9,3
38 mm	3	-0,7	6,5
35 mm	1	-5,1	20,2
33 mm	2	-1,7	19,5

Fig. 3.11: *Dependence of the MER evaluated for each analyzed length of the DCF sample presented in Fig.3.6a.*

All the values of SS, MER and MSC are reported in the tables as insets in Fig.3.11. The maximum number of SSs was determined to be 3 at 38 mm fiber length. However, at this fiber length MER and MSC values are far from the optimal ones. The maximum value of MER and MSC were recorded at the shorter 35 mm long fiber. The general trend presented in Fig.3.11 reveals that the switching performance improves by shortening the fiber down to the length of 35 mm. Further shortening of the fiber (< 35 mm) results in significantly worse MER value. Therefore, it was possible to register MER value below -3 dB only at the optimal length.

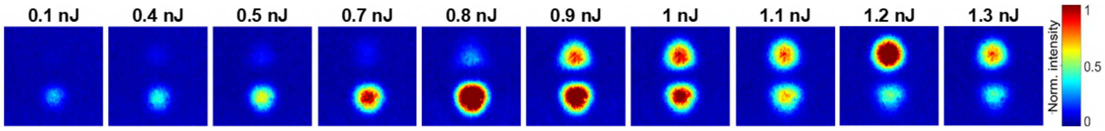

Fig. 3.12: *Infrared camera images of the output of the 35 mm DCF with lower DC asymmetry (Fig.3.6a) under increasing energies of 1560 nm, 75 fs input pulses.*

Fig.3.12 shows the best series of camera images recorded at optimal length 35 mm. The single SS experienced under 1560 nm, 75 fs is advantageous for optical communications applications because it ensures better separation between the excited and non-excited core states of the light at the output of the DCF, and it is less sensitive on the fluctuation of the input energy. It is in fact a promising demonstration of the optimal nonlinearly-induced bistability I introduced in section 1.4, which allows the fiber-type coupler to operate as an efficient switching device. The transition between one core to the second is only determined by the energy level of the input pulse [277]. In order to acquire deeper insight into the observed advantageous switching performance, I processed the separately recorded spectra at the outputs of each core, $S_{\text{bottom}}(\lambda)$ and $S_{\text{top}}(\lambda)$. They were acquired at the same experimental conditions as the camera images and at each input energy level E_{in}. Then, I calculated the spectrally-resolved DC *ER* using Eq.(3.2).

Fig.3.13 reports two $ER(\lambda, E_{\text{in}})$ curves at the energy levels ensured the MSC identified by the camera recordings at 0.1 nJ and 1.3 nJ, respectively. $ER(\lambda, E_{\text{in}})$ at a specific wavelength λ is positive in the case of fast core and negative in case of slow core dominance. The switching performance expresses broadband character, with a bandwidth extending from 1440 to 1630 nm, which entirely covers the optical communication C-band (1530 - 1565 nm). The curves at 0.1 nJ (violet) and 1.3 nJ (fuchsia) are entirely in the positive and negative half of the graph, respectively, in that spectral range, with small exception around 1540 nm in the case of the lower energy. This means that an efficient exchange of the pulse energy between the excited and non-excited core takes place with high SCs for all spectral components. I selected three wavelengths along the switching band with extreme values of the SC.

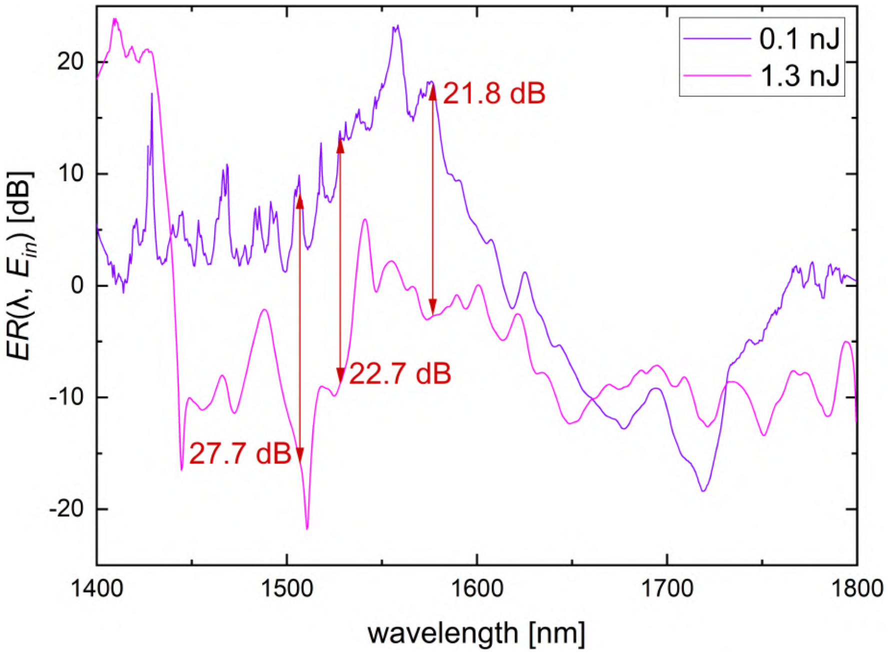

Fig. 3.13: *Spectrally-resolved $ER(\lambda, E_{in})$ between the output intensities of the two fiber cores, measured at energy levels 0.1 and 1.3 nJ in the same experimental conditions as in the case of camera recordings presented in Fig.3.12. The three arrows indicate the selected wavelengths with extreme SC: 1508 nm (27.7 dB), 1527 nm (22.7 dB), 1577 nm (21.8 dB).*

The SC at these wavelengths is marked with red arrows in Fig.3.13 and they are 27.7

dB (1508 nm), 22.7 dB (1527 nm) and 21.8 dB (1577 nm). These spectral results represent a convincing confirmation of the camera outcomes, not only due to the broadband and homogeneous character, but due to the same level of SC. An important novelty of this work is that I obtained for the first time a spectrally-resolved SC above 20 dB level in the C-band. The switching performance has also improved with respect to the one using longer fiber length (43 mm) and presented in section 3.3.1. In that case, the results showed that a 20 dB SC level was reached only at shorter wavelengths of the S-band (1460 - 1530 nm).

3.4 Ultrafast soliton switching at 1700 nm

On the experimental side, the first-time demonstration of ultrafast switching has been already observed using the soft glass DC PCF [3]. However, the energy transfer between the cores took place only for some fundamental soliton components of the pulse because of the complex nature of high-order solitonic propagation and significant soliton fission phenomena. Moreover, the excitation wavelength was 1800 nm, which is longer the 1560 nm used in the experiments described so far. As it is shown in that work, the increase of the excitation wavelength weakens more the DC asymmetry effect, improving the power transfer ratio between the excited and the non-excited core in linear regime. It has also a positive effect on the nonlinear coupling performance [194]. As a confirmation of this statement, the best switching performance using the air-glass PCF was achieved only at 1788 nm, using a 10 mm length sample and sub-nanojoule pulse energies; however, it was not broadband, but only limited to a narrow spectral window close to excitation wavelength (±3 nm). Therefore, to provide a stronger proof of the thesis, I performed some linear simulations and experiments at 1700 nm using the optimized all-solid DCF from the first generation (with same geometrical parameters in the central column of Table 2.7). According to Table 2.8, it shows higher level of DC asymmetry than the fiber from the second generation. In addition, no switching performance in the C-band has been recorded using it. My goal is to demonstrate that the longer excitation wavelength provides better switching results than in the case of the 1560 nm alternative, even using fibers with higher DC asymmetry. The advantage of the longer wavelength should rely also on the dispersion profile of the fiber, which reveals a negligible TOD at 1700 nm. Therefore, as underlined in section 1.2.3, a weaker dispersive wave generation and a less disturbed solitonic propagation is expected at this wavelength [67].

This section presents the experimental results of solitonic all-optical switching of femtosecond pulses using the DCF from the first generation. I show, that, by thorough cut-back of the fiber, an optimal switching performance can be achieved at 40 mm fiber length under monotonic increase of the input pulse energy. In addition, I present the outcomes recorded at 35 mm length, where I observed a broadband character of the complex switching, showing 3 SSs. The best switching performance expresses SC of the integral energy at the level of 20 dB, overcoming previous experimental works conducted at the same excitation wavelength. At the end of the section, I prove that the propagation scenario recorded at this length has a solitonic character. The possible interpretations of the physical phenomenon will be then discussed at the end of the section.

3.4.1 Numerical simulation of the DCF linear optical properties

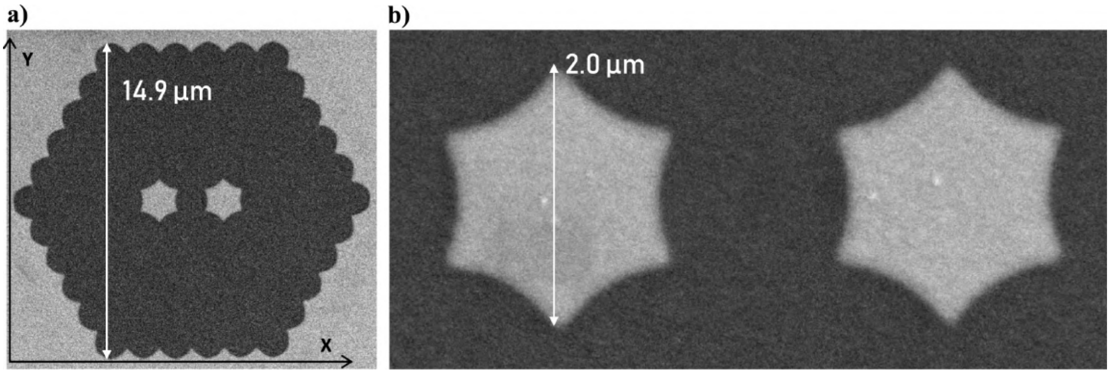

Fig. 3.14: *SEM images of the cross-section of the all-solid dual-core optical fiber with 5 rings around the central rod at two different magnifications: (a) 5000x, (b) 20000x.*

Fig.3.14 presents the SEM images of the cross-section of DCF composed of 5 rings of glass rods with the magnification of 20000. The distance between the centers of the DCF cores is 3.1 µm (outer cladding diameter of 111 µm) and effective mode area A_{eff} of a single core is 1.86 µm^2. To calculate the linear optical properties of the DCF, I used a similar method as the one described in section 3.3.2. In order to include the deviation from the symmetrical optimized structure to the star-like shaped cores as resulted from the fabrication process (section 2.5.1), I approximated the DCF cross-section of the SEM picture by simple geometrical objects. Fig.3.15 reports the resulting structures as insets. For each core, I fitted the curvatures between the two glass borders by circles, eventually by circle sections, because are easy to apply in the mode solver. In the inset images, all the objects made of UV-710 glass have different colors than dark red one, which represent the PBG-08 glass. First, I analyzed the single core structure in order to determine the dispersion profile. The final curves are reported in Fig.3.15: a broad anomalous dispersion, which determine the character of the solitonic propagation, can be identified between the two zero dispersion wavelengths 1295 and 2360 nm, with the maximum dispersion parameter of 66 ps/km/nm at 1720 nm. These results are in accordance with the ones obtained for the hexagonal core symmetric structure reported in Fig.2.12. The sensitivity to the polarization between the dispersion profiles for the parallel X- and the perpendicular Y-polarizations in Fig.3.15a is negligible. In the second step, I analyzed the DC structure in order to calculate the CL characteristics using the expression in Eq.(1.76). The results are in Fig.3.15b. In this case, L_{c} is shorter than the one predicted for the optimized hexagonal core structure with a 3.2 µm core distance. This is an indication of stronger coupling between the cores, which is justified by the shorter core distance of the real structure (3.1 µm). Moreover, the single core effective mode area A_{eff} slightly increases with respect to the optimal case (from 1.84 to 1.86 µm^2), which is caused by the deviation of the core shape from the hexagonal (predicted) to the star-like one. As I have previously pointed out in section 3.3.2, in fact, the determination of the CL is based on the overlap integrals including the evanescent field of one core in the area of the second core [6]. L_{c} is rather polarization-sensitive because the curves for the two orthogonal polarization are slightly different. This is another effect of the slight changes of micro-dimensions of the real fiber structure with respect to the ideal one. The coupling is stronger in the case of the X-polarized field than in the Y-polarized one: the field oscillation vector is oriented towards the opposite core, thus it experiences shorter CLs. In the case of the hypothetical hexagonal and real star-like core structures, the CL decreases from 24 to 13 mm at 1560 nm and from 9 to 5 mm at 1700 nm, respectively, in the case of X-polarized field. The performed numerical analysis of linear properties of the DCF is essential for the proper choice of the conditions of the nonlinear experiments and for the interpretation of the obtained results.

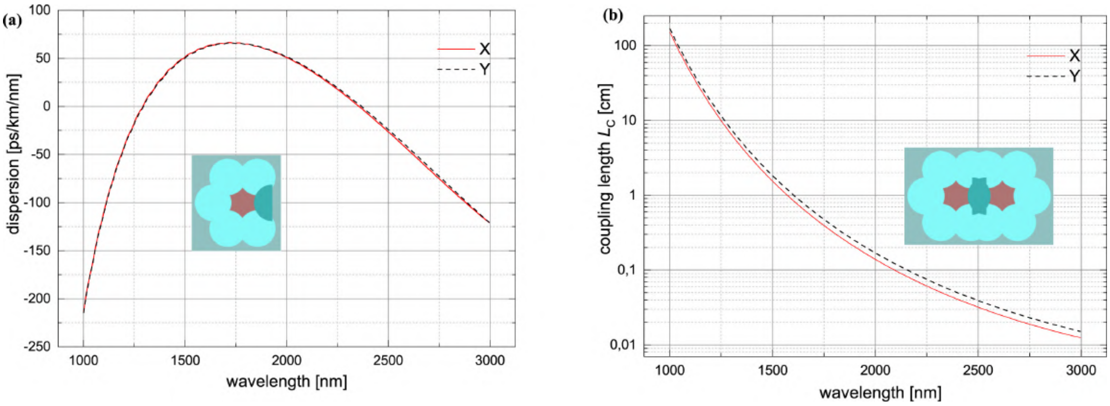

Fig. 3.15: *Spectral characteristics of the (a) single core structure dispersion and (b) DC structure CL for the both orthogonal polarization directions. The pictures of the analyzed simplified structures are in insets.*

3.4.2 Experimental investigation of the nonlinear switching performance

The experimental study was performed using the apparatus depicted in Fig.3.16. It is rather identical to the one in Fig.3.5, with some changes on the source of the excitation pulses, on the high sensitivity camera and spectrometer used for the recording. The source was an OPA operating at 10 kHz repetition rate and tuneable in the spectral range of 1500 - 1900 nm. A frequency doubled output of a commercial Yb:KGW amplifier (Pharos, Light Conversion) worked as pump for a two stage OPA, based on type I barium borate (BBO) crystals. The control of the dispersion with a prism compressor based on a pair of SF10 prisms allowed to set the pulse duration in the range 70 - 100 fs in the whole spectral range of the idler radiation. The energy of generated pulses was attenuated from a few µJ to a few nJ level in order to prevent the damage of the DCF facet. The same set of two half-wave plates and Glan-Taylor polarizer was placed for fine attenuation of the pulse energy and fine tuning the pulse polarization, respectively. The in-coupling and out-coupling of the radiation was managed again by 40x microscope objectives mounted on two identical 3D positioning stages having a sub-micrometer precision. The infrared camera chip was exchanged from AST to Xeva 1.7 320 (Xenics), which has higher sensitivity in the range 1700 - 1800 nm. The spectrometer was changed as well from Yokogawa to NIRQuest, Ocean Optics). The default output field propagation was towards the end facet of multimode collecting fiber attached to the spectrometer. The tilt of a flip mirror enabled the acquisition of the camera images. An iris aperture was used before the flip mirror to cut out the image of the second core and perform the spectral recording for one core only. The effectiveness of the broadband spectral recording was enhanced by focusing the light transmitted through the aperture with a 25 mm objective into the collecting fiber.

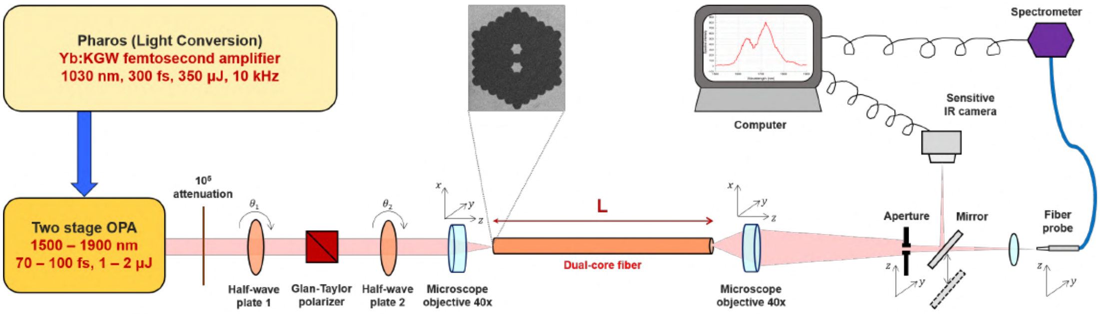

Fig. 3.16: *Experimental apparatus for the investigation of the nonlinear switching in the DCF under excitation by 1700 nm, 100 fs pulses.*

To show that the DC asymmetry effect is weakened by increasing wavelength [3], I chose the 1700 nm excitation wavelength, which represents the longest one where the infrared camera has nearly flat spectral sensitivity. It is very close to the longer limit of the optical communication U-band (1625 - 1675 nm). The advantage of the longer wavelength relies also on the dispersion profile of the fiber (Fig.3.15a), which shows a negligible TOD at 1700 nm (flat dispersion curve). Therefore, weaker dispersive wave generation is expected at this wavelength, which supports less disturbed solitonic propagation [76]. Preliminary experiments were confirmed using the sample belonging to the first generation of DCF with 3.1 µm core distance and DC optical asymmetry $\delta \approx 10^{-6}$ m^{-1} at 1700 nm (Fig.3.14, reported also in Fig.3.17a) and using pulses at 1700 nm pulses and 70 fs width.

The pulse width was optimized empirically and the 100 fs one was chosen because it is more advantageous for the switching than the previously used 75 fs one. Then, the investigation was performed by cutting the fiber back in the range of 45 - 25 mm. At each length and at distinct polarization angles, which supported the highest SC, series of camera images were collected with increasing pulse energy in the range of 0.5 - 3 nJ. As DCFs are inherently birefringent, the investigation of the effect of polarization, which is performed by rotating the second half-wave plate, was done after every cut of the fiber.

The fast core of the DCF in Fig.3.17a was then excited by 1700 nm, 100 fs pulses with increasing energy in the range 1.5 nJ - 3.2 nJ, taking into consideration again the 50% IE. As for the ones presented in Fig.3.6b, the camera recordings in Fig.3.17b do not exhibit any switching behavior. Moreover, there is a slight worsening of the MER, which is only 1.7 dB (positive) at input energy of 2.8 nJ. More importantly, the required energies are an order of magnitude higher than the case in Fig.3.6b, which means that are far from the ones predicted by the corresponding numerical simulations [6].

3.4.3 Fiber length effect at 1700 nm

The fiber length effect was once again investigated by performing a cut-back study with 2-5 mm steps of the DCF in Fig.3.17a from 45 up to 25 mm [12]. The excitation conditions and the pulse energy ranges were kept the same as in the case of full lengths

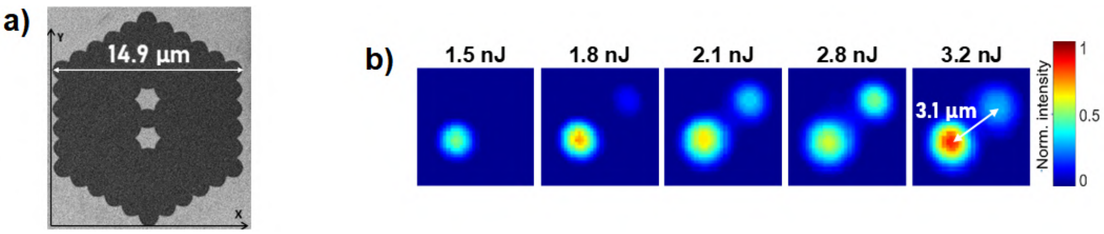

Fig. 3.17: *(a) SEM image of the cross-section of the DCF with higher dual-core asymmetry. (b) Infrared camera images of the output facet of the 45 mm DCF at different energies of 1700 nm, 100 fs input pulses. The cores distance to be 3.1 µm is indicated by a white arrow on the right-hand side image.*

of the fiber (45 mm, Fig.3.17). Fig.3.18 shows the dependences of the MER values on the fiber length L. The first negative value of $MER(E_{\text{in}})$ series was observed at 40 mm, with a value of -5.2 dB. This result is similar to the optimal one obtained at 35 mm using the second generation DCF (Fig.3.11) under 1560 nm excitation. 40 mm appears to be the optimal length of the first generation DCF because the further cut-back of the fiber results in a deterioration of all three parameters. As in the case of the best C-band switching performance, MSC is again slightly above 20 dB and it was recorded at switching pulse energies of 0.3 and 1 nJ. For the first generation DCF (Fig.3.18), at least one SS was observed for all fiber lengths, with exception of 45 and 28 mm, where MER>0. At 40 mm length, even the record number of 4 SSs was observed. It is important to notice that the determined MER and MSC values at 40 mm and 35 mm for the first (Fig.3.18) and second generation DCF (Fig.3.11), respectively, are comparable. They reveal the same application potential for both DCFs; however, the first generation one requires longer operation wavelength. Moreover, the 1560 nm excitation expressed 5 mm shorter fiber length than the one used in the case of 1700 nm excitation of the first generation sample. This means that technological improvements ensuring better DC symmetry enabled high-contrast switching already in the C-band at relatively short fiber length.

Fig.3.18 reports the values of SS, MER and MSC in the inset table. The highest number of SSs (4) was recorded solely at 40 mm fiber length. For the second generation DCF, the maximum number of SSs was determined to be 3 at 38 mm fiber length (see table in Fig.3.11). However, at this fiber length MER and MSC values are far from the optimal ones. The maximum value of MER and MSC were recorded at the shorter 35-mm long fiber.

Along the fiber cut-back study, the switching performance that showed a convincing evidence of switching of self-trapped soliton was observed at 35 mm. From Fig.3.19, the camera images show a rich switching performance under monotonic increase of the input pulse energy E_{in}. The identified switching performance comprises 3 steps: 1) a first SS between 0.89 and 1.65 nJ; 2) a back-SS between 1.65 nJ and 2.27 nJ; 3) a second SS between 2.27 and 2.62 nJ. These results represent a significant progress in comparison to previous experimental works [3, 5].

To process the camera images numerically, I used the same method described in section 3.2. The captured images were integrated across the area of both cores individually for every input pulse energy to get the relative values $E_{\text{bottom}}(E_{\text{in}})$ and $E_{\text{top}}(E_{\text{in}})$. Then, I calculated $ER(E_{\text{in}})$ according to Eq.(3.1) and the SC by simply subtracting between the two extreme positive and negative values of the $ER(E_{\text{in}})$ series.

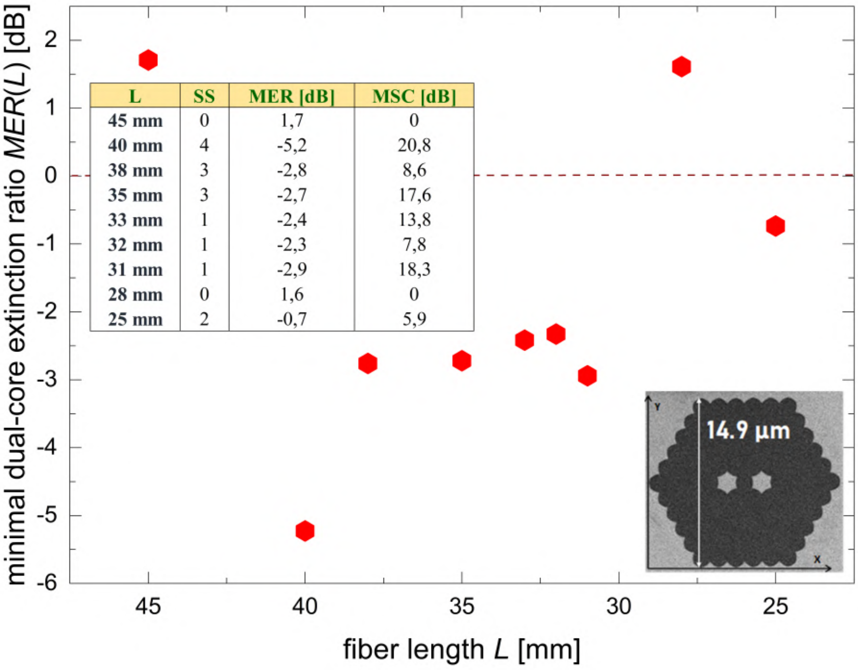

L	SS	MER [dB]	MSC [dB]
45 mm	0	1,7	0
40 mm	4	-5,2	20,8
38 mm	3	-2,8	8,6
35 mm	3	-2,7	17,6
33 mm	1	-2,4	13,8
32 mm	1	-2,3	7,8
31 mm	1	-2,9	18,3
28 mm	0	1,6	0
25 mm	2	-0,7	5,9

Fig. 3.18: *Dependence of the minimal ER (MER) evaluated for each analyzed length of the first generation DCF sample under 1700 nm, 100 fs excitation presented in Fig.3.17a.*

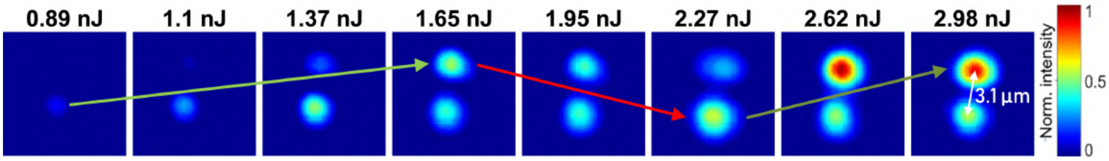

Fig. 3.19: *Infrared camera images of the output of a 35 mm first generation DCF at different energies of 1700 nm, 100 fs input pulses. Double switching with the maximum SC of 16.7 dB is observed when the input pulse energy exchanges between levels 0.89 and 2.62 nJ.*

Fig.3.20a presents the dependence of the $ER(E_{\text{in}})$ on the input pulse energy E_{in}. While increasing the pulse energy monotonically, the values of *ER* experience a change of the sign from positive to negative twice, which is an indication of the double switching performance. The MSC of 16.7 dB was identified between the energy levels 0.89 and 2.62 nJ and it's marked by a vertical arrow in Fig.3.20a.

The spectrally-resolved $ER(\lambda, E_{\text{in}})$ was calculated using Eq.(3.2). Fig.3.20b shows the dependence of $ER(\lambda, E_{\text{in}})$ on the input pulse energy at selected levels of E_{in} expressing the extreme $ER(\lambda)$ profiles. The recordings in the spectral domain confirm also the double switching performance with 3 SSs. The global nonlinear switching trend is evident when increasing the pulse energy from 0.71 nJ (black dotted curve) to 3.14 nJ (black solid curve). The two corresponding $ER(\lambda, E_{\text{in}})$ curves in Fig.3.20b are well separated in the positive and negative sections with an exception in the area between 1720 nm and 1740 nm. Thus, they exhibit the same switching performance as identified in the camera images in Fig.3.19: a positive *ER* value at low energies and a negative one at high energies, respectively. The inset Fig.3.20b shows the spectrum for the top core in the case of the highest applied pulse energy of 3.14 nJ. It reveals that the

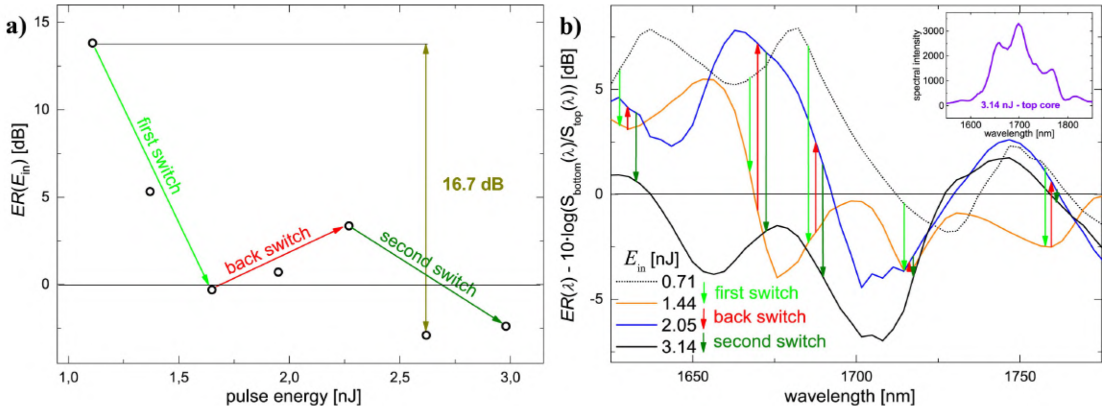

Fig. 3.20: *(a) Spatially resolved DC ER on the input pulse energy E_{in} after processing the camera images in Fig.3.19. (b) Spectrally-resolved $ER(\lambda, E_{in})$ curves at selected pulse energies, calculated using Eq.(3.2). The three arrows denote the first switch, back switch and second switch steps between the corresponding curves in different spectral areas. the inset reports an example of spectrum acquired from the top core under 3.14 nJ pulse energy excitation.*

switching covers the broadest recorded spectral bandwidth, when this maximum pulse energy was applied.

Moreover, a double switching behavior is observed at intermediate pulse energies of 1.44 nJ and 2.05 nJ. The first switch, back switch and the second switch steps are marked with arrows between the corresponding curves in consecutive order and directed always towards the increasing E_{in}: 1) first SS between 0.71 nJ and 1.44 nJ energy levels; 2) back-SS in the energy range 1.44 - 2.05 nJ; 3) second SS between energy levels of 2.05 and 3.14 nJ. The first step is rather convincing: the 1.44 nJ curve is situated below the 0.71 nJ one and it is located below the 0 dB level in most of the considered spectral window. The 2.05 nJ curve has opposite location (above the 0 dB level), with some exception around 1700 nm and at the low intensity wings. Finally, the highest energy curve (3.14 nJ) is situated nearly completely below the 2.05 nJ curve, with a major displacement in the negative and positive sections, respectively. Thus, the spectral profiles of *ER* also confirm the double switching performance, which had been previously identified from the camera images. However, the SC calculated from the spectral results exhibit lower global SCs than the spatially resolved one. In fact, the spectrally-resolved *ER* difference between the black curves (0.71, 3.14 nJ) is at maximum at the level of 10 dB, which is lower than the 16.7 dB of spatially resolved one calculated for similar switching energy levels. This is justified by the chromatic aberrations generated by the recording setup, which contains two lenses and iris aperture for proper isolation of the monitored core (Fig.3.16). The aberrations distort differently the $S_{\text{bottom}}(\lambda, E_{\text{in}})$ and $S_{\text{top}}(\lambda, E_{\text{in}})$ during their separate recording. In addition, the spectra were affected also by power fluctuations of the OPA, because the two mentioned energy dependent spectral series were recorded consecutively after the realignment of whole recording part of the apparatus. Therefore, the camera images, which are free from the above-mentioned distortions, are more appropriate for the evaluation of the integral SC. Even more convincing spectral results and higher values of spectrally-resolved SC would be obtainable in the case of distortion-free experimental conditions.

Despite of the described drawbacks, the spectral results in Fig.3.20b are a convincing demonstration of the broadband character of the studied switching performance. This property is also important from the application point of view because the switched pulses are not affected by break-up in a wide spectral range. The solitonic regime in the anomalous spectral region prevents the pulse distortion and can support such advantageous nonlinear spatial transformation. However, this is the first observation of broadband switching performance at 1700 nm (close to the optical telecommunication U-band) using DCF-based couplers. Based on the obtained results, the solitonic propagation concept is supported by the following findings:

1. The excitation wavelength was in the middle of the DCF anomalous dispersion region;
2. The pulse energies was rather moderate, around 1 nJ, taking into consideration the 50% IE;
3. The broadband character is observed in all three steps of the switching performance;
4. Only a moderate spectral broadening was recorded with a rather smooth spectra even in the case of highest applied pulse energy.

All these aspects indicate that, at the implemented experimental conditions, low-order solitons undergo nonlinear transformations and can be redirected forth and back between the two cores. Nevertheless, the spectral recording were affected by the power fluctuations of the OPA because the light field at the fiber output was recorded separately from each core, after blocking the one from the other core with the aperture (Fig.3.16). It means that the power stability of the source should be improved, for example by using an oscillator-based source instead of the presented complex amplifier–OPA system [278]. Even the optical apparatus for the spectral recordings (aperture and focusing lens) should be adjusted in order to limit the effect of chromatic aberration and other sources of distortions. More importantly, a new strategy that can give an real-time experimental proof of the self-trapped solitonic propagation is the cross frequency-resolved optical gating (XFROG) diagnostics of the output field. By measuring the spectrally resolved pulse autocorrelation at the output of each core, it is possible to retrieve the precise pulse amplitude and phase as a function of time [279] and also evaluate the pulse shape evolution at different fiber lengths.

Generally speaking, the character of the nonlinear switching performance at 1700 nm pulses in the case of 35 mm fiber is similar to the one observed in the C-band and described in section 3.3. First, the value of the spatially-resolved SC calculated from the camera images is higher than 15 dB (17.2 dB at 1700 nm vs 20.2 dB at 1560 nm), never achieved using the air-glass DC PCF [3, 5]. Second, both are broadband in a spectral window of approximately 200 nm, as identified in the results in Fig.3.20 and 3.13. However, the switching performance at 1700 nm using the 35 mm first generation fiber comprises multiple steps (SS = 3) instead of a single step recorded at 1560 nm and using the 35 mm second generation fiber (Fig3.12).

The switching performance at 35 mm under excitation with 1700 nm pulses presented in this section cannot be completely explained by the classical NLDC theory. In fact, it explains only one single switching step (SS = 1) from the non-excited to the excited core, which is achieved by nonlinear balancing of the DC asymmetry [68].

The obtained results indicate a special regime of nonlinear solitonic propagation, which supports high contrast broadband switching with reversible character under monotonic increase of the pulse energy. Moreover, the character of the switching performance is broadband, which indicates that most of the pulse spectral components are efficiently redirected between the cores. According to the classical NLDC theory, the most effective switching process should exactly at $L_\mathrm{c} = 5$ mm in the case of the studied fiber at wavelength 1700 nm (Fig.3.15b). On the contrary, the experimental results reveal an effective switching performance at 35 mm fiber length (Fig.3.19), which is 7 times longer than the L_c, respectively. In fact, the double switching behavior disappeared sequentially for both shorter and longer fibers because any switching performance was observed at lengths of 28 mm or 45 mm. One possible interpretation of the results presented in this section is the switchable self-trapping of high order solitons, which promises broadband character and high SCs [2, 63]. In the frame of the numerical studies of a similar hexagonal core DCF, I obtained a comparable optimal fiber length at 32 mm for high contrast switching, considering a 1700 nm excitation wavelength [6]. All of these achievements indicate the switching performance is based on the soliton self-trapping predicted by the numerical simulations performed in similar conditions. Moreover, the processed spectral curves revealed a broadband character of the switching performance, which also have promising application potential in fiber-based all-optical signal processing.

Nevertheless, the experimental results at 1700 nm presented in Fig.3.19 and 3.20 reveal higher switching energies by one order of magnitude than the numerical simulations (section 2.4.3). Such discrepancy could be caused by dissipation effects in the linear and nonlinear regime as scattering attenuation of the fiber and dispersive wave generation [140, 142], respectively. These effects were taken into consideration in the numerical model presented in section 2.4 just partially; however, they should not cause so pronounced pulse energy enhancement. According to my actual understanding, the combination of these effects with the DC asymmetry is behind the observed discrepancy. The enhanced DC asymmetry requires higher pulse energies to ensure comparable energy transfer from the fast to the slow core, as demonstrated in [3]. These aspects represent motivation for further improvements of the numerical approach and the fabrication technology toward totally symmetrical structures.

3.5 Discussion and comparison

Table 3.1 displays the experimental conditions and the parameters of the best switching performances (in particular, the optimal fiber length L, SS, MER, and MSC) acquired using the first and second generation DCF under excitation at 1700 and 1560 nm, respectively [12].

It is important to underline that the results presented in Fig.3.19 and 3.20 do not belong to the optimal switching performance at 1700 nm, but they were acquired at shorter length of the second generation fiber (35 mm vs. the optimal 40 mm one). However, the results at 35 mm showed a convincing demonstration of soliton self-trapping, identified both in temporal and spectral domains thanks to the camera and spectra recordings. Unfortunately, it was not possible to reach the same correspondence between camera and spectra recordings at 40 mm. The motivations were the strong chromatic aberration generated by the recording setup (mostly caused by lenses and aperture) and the power instability of the OPA, which caused significant deformations of the pulses at the DCF output.

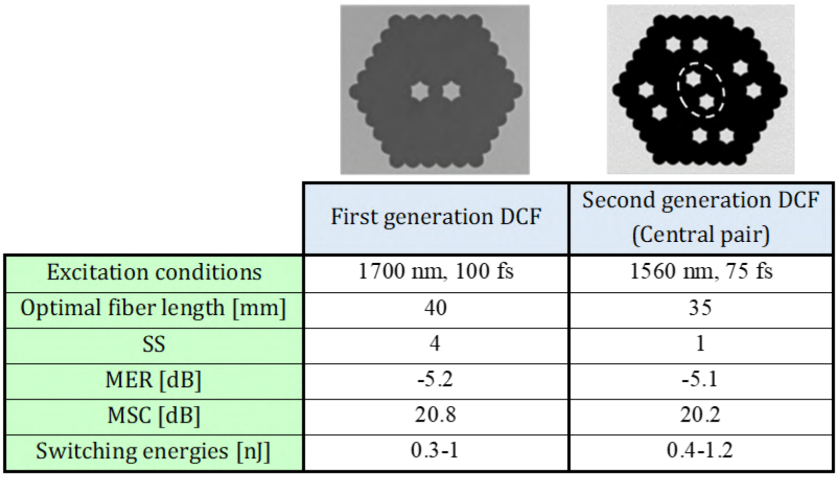

	First generation DCF	Second generation DCF (Central pair)
Excitation conditions	1700 nm, 100 fs	1560 nm, 75 fs
Optimal fiber length [mm]	40	35
SS	4	1
MER [dB]	-5.2	-5.1
MSC [dB]	20.8	20.2
Switching energies [nJ]	0.3-1	0.4-1.2

Table 3.1: *Experimental conditions and best switching performance parameters acquired using the two studied DCF samples.*

A comparison of the two sets of data proves that the second DCF, with improved dual-core symmetry demonstrates comparable values of all monitored parameters, but at shorter excitation wavelength situated in the C-band. Moreover, it was achieved with the advantage of a 5 mm shorter fiber length at the similar level of switching energies. Taking into consideration the 50% IE, these values are in the sub-nanojoule range. Therefore, together with the high SC, the relatively short fiber lengths and the single switching character, it represents an applicable all-optical switching approach based on the presented novel DCF technology. Furthermore, the switching performance exhibited a broadband character within a 200 nm bandwidth, entirely covering the S, C and L optical communication bands.

As mentioned in the previous section, the studied phenomenon with the SS higher than 1 cannot be explained by the classical NLDC theory, which is based on switching from the non-excited to the excited core by nonlinearly induced asymmetry [43, 280]. Moreover, the studied reversible switching process is broadband, as it was confirmed by simultaneous spectral recordings, which indicates that the whole pulses are redirected between the cores [11, 13]. The interpretation of the broadband high contrast switching process is once again the self-trapping of high order solitons, which has potential to ensure a reversible exchange of the trapping core under monotonic increase of their energy [2, 44]. Such solitonic switching performance was predicted by the numerical presented in section 2.4.3, where an hypothetical symmetrical DCF structure with comparable length was considered [6, 9].

3.6 Conclusions and theses verification

In this chapter of the dissertation, I demonstrated experimentally an efficient non-linear self-switching of femtosecond pulses with 1560 and 1700 nm central wavelengths in two DCFs fabricated at Ł-IMIF. First, I showed a reversible high-contrast switching performance of ultrafast solitons in the C-band using the second generation DCF, consisting of two steps: first switching from excited to non-excited core and then back-retention in the excited core (Fig.3.7 and 3.8). This scenario was confirmed by the numerical simulations of the LCNLSE with a simplified model than the one presented in Fig.3.10. Moreover, the broadband switching character presented in Fig.3.13 and the camera images of the switching performance with optimal SC in Fig.3.12 reveal an efficient self-trapping mechanism [2, 9], where almost the entire pulse is redirected between the cores. This scenario was also predicted by numerical simulations in similar hypothetical symmetrical DC structures at comparable fiber lengths (section 2.4.3).

Further strong indications of the self-trapping mechanism originate from the fiber length dependence study of the switching performance in the case of the first generation DCF at 1700 nm, which was presented in section 3.4 (Fig.3.18). The experimental investigation brought a switching performance with the highest SC and highest number of SSs (4) at the optimal 40 mm fiber length using 1700 nm, 100 fs pulses [12]. Moreover,the processed spectral curves revealed a broadband character of the switching performance under moderate nonlinear broadening, which was predicted by the numerical simulations of ultrafast nonlinear propagation presented in section 2.4.3 (especially in Fig.2.26). The obtained results represent a significant progress in comparison to the previous experimental works [3, 5], as they reveal SCs higher than 20 dB, broadband switching character both at 1560 nm and 1700 nm and a multi-step reversible switching behavior (Fig.3.8). These achievements indicate the first realization of a special switching principle based on the soliton self-trapping, which was predicted by the theoretical works in similar conditions [6, 9].

In summary, the experimental results presented in this chapter prove both the first and the second claims reported at the beginning of the dissertation. In fact, I showed that the new all-solid DCFs designed and fabricated at Ł-IMIF, supports the self-trapping of femtosecond solitons in the NIR region, covering a significant range of the third optical communication window (1400 - 1700 nm). It totally includes the C-band, where the losses of silica fibers are the lowest [272] and erbium-doped high-performance fiber amplifiers are available [281]. Furthermore, the elongation of the excitation wavelength enabled the experimental observation of a switching performance even using the first generation of DCF, which had higher level of DC asymmetry than the second generation one.

Even though the experimental results presented in this chapter are quite encouraging, the optimal switching energies reported in Table 3.1 are more than one order of magnitude higher than the ones predicted by the numerical simulations (section 2.4.3). As mentioned in the section 2.6, the estimated energies required for soliton self-trapping (E_{st} - Eq.(2.10)) are 3.9 and 10 nJ using the first and the second generation DCFs, respectively. These values are more than two orders of magnitude higher than the predicted switching energies in Table 2.2 and 2.3 and about one order of magnitude higher than the ones recorded during the experiments. It means that the DC symmetry should be further improved to achieve the self-trapping condition using ultrashort pulses with energies in the sub-nJ regime. Moreover, the difference in the predicted and measured switching energies could be also caused by linear and nonlinear dissipation effects, which were not taken into consideration in the numerical study and by the DC asymmetry of the real samples. In addition, I have not investigated the influence of the DC asymmetry on the other optical parameters of the real fibers, except the effective refractive indices, the propagation constants of the cores (Table 2.8) and the CL (Fig.3.15 vs. Fig.2.13). These aspects represent motivation for further improvements of the numerical approach and the fabrication technology towards totally symmetrical structures. These aspects represent motivation for further improvements of the numerical approach and the fabrication technology towards totally symmetrical structures.

To limit even more the effect of the DC asymmetry and consequently improve the switching performance in terms of SC, I purpose a novel experimental method for the investigation of DCF. It requires an initial level DC asymmetry and actually exploits its effect involving a combination of two synchronized ultrashort pulses. It is called *dual-wavelength switching experiment* and it is the topic of the next chapter.

CHAPTER 4

Ultrafast all-optical dual wavelength switching in dual-core fibers

The studies of ultrafast soliton switching in DCFs presented in the previous chapters can be grouped into a macro-area of all-optical switching called **self-switching**. As I have already shown in the previous chapters, the redistribution of the input optical field between the two output cores of the DCF can be performed by acting uniquely on the energy input pulse itself, which can rearrange itself along the propagation and benefit of the high nonlinear properties of the guiding media (in our DCFs, the PBG-08 glass). A novel all-optical switching I performed using DCFs is the so-called **dual wavelength switching experiment**, which has some interesting applications for telecommunication and single-shot ultrafast spectroscopy as well. It is based on the possibility to launch not just a single femtosecond pulse - as for the self-switching approach - but a combination of two synchronized pulses into one fiber core: the first is a signal pulse, with central wavelength λ_{signal}, while the second is a control one, at λ_{control}. Similarly to the case of self-switching, the working principle of the dual wavelength switching relies on the **nonlinearly-induced DC asymmetry** (section 1.4). After exciting the fast core with the synchronized pulse with proper energy of the control pulse, the signal pulse can switch from the excited to the non-excited core without distortions. In this chapter, I show that this strategy is more effective than the self-switching one to limit the effect of the unavoidable DC asymmetry. As a consequence, I can get lower values of MER (below -20 dB) and, consequently, higher than the 20 dB SC recorded during the previous experiments (Table 3.1).

In this chapter, I present a novel dual wavelength control/signal switching approach using the DCF with 3.1 µm distance between the cores and cross-section as in Fig.3.17a). It has the same geometrical and optical characteristics as in Table 2.7 and 2.8, respectively. The effective refractive index difference between the two cores is Δn = 0.00022 (higher level of DC asymmetry). My original contributions to this study are the setup assembly, the investigation of the switching performance of the signal pulses under increase of the energy control one, and the fiber length effect of the dual wavelength approach. The results are published in the peer-reviewed article *Journal of Lightwave Technology*, 39(15):5111-5117, 2021 [14].

4.1 Motivation for the dual wavelength switching experiment

As the self-switching one, the novel experiment of dual wavelength switching can be located into the macro-sector of all-optical signal processing, which is called **all-optical cross-connect switching**. It is one of the most targeted signal manipulations and it is fundamental for the design of high-capacity and high-data-rate optical networks [282, 283]. It is also required for the development of digital optical computers [284] and it is one of the most indispensable logic operations for the realization of optical buffers [285], wavelength division multiplexed interconnects [30] and data center networks [286]. All-fiber based cross-connects have the potential for lower opto-mechanical complexity, device dimension, and optical power consumption than free-space interconnections [287,288]. Moreover, DCFs represent one of the simplest architectures to ensure the all-optical cross-connect switching. They are even much easier to produce than other more sophisticated single channel techniques, such as those based on the use of metamaterials [39], ring resonators [40], electro-optical semiconductor amplifiers [289] or plasmonic waveguides [41]. In addition, DCFs do not need to be duplicated and outfitted with a proper input signal splitter to act as a cross-connect switch like the other mentioned cases.

One of the most elegant approaches of cross-switching is the NOLM, which recently ensured high contrast dropping of the signal from 10 Tb/s data rate stream requiring control pulses at the level of only 2 pJ [42]. It was demonstrated over a 300 km fiber link in a configuration, which ensure seamless integration into an optical fiber communication network. On the other hand, such an ultrafast device with a low power consumption comprises 20 m of optical fiber and a wavelength division multiplexer on both the input and the output ends, which are required to separate the signal and control pulses. Consequently, the NOLM technique is rather bulky, complex and its cascading is cumbersome; therefore, it is not a perspective approach for multichannel cross-connect switching. In conclusion, DCFs remain promising candidates for all-optical signal processing, particularly for cross-switching tasks.

4.2 Experimental conditions

Fig.4.1 shows a schematic of the experimental setup for dual wavelength switching. I launched two timely synchronized femtosecond pulses with different central wavelength into one fiber core with 10 kHz repetition rate:

1. **Control pulses** at 1030 nm with 270 fs width, generated by a commercial ultrafast Yb:KGW amplifier (Pharos, Light Conversion);
2. **Signal pulses** at 1560 nm with 75 fs width, generated in a double pass OPA, pumped by frequency doubled output of the same Yb:KGW amplifier.

The energy and the polarization of the control pulses was independently controlled by the series of two half-wave plates and a Glan polarizer between them, as in the setup in Fig.3.16. The control and the beam pulses were combined together by a dichroic mirror and then the polarization of the combined beam was controlled by another half-wave plate. I used a delay line unit in the control arm to set the proper time shift between the signal and control pulses. Additionally, I placed a telescopic system into the signal arm with adjustable distance between their two objectives in order to set the same diameter of both beams at the input fiber facet. The in-coupling of the combined beam into one of the fiber core was ensured using a microscopic objective with 40x magnification ensuring the in-coupling into one of the DCF cores. A second micro-objective imaged the output facet of the DCF onto an infrared camera chip (Xeva 1.7 320, Xenics) or onto a multimode collecting fiber attached to a spectrometer (NIRQuest, Ocean Optics). The direct path was towards the spectrometer, while the tilt of a mirror enabled the image acquisition from the camera. The energy of the signal pulses was set at 100 pJ level, which led to their linear propagation in the absence of control pulses. I recorded a series of camera images of the spatial distribution of the signal field (1560 nm) with increasing the energy of control pulses in range of 1 - 10 nJ, while suppressing the control field at the output of the fiber using a dichroic mirror. Under unchanged experimental conditions, I separately acquired the spectra of signal pulses coming out from the excited and non-excited core. I repeated the recording of the signal field dependence on the control pulse energy for different fiber lengths in order to identify the optimal one for high contrast signal pulse switching.

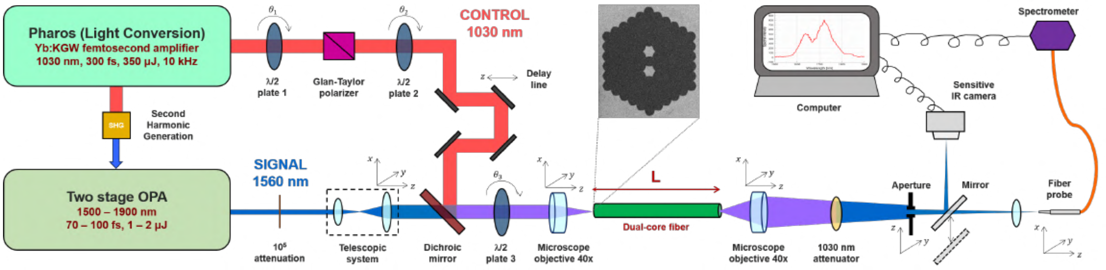

Fig. 4.1: *Experimental scheme containing the laser source of the synchronized control and signal pulses and the setups of the controlled DC excitation and the output signal recording.*

4.3 Results and discussion

Fig.4.2 presents the dependence of the output signal field spatial distribution on the energy of the control pulses under combined beam excitation of the right (top series) and the left (bottom series) core of a DCF with optimized length of 14 mm. The false colors in the images represent the normalized registered intensity on linear scale in accordance to the legend at the right side of Fig.4.2. In the case of the bottom series, I did not observe any notable change in the camera images by increasing the control pulse energy. Nevertheless, in the case of right core excitation, a high-contrast switching performance took place. At initial 1.1 nJ control pulse energy, only the right core was excited; however, at 3.8 nJ energy of the control pulse, nearly the whole signal field was transferred to the non-excited (left) core. After further increase of the control pulse energy, the SC between the excited and non-excited cores worsens and, at 6.4 nJ, the signal field is transferred back to the excited (right) core. Then, the right core dominance is maintained even after further increase of the control pulse energy up to 8.9 nJ. The value of the experimentally determined fiber length is very close to the one of the numerically simulated coupling length L_c in Fig.3.15b [13]. It was performed on the basis of the SEM image of the fiber cross-section and resulted in values of 13 mm and 116 mm at 1560 nm and 1030 nm wavelengths, respectively. The significantly longer L_c than the fiber length at 1030 nm indicates that the control pulses propagate mostly in the excited core, with negligible energy transfer to the non-excited one.

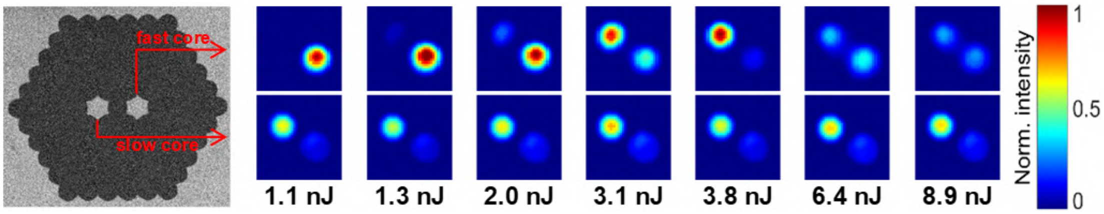

Fig. 4.2: *Scanning electron microscope image of the cross-section of the all-solid DCF structure (left). Infrared camera images of the 1560 nm, 77 fs signal field at the DCF output under increasing energy of 1030 nm, 270 fs control pulses, while the right (top series) and the left (bottom series) fiber core was excited by the combined beam.*

The explanation of the efficient energy transfer at 3.8 nJ control pulse energy at optimized fiber length is the nonlinearly induced asymmetry balancing between the two fiber channels. The positive sign of the Kerr nonlinearity in the guiding glass causes decrease of the group velocity v_g of the excited right (fast) core in the time window of the control pulse duration to the level of the non-excited left (slow) core v_g [14]. Under low control pulse energy excitation (camera image at 1.1 nJ in Fig.4.2), the whole signal pulse energy remains mostly in the excited core because the DC asymmetry compromises the energy transfer. Afterwards, the increase of the control pulse energy allows the redirection of the signal pulse to the non-excited core with high *ER*s. In the case of optimal control pulse energy of 3.8 nJ and Gaussian pulse profile with duration of 270 fs, the peak power required to establish the asymmetry balancing [35] is estimated to be 14 kW. If peak power (pulse energy) is lower or higher than this value, the energy transfer is only partial: above this level, the fast core becomes already slower than the non-excited (originally slow) core. The same behavior is observed in the camera images in Fig.4.2: above the 3.8 nJ pulse energy level, the excited (right) core output intensity decreases monotonically with increasing energy. However, the DC field distribution doesn't have its original character observed at 1.1 nJ due to the strong nonlinear deformation of the signal field at higher control energies. Anyway, for practical reasons, it is not necessary to use pulse energies above the optimal switching energy of 3.8 nJ.

Fig.4.3 shows the spectrally-resolved DC *ER* dependence on the control pulse input energy in the spectral domain in the case of right core excitation of 14-mm length DCF. It was calculated using Eq.(3.2), more specifically $ER(\lambda) = 10\log(S_\mathrm{r}(\lambda)/S_\mathrm{l}(\lambda))$, where $S_\mathrm{r,l}(\lambda)$ are the spectral intensity in the right (excited) and left core, respectively. To verify the results presented in top row of the Fig.4.2 (right core excitation), I repeated the recording of the camera images during the spectral measurements. Some of them were selected and reported as insets in Fig.4.3a. This figure displays the dependence of the DC extinction ratio spectral profile on the control pulse energy in the range 1.1 - 3.8 nJ. As in Fig.3.15b and Fig.3.13, the positive $ER(\lambda)$ values mean higher spectral intensity in the excited core, while the negative ones in the non-excited core. The dashed curve is the *ER* spectrum acquired at 2.5 nJ pulse energy. It is the closest to the 0 dB level, which represents the best balance between curves $S_\mathrm{r}(\lambda)$ and $S_\mathrm{l}(\lambda)$ in the considered spectral range. The camera image recorded at this energy level shows the same scenario, i.e. an equalization between the intensities coming from both cores. The general trend of the curves is a **monotonic decrease of *ER*** within the whole spectral bandwidth with some anomalies at the wings, i.e. at wavelengths lower than 1500 nm and greater than 1600 nm. However, the monotonic trend is observed without exceptions in the spectral range of 1515 - 1565 nm, and the maximum SC (difference of maximal and minimal ER, in this case between *ER* at 1.1 nJ and 3.8 nJ) has a value of 21.4 dB at the particular wavelength of 1560 nm. Moreover, the displacement of the extreme *ER* values with respect to the 0 level is rather symmetrical. Both the positive and the negative extremes of the DC *ER* are at the level of 10 dB and the dominance of the excited (right) and non-excited (left) cores are confirmed by the two corresponding camera images at the output facet of the DCF reported as insets, on the top and bottom side of Fig.4.3a. The observation that the peak intensities in these images are rather similar reveals that nearly the entire pulse energy was transferred between the two cores due to the nonlinear switching process.

Fig.4.3b presents the spectra of the *ER* recorded at control pulse energies in the range 3.8 nJ - 7.6 nJ. The spectral profiles have an opposite trend than the lower energy case in Fig.4.3a: *ER* in the spectral range of 1515 - 1565 nm monotonically increases with the increasing control pulse energy. Consequently, the two sets of spectra confirm the optimal switching energy of 3.8 nJ. Both below and above this level, $ER(\lambda)$ increases and this trend is in correspondence with the recorded camera images in Fig.4.2. It represents a further indication of the nonlinear balancing of the slight DC asymmetry, which ensures maximal transfer between the cores at a distinct control pulse energy.

Fig.4.4a shows the spectra of the control pulse recorded at the output of the excited (fast) core, while Fig.4.4b displays the normalized spectra of the signal pulse collected at the output of the corresponding dominant core: excited (left) core at energy levels 1.1 and 1.3 nJ, non-excited (right) core at energy levels 3.1, 3.8 and 4.5 nJ. The lower energy spectra in the excited (fast) core are depicted by solid lines, while the higher energy ones in the non-excited (slow) core are reported in dashed lines. At lower control pulse energies (spectra with solid line in Fig.4.4a), the spectra in Fig.4.4b have rather similar profiles, which shows that - under these conditions - the propagation of the signal pulses is affected by limited nonlinear deformations. At higher control pulse energies, only a slight monotonic blue shift and spectral narrowing tendency were observed with increasing the control pulse energy. The central wavelength shifts only by 5 nm, while at the 3.8 nJ control pulse energy the bandwidth became narrower by 20% than the low energy spectral profiles. Above this, the spectra remain smooth and do not exhibit any asymmetry. In conclusion, I can state the, under monotonic increase of the control pulse energy Fig.4.4a, the shape of the signal pulses in the corresponding dominant core undergoes minor deformations, with only a slight blue shift and narrowing in case of control pulse energies above 3.1 nJ.

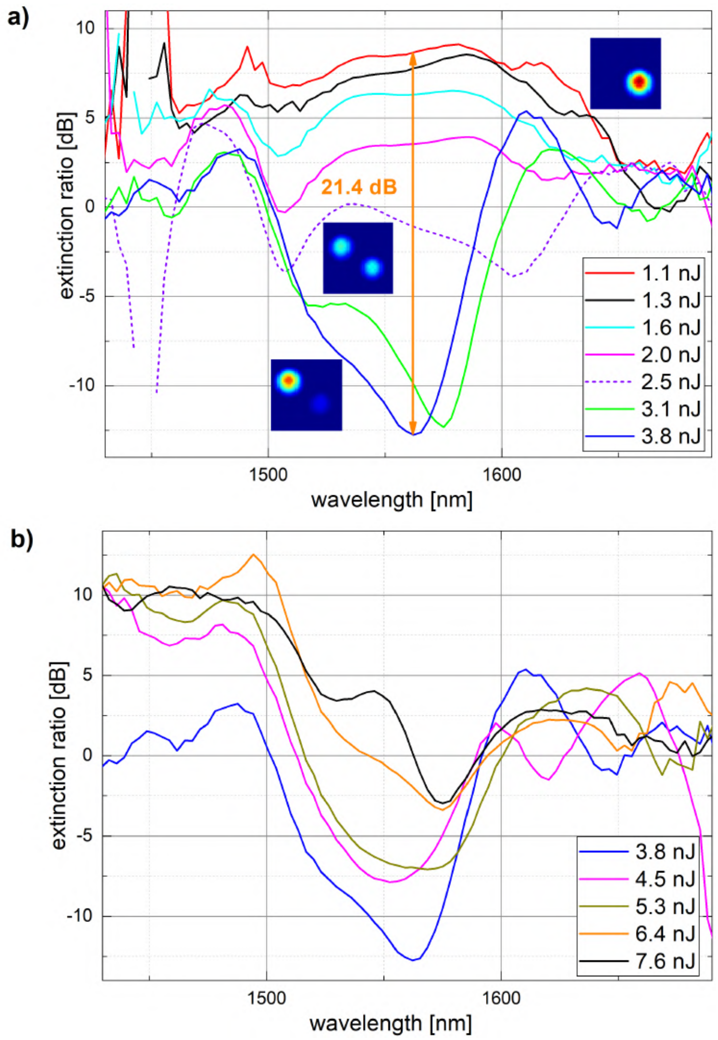

Fig. 4.3: *Dependence of extinction ratios spectral profile on control pulse energy (indicated) in range of (a) 1.1 - 3.8 nJ and (b) 3.8 - 7.6 nJ. Infrared camera images of the output fiber facet at energies 1.1, 2.5 and 3.8 nJ are in the insets, placed at the correspondent spectral curves.*

Taking into consideration Gaussian-like spectral profiles, the output spectral width at the low energy and the switching energy correspond to a bandwidth limited pulse duration of 66 and 85 fs, respectively. The performed input pulse diagnostics performed by frequency resolved optical gating method resulted in 75 fs bandwidth limited pulse width. Thus, at the output of the fiber, the spectra are just slightly broader and narrower than compared to the input pulse. In the case of standard integral type recording used in optical communication technologies, the observed pulse lengthening should not have any pronounced effect on the switching performance. Moreover, such output signal is repeatedly switchable with high contrast by the same approach of the nonlinear balancing of DC asymmetry using the significantly longer control pulse. The different group velocities at wavelengths 1030 nm and 1560 nm cause walk-off of about 152 fs for 14 mm long fiber and faster propagation of the signal pulse. During the experiment, the delay between the control and signal pulses was optimized after every change of the experimental conditions in order to maximize the switching effectiveness. Therefore, I

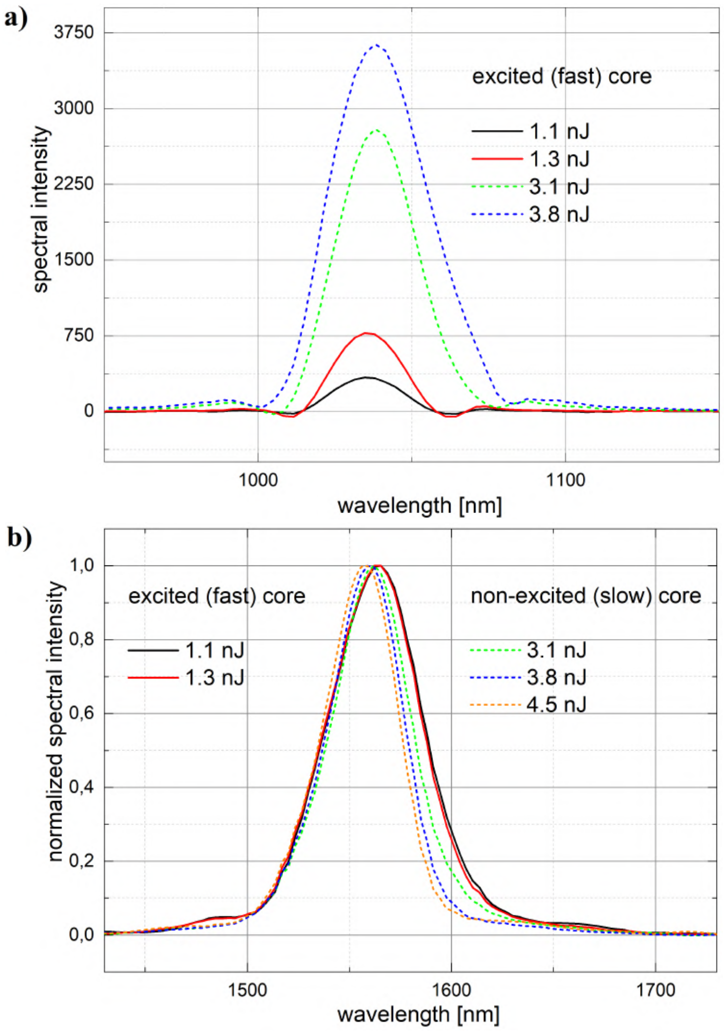

Fig. 4.4: *(a) Spectra of the control pulses with increasing energy recorded at the output of the excited (fast) core. (b) Normalized signal pulses spectra collected at low control pulse energies from the excited core (solid) and around the switching energy from the non-excited core (dashed).*

assume that the optimal switching was achieved in the situation when the control and signal pulses overlapped in the central part of the fiber. Consequently, signal pulses at the input of the fiber were delayed during the initial phase of the co-propagation so they were overlapped with the trailing part of the control pulses. In contrast, during the end phase of the co-propagation closer to the fiber output the signal pulses were overlapped with the leading part of the control pulse. Therefore, the cross-phase modulation caused changes have opposite sign comparing this two propagation phases thus eliminate the effect of each other. The co-propagation under nearly overlapped peaks of the interacting pulses in the middle phase of the co-propagation has weaker influence because the 270 fs control pulse expresses just slight intensity changes along the 75 fs signal pulse width.

Observing the series of camera images in Fig.4.2, the real SCs is expected to be higher than 21.4 dB because very low intensities were registered in the vicinity of the excited (right) core at 3.8 nJ. I also calculated the spatially resolved *ER* of the output signal energy using the camera images series in Fig.4.2. It was performed as separate integration of the field distribution at the output of both cores and then calculating $ER(E_{\text{control}})$ with Eq.(3.1). The minimal $ER(E_{\text{control}})$ value for the series in Fig.4.2 was -23.2 dB in case of 3.8 nJ control pulse energy, which is an excellent value from the application point of view. Unfortunately, I was not able to reach the same MER level during the spectral recording phase, which was only -12.8 dB at 1560 nm and 3.8 nJ energy of the control pulse (Fig.4.3a). The main reason of this discrepancy between integral and spectrally-resolved *ER* values is the chromatic aberrations of the recording setup, which contains two lenses and iris aperture for proper isolation of the monitored core (Fig.4.1). Therefore, one possible improvement of the setup in Fig.4.1 could be to substitute the standard refraction micro-objective with a reflective one, which removes the effect of chromatic aberrations and wavelength-dependent focusing. This strategy could be promising to record spectrally-resolved MER below -20 dB. Therefore, I assume that, in the frame of the dual wavelength switching experiment, the camera images give more reliable results than the spectral recordings; moreover, they are more relevant from practical point of view because the majority of applications do not require spectral resolution of the output signal. However, I expect that, after the suggested improvements of the experimental setup I mentioned above, SCs higher than 40 dB can be recorded even in the spectral domain.

As for the self-switching experiment, I investigated the fiber length effect of the dual wavelength switching performance. The DCF in Fig.4.2a was cut in the range of 16 - 10.5 mm with approximately 2 mm step. Table 4.1 reports the MER values for the analyzed fiber lengths. It shows that the minimum MER of -23.2 dB was reached at 14 mm length, which is exactly the case presented at the beginning of section 4.3 (Fig.4.2, first row). A 2-mm shortening of the fiber resulted in a increase of MER of about 3 dB; however, the MER is still below -20 dB, which is very promising for potential applications of the dual wavelength switching method.

Length [mm]	MER [dB]
16	-6.7
14	**-23.2**
12	-20.2
10.5	-5.7

Table 4.1: *Fiber length dependence of the dual wavelength switching MER. A minimum of -23.4 dB MER was reached at 14 mm length of the used DCF.*

By taking into account the difference of effective refractive index of the two fiber cores, it is possible to estimate the control pulse energy, at which the balancing of the DC asymmetry can be achieved. The Kerr nonlinearity induces change of the refractive index $\Delta n = n_2 I$, where n_2 is the nonlinear index of refraction, which is equal to 4.3 $\cdot 10^{-19}$ m^2/W in the case of the PBG-08 glass used for the fiber core [263] and I is the field intensity. Considering effective mode area of 1.41 µm^2 [13], pulse duration of 270 fs and IE of 50% (section 3.1.2), I obtain the value of 0.76 nJ. It is 5 times lower than the experimentally determined optimal switching energy of 3.8 nJ. Even though, taking into account the walk-off between the signal and control pulses at the level of 152 fs, it represents a decent estimate. The walk-off between the pulses results in higher control pulse energy required to induce asymmetry balancing between the two fiber cores, since the signal pulse experiences lower control field intensities at its leading and trailing edges. Another factor leading to higher experimentally determined control pulse energy is the attenuation and stretching of control pulses during propagation along the fiber in the normal dispersion region, in contrast to the anomalous region propagation of the signal pulse (see Fig.3.15a) [13]. It is important to emphasize that the 1030 nm pulse can have higher attenuation than the signal one and it is nonlinearly more deteriorated due to the SPM effect. Control pulses experienced spectral broadening of 25% at the switching energy of 3.8 nJ, which indicates pulse stretching during propagation in the normal dispersion region. Therefore, the estimated energy of 0.76 nJ is in correspondence with the concept of nonlinear balancing of DC asymmetry.

Since temporal walk-off can be minimized by choosing properly paired wavelengths of the control and switching pulses as well as by targeted redesigning of the fiber structure, a dual wavelength switching with sub-nJ control pulses sounds feasible. Moreover, the reduction of the walk-off would allow the use of shorter control pulses, and, consequently, the switching at 100 pJ energy levels. Moreover, to significantly reduce the system complexity, a novel fiber design can be studied in order to reach a balance of the group velocities at the wavelength pair of 780 nm and 1560 nm. They correspond to second and fundamental harmonics of an Er-doped fiber oscillator, respectively. However, the power of the harmonics should be balanced in such a way that the signal pulses at 1560 nm reach at least a few milliwatts output power (considering 100 MHz repetition rates) and can be easily detected by an high-sensitivity infrared camera. Therefore, the pump at 780 nm should have at least few microjoule power to enable the second harmonic generation at 1560 nm. This can be obtained by a proper setting of the two-stage OPA parameters, similarly to the one reported in Fig.4.1. In combination with low power requirement the approach of the dual wavelength switching by using Er-doped fiber oscillators with fundamental and second harmonic outputs seems to be a promising new avenue for effective all-optical switches in telecommunication C-band.

4.4 Conclusion and thesis verification

In this chapter, I showed that DCFs are possible tools for cross-connect switching due to their short length, simple structure and achieved ultrafast switching rates with high SCs. This new strategy based on nonlinear balancing of the DC asymmetry overcomes the self-switching one in many aspects. First of all, I reached SC of more than 20 dB (in the optimal case, 44.1 dB at 1560 nm) exceeding both the best experimental results obtained in the C-band (section 3.3.3) and the theoretical predictions of ultrafast solitonic self-trapping in highly nonlinear DCFs presented in chapter 2 [9]. Second, the control/signal approach causes minimal pulse distortions, resulting in spectrally homogeneous switching performance. It is rather hard to achieve such character in the case of self-switching because higher level of nonlinear interaction result in significant spectral broadening and pulse deformations (for example, see Fig.3.20b and Fig.3.13). Finally, the fiber length is only 14 mm, which is more than half shorter than the 35 mm one, where I achieved the highest contrast of self-switching at 1560 nm (section 3.3.3). Thus, the demonstrated novel approach represents a promising direction in ultrafast all-optical signal processing with scaling potential in terms of control and signal energy, fiber length and repeatability. Moreover, the results presented in this chapter are as well a stronger proof of the third claim of the dissertation. In fact, the new all-optical switching technique based on the nonlinear balancing of the DC symmetry benefits not only on the improved fabrication technology of the all-solid DCF, but also on the strong nonlinear interactions between the control and signal pulses, which results in a more effective switching performance in the C-band.

One of the most crucial disadvantage of the dual wavelength switching approach is the relatively high energy of the control pulses in the order of few nJ. The motivation for this is the relatively large control pulse duration than the ones in the self-switching experiments (270 vs 75 fs), and the walk-off between the switching and control pulses. However, this drawback could be eliminated by improving the DC symmetry of the fiber and by better synchronization of signal and control pulses by properly adjusting the delay between them. Another disadvantage of the current approach is the chromatic aberration, which is caused by the combination of iris aperture and focusing lens before the fiber probe. It does not allow to reach the same level of integral and spectrally-resolved MER. My suggestion to limit this effect is using a reflective micro-objective at the output of the fiber, which could prevent undesired spectral deformations and out-of-focus effects.

In order to shorten the device length and eliminate of the undesired walk-off effect, I suggest a redesigning of the DCF structure, considering that the CL is strongly dependent on the distance between the two cores. Furthermore, it is possible to reduce the energy of the signal pulse. In the experiments presented in this chapter, I set it to the level of 100 pJ just because the output field was easy to be detected by the infrared camera and spectrometer. Moreover, it also meets the recent standards of the optical communication systems [290]. However, the signal pulses energy can be reduced even below 1 pJ using instrumentation with higher sensitivity, improved recording techniques or higher repetition rates of the laser source [291].

For these reasons, I have already planned to continue the study of the dual wavelength switching approach using the second generation DCF (Fig.3.6a), which has higher level of DC symmetry (Table 2.8). Moreover, I would like to reduce the walk-off between control and signal pulses by improving their synchronization and alignment at the input of the fiber.

Conclusions

In this dissertation, I presented a study - both numerical and experimental - devoted to all-optical switching based on self-trapping of ultrashort soliton-like pulses using soft-glass DCFs. I developed an all-solid DCF made of two thermally-matched glasses synthesized in-house. I studied numerically the coupling and nonlinear characteristics of the fiber and optimized its structure. Then, I studied the nonlinear propagation of femtosecond pulses in the optimized DCFs in order to support an efficient switching performance. Finally, I investigated experimentally the switching performance using the fabricated fibers and two approaches: self-switching and dual wavelength one.

Verification of the dissertation theses

Along the four chapters, I have proven all the three theses listed in the introductory section of this dissertation. The accomplished objectives mentioned at the beginning of the dissertation are summarized below:

- To verify the **first claim** *The soft-glass all-solid DCF supports nonlinear controllable self-trapping of femtosecond solitons with central wavelength in the near-infrared (NIR) region, in particular at 1560 nm (optical telecom C-band)*, I showed the optimization process of the DCF in terms of proper choice of the materials (PBG-08 and UV-710 glasses, **section 2.2**), structural parameters (lattice pitch, core diameters) and linear optical properties (dispersion profile and CL). The study is reported in **section 2.3 of chapter 2**. First, I started with the optimization process of the fiber structure including air-glass PCF, all-solid PCF and simple all-solid alternatives. The goal was to ensure the soliton self-trapping propagation regime, which is the comparable value of coupling and soliton compression length (Eq.1.93) using sub-100 pJ ultrafast pulses. The air-glass PCF was already studied [2] and did not bring the expected results due to a strong DC asymmetry [3]. Therefore, I focused on the optimization of the all-solid PCF made of the thermally-matched glasses PBG-08/UV-710. They express a contrast of the refractive indices at the level of 0.4 in the near infrared. Then, I performed numerical calculations of the dispersion and coupling dispersion profiles by systematically changing the geometrical parameters of the structure, such as core diameters and photonic lattice pitch. The requirements were maximized anomalous dispersion, coupling length in the millimeters/centimeters range and TOD minimization (**section 2.3**). The study resulted in an optimized PCF structure with cores of hexagonal shape and 1.7 µm diameter. The UV-710 rods of the photonic lattice have also hexagonal shape and they are separated between each other by 130 nm small PBG-08 bridges, resulting in a filling factor of 94%. Then, I studied numerically the nonlinear propagation of hyperbolic secant pulses (sech^2-type) in the optimized fiber structure at different excitation wavelengths (1400 - 1800 nm) and at different pulse widths (75 - 150 fs). I concluded that the optimized all-solid PCF did not support a more effective switching performance than the previous air-glass PCF [6]. Therefore, in a following step, I considered a simple DCF structure with homogeneous cladding, made with the same couple of soft glasses and with 1.85 µm cores diameter and 1.6 µm lattice pitch (filling factor of 100%).

One important verification of the first claim were the numerical simulation results of nonlinear propagation of ultrafast femtosecond pulses in the optimized DCF. They are presented in **section 2.4 of chapter 2**. I studied numerically the nonlinear propagation of hyperbolic secant pulses (sech^2-type) in the optimized fiber structure at different excitation wavelengths (1400 - 1800 nm) and at different pulse widths (75 - 150 fs). I concluded that the optimized all-solid PCF did not support a more effective switching performance than the previous air-glass PCF [6]. Therefore, in a following step, I considered a simple DCF structure with homogeneous cladding, made with the same couple of soft glasses and with 1.85 µm cores diameter and 1.6 µm lattice pitch (filling factor of 100%). Additionally, this fiber with simple cladding has also the highest and flattest anomalous dispersion in the wavelength range 1400 - 1700 nm, which is effective for the soliton generation and minimization of the TOD effects, respectively. I showed that the highest SC of 46 dB in the time window of the ultrashort soliton was predicted at 43 mm fiber length in case of excitation with 1500 nm, 75 fs hyperbolic secant pulses with energies at the level of 20 pJ. These results, especially the 6-times lower in-coupled pulse energies, are the best one ever achieved using DCFs and also represent a significant progress with respect to the ones obtained analyzing the air-glass PCF [2]. Additionally, the analysis of the spectrally-resolved *ER* showed a broadband and uniform character of the switching performance, with switching contrasts exceeding 30 dB at three different wavelengths in the standard optical communication range.

The main verification of the claim is certainly the experimental results in the C-band presented in **section 3.3 of chapter 3**. In the frame of the self-switching experiments presented in **section 3.2**, I observed for the first time a switching performance in the C-band (1560 nm, 75 fs), with both reversible and solitonic character, using a 43 mm sample from the second generation fiber with improved DC symmetry δ (section 3.3.1). The results were also confirmed by the dedicated numerical simulations performed with a simple model of CGNLSE system [11]. The fiber length effect study brought an excellent switching performance using 35 mm fiber and the same excitation conditions: switching energies around 1 nJ, single SS, MER below -5 dB, more than 20 dB MSC, broadband within 200 nm, covering the C, L, and U optical telecommunication bands. These results were never reached before using a DCF.

Moreover, the outcomes in **chapter 4** are as well a more convincing and effective demonstration of the nonlinear balancing of the DC asymmetry using femtosecond solitons with central wavelength located in the C-band. It allowed to improve the SCs above 25 dB, even overcoming the optimal results achieved with the self-switching approach. Moreover, it requires shorter fiber lengths below only 15 mm and shows just minimal distortions of the switched pulse;

- To verify the **second claim** *The optimized DCF allows a high-contrast switching performance enabled by the self-trapping phenomenon in a broad range of excitation wavelengths up to 1700 nm*, I showed the experimental results of the switching performance at 1700 nm. In the frame of complex fiber length study using the first generation DCF, I observed double switching behavior with MSC of 16.7 dB between 0.89 nJ and 2.62 nJ input energies at 35 mm length. It was identified both from the camera images, as well from spectral recordings of the fiber output field. Even in this case, the switching performance was broadband, covering a 200 nm spectral range between 1700 nm. The achievements at this wavelength indicate that the switching performance was based on soliton-like self-trapping and confirmed the predicted assumptions from the theoretical simulations. The results are reported in **section 3.4 of chapter 3**;

- For the **third claim** *In the fabricated dual-core fiber, the influence of asymmetry on the coupling efficiency can be mitigated by taking advantage of nonlinear Kerr-effect introduced by femtosecond pulses and by the all-solid soft-glass approach. Consequently, the switching performance can be improved in a broadband wavelength range, when pumped at 1560 and 1700 nm wavelengths*, I first explained the stack-and-draw fabrication process for the designed DCFs, in **section 2.5 of chapter 2**. Two generations of DCFs were then fabricated at Ł-IMIF, following the optimized design and using the stack-and-draw method [10]: 1) a DCF with simple cladding and 3.1 µm distance between cores, shorter than the optimal of 3.2 µm identified during the simulation phase (first generation DCF); one simple DCF, which includes 5 waveguides and having the central waveguide with 3.3 µm core distance, longer than the optimal one (second generation DCF). The final fibers have an improved DC symmetry than the previously investigated air-glass PCF (Table 2.8). Moreover, according to the results of the experiments in the linear regime, the fiber has low losses (attenuation coefficient $\alpha = 8$ dB/m) and IE of 50%, higher than the air-glass one [3]. This study is presented in **section 2.5 of chapter 2**. The improved fabrication technology of the DCFs at Ł-IMIF allowed to reach a high level of DC symmetry, with only 0.5% deviation of the main structural parameters (diagonals and area) between the cores. The all-solid DCFs with improved DC symmetry allowed the first- time demonstration of a switching performance of femtosecond solitons at two excitation wavelengths (1560 and 1700 nm). Consequently, all the experimental results presented in this dissertation (chapters 3 and 4) rely on the high level of the DC symmetry, contributing to the verification of the last and most important claim of the dissertation.

Comparison between switching approaches and future perspectives

The role of the DC asymmetry is different in the case of the two presented approaches. The self-switching is based on the soliton self-trapping phenomenon, predicted by numerical simulations supporting the experimental results (section 3.3.2). The self-trapping phenomenon causes the compression of higher-order soliton during the initial phase of propagation, which induces nonlinearly a strong asymmetry between the cores and prevents the linear coupling. Therefore, in general it does not require an initial DC asymmetry, which only perturbs the self-trapping process and results in different switching performance by separately exciting the fast and slow core.

On the other hand, the strong nonlinear interaction causes a broadband switching illustrated in Fig.3.12 and in [9]. In the dual wavelength switching case, the asymmetry assists the switching process. A sufficiently high level of the asymmetry is required because, when the control field is absent, the transfer of the signal pulse to the non-excited core is prevented. On the contrary, when control pulses of appropriate energy co-propagate with the signal in the time window of the control pulse duration, the Kerr nonlinearity causes a decrease of the group velocity v_g in the excited core to the level of the non-excited core [14]. This interpretation is supported by the calculations of the coupling length of the hypothetically symmetrical DCF structure reported in 2.13. It resulted in 13 mm at 1560 nm, which is very close to the experimentally identified value of 14 mm. The highly nonlinear glass used for the fiber core enabled that the relatively strong DC asymmetry was balanced by pulses having only nanojoule energy. Based on our calculations presented in section 2.4.3, even picojoule-level control pulse energy should be sufficient for high contrast switching eliminating the walk-off between the signal and control pulses [9].

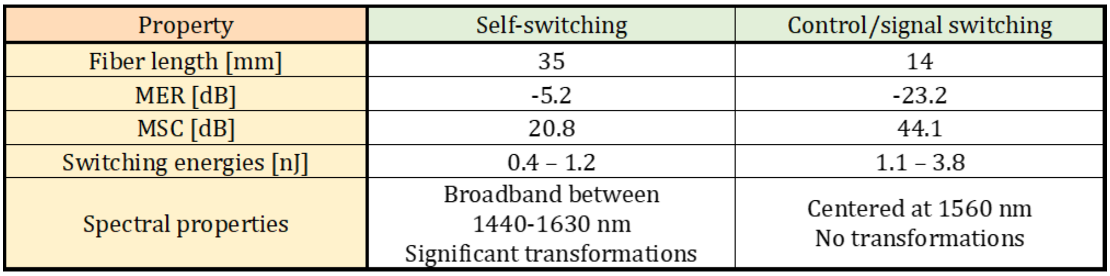

Property	Self-switching	Control/signal switching
Fiber length [mm]	35	14
MER [dB]	-5.2	-23.2
MSC [dB]	20.8	44.1
Switching energies [nJ]	0.4 – 1.2	1.1 – 3.8
Spectral properties	Broadband between 1440-1630 nm Significant transformations	Centered at 1560 nm No transformations

Table 4.2: *Fiber length dependence of the dual wavelength switching MER. A minimum of -23.4 dB MER was reached at 14 mm length of the used DCF.*

Table 4.2 resumes the main results of the switching performance using the two self-switching and cross switching approaches. It is evident that the control/signal-switching approach enables lower MERs (and consequently higher MSCs) than the self-switching one, with the advantage of using shorter DCFs. The higher optical asymmetry in the case of the control/signal approach is advantageous because ensures better SCs, keeping the signal pulse intensity of only few pJ (100 pJ in the case presented in chapter 4).

A systematic study to identify the optimal level of asymmetry should be performed in the future. It represents a motivation for further improvements of the numerical approach and the soft-glass DCF fabrication technology. Such efforts promise the demonstration of our novel all-optical switching scheme already in the picojoule energy range, meeting the standards of the optical communication systems and networking technology [291,292].

Another valuable future work is the XFROG diagnostics of the output field, both in case of self-switching and dual wavelength switching approach. I have already mentioned this strategy in section 3.4.3. With this method, it is possible to investigate in real-time the self-trapped solitonic propagation in DCFs at different fiber lengths. However, its realization is challenging in case of DCFs because the preliminary numerical simulations predicted the soliton self-trapping already at 20 pJ in-coupled pulse energies, which are very low to be detected with the apparatus presented in Fig.3.5. Therefore, another technique could be a pure spectral domain method based on interference. It was used already in the case of weak broadband pulses generated in PCFs [293]. Another possibility is to use femtosecond sources at longer wavelength than 1560 nm, for example at 1700 nm as, for the study of the second generation DCF presented in Fig.3.6a. The experimental results in Fig.3.19 and Fig.3.12 reveal that the establishment of the self-trapped solitonic propagation requires higher pulse energies (in the nJ range) with respect to shorter excitation wavelength at 1560 nm (sub-nJ range, as in Fig.3.12). Even so, the use of pulses with longer central wavelengths is more advantageous also from the point of view of elimination of the asymmetry effect, as I showed in section 3.4.

Regarding the dual wavelength switching approach presented in chapter 4, its main drawback is the relatively high energy of control pulses, which were at the level of few nanojoules. It is related to a relatively large control pulse duration than the one used during the self-switching experiments (270 fs vs 75-100 fs, respectively), and a temporal walk-off between the switching and control pulses. As mentioned in section 4.4, both the control pulse energy and duration can be minimized by improving the DC symmetry (which is also effective for the self-switching approach) and the synchronization between the two pulses. It means that the second generation DCF with improved DC symmetry (Fig.3.6a) is expected to allow the demonstration of even higher switching contrasts than the ones presented in chapter 4, with expected sub-nJ switching energies and reduced walk-off between control and signal pulses. Moreover, since the coupling length L_c depends strongly on the distance between the two cores, a redesigning of the DCF can be also potential for further reduction of the device length.

List of publications

Publications in peer-reviewed journals

1. M. Longobucco, I. Astrauskas, A. Pugžlys, N. T. Dang, D. Pysz, F. Uherek, A. Baltuška, R. Buczyński and I. Bugár. Complex study of solitonic ultrafast self-switching in slightly asymmetric dual-core fibers. *Applied Optics*, 60(32):10191-10198, 2021. **This manuscript was selected as an Editor's Pick, which highlights articles with excellent scientific quality and are representative of the work taking place in a specific field.**

2. M. Longobucco, I. Astrauskas, A. Pugžlys, N. T. Dang, D. Pysz, F. Uherek, A. Baltuška, R. Buczyński and I. Bugár. High contrast all-optical dual wavelength switching of femtosecond pulses in soft glass dual-core optical fiber. *Journal of Lightwave Technology*, 39(15):5111-5117, 2021.

3. M. Longobucco, J. Cimek, D. Pysz, R. Buczyński and I. Bugár. All-optical switching of ultrafast solitons at 1560 nm in dual-core fibers with high contrast of refractive index. *Optical Fiber Technology*, 63:102514, 2021.

4. V.H. Nguyen, L.X. The Tai, I. Bugar, M. Longobucco, R. Buczyński, B.A. Malomed and M. Trippenbach. Reversible ultrafast soliton switching in dual-core highly nonlinear optical fibers. *Optics Letters*, 45:5221-5224, 2020.

5. M. Longobucco, I. Astrauskas, A. Pugžlys, N. T. Dang, D. Pysz, F. Uherek, A. Baltuška, R. Buczyński and I. Bugár. Broadband self-switching of femtosecond pulses in highly nonlinear high index contrast dual-core fibre. *Optics Communications*, 472:126043, 2020.

6. M. Longobucco, P. Stajanča, L. Čurilla, R. Buczyński and I. Bugár. Applicable ultrafast all-optical switching by soliton self-trapping in high index contrast dual-core fibre. *Laser Physics Letters*, 17:025102, 2020.

7. M. Longobucco, J. Cimek, L. Čurilla, D. Pysz, R. Buczyński and I. Bugár. All-optical switching based on soliton self-trapping in dual-core high-contrast optical fibre. *Optical Fiber Technology*, 51:48–58, 2019.

Conference contributions

1. M. Longobucco, I. Astrauskas, A. Pugžlys, N. T. Dang, D. Pysz, F. Uherek, A. Baltuška, R. Buczyński and I. Bugár. Study of all-optical switching of 1560 nm femtosecond pulses using soft glass dual-core fibers. In *The sixth Workshop of Vietnamese Students in Poland - WVSP2021*, November 20-21, 2021 (ISBN 978-83-8084-738-5). Oral presentation given by M. Longobucco;

2. M. Longobucco, I. Astrauskas, A. Pugžlys, D. Pysz, F. Uherek, A. Baltuška, R. Buczyński and I. Bugár. Ultrafast All-Optical Two-Colour Switching in Asymmetric Dual-Core Fibre. In *2021 Conference on Lasers and Electro-Optics Europe and European Quantum Electronics Conference*, p. 1-1, paper cd_p_16, 2021. Poster presentation given by M. Longobucco;

3. M. Longobucco, I. Astrauskas, A. Pugžlys, D. Pysz, F. Uherek, A. Baltuška, R. Buczyński and I. Bugár. Self-Switching of Femtosecond Pulses in Highly Nonlinear Dual-Core Fibre. In *2020 IEEE Photonics Conference (IPC)*, pp. 1-4, 2020. Oral presentation given by M. Longobucco;

4. M. Longobucco, I. Astrauskas, A. Pugžlys, D. Pysz, F. Uherek, A. Baltuška, R. Buczyński and I. Bugár. High Contrast All-Optical Cross-Switching of C-band Femtosecond Pulses in Highly Nonlinear Soft Glass Dual Core Optical Fibre. In *2020 22nd International Conference on Transparent Optical Networks (ICTON)*, pp. 1-2, 2020. Oral presentation given by I. Bugár;

5. M. Longobucco, P. Stajanča, L. Čurilla, D. Pysz, R. Buczyński and I. Bugár. Applicable ultrafast all-optical switching by soliton self-trapping in high index contrast dual-core fiber. In *Integrated Optics - Sensors, Sensing Structures and Methods - IOS'2020*, February 24-28, 2020, Szczyrk, Poland. Oral presentation given by M. Longobucco;

6. M. Longobucco, I. Astrauskas, A. Pugžlys, D. Pysz, F. Uherek, A. Baltuška, R. Buczyński and I. Bugár. Experimental investigation of ultrafast solitonic all-optical switching in a high index contrast dual-core optical fiber. In *2019 Conference on Lasers and Electro-Optics Europe and European Quantum Electronics Conference*, OSA Technical Digest (Optical Society of America), paper cd_p_16, 2019. Poster presentation given by M. Longobucco;

7. M. Longobucco, I. Astrauskas, A. Pugžlys, D. Pysz, F. Uherek, A. Baltuška, R. Buczyński and I. Bugár. All-optical switching of ultrafast solitons in high-index contrast soft glass dual-core optical fibers. In *7th international conference on Advances in Electronic and Photonic Technologies - ADEPT 2019*, June 24-27, 2019, Štrbské Pleso, Slovak Republic. Oral presentation given by I. Bugár;

8. M. Longobucco, II. Astrauskas, A. Pugžlys, D. Pysz, F. Uherek, A. Baltuška, R. Buczyński and I. Bugár. All-optical switching of ultrafast solitons in high index contrast soft-glass dual-core optical fibers. In *14. výročný vedecký seminár Medzinárodného laserového centra Fotonika 2018*, February 7-8, 2019, Senec, Slovak Republic. Oral presentation given by I. Bugár;

9. M. Longobucco, I. Astrauskas, A. Pugžlys, D. Pysz, F. Uherek, A. Baltuška, R. Buczyński and I. Bugár. Controllable propagation of ultrafast solitons in high index contrast soft glass dual-core fiber. In *Optoelectronics and Photonics Winter School - NLP2019*, January 20-26, 2019, Andalo (Tn), Italy, P40 on 22 January 2019. Poster presentation given by M. Longobucco;

10. M. Longobucco, J. Cimek, D. Pysz, A. Baltuška, R. Buczyński and I. Bugár. Nonlinear propagation of femtosecond solitons in all-solid dual-core photonic crystal fibre optimized for all-optical switching applications. In *18th Conference on Optical Fibers and Their Applications - TAL 2018*, November 20-23, 2018, Nałęczów, Poland (invited). Oral presentation given by M. Longobucco;

11. I. Bugár, P. Stajanča, L. Čurilla, M. Longobucco, D. Pysz, F. Uherek, A. Baltuška and R. Buczyński. Ultrafast All-Optical Switching Using Dual-Core Photonic Crystal Fibers. In *The 21st Czech-Polish-Slovak Optical Conference On Wave and Quantum Aspects of Contemporary Optics*, September 3-7, 2018, Lednice, Czech Republic (invited). Oral presentation given by I. Bugár;

12. M. Longobucco, J. Cimek, L. Čurilla, D. Pysz, R. Buczyński and I. Bugár. Development of an all-solid dual-core photonic crystal fibre for all-optical switching applications. In *OSA Siegman International Summer School on lasers*, July 28 - August 4, 2018, island of Hven, Sweden. Poster presentation given by M. Longobucco.

13. M. Longobucco, J. Cimek, L. Curilla, D. Pysz, R. Buczynski and I. Bugar. Development of an All-Solid Dual-Core Photonic Crystal Fibre for All-Optical Switching Applications. In *2018 20nd International Conference on Transparent Optical Networks (ICTON)* pp. 1–4, 2018. Poster presentation given by M. Longobucco. **This poster was awarded with Student Poster Prize from ICTON 2018 scientific committee**;

14. I. Bugar, M. Longobucco, J. Cimek, L. Curilla, D. Pysz and R. Buczynski. Ultrafast All-Optical Switching Using All-Solid Dual-Core Photonic Crystal Fiber. In *2018 20nd International Conference on Transparent Optical Networks (ICTON)* pp. 1–4, 2018. Oral presentation given by I. Bugár.

Acknowledgments

In these final pages, I would like to express my gratitude to all the people who contribute to the conclusion of my Ph.D. studies and the realization of this dissertation. First, I would like to express my sincere gratitude to my supervisor, prof. dr hab. inż. Ryszard Buczyński, for giving me the opportunity to start a new phase of my scientific carrier and join the field of fiber optics and photonics. I would like to thank him for his constant support, motivation and fruitful advice, as well to have given me the opportunity to join his group at FUW and Ł-IMIF, full of motivated and smart researchers. I am particularly thankful to my assistant supervisor, dr Ignác Bugár, whose constant and kind assistance was absolutely fundamental for the realization of this work. I greatly appreciate the knowledge and skills that he imparted me not only about dual-core fibers, but also on optics experiments and instrumentation. I am especially thankful for his commendable patience and all-out support through these four years, and for being always present in the most crucial parts of my Ph.D. studies.

I would like to spend a few words of gratitude for the group at PI-TUW. A significant part of the experimental results chapter would not be possible without the support and help of the people working at the Photonic Institute. In particular, my greetings are for prof. Andrius Baltuška, for giving me the opportunity to join his group at PI-TUW several times and for his precious advice during the experiments there, Dr. Audrius Pugžlys, for his constant presence and support at PI-TUW and his assistance during manuscript preparation and revisions, and prof. Evgeni Sorokin, for giving me access to his lab space at PI-TUW. My warmful gratitude goes to Ph.D. Ignas Astrauskas, for his unlimited patience, his constant support and precious help with the laser and OPA, which were essential for the successful realization of my experiments in the lab at PI-TUW.

I would to thank all of my Ph.D. student colleagues and friends for creating a positive, enriching - and also multicultural - atmosphere during my Ph.D. studies and everyday life in Warsaw. My gratitude goes to Anupamaa (Anu), for her positive attitude, determination and patience, especially while sharing the Menlo laser with me at Ł-IMIF and IChF, and her spirit of initiative; Damian, for helping with Lumerical software, for being a supportive companion at Ł-IMIF and also at the squash court, for his hospitality in his hometown and his help with my apartment, and for being the political and diplomatic member of the group; Dominik Dobrakowski, for his never-ending patience and kindness, his support with Comsol and with my application for PRELUDIUM 17 project, and for being always classy and polite with everybody indistinctly; Hoang (Vitek), for his positive attitude to life, for his enthusiasm and desire to learn something new about fibers and optics, for his hilariousness and lightheartedness, and for being always in contact with me even if he is in France now; Hue Thi Nguyen (Lily), for being always present and supporting in every moment of my life here in Poland, for being hard working with a positive and sweet energy, for the long working nights at FUW together, for introducing me her family and Vietnamese cultural habits and for the good and healthy table tennis matches and cycling tours around Warsaw; Dang (Nhat), for your assistance in the lab during my experiments, for your kindness and for your company during my walks through Warsaw; Paweł, for helping me with Polish language and being immediately part of the group even if he joined Ł-IMIF just recently; Przemesław (Przemek), for being my hug dispenser, for our discussions and funny moments at Ł-IMIF, for introducing me every day to the world of glass synthesis, for your sincerity and for your family-caring attitude; Xuan (Tai), for your calmness, for your frequent updates, Skype calls and help in my last months new project and for being part of our group even if you are not formally; Tanvi, for being my psychological supporter during my down moments during my Ph.D., for your strong character and determination, for our long discussions at FUW and for introducing me to Indian culture, as well as to the craziest Indian group in town; Xavier, for your energy and help in setting myself up in my early days at Ł-IMIF and in Warsaw.

I would like to express my sincere thanks to all the postdocs in my group for their support and sincere help in these years: dr Adam Filipkowski, Alicja Anuszkiewicz, Grzegorz Stępniewski (Grześ) and Marcin Franczyk. Particular thanks go to dr Jarosław Cimek (Jarek) for his wise knowledge on glass materials and their fabrication process, and dr Tomasz (Tomek) Stefaniuk, for his assistance and training with Matlab and Lumerical at the beginning of my Ph.D. studies. I would express my regards to dr inż. Dariusz Pysz for his support and expertise on the fabrication process of nanostructured fibers at Ł-IMIF. Moreover, I would like to thank dr Rafał Kasztelanic for his frequent help with Matlab and his wise programming skills, and dr Mariusz Klimczak, for setting up my work at IChF, his assistance in the labs at FUW and for helping me in the writing of this dissertation. Many thanks go also to mgr Anna Haraśna and mgr Katarzyna Dyl (Kasia) for their important help with the administration and documents at Ł-IMIF and FUW, respectively.

Finally, I would like to express my gratitude to my family, who supported my Ph.D. studies from long distance and never allowed the spirit of Cuncuardia (my hometown) to abandon me. I would like to dedicate this dissertation to my dad Antonio (Little Tony Nice): I apologize myself for understanding your value in my life and how much you love me just recently, this work is a small reward to you as well. I thank also my mum Annabruna (Brown), for her support and dedication in my life, for being proud of me in spite of everything, and for her strong character. My warmful greetings go to my sister Ilaria (Lalla) too, for being the guiding spirit of the family, for her constant psychological support, her positive attitude to life and free spirit, and for her precious help with my health issues. A sweet regard goes as well to my niece Amrita, for our funny moments together and her wonderful smile which shines even from long distance, and to her daddy Fausto, for his integrity, attachment to family and dedication to work.

I would like to express my gratitude also to all my remaining - but not less important - relatives. I am particularly grateful to my cousins Martina and Sean (Martiszon) for being so helpful with me during my first phases of transfer from Italy to Warsaw and during the entire four years spent here in Poland. I will never forget our time and discussions together, the warm - and multilingual - family atmosphere, the long and funny game moments with Kilian and Matteo and the immense support and hospitality they reserve to me. The successful realization of this work is mainly due to them. Many thanks go to aunts and uncles Melina/Lucio and Mirka/Franco, and all my cousins - especially Angela from Altamura -, for always being in touch with me and for your sweet support.

At the end, I would like to thank all my secondary-school and university friends from Portogruaro and Milan, respectively. I have already written my specific greetings to them in my Master's thesis, my feelings for them haven't changed since then. Special greetings go to all the new friends I met in Warsaw, in conferences, winter and summer schools around the world.

And of course thank you to my brother Federico and all my relatives that are not here with us in this world anymore. I can feel your presence in my everyday life, and I can't help but be grateful for that.

Dziękuję Wszystkim serdecznie, będę Wam wdzięczny na zawsze!

With my best greetings and feelings to all of you,

Mattia Longobucco

APPENDIX A

The Split-Step Fourier method

The split-step Fourier method (SSFM) is the most common approach to solve GNLSE because it involves only linear operators in both temporal and spectral domain. It is advantageous for practical implementation reasons and fast computational speeds. The losses, propagation constant and coupling coefficient are applied always at one single frequency step by multiplying a single number for each component of the signal at given frequency. This means that it considers the whole spectral behavior of the linear parameters of the equations. However, the computation of the nonlinear part is performed in the time domain.

Therefore, SSFM is based on the assumption that the linear and nonlinear parts of the GNLSE can be evaluated separately in their respective domains and then combined together to reach a final solution of the equation. It involves the use of the Fast-Fourier transform (FFT) algorithm utilized in order to operate an efficient exchange between the two domains. In order to keep the pulse in the defined temporal window, the retarded time frame $T = t - \beta_1 z$ is used, the same as the one defined for the GNLSE expression in Eq.1.1. First, we introduce the SSFM concept in the simpler case of single-core fiber. Then, we extend the model for the more complicated DCF case.

A.1 SSFM for single-core GNLSE

We start from the GNLSE in Eq.(1.47) and defined the linear dispersion $\hat{D}$ and the nonlinear $\hat{N}$ operators in this way:

$$\hat{D} = -\frac{\alpha(\omega_0)}{2} + \sum_{p\geq 2} \frac{i^{p+1}}{p!}\beta_p(\omega_0)\frac{\partial^p}{\partial T^p} \tag{A.1}$$

$$\hat{D} = i\gamma(\omega_0)\left(1 + i\tau_{\text{shk}}\frac{\partial}{\partial T}\right)\left[\int_{-\infty}^{+\infty} R(T') \times |A(z, T - T')|^2 dT'\right]. \tag{A.2}$$

$\hat{D}$ and $\hat{N}$ are not-commuting operators. All the other parameters have been already introduced in Section 1.3.2. In the frame of the SSFM, the GNLSE in Eq.(1.47) can be written as a function of the sum of the two operators as

$$\frac{\partial A}{\partial z} = (\hat{D} + \hat{N})A \tag{A.3}$$

If the step size l along the propagation direction z is sufficiently small, $\hat{N}$ can be considered constant and the one-step solution of Eq.(A.3) is

$$A(z_0 + l) = \exp[(\hat{D} + \hat{N})l]A(z_0) \tag{A.4}$$

We can decompose this solution into three separate steps in such way:

$$A(z_0 + l) = \exp\left(\hat{D}\frac{l}{2}\right)\exp(\hat{N}l)\exp\left(\hat{D}\frac{l}{2}\right)A(z_0) \tag{A.5}$$

First, the linear half-step is calculated in the spectral domain. Then, the partial solution is transferred to the time domain using the FFT algorithm and the nonlinear step is calculated. At the end, the solution is transferred back to the spectral domain and the second linear half-step is applied. In order to improve the accuracy of the solution, the nonlinear operator $\hat{N}$ may take the integral form instead of being constant along the step l. The solution takes this form:

$$A(z_0 + l) = \exp\left(\hat{D}\frac{l}{2}\right)\exp\left(\int_{z_0}^{z_0+l} \hat{N}dz\right)\exp\left(\hat{D}\frac{l}{2}\right)A(z_0) \tag{A.6}$$

To ensure the stability of the algorithm and acceptable computation times, the integration of nonlinear step was performed with the second-order Runge-Kutta method [140]. We chose the span of the temporal and spectral window (T_{span} and F_{span}, respectively) to respect the Nyquist sampling theorem, This means to satisfy the relation $T_{\text{span}}F_{\text{span}} = N$, where N is the number of discretization points.

A.2 SSFM for CGNLSE

CGNLSE in Eq.1.82 and 1.83 can be written in the operator form in this way:

$$\partial\partial A(z, T)\partial z = \hat{M}A(z, T) \tag{A.7}$$

$A(z, T)$ and $\hat{M}$ can be defined as a column vector and a matrix operator, respectively:

$$A(z, T) = \begin{bmatrix} A_1(z, T) \\ A_2(z, T) \end{bmatrix} \tag{A.8}$$

$$\hat{M} = \hat{L} + \hat{N} = \begin{bmatrix} \hat{D}_1 & \hat{C}_1 \\ \hat{C}_2 & \hat{D}_2 \end{bmatrix} + \begin{bmatrix} \hat{N}_1 & 0 \\ 0 & \hat{N}_2 \end{bmatrix} = \begin{bmatrix} \hat{D}_1 + \hat{N}_1 & 0 \\ 0 & \hat{D}_2 + \hat{N}_2 \end{bmatrix} \tag{A.9}$$

The individual dispersion $\hat{D}_m$, coupling $\hat{D}_m$ and nonlinear $\hat{N}_m$ operators for m-th fiber core are in our case defined in this way:

$$\hat{D}_m = i(-1)^{m+1}\delta_0 + (-1)^m\delta_1\frac{\partial}{\partial T} - \frac{1}{2}\sum_{o\geq 0}\frac{i^o}{o!}\alpha_o^{(m)}\frac{\partial^o}{\partial T^o} + \sum_{p\geq 2}\frac{i^{p+1}}{p!}\beta_p^{(m)}\frac{\partial^p}{\partial T^p} \quad \text{(A.10)}$$

$$\hat{C}_m = \sum_{q\geq 0}\frac{i^{q+1}}{q!}k_q^{(m,3-m)}\frac{\partial^q}{\partial T^q} \quad \text{(A.11)}$$

$$\hat{N}_m = i\gamma^{(m)}\left[\left(1 + i{\tau_{\text{shk}}}^{(m)}\frac{\partial}{\partial T}\right)\int_{-\infty}^{+\infty} R(T') \times |A_m(z, T-T')|^2 dT' + \sigma^{(m)}|A_{3-m}|^2\right]. \quad \text{(A.12)}$$

The composition of the one-step solution is performed as for the single-core case:

$$A(z_0 + l, T) = \exp\hat{M}lA(z_0, T) \approx \exp\left(\hat{L}\frac{l}{2}\right)\exp(\hat{N}l)\exp\left(\hat{L}\frac{l}{2}\right)A(z_0, T) \quad \text{(A.13)}$$

The expansion to the second order yields to

$$\exp\hat{M}l \approx \begin{bmatrix}1 & 0\\ 0 & 1\end{bmatrix} + \begin{bmatrix}\hat{D}_1 + \hat{N}_1 & 0\\ 0 & \hat{D}_2 + \hat{N}_2\end{bmatrix} l + \quad \text{(A.14)}$$

$$+\frac{1}{2}\begin{bmatrix}\hat{D}_1^{\,2} + \hat{D}_1\hat{N}_1 + \hat{N}_1\hat{D}_1 + \hat{N}_1^{\,2} + \hat{C}_1\hat{C}_2 & \hat{D}_1\hat{C}_1 + \hat{C}_1\hat{D}_2 + \hat{C}_1\hat{N}_2 + \hat{N}_1\hat{C}_1\\ \hat{D}_1\hat{C}_2 + \hat{C}_2\hat{D}_2 + \hat{C}_2\hat{N}_1 + \hat{N}_2\hat{C}_2 & \hat{D}_2^{\,2} + \hat{D}_2\hat{N}_2 + \hat{N}_2\hat{D}_2 + \hat{N}_2^{\,2} + \hat{C}_2\hat{C}_1\end{bmatrix}$$

The diagonal elements in the second-order term show the intensity distribution, the coupling affects and also the dispersion of individual cores (through $\hat{C}_2\hat{C}_1$ and $\hat{C}_2\hat{C}_1$ terms). As said in the previous section, the fiber guiding characteristics and parameters, which are indispensable to implement the CGNLSEs-based model, are obtained by means of an eigenmode analysis with the help of commercial eigenmode solver (Mode Solutions’ Lumerical). Namely, the required parameters are the loss coefficient $\alpha^{(m)}(\omega)$, the propagation constant $\beta^{(m)}(\omega)$, the coupling coefficient $k^{(m,3-m)}(\omega)$, the effective mode area ${A_{\text{eff}}}^{(m)}(\omega)$, the XPM coefficient of the m-th core $\sigma^{(m)}(\omega)$ and propagation constants of the DC structure supermodes $\beta_S^{(m)}(\omega)$ and $\beta_A^{(m)}(\omega)$.

List of acronyms

Ł-IMIF	Łukasiewicz - Institute of Microelectronics & Photonics. IX–XII, XVI, XVII, 48, 49, 52, 81–83, 86, 97, 116, 131, 139, 140, 154, 155
ER	Extinction ratio. 69, 71, 75, 80, 98, 99, 105, 111, 112, 121, 122, 124, 125, 130, 156, 157
B-DW	Blue-shifted dispersive waves. 19–21, 31, 151
BBO	Barium borate. 108
CCD	Charge-coupled device. 97
CFWM	Cascaded four-wave mixing. 19, 20
CGNLSE	Coupled generalized nonlinear Schrödinger equation. IX, X, XII, XVI, XIX, 34–36, 46, 58, 66, 67, 92, 97, 130, 144, 145
CL	Coupling length. XIX, 28–32, 36, 40–44, 46, 47, 56, 57, 61, 62, 64, 65, 67, 68, 73, 74, 76, 77, 79, 88, 90, 93–95, 98, 102, 107, 108, 117, 127, 129, 152, 153, 155, 156
CME	Coupled-mode equations. 26–29, 31, 33, 34
CMT	Coupled-mode theory. 26, 29, 40
CW	Continuous wave. 2, 6–8, 27, 28, 31–34, 36, 37, 51, 151
DC	Dual-core. VIII, X–XIII, XV–XVII, XIX, 26–30, 32, 33, 35, 37, 39, 42, 44, 47–52, 57, 58, 61, 62, 67, 69, 72, 73, 76, 79–81, 83–94, 96–98, 101, 104–110, 112–114, 116–123, 125–127, 129–133, 145, 151–158

DCF	Dual-core fiber. VIII–XIX, 10, 22, 24–26, 30–34, 40–55, 57, 62–67, 72–76, 78–101, 103–111, 113–122, 125–127, 129–133, 143, 151–159
DW	Dispersive wave. 19–21, 38
FF	Filling factor. 58–60, 62–64, 153
FFT	Fast Fourier transform. 143, 144
FOD	Forth-order dispersion. 14, 15
FUW	Faculty of Physics - University of Warsaw. IX, X, XII, XVII, 49, 139, 140
FWHM	Full width at half-maximum. 6
GNLSE	Generalized nonlinear Schrödinger equation. XIX, 2, 13–15, 17, 22, 23, 34, 35, 66, 143–145
GVD	Group velocity dispersion. 4, 8, 10, 11, 14, 16, 18, 20, 23, 24, 31, 33, 38, 46, 61, 67
IE	In-coupling efficiency. 26, 63, 65, 66, 75, 79, 92, 95, 96, 98, 104, 109, 113, 115, 125, 131, 155
IMD	Intermodal dispersion. 40, 41, 43
LCNLSE	Linearly coupled nonlinear Schrödinger equation. 100, 116
MER	Minimal extinction ratio. 99, 103, 104, 109–111, 114, 118, 125, 127, 131, 132, 156, 159
MI	Modulation instability. XVIII, 2, 6, 8, 15
MSC	Maximal switching contrast. 50, 103–105, 110, 111, 114, 131, 132
NCN	National Science Centre of Poland. IX
NIR	Near-infrared. IX, 3, 12, 66, 116, 129
NLDC	Nonlinear directional coupler. X, XII, XIV–XVI, 24, 25, 33, 34, 36, 37, 40, 42, 43, 47, 48, 51, 54, 113–115, 151
NLSE	Nonlinear Schrödinger equation. 2, 8, 11, 100
NOLM	Nonlinear optical loop mirror. XIV, 119
OPA	Optical parametric amplifier. IX, XIII, 108, 112, 113, 115, 119, 126, 139

PCF	Photonic crystal fiber. VIII, IX, XII, XV, XVI, XIX, 13, 39, 43, 46–52, 57–73, 75, 79, 80, 83, 90, 91, 96, 97, 106, 113, 129–131, 133, 152–154, 158
PI-TUW	Photonic Institute - Technische Universität Wien. IX–XI, XIII, XVII, 49, 139
R-DW	Red-shifted dispersive waves. 19, 21, 151
RIFS	Raman-induced frequency shift. 17, 18, 150
SC	Switching contrast. 50, 67, 70, 72, 73, 76–81, 90, 99, 105, 106, 109–118, 121, 122, 124–126, 130–132, 154, 156, 158
SEM	Scanning electron microscope. 82–87, 97, 98, 101, 107, 110, 121, 154–156
SPM	Self-phase modulation. 5, 6, 8, 10, 11, 16, 18, 23, 31–33, 38, 44, 126
SRS	Stimulated Raman scattering. 15–18, 21–24, 38, 39, 45, 66–68, 100, 103, 150, 152
SS	Switching step. 18, 103, 104, 106, 110–116, 131
SSFM	Split-step Fourier method. XIX, 143–145
SST	Self-steepening. 18, 21, 23, 24, 35, 37, 38, 45, 46, 66–68, 100, 103, 151
TOD	Third-order dispersion. 4, 13–15, 18, 19, 21–23, 37–39, 56, 58–60, 63–65, 67, 68, 70, 72, 100, 103, 106, 109, 130, 152
XFROG	Cross frequency-resolved optical gating. 113, 133
XPM	Cross-phase modulation. 20, 31, 35, 66, 67, 145
ZDW	Zero-dispersion wavelength. 14, 15, 19–21, 151

List of Figures

List of Tables

Bibliography

[1] A. Betlej, S. Suntsov, K. G. Makris, L. Jankovic, D. N. Christodoulides, G. I. Stegeman, J. Fini, R. T. Bise, and D. J. DiGiovanni. All-optical switching and multifrequency generation in a dual-core photonic crystal fiber. *Opt. Lett.*, 31(10):1480–1482, May 2006.

[2] P. Stajanca and I. Bugar. Nonlinear ultrafast switching based on soliton self-trapping in dual-core photonic crystal fibre. *Laser Phys. Lett.*, 13(11):116201, 2016.

[3] L. Curilla, I. Astrauskas, A. Pugzlys, P. Stajanca, D. Pysz, F. Uherek, A. Baltuska, and I. Bugar. Nonlinear performance of asymmetric coupler based on dual-core photonic crystal fiber: Towards sub-nanojoule solitonic ultrafast all-optical switching. *Opt. Fiber Technol.*, 42:39 – 49, 2018.

[4] M. Koys, I. Bugar, I. Hrebikova, V. Mesaros, R. Buczynski, and F. Uherek. Spectral switching control of ultrafast pulses in dual core photonic crystal fibre. *J. Eur. Opt. Soc.*, 8(0), 2013.

[5] P. Stajanca, D. Pysz, G. Andriukaitis, T. Balciunas, G. Fan, A. Baltuska, and I. Bugar. Ultrafast multi-wavelength switch based on dynamics of spectrally-shifted solitons in a dual-core photonic crystal fiber. *Opt. Express*, 22(25):31092–31101, Dec 2014.

[6] M. Longobucco, P. Stajanča, L. Čurilla, R. Buczyński, and I. Bugár. Applicable ultrafast all-optical switching by soliton self-trapping in high index contrast dual-core fibre. *Laser Phys. Lett.*, 17:025102, 2020.

[7] M. Longobucco, J. Cimek, L. Curilla, D. Pysz, R. Buczyński, and I. Bugar. Development of an all-solid dual-core photonic crystal fibre for all-optical switching applications. In *2018 20th International Conference on Transparent Optical Networks (ICTON)*, pages 1–4, 2018.

[8] I. Bugar, M. Longobucco, J. Cimek, L. Curilla, D. Pysz, and R. Buczynski. Ultrafast all-optical switching using all-solid dual-core photonic crystal fiber. In *2018 20th International Conference on Transparent Optical Networks (ICTON)*, pages 1–4, 2018.

[9] M. Longobucco, J. Cimek, L. Čurilla, D. Pysz, R. Buczyński, and I. Bugár. All-optical switching based on soliton self-trapping in dual-core high-contrast optical fibre. *Opt. Fiber Technol.*, 51:48–58, 2019.

[10] M. Longobucco, J. Cimek, D. Pysz, R. Buczyński, and I. Bugár. All-optical switching of ultrafast solitons at 1560 nm in dual-core fibers with high contrast of refractive index. *Opt. Fiber Technol.*, 63:102514, 2021.

[11] V. H. Nguyen, L. X. T. Tai, I. Bugar, M. Longobucco, R. Buczyński, B. A. Malomed, and M. Trippenbach. Reversible ultrafast soliton switching in dual-core highly nonlinear optical fibers. *Opt. Lett.*, 45(18):5221–5224, Sep 2020.

[12] M. Longobucco, I. Astrauskas, A. Pugžlys, N. T. Dang, D. Pysz, F. Uherek, A. Baltuška, R. Buczyński, and I. Bugár. Complex study of solitonic ultrafast self-switching in slightly asymmetric dual-core fibers. *Appl. Opt.*, 60(32):10191–10198, Nov 2021.

[13] M. Longobucco, I. Astrauskas, A. Pugžlys, D. Pysz, F. Uherek, A. Baltuška, R. Buczyński, and I. Bugár. Broadband self-switching of femtosecond pulses in highly nonlinear high index contrast dual-core fibre. *Opt. Commun.*, 472:126043, 2020.

[14] M. Longobucco, I. Astrauskas, A. Pugžlys, D. Pysz, F. Uherek, A. Baltuška, R. Buczyński, and I. Bugár. High contrast all-optical dual wavelength switching of femtosecond pulses in soft glass dual-core optical fiber. *J. Lightwave Technol.*, 39(15):5111–5117, 2021.

[15] A. E. Willner, S. Khaleghi, M. R. Chitgarha, and O. F. Yilmaz. All-optical signal processing. *J. Lightwave Technol.*, 32(4):660–680, 2014.

[16] E. Agrell, M. Karlsson, A. R. Chraplyvy, D. J. Richardson, P. M. Krummrich, P. Winzer, K. Roberts, J. K. Fischer, S. J Savory, B. J. Eggleton, M. Secondini, F. R. Kschischang, A. Lord, J. Prat, I. Tomkos, J. E. Bowers, S. Srinivasan, M. Brandt-Pearce, and N. Gisin. Roadmap of optical communications. *J. Opt.*, 18(6):063002, 2016.

[17] O. Melchert, C. Brée, A. Tajalli, A. Pape, R. Arkhipov, S. Willms, I. Babushkin, D. Skryabin, G. Steinmeyer, U. Morgner, and A. Demircan. All-optical supercontinuum switching. *Commun. Phys.*, 3:146, 2020.

[18] J. Li, B.-E. Olsson, M. Karlsson, and P. A. Andrekson. Otdm add-drop multiplexer based on xpm-induced wavelength shifting in highly nonlinear fiber. *J. Lightwave Technol.*, 23(9):2654, Sep 2005.

[19] Jie Li, B. . Olsson, M. Karlsson, and P. A. Andrekson. Otdm demultiplexer based on xpm-induced wavelength shifting in highly nonlinear fiber. *IEEE Photon. Technol. Lett.*, 15(12):1770–1772, 2003.

[20] A. W. Brown and M. Xiao. All-optical switching and routing based on an electromagnetically induced absorption grating. *Opt. Lett.*, 30(7):699–701, Apr 2005.

[21] M. Saruwatari. All-optical signal processing for terabit/second optical transmission. *IEEE J. Sel. Top. Quantum Electron.*, 6(6):1363–1374, 2000.

[22] A. Rostami, H. B. A. Nejad, R. M. Qartavol, and H. R. Saghai. Tb/s optical logic gates based on quantum-dot semiconductor optical amplifiers. *IEEE J. Quantum Electron.*, 46(3):354–360, 2010.

[23] D. Solli and B. Jalali. Analog optical computing. *Nat. Photonics*, 9:704–706, 2015.

[24] J. N. Roy and D. Kumar Gayen. Integrated all-optical logic and arithmetic operations with the help of a toad-based interferometer device–alternative approach. *Appl. Opt.*, 46(22):5304–5310, Aug 2007.

[25] Z. Li, Z. Chen, and B. Li. Optical pulse controlled all-optical logic gates in sige/si multimode interference. *Opt. Express*, 13(3):1033–1038, Feb 2005.

[26] Q. Li, J. Song, X. Chen, M. Bi, M. Hu, and S. Li. All-optical logic gates based on cross phase modulation effect in a phase-shifted grating. *Appl. Opt.*, 55(25):6880–6886, Sep 2016.

[27] Y. Song, Y. Chen, X. Jiang, W. Liang, K. Wang, Z. Liang, Y. Ge, F. Zhang, L. Wu, J. Zheng, J. Ji, and H. Zhang. Nonlinear few-layer antimonene-based all-optical signal processing: Ultrafast optical switching and high-speed wavelength conversion. *Adv. Opt. Mater.*, 6(13):1701287, 2018.

[28] H. J. S. Dorren, M. T. Hill, Y. Liu, N. Calabretta, A. Srivatsa, F. M. Huijskens, H. de Waardt, and G. D. Khoe. Optical packet switching and buffering by using all-optical signal processing methods. *J. Lightwave Technol.*, 21(1):2, Jan 2003.

[29] H. Jia, T. Zhou, L. Zhang, J. Ding, X. Fu, and L. Yang. Optical switch compatible with wavelength division multiplexing and mode division multiplexing for photonic networks-on-chip. *Opt. Express*, 25(17):20698–20707, Aug 2017.

[30] W. Miao, F. Yan, and N. Calabretta. Towards petabit/s all-optical flat data center networks based on wdm optical cross-connect switches with flow control. *J. Lightwave Technol.*, 34(17):4066–4075, Sep 2016.

[31] Chunfei Li. *All-Optical Switch Based on Nonlinear Optics*, pages 279–386. Springer Singapore, Singapore, 2017.

[32] W. Yoshiki and T. Tanabe. All-optical switching using kerr effect in a silica toroid microcavity. *Opt. Express*, 22(20):24332–24341, Oct 2014.

[33] K. Kieu, L. Schneebeli, E. Merzlyak, J. M. Hales, A. DeSimone, J. W. Perry, R. A. Norwood, and N. Peyghambarian. All-optical switching based on inverse raman scattering in liquid-core optical fibers. *Opt. Lett.*, 37(5):942–944, Mar 2012.

[34] Yang Zhao. All-optical power-controlled switching in four-wave mixing. *Opt. Lett.*, 14(19):1085–1087, Oct 1989.

[35] S. Trillo and S. Wabnitz. Nonlinear nonreciprocity in a coherent mismatched directional coupler. *Appl. Phys. Lett.*, 49(13):752–754, 1986.

[36] K. Wysokiński, D. Budnicki, J. Fidelus, Ł. Szostkiewicz, Ł. Ostrowski, M. Murawski, M. Staniszewski, M. Staniszewska, M. Napierała, and T. Nasiłowski. Dual-core all-fiber integrated immunosensor for detection of protein antigens. *Biosens. Bioelectron.*, 114:22–29, 2018.

[37] V. Ribeiro, M. Karlsson, and P. Andrekson. Parametric amplification with a dual-core fiber. *Opt. Express*, 25(6):6234–6243, Mar 2017.

[38] Z. Lian, P. Horak, X. Feng, L. Xiao, K. Frampton, N. White, J. A. Tucknott, H. Rutt, D. N. Payne, W. Stewart, and W. H. Loh. Nanomechanical optical fiber. *Opt. Express*, 20(28):29386–29394, Dec 2012.

[39] M. Papaioannou, E. Plum, J. Valente, E. T. F. Rogers, and N. I. Zheludev. All-optical multichannel logic based on coherent perfect absorption in a plasmonic metamaterial. *APL Photonics*, 1(9):090801, 2016.

[40] S.-P. Su, C.-L. Wu, C.-H. Cheng, B.-J. Huang, H.-Y. Wang, C.-T. Tsai, Y.-H. Lin, Y.-C. Chi, M.-H. Shih, C.-K. Lee, and G.-R. Lin. Nonstoichiometric sic bus/ring waveguide based all-optical data format follower and inverter. *ACS Photonics*, 3(5):806–818, 2016.

[41] M. Ono, M. Hata, M. Tsunekawa, K. Nozaki, H. Sumikura, H. Chiba, and M. Notomi. Ultrafast and energy-efficient all-optical switching with graphene-loaded deep-subwavelength plasmonic waveguides. *Nat. Photonics*, 14:37–43, 2020.

[42] T. Hirooka, R. Hirata, J. Wang, M. Yoshida, and M. Nakazawa. Single-channel 10.2 tbit/s (2.56 tbaud) optical nyquist pulse transmission over 300 km. *Opt. Express*, 26(21):27221–27236, Oct 2018.

[43] S. R. Friberg, A. M. Weiner, Y. Silberberg, B. G. Sfez, and P. S. Smith. Femotosecond switching in a dual-core-fiber nonlinear coupler. *Opt. Lett.*, 13(10):904–906, Oct 1988.

[44] S. Trillo, S. Wabnitz, E. M. Wright, and G. I. Stegeman. Soliton switching in fiber nonlinear directional couplers. *Opt. Lett.*, 13(8):672–674, Aug 1988.

[45] S.K. Turitsyn. Spatial dispersion of nonlinearity and stability of multidimensional solitons. *Theor. Math. Phys.*, 64:797–801, 1985.

[46] D. Mihalache, D. Mazilu, F. Lederer, Y. V. Kartashov, L.-C. Crasovan, and L. Torner. Stable three-dimensional spatiotemporal solitons in a two-dimensional photonic lattice. *Phys. Rev. E*, 70:055603, Nov 2004.

[47] L. F. Mollenauer, S. G. Evangelides, and H. A. Haus. Long-distance soliton propagation using lumped amplifiers and dispersion shifted fiber. *J. Lightwave Technol.*, 9(2):194–197, 1991.

[48] S. Gatz and J. Herrmann. Soliton propagation and soliton collision in double-doped fibers with a non-kerr-like nonlinear refractive-index change. *Opt. Lett.*, 17(7):484–486, Apr 1992.

[49] H. Ghafouri-Shiraz, P. Shum, and M. Nagata. A novel method for analysis of soliton propagation in optical fibers. *IEEE J. Quantum Electron.*, 31(1):190–200, 1995.

[50] S. Kumar and A. Hasegawa. Quasi-soliton propagation in dispersion-managed optical fibers. *Opt. Lett.*, 22(6):372–374, Mar 1997.

[51] N. N. Akhmediev and A. V. Buryak. Soliton states and bifurcation phenomena in three-core nonlinear fiber couplers. *J. Opt. Soc. Am. B*, 11(5):804–809, May 1994.

[52] S. L. Doty, J. W. Haus, YunJe Oh, and R. L. Fork. Soliton interactions on dual-core fibers. *Phys. Rev. E*, 51:709–717, Jan 1995.

[53] A.V. Buryak and N.N. Akhmediev. Stationary pulse propagation in n-core nonlinear fiber arrays. *IEEE J. Quantum Electron.*, 31(4):682–688, 1995.

[54] J. Knight. Photonic crystal fibers. *Nature*, 424(6):847–851, 2003.

[55] P. Russell. Photonic crystal fibers. *Science*, 299(5605):358–362, 2003.

[56] J.R.R. Sousa, A.F.G.F. Filho, A.C. Ferreira, G.S. Batista, C.S. Sobrinho, A.M. Bastos, M.L. Lyra, and A.S.B. Sombra. Generation of logic gates based on a photonic crystal fiber michelson interferometer. *Opt. Commun.*, 322:143–149, 2014.

[57] G.S.B. Filho, D.G. Correia, W.B. de Fraga, and G.F. Guimarães. Obtaining optical logic gates – or, xor, and and logic functions using asymmetric mach-zehnder interferometer based on photonic crystal fiber. *Opt. Laser Technol.*, 97:370–378, 2017.

[58] T. Uthayakumar and R. Vasantha Jayakantha Raja. Logic gates based all-optical binary half adder using triple core photonic crystal fiber. *J. Opt.*, 20:065503, 2018.

[59] A. G. Coelho Jr., M. B. C. Costa, A. C. Ferreira, M. G. da Silva, M. L. Lyra, and A. S. B. Sombra. Realization of all-optical logic gates in a triangular triple-core photonic crystal fiber. *J. Lightwave Technol.*, 31(5):731–739, Mar 2013.

[60] M. Vieweg, S. Pricking, T. Gissibl, Y. V. Kartashov, L. Torner, and H. Giessen. Tunable ultrafast nonlinear optofluidic coupler. *Opt. Lett.*, 37(6):1058–1060, Mar 2012.

[61] A. K. Sarma. Soliton switching in a highly nonlinear dual-core holey fiber coupler. *Jpn. J. Appl. Phys.*, 47:5493, 2008.

[62] R. Y. Chiao, E. Garmire, and C. H. Townes. Self-trapping of optical beams. *Phys. Rev. Lett.*, 13:479–482, Oct 1964.

[63] S. Minardi, F. Eilenberger, Y. V. Kartashov, A. Szameit, U. Röpke, J. Kobelke, K. Schuster, H. Bartelt, S. Nolte, L. Torner, F. Lederer, A. Tünnermann, and T. Pertsch. Three-dimensional light bullets in arrays of waveguides. *Phys. Rev. Lett.*, 105:263901, Dec 2010.

[64] F. Eilenberger, K. Prater, S. Minardi, R. Geiss, U. Röpke, J. Kobelke, K. Schuster, H. Bartelt, S. Nolte, A. Tünnermann, and T. Pertsch. Observation of discrete, vortex light bullets. *Phys. Rev. X*, 3:041031, Dec 2013.

[65] K. Tai, A. Hasegawa, and N. Bekki. Fission of optical solitons induced by stimulated raman effect. *Opt. Lett.*, 13(5):392–394, May 1988.

[66] A. V. Husakou and J. Herrmann. Supercontinuum generation of higher-order solitons by fission in photonic crystal fibers. *Phys. Rev. Lett.*, 87:203901, Oct 2001.

[67] J. Herrmann, U. Griebner, N. Zhavoronkov, A. Husakou, D. Nickel, J. C. Knight, W. J. Wadsworth, P. St. J. Russell, and G. Korn. Experimental evidence for supercontinuum generation by fission of higher-order solitons in photonic fibers. *Phys. Rev. Lett.*, 88:173901, Apr 2002.

[68] G. P. Agrawal. Chapter 5 - optical solitons. In Govind Agrawal, editor, *Nonlinear Fiber Optics (Fifth Edition)*, Optics and Photonics, pages 129 – 191. Academic Press, Boston, fifth edition edition, 2013.

[69] V.E. Zakharov and L.A. Ostrovsky. Modulation instability: The beginning. *Phys. D: Nonlinear Phenom.*, 238(5):540 – 548, 2009.

[70] F. Copie, S. Randoux, and P. Suret. The physics of the one-dimensional nonlinear schródinger equation in fiber optics: Rogue waves, modulation instability and self-focusing phenomena. *Rev. Phys.*, 5:100037, 2020.

[71] G. P. Agrawal. Modulation instability in erbium-doped fiber amplifiers. *IEEE Photon. Technol. Lett.*, 4(6):562–564, 1992.

[72] S. Trillo and S. Wabnitz. Ultrashort pulse train generation through induced modulational polarization instability in a birefringent kerr-like medium. *J. Opt. Soc. Am. B*, 6(2):238–249, Feb 1989.

[73] J. M. Dudley, G. Genty, F. Dias, B. Kibler, and N. Akhmediev. Modulation instability, akhmediev breathers and continuous wave supercontinuum generation. *Opt. Express*, 17(24):21497–21508, Nov 2009.

[74] D. Y. Tang, J. Guo, Y. F. Song, G. D. Shao, L. M. Zhao, and D. Y. Shen. Temporal cavity soliton formation in an anomalous dispersion cavity fiber laser. *J. Opt. Soc. Am. B*, 31(12):3050–3056, Dec 2014.

[75] G. Ghosh, M. Endo, and T. Iwasaki. Temperature-dependent sellmeier coefficients and chromatic dispersions for some optical fiber glasses. *J. Lightwave Technol.*, 12(8):1338–1342, 1994.

[76] R. Buczynski, H.T. Bookey, D. Pysz, R. Stepien, I. Kujawa, J.E. McCarthy, A.J. Waddie, A.K. Kar, and M.R. Taghizadeh. Supercontinuum generation up to 2.5 µm in photonic crystal fiber made of lead-bismuth-galate glass. *Laser Phys. Lett.*, 7(9):666–672, 2010.

[77] J. Cimek, R. Stępień, G. Stępniewski, B. Siwicki, P. Stafiej, M. Klimczak, D. Pysz, and R. Buczyński. High contrast glasses for all-solid fibers fabrication. *Opt. Mater.*, 62:159–163, 2016.

[78] S. O. Kasap. Chapter 2 - dielectric waveguides and optical fibers. In *Optoelectronics & Photonics: Principles & Practices*, pages 95–178. Pearson, 2013.

[79] J. C. Knight, J. Arriaga, T. A. Birks, A. Ortigosa-Blanch, W. J. Wadsworth, and P. S. J. Russell. Anomalous dispersion in photonic crystal fiber. *IEEE Photon. Technol. Lett.*, 12(7):807–809, 2000.

[80] S. Afshar V. and T. M. Monro. A full vectorial model for pulse propagation in emerging waveguides with subwavelength structures part i: Kerr nonlinearity. *Opt. Express*, 17(4):2298–2318, Feb 2009.

[81] I. D. Rukhlenko, M. Premaratne, and G. P. Agrawal. Effective mode area and its optimization in silicon-nanocrystal waveguides. *Opt. Lett.*, 37(12):2295–2297, Jun 2012.

[82] C. Finot, F. Chaussard, and S. Boscolo. Simple guidelines to predict self-phase modulation patterns. *J. Opt. Soc. Am. B*, 35(12):3143–3152, Dec 2018.

[83] S. Boscolo, F. Chaussard, E. Andresen, H. Rigneault, and C. Finot. Impact of initial pulse shape on the nonlinear spectral compression in optical fibre. *Opt. Laser Technol.*, 99:301 – 309, 2018.

[84] S. Boscolo, F. Audo, and C. Finot. Impact of initial pulse characteristics on the mitigation of self-phase modulation by sinusoidally time varying phase. *Opt. Quant. Electron.*, 50(62), 2018.

[85] G. Pu, L. Yi, L. Zhang, C. Luo, Z. Li, and W. Hu. Intelligent control of mode-locked femtosecond pulses by time-stretch-assisted real-time spectral analysis. *Light Sci App*, 9(13), 2020.

[86] M. C. Phan Huy, A. Baron, S. Lebrun, R. Frey, and P. Delaye. Characterization of self-phase modulation in liquid filled hollow core photonic bandgap fibers. *J. Opt. Soc. Am. B*, 27(9):1886–1893, Sep 2010.

[87] S. Trillo and S. Wabnitz. Dynamics of the nonlinear modulational instability in optical fibers. *Opt. Lett.*, 16(13):986–988, Jul 1991.

[88] M. Alem, M. A. Soto, and L. Thévenaz. Analytical model and experimental verification of the critical power for modulation instability in optical fibers. *Opt. Express*, 23(23):29514–29532, Nov 2015.

[89] M. Remoissenet. Solitons and modulational instability. *Ann. Télécommun.*, 51:297–303, 1996.

[90] Z.-Z. Lan, Y.-T. Gao, J.-W. Yang, C.-Q. Su, C. Zhao, and Z. Gao. Solitons and bäcklund transformation for a generalized (3+1)-dimensional variable-coefficient b-type kadomtsev-petviashvili equation in fluid dynamics. *Appl. Math. Lett.*, 60:96 – 100, 2016.

[91] M. Peccianti and G. Assanto. Nematicons. *Phys. Rep.*, 516(4):147 – 208, 2012. Nematicons.

[92] M. Borghesi, S. Bulanov, D. H. Campbell, R. J. Clarke, T. Zh. Esirkepov, M. Galimberti, L. A. Gizzi, A. J. MacKinnon, N. M. Naumova, F. Pegoraro, H. Ruhl, A. Schiavi, and O. Willi. Macroscopic evidence of soliton formation in multiterawatt laser-plasma interaction. *Phys. Rev. Lett.*, 88:135002, Mar 2002.

[93] D. Farina and S. V. Bulanov. Dynamics of relativistic solitons. *Plasma Phys. Control. Fusion*, 47:A73, 2005.

[94] J. C. Eilbeck, J. D. Gibbon, P. J. Caudrey, and R. K. Bullough. Solitons in nonlinear optics. i. a more accurate description of the 2π pulse in self-induced transparency. *J. Phys. A: Math. Nucl. Gen.*, 6(1337), 1973.

[95] Y. S. Kivshar. Dark solitons in nonlinear optics. *IEEE J. Quantum Electron.*, 29(1):250–264, 1993.

[96] A. V. Buryak and Y. S. Kivshar. Solitons due to second harmonic generation. *Phys. Lett. A*, 197(5):407 – 412, 1995.

[97] W. Yu, Q. Zhou, M. Mirzazadeh, W. Liu, and A. Biswas. Phase shift, amplification, oscillation and attenuation of solitons in nonlinear optics. *J. Adv. Res.*, 15:69 – 76, 2019.

[98] X.-M. Wang and X.-X. Hu. Interactions among periodic optical solitons for the variable coefficient coupled nonlinear schrödinger equations. *Optik*, 226:165621, 2021.

[99] W. Krolikowski, O. Bang, J. J. Rasmussen, and J. Wyller. Modulational instability in nonlocal nonlinear kerr media. *Phys. Rev. E*, 64:016612, Jun 2001.

[100] W. Królikowski and O. Bang. Solitons in nonlocal nonlinear media: Exact solutions. *Phys. Rev. E*, 63:016610, Dec 2000.

[101] W Królikowski, O. Bang, N. I. Nikolov, D. Neshev, J. Wyller, J. J. Rasmussen, and D. Edmundson. Modulational instability, solitons and beam propagation in spatially nonlocal nonlinear media. *J. Opt. B: Quantum Semiclass. Opt.*, 6:S288, 2004.

[102] A. W. Snyder, D. J. Mitchell, L. Poladian, and F. Ladouceur. Self-induced optical fibers: spatial solitary waves. *Opt. Lett.*, 16(1):21–23, Jan 1991.

[103] T. Colin. On the standing wave solutions to a nonlocal, nonlinear schrödinger equation occurring in plasma physics. *Phys. D: Nonlinear Phenom.*, 64(1):215 – 236, 1993.

[104] A. Hasegawa and F. Tappert. Transmission of stationary nonlinear optical pulses in dispersive dielectric fibers. i. anomalous dispersion. *Appl. Phys. Lett.*, 23(3):142–144, 1973.

[105] L. F. Mollenauer, R. H. Stolen, and J. P. Gordon. Experimental observation of picosecond pulse narrowing and solitons in optical fibers. *Phys. Rev. Lett.*, 45:1095–1098, Sep 1980.

[106] B. A. Malomed, D. Mihalache, F. Wise, and L. Torner. Spatiotemporal optical solitons. *J. Opt. B: Quantum Semiclass. Opt.*, 7(5):R53–R72, Apr 2005.

[107] F. D. Tappert and N. J. Zabusky. Gradient-induced fission of solitons. *Phys. Rev. Lett.*, 27:1774–1776, Dec 1971.

[108] Hermann A. Haus and William S. Wong. Solitons in optical communications. *Rev. Mod. Phys.*, 68:423–444, Apr 1996.

[109] F. Mitschke. Chapter 5 - a brief history of fiber-optic soliton transmission. In Gang-Ding Peng, editor, *Handbook of Optical Fibers*, Optics and Photonics. Springer Singapore, 2019.

[110] C.-L. Chen. Chapter 14 - optical solitons in optical fibers. In *Foundations for Guided-Wave Optics*, pages 390 – 391. John Wiley & Sons, 2006.

[111] Q. Li and Z. Cheng. Single mode fibers for two stage higher-order soliton compression. *Opt. Fiber Technol.*, 38:24 – 29, 2017.

[112] A. Hasegawa and Y. Kodama. Amplification and reshaping of optical solitons in a glass fiber—i. *Opt. Lett.*, 7(6):285–287, Jun 1982.

[113] P. A. Wai and W. Cao. Ultrashort soliton generation through higher-order soliton compression in a nonlinear optical loop mirror constructed from dispersion-decreasing fiber. *J. Opti. Soc. Am. B*, 20:1346–1355, 2003.

[114] A. N. Ghosh, M. Meneghetti, C. R. Petersen, O. Bang, L. Brilland, S. Venck, J. Troles, J. M. Dudley, and T. Sylvestre. Chalcogenide-glass polarization-maintaining photonic crystal fiber for mid-infrared supercontinuum generation. *J. Phys. Photonics*, 1(4):044003, Sep 2019.

[115] A. W. Snyder and J. D. Love. *Material absorption*, pages 120–133. Springer US, Boston, MA, 1983.

[116] D. J. Kaup. A perturbation expansion for the zakharov-shabat inverse scattering transform. *SIAM J. Appl. Math.*, 31(1):121–133, 1976.

[117] P. K. A. Wai, C. R. Menyuk, Y. C. Lee, and H. H. Chen. Nonlinear pulse propagation in the neighborhood of the zero-dispersion wavelength of monomode optical fibers. *Opt. Lett.*, 11(7):464–466, Jul 1986.

[118] S. V. Gurevich, C. Schelte, and J. Javaloyes. Impact of high-order effects on soliton explosions in the complex cubic-quintic ginzburg-landau equation. *Phys. Rev. A*, 99:061803, Jun 2019.

[119] S. Roy, M. Santagiustina, P. Colman, S. Combrie, and A. De Rossi. Modeling the dispersion of the nonlinearity in slow mode photonic crystal waveguides. *IEEE Photonics J.*, 4(1):224–233, 2012.

[120] A. Höök and M. Karlsson. Ultrashort solitons at the minimum-dispersion wavelength: effects of fourth-order dispersion. *Opt. Lett.*, 18(17):1388–1390, Sep 1993.

[121] N. Akhmediev and M. Karlsson. Cherenkov radiation emitted by solitons in optical fibers. *Phys. Rev. A*, 51:2602–2607, Mar 1995.

[122] T. P. Horikis and J. N. Elgin. Soliton radiation in an optical fiber. *J. Opt. Soc. Am. B*, 18(7):913–918, Jul 2001.

[123] A.B. Shabat V.E. Zakharov. Interaction between solitons in a stable medium. *J. Exp. Theor. Phys.*, 37(5):823, Nov 1973.

[124] F. Mitschke, C. Mahnke, and A. Hause. Soliton content of fiber-optic light pulses. *Appl. Sci.*, 7(6), 2017.

[125] J. Satsuma and N. Yajima. B. Initial Value Problems of One-Dimensional Self-Modulation of Nonlinear Waves in Dispersive Media. *Prog. Theor. Phys. Supplement*, 55:284–306, 01 1974.

[126] Q. Li and Z. Cheng. Cascaded photonic crystal fibers for three-stage soliton compression. *Appl. Opt.*, 55(31):8868–8875, Nov 2016.

[127] R. H. Stolen, Clinton Lee, and R. K. Jain. Development of the stimulated raman spectrum in single-mode silica fibers. *J. Opt. Soc. Am. B*, 1(4):652–657, Aug 1984.

[128] J. P. Gordon. Theory of the soliton self-frequency shift. *Opt. Lett.*, 11(10):662–664, Oct 1986.

[129] E. M. Dianov, A. I. Karasik, P. V. Mamyshev, A. M. Prokhorov, and V. N. Serkin. Stimulated-Raman conversion of multisoliton pulses in quartz optical fibers. *ŽÈTF, Pisma red.*, 41:242–244, March 1985.

[130] J. Santhanam and G. P. Agrawal. Raman-induced spectral shifts in optical fibers: general theory based on the moment method. *Opt. Commun.*, 222(1):413–420, 2003.

[131] K. J. Blow and D. Wood. Theoretical description of transient stimulated raman scattering in optical fibers. *IEEE J. Quantum Electron.*, 25(12):2665–2673, 1989.

[132] P. V. Mamyshev and S. V. Chernikov. Ultrashort-pulse propagation in optical fibers. *Opt. Lett.*, 15(19):1076–1078, Oct 1990.

[133] Q. Lin and G. P. Agrawal. Raman response function for silica fibers. *Opt. Lett.*, 31(21):3086–3088, Nov 2006.

[134] A.D. Boardman and G.S. Cooper. Nonlinear wave propagation in optical fibres. *Appl. Sci. Res.*, 41(6):333–343, 1984.

[135] S. M. Hernandez, J. Bonetti, N. Linale, D. F. Grosz, and P. I. Fierens. Soliton solutions and self-steepening in the photon-conserving nonlinear schrödinger equation. *Waves Random Complex Media*, pages 1–17, 2020, Advanced online publication.

[136] A. A. Voronin and A. M. Zheltikov. Soliton self-frequency shift decelerated by self-steepening. *Opt. Lett.*, 33(15):1723–1725, Aug 2008.

[137] J. R. de Oliveira, M. A. de Moura, J. M. Hickmann, and A. S. L. Gomes. Self-steepening of optical pulses in dispersive media. *J. Opt. Soc. Am. B*, 9(11):2025–2027, Nov 1992.

[138] T. Do Thanh, T. V. Nguyen, D. T. Bui, and V. Cao Long. Influence of self-steepening and higher dispersion effects on the propagation characteristics of solitons in optical fibers. *Comput. Methods Sci. Technol.*, 22(6):239–243, 2016.

[139] A. Demircan O. Melchert and A. Yulin. Multi-frequency radiation of dissipative solitons in optical fiber cavities. *Sci. Rep.*, 10:8849, 2020.

[140] I. Cristiani, R. Tediosi, L. Tartara, and V. Degiorgio. Dispersive wave generation by solitons in microstructured optical fibers. *Opt. Express*, 12(1):124–135, Jan 2004.

[141] W. Wang, H. Yang, P. Tang, C. Zhao, and J. Gao. Soliton trapping of dispersive waves in photonic crystal fiber with two zero dispersive wavelengths. *Opt. Express*, 21(9):11215–11226, May 2013.

[142] K. E. Webb, Y. Q. Xu, M. Erkintalo, and S. G. Murdoch. Generalized dispersive wave emission in nonlinear fiber optics. *Opt. Lett.*, 38(2):151–153, Jan 2013.

[143] Z. Deng and M. Zhang. Blue solitary waves from infrared continuous wave pumping of optical fibers. *Adv. Condens. Matter Phys.*, 2017:1268230, 2017.

[144] J. C. Travers. Blue solitary waves from infrared continuous wave pumping of optical fibers. *Opt. Express*, 17(3):1502–1507, Feb 2009.

[145] D. V. Skryabin and A. V. Yulin. Theory of generation of new frequencies by mixing of solitons and dispersive waves in optical fibers. *Phys. Rev. E*, 72:016619, Jul 2005.

[146] S. Kedenburg, T. Steinle, F. Mörz, A. Steinmann, D. Nguyen, D. Rhonehouse, J. Zong, A. Chavez-Pirson, and H. Giessen. Solitonic supercontinuum of femtosecond mid-ir pulses in w-type index tellurite fibers with two zero dispersion wavelengths. *APL Photonics*, 1:086101, 2016.

[147] C. Liu, E. J. Rees, T. Laurila, S. Jian, and C. F. Kaminski. Periodic interactions between solitons and dispersive waves during the generation of non-coherent supercontinuum radiation. *Opt. Express*, 20(6):6316–6324, Mar 2012.

[148] X. Yi, Q. F. Yang, and X. Zhang. Single-mode dispersive waves and soliton microcomb dynamics. *Nat. Commun.*, 8:14689, 2017.

[149] A. Kudlinski, A. Mussot, M. Conforti, and D. V. Skryabin. *Emission of Dispersive Waves from Solitons in Axially Varying Optical Fibers*, pages 1–16. Springer Singapore, Singapore, 2017.

[150] D. R. Austin, C. Martijn de Sterke, B. J. Eggleton, and T. G. Brown. Dispersive wave blue-shift in supercontinuum generation. *Opt. Express*, 14(25):11997–12007, Dec 2006.

[151] M. Erkintalo, Y. Q. Xu, S. G. Murdoch, J. M. Dudley, and G. Genty. Cascaded phase matching and nonlinear symmetry breaking in fiber frequency combs. *Phys. Rev. Lett.*, 109:223904, Nov 2012.

[152] A. V. Cherenkov, V. E. Lobanov, and M. L. Gorodetsky. Dissipative kerr solitons and cherenkov radiation in optical microresonators with third-order dispersion. *Phys. Rev. A*, 95:033810, Mar 2017.

[153] A.V. Gorbach, D.V. Skryabin, J.M. Stone, and J.C. Knight. Four-wave mixing of solitons with radiation and quasi-nondispersive wave packets at the short-wavelength edge of a supercontinuum. *Opt. Express*, 14(21):9854–9863, Oct 2006.

[154] F. Biancalana, D. V. Skryabin, and A. V. Yulin. Theory of the soliton self-frequency shift compensation by the resonant radiation in photonic crystal fibers. *Phys. Rev. E*, 70:016615, Jul 2004.

[155] G. Genty, M. Lehtonen, H. Ludvigsen, J. Broeng, and M. Kaivola. Spectral broadening of femtosecond pulses into continuum radiation in microstructured fibers. *Opt. Express*, 10(20):1083–1098, Oct 2002.

[156] Skryabin D. Gorbach A. Light trapping in gravity-like potentials and expansion of supercontinuum spectra in photonic-crystal fibres. *Nat. Photonics*, 1:653–657, 2007.

[157] H. Yang, B. Wang, N. Chen, X. Tong, and S. Zhao. The impact of self-steepening effect on soliton trapping in photonic crystal fibers. *Opt. Commun.*, 359:20–25, 2016.

[158] Y. Silberberg. Solitons and two-photon absorption. *Opt. Lett.*, 15(18):1005–1007, Sep 1990.

[159] M. R. E. Lamont, M. Rochette, D. J. Moss, and B. J. Eggleton. Two-photon absorption effects on self-phase-modulation-based 2r optical regeneration. *IEEE Photon. Technol. Lett.*, 18(10):1185–1187, 2006.

[160] I. S. Maksymov, L. F. Marsal, and J. Pallarès. Modeling of two-photon absorption in nonlinear photonic crystal all-optical switch. *Opt. Commun.*, 269(1):137–141, 2007.

[161] J. M. Fang and M. J. Potasek. Optical switching in the presence of two-photon absorption for a nonlinear directional coupler. *Phys. Rev. A*, 45:5305–5307, Apr 1992.

[162] V. Mizrahi, K. W. DeLong, G. I. Stegeman, M. A. Saifi, and M. J. Andrejco. Two-photon absorption as a limitation to all-optical switching. *Opt. Lett.*, 14(20):1140–1142, Oct 1989.

[163] M. A. Farahani and T. Gogolla. Spontaneous raman scattering in optical fibers with modulated probe light for distributed temperature raman remote sensing. *J. Lightwave Technol.*, 17(8):1379, Aug 1999.

[164] G. Bolognini, J. Park, M. A. Soto, N. Park, and F. Di Pasquale. Analysis of distributed temperature sensing based on raman scattering using otdr coding and discrete raman amplification. *Meas. Sci. Technol.*, 28(10):3211, 2007.

[165] Y. Muanenda, C. J. Oton, and F. Di Pasquale. Application of raman and brillouin scattering phenomena in distributed optical fiber sensing. *Front. Phys.*, 7:155, 2019.

[166] T. Ferreira da Silva, G. B. Xavier, G. P. Temporão, and J. P. von der Weid. Impact of raman scattered noise from multiple telecom channels on fiber-optic quantum key distribution systems. *J. Lightwave Technol.*, 32(13):2332–2339, 2014.

[167] T. Hirooka, S. Ono, K. Hagiuda, and M. Nakazawa. Stimulated brillouin scattering in dispersion-decreasing fiber with ultrahigh-speed femtosecond soliton pulse compression. *Opt. Lett.*, 30(4):364–366, Feb 2005.

[168] M. Koyš. *Supercontinuum generation in dual-core photonic crystal fiber*. PhD thesis, Faculty of Mathematics, Physics and Informatics - Comenius University in Bratislava, 2010.

[169] D. Krylov, L. Leng, K. Bergman, J. C. Bronski, and J. N. Kutz. Observation of the breakup of a prechirped n-soliton in an optical fiber. *Opt. Lett.*, 24(17):1191–1193, Sep 1999.

[170] S. R. Friberg and K. W. DeLong. Breakup of bound higher-order solitons. *Opt. Lett.*, 17(14):979–981, Jul 1992.

[171] Y. Kodama and A. Hasegawa. Nonlinear pulse propagation in a monomode dielectric guide. *IEEE J. Quantum Electron.*, 23(5):510–524, 1987.

[172] P. L. François. Nonlinear propagation of ultrashort pulses in optical fibers: total field formulation in the frequency domain. *J. Opt. Soc. Am. B*, 8(2):276–293, Feb 1991.

[173] F. Poletti and P. Horak. Description of ultrashort pulse propagation in multimode optical fibers. *J. Opt. Soc. Am. B*, 25(10):1645–1654, Oct 2008.

[174] T. Brabec and F. Krausz. Nonlinear optical pulse propagation in the single-cycle regime. *Phys. Rev. Lett.*, 78:3282–3285, Apr 1997.

[175] N. Karasawa. Computer simulations of nonlinear propagation of an optical pulse using a finite-difference in the frequency-domain method. *IEEE J. Quantum Electron.*, 38(6):626–629, 2002.

[176] G. Chang, T. B. Norris, and H. G. Winful. Optimization of supercontinuum generation in photonic crystal fibers for pulse compression. *Opt. Lett.*, 28(7):546–548, Apr 2003.

[177] J. R. Salgueiro and Y. S. Kivshar. Nonlinear dual-core photonic crystal fiber couplers. *Opt. Lett.*, 30(14):1858–1860, Jul 2005.

[178] S. Jensen. The nonlinear coherent coupler. *IEEE J. Quantum Electron.*, 18(10):1580–1583, 1982.

[179] M. Pu, N. Yao, C. Hu, X. Xin, Z. Zhao, C. Wang, and X. Luo. Directional coupler and nonlinear mach-zehnder interferometer based on metal-insulator-metal plasmonic waveguide. *Opt. Express*, 18(20):21030–21037, Sep 2010.

[180] A. Villeneuve, C. C. Yang, P. G. J. Wigley, G. I. Stegeman, J. S. Aitchison, and C. N. Ironside. Ultrafast all-optical switching in semiconductor nonlinear directional couplers at half the band gap. *Appl. Phys. Lett.*, 61(2):147–149, 1992.

[181] F. Cuesta-Soto, A. Martínez, J. García, F. Ramos, P. Sanchis, J. Blasco, and J. Martí. All-optical switching structure based on a photonic crystal directional coupler. *Opt. Express*, 12(1):161–167, Jan 2004.

[182] M. Danaie and H. Kaatuzian. Improvement of power coupling in a nonlinear photonic crystal directional coupler switch. *Photonics Nanostructures: Fundam. Appl.*, 9(1):70–81, 2011.

[183] P. B. Hansen, A. Kloch, T. Aakjer, and T. Rasmussen. Switching power reduction in asymmetrically designed nonlinear directional couplers. *Opt. Commun.*, 119(1):178–182, 1995.

[184] B. A. Malomed, I. M. Skinner, P. L. Chu, and G. D. Peng. Symmetric and asymmetric solitons in twin-core nonlinear optical fibers. *Phys. Rev. E*, 53:4084–4091, Apr 1996.

[185] Y. Gao and I. Shadrivov. Nonlinear coupling in graphene-coated nanowires. *Sci. Rep.*, 6(12):38924, 2016.

[186] M. A. Karpierz, T. R. Woliński, and M. Świllo. All-optical switching in a liquid crystalline directional coupler. *Mol. Cryst. Liq. Cryst. Sci. Technol. Sec. A. Mol. Cryst. Liq. Cryst.*, 282(1):365–372, 1996.

[187] J. Wilson, G. I. Stegeman, and E. M. Wright. Soliton switching in an erbium-doped nonlinear fiber coupler. *Opt. Lett.*, 16(21):1653–1655, Nov 1991.

[188] P. L. Chu and B. Wu. Optical switching in twin-core erbium-doped fibers. *Opt. Lett.*, 17(4):255–257, Feb 1992.

[189] S. Zhang and T. Tamir. Rigorous analysis of power transfer in grating-assisted couplers. *Opt. Lett.*, 20(7):803–805, Apr 1995.

[190] Y. Chen and A. W. Snyder. Grating-assisted couplers. *Opt. Lett.*, 16(4):217–219, Feb 1991.

[191] P. Peterka and J. Kanka. Erbium-doped twin-core fibre narrow-band filter for fibre lasers. *Opt. Quantum Electron.*, 33:571–581, 2001.

[192] E. Weinert-Rączka. Optically induced grating in a directional coupler. *J. Opt. Soc. Am. B*, 11(12):2340–2346, Dec 1994.

[193] F. Setzpfandt, A. S. Solntsev, J. Titchener, C. W. Wu, C. Xiong, R. Schiek, T. Pertsch, D. N. Neshev, and A. A. Sukhorukov. Tunable generation of entangled photons in a nonlinear directional coupler. *Laser Photonics Rev.*, 10(1):131–136, 2016.

[194] G. P. Agrawal. Chapter 2 - fiber couplers. In *Applications of Nonlinear Fiber Optics (Second Edition)*, pages 54–99. Academic Press, Burlington, second edition edition, 2008.

[195] S. V. Manakov. On the theory of two-dimensional stationary self-focusing of electromagnetic waves. *Sov. J. Exp. Theor. Phys.*, 38:248–253, 1974.

[196] Allan W. Snyder. Coupled-mode theory for optical fibers. *J. Opt. Soc. Am.*, 62(11):1267–1277, Nov 1972.

[197] D. Marcuse. Coupled mode theory of round optical fibers. *Bell Syst. Techn. J.*, 52(6):817–842, 1973.

[198] K. S. Chiang. Propagation of short optical pulses in directional couplers with kerr nonlinearity. *J. Opt. Soc. Am. B*, 14(6):1437–1443, Jun 1997.

[199] D. Gloge. Weakly guiding fibers. *Appl. Opt.*, 10(10):2252–2258, Oct 1971.

[200] C.-M. Chen and P. L. Kelley. Nonlinear pulse compression in optical fibers: scaling laws and numerical analysis. *J. Opt. Soc. Am. B*, 19(9):1961–1967, Sep 2002.

[201] C. Xia, N. Bai, I. Ozdur, X. Zhou, and G. Li. Supermodes for optical transmission. *Opt. Express*, 19(17):16653–16664, Aug 2011.

[202] L. Szostkiewicz, M. Napierala, A. Ziolowicz, A. Pytel, T. Tenderenda, and T. Nasilowski. Cross talk analysis in multicore optical fibers by supermode theory. *Opt. Lett.*, 41(16):3759–3762, Aug 2016.

[203] L. Zhang and C. Yang. Polarization-dependent coupling in twin-core photonic crystal fibers. *J. Lightwave Technol.*, 22(5):1367–1373, 2004.

[204] L. Zhang and Ch. Yang. A novel polarization splitter based on the photonic crystal fiber with nonidentical dual cores. *IEEE Photon. Technol. Lett.*, 16(7):1670–1672, 2004.

[205] Z. Lu, Y. Wang, F. Zhang, N. A. F. Jaeger, and L. Chrostowski. Wideband silicon photonic polarization beamsplitter based on point-symmetric cascaded broadband couplers. *Opt. Express*, 23(23):29413–29422, Nov 2015.

[206] P.D. Drummond, T.A.B. Kennedy, J.M. Dudley, R. Leonhardt, and J.D. Harvey. Cross-phase modulational instability in high-birefringence fibers. *Opt. Commun.*, 78(2):137–142, 1990.

[207] M. N. Islam, L. F. Mollenauer, R. H. Stolen, J. R. Simpson, and H. T. Shang. Cross-phase modulation in optical fibers. *Opt. Lett.*, 12(8):625–627, Aug 1987.

[208] Y. S. Kivshar and M. L. Quiroga-Teixeiro. Influence of cross-phase modulation on soliton switching in nonlinear optical fibers. *Opt. Lett.*, 18(12):980–982, Jun 1993.

[209] A. D. Boardman, A. Shivarova, S. Tanev, and D. Zyapkov. Nonlinear coefficients and the effective area of cross-phase modulation coupling of lp01 optical fibre modes. *J. Mod. Opt.*, 42(11):2361–2371, 1995.

[210] K. Zegadlo, V. H. Nguyen, A. Ramaniuk, M. Trippenbach, and B. Malomed. Symmetry breakings in dual-core systems with double-spot localization of nonlinearity. *Symmetry*, 10(5):156, May 2018.

[211] D. D. Gusovskiǐ, E. M. Dianov, A. A. Maǐer, V. B. Neustruev, E. I. Shklovskiǐ, and I. A. Shcherbakov. Nonlinear light transfer in tunnel-coupled optical waveguides. *Sov. J. Quantum Electron.*, 15(11):1523–1526, 1985.

[212] S. Friberg, Y. Silberberg, M. K. Oliver, M. Andrejco, M. A. Saifi, and P. Smith. Ultrafast all-optical switching in a dual-core fiber nonlinear coupler. *Appl. Phys. Lett.*, 51:1135–1137, 1987.

[213] A. M. Weiner, Y. Silberberg, H. Fouckhardt, D. E. Leaird, M. A. Saifi, M. J. Andrejco, and P. W. Smith. Use of femtosecond square pulses to avoid pulse breakup in all-optical switching. *IEEE J. Quantum Electron.*, 25(12):2648–2655, 1989.

[214] A. M. Weiner, Y. Silberberg, H. Fouckhardt, D. E. Leaird, M. A. Saifi, M. J. Andrejco, and P. W. Smith. Use of femtosecond square pulses to avoid pulse breakup in all-optical switching. *IEEE J. Quantum Electron.*, 25(12):2648–2655, 1989.

[215] X. He, K. Xie, and A. Xiang. Optical solitons switching in asymmetric dual-core nonlinear fiber couplers. *Optik*, 122(14):1222–1224, 2011.

[216] A. W. Snyder and A. P. Sheppard. Collisions, steering, and guidance with spatial solitons. *Opt. Lett.*, 18(7):482–484, Apr 1993.

[217] M. Romagnoli, S. Trillo, and S. Wabnitz. Soliton switching in nonlinear couplers. *Opt. Quant. Electron.*, 24:S1237–S1267, 1992.

[218] G.I. Stegeman and E.M. Wright. Soliton switching in nonlinear couplers. *Opt. Quant. Electron.*, 22:95–122, 1990.

[219] M. Santagiustina, C. G. Someda, G. Vadalà, S. Combrié, and A. De Rossi. Theory of slow light enhanced four-wave mixing in photonic crystal waveguides. *Opt. Express*, 18(20):21024–21029, Sep 2010.

[220] M. Liu and Chiang K. S. Study of ultra-fast optical pulse propagation in a nonlinear directional coupler. *Appl. Phys. B*, 98:815–820, 2010.

[221] Y. Wang and W. Wang. Nonlinear optical pulse coupling dynamics. *J. Lightwave Technol.*, 24(6):2458, Jun 2006.

[222] A. K. Sarma. Vector soliton switching in a fiber nonlinear directional coupler. *Opt. Commun.*, 284(1):186–190, 2011.

[223] Y. Wang and W. Wang. Study of ultra-fast optical pulse propagation in a nonlinear directional coupler. *Appl. Phys. B*, 79(1):51–55, 2004.

[224] K. S. Chiang. Intermodal dispersion in two-core optical fibers. *Opt. Lett.*, 20(9):997–999, May 1995.

[225] K.S. Chiang, Y.T. Chow, D.J. Richardson, D. Taverner, L. Dong, L. Reekie, and K.M. Lo. Experimental demonstration of intermodal dispersion in a two-core optical fibre. *Opt. Commun.*, 143(4):189–192, 1997.

[226] L. F. Mollenauer, R. H. Stolen, J. P. Gordon, and W. J. Tomlinson. Extreme picosecond pulse narrowing by means of soliton effect in single-mode optical fibers. *Opt. Lett.*, 8(5):289–291, May 1983.

[227] A. Blanco-Redondo, C. Husko, D. Eades, Y. Zhang, J. Li, T. F. Krauss, and B. J. Eggleton. Observation of soliton compression in silicon photonic crystals. *Nat. Commun.*, 5:3160, 2014.

[228] K. C. Chan and H. F. Liu. Effect of third-order dispersion on soliton-effect pulse compression. *Opt. Lett.*, 19(1):49–51, Jan 1994.

[229] C. Ciret, S.-P. Gorza, C. Husko, G. Roelkens, B. Kuyken, and F. Leo. Physical origin of higher-order soliton fission in nanophotonic semiconductor waveguides. *Sci Rep*, 8:17177, May 2018.

[230] M. Zitelli, F. Mangini, M. Ferraro, A. Niang, D. Kharenko, and S. Wabnitz. High-energy soliton fission dynamics in multimode grin fiber. *Opt. Express*, 28(14):20473–20488, Jul 2020.

[231] S. Droulias, M. Manousakis, and K. Hizanidis. Switching dynamics in nonlinear directional fiber couplers with intermodal dispersion. *Opt. Commun.*, 240(1):209–219, 2004.

[232] K. S. Chiang. Coupled-mode equations for pulse switching in parallel waveguides. *IEEE J. Quantum Electron.*, 33(6):950–954, 1997.

[233] I. Bugar, I. V. Fedotov, A. B. Fedotov, M. Koys, R. Buczynski, D. Pysz, J. Chlpik, F. Uherek, and A. M. Zheltikov. Polarization-controlled dispersive wave redirection in dual-core photonic crystal fiber. *Laser Phys.*, 18:1420–1428, 2008.

[234] K. Nithyanandan, R. Vasantha Jayakantha Raja, and K. Porsezian. Modulational instability in a twin-core fiber with the effect of saturable nonlinear response and coupling coefficient dispersion. *Phys. Rev. A*, 87:043805, Apr 2013.

[235] W. H. Reeves, D. V. Skryabin, F. Biancalana, J. C. Knight, P. St. J. Russell, F. G. Omenetto, A. Efimov, and A. J. Taylor. Transformation and control of ultra-short pulses in dispersion-engineered photonic crystal fibres. *Nature*, 424:511–515, 2003.

[236] M. Mitchell and M. Segev. Self-trapping of incoherent white light. *Nature*, (387):880–883, May 1997.

[237] Z. Chen, M. Mitchell, M. Segev, T. H. Coskun, and D. N. Christodoulides. Self-trapping of dark incoherent light beams. *Science*, 280(5365):889–892, 1998.

[238] D. Song, C. Lou, L. Tang, X. Wang, W. L., X. Chen, K. J. H. Law, H. Susanto, P. G. Kevrekidis, J. Xu, and Z. Chen. Self-trapping of optical vortices in waveguide lattices with a self-defocusing nonlinearity. *Opt. Express*, 16(14):10110–10116, Jul 2008.

[239] A. B. Aceves, C. De Angelis, T. Peschel, R. Muschall, F. Lederer, S. Trillo, and S. Wabnitz. Discrete self-trapping, soliton interactions, and beam steering in nonlinear waveguide arrays. *Phys. Rev. E*, 53:1172–1189, Jan 1996.

[240] C. C. Yang. All-optical ultrafast logic gates that use asymmetric nonlinear directional couplers. *Opt. Lett.*, 16(21):1641–1643, Nov 1991.

[241] J. K. George and V. J. Sorger. Graphene-based solitons for spatial division multiplexed switching. *Opt. Lett.*, 42(4):787–790, Feb 2017.

[242] Hassid C. Gurgov and Oren Cohen. Spatiotemporal pulse-train solitons. *Opt. Express*, 17(9):7052–7058, Apr 2009.

[243] F. Lederer, G. I. Stegeman, D. N. Christodoulides, G. Assanto, M. Segev, and Y. Silberberg. Discrete solitons in optics. *Phys. Rep.*, 463(1):1–126, 2008.

[244] S. Raghavan and Govind P. Agrawal. Spatiotemporal solitons in inhomogeneous nonlinear media. *Opt. Commun.*, 180(4):377–382, 2000.

[245] P. Stajanča. *Broadband nonlinear steering of ultrafast solitons in dual-core photonic crystal fibers*. PhD thesis, Faculty of Mathematics, Physics and Informatics - Comenius University in Bratislava, 2016.

[246] Y. S. Kivshar. Switching dynamics of solitons in fiber directional couplers. *Opt. Lett.*, 18(1):7–9, Jan 1993.

[247] B.A. Malomed. Handbook of optical fibers. In *A variety of dynamical settings in dual-core nonlinear fibers*. Springer, Singapore, 2018.

[248] N. Munera and R. Acuna Herrera. Modelling a nonlinear optical switching in a standard photonic crystal fiber infiltrated with carbon disulfide. *Opt. Commun.*, 368:185–189, 2016.

[249] S. R. Vigil, Z. Zhou, B. K. Canfield, J. Tostenrude, and M. G. Kuzyk. Dual-core single-mode polymer fiber coupler. *J. Opt. Soc. Am. B*, 15(2):895–900, Feb 1998.

[250] D. Marchese, M. De Sario, A. Jha, A. K. Kar, and E. C. Smith. Highly nonlinear ges2-based chalcohalide glass for all-optical twin-core-fiber switching. *J. Opt. Soc. Am. B*, 15(9):2361–2370, Sep 1998.

[251] K. R. Khan and T. X. Wu. Short pulse propagation in wavelength selective index-guided photonic crystal fiber coupler. *IEEE J. Sel. Top. Quantum Electron.*, 14(3):752–757, 2008.

[252] K. Saitoh, M. Koshiba, T. Hasegawa, and E. Sasaoka. Chromatic dispersion control in photonic crystal fibers: application to ultra-flattened dispersion. *Opt. Express*, 11(8):843–852, Apr 2003.

[253] D. Pysz, I. Kujawa, R. Stępień, M. Klimczak, A. Filipkowski, M. Franczyk, L. Kociszewski, J. Buźniak, K. Haraśny, and R. Buczyński. Stack and draw fabrication of soft glass microstructured fiber optics. online, 2014.

[254] D. Lorenc, I. Bugar, M. Aranyosiova, R. Buczynski, D. Pysz, D. Velic, and D. Chorvat. Linear and nonlinear properties of multicomponent glass photonic crystal fibers. *Laser Phys.*, 18(11):270–276, 2008.

[255] X. Feng, T. M. Monro, P. Petropoulos, V. Finazzi, and D. Hewak. Solid microstructured optical fiber. *Opt. Express*, 11(18):2225–2230, Sep 2003.

[256] M. Klimczak, B. Siwicki, P. Skibiński, D. Pysz, R. Stępień, A. Heidt, C. Radzewicz, and R. Buczyński. Coherent supercontinuum generation up to 2.3 µm in all-solid soft-glass photonic crystal fibers with flat all-normal dispersion. *Opt. Express*, 22(15):18824–18832, Jul 2014.

[257] L. Wang, D. He, S. Feng, C. Yu, L. Hu, J. Qiu, and D. Chen. Yb/er co-doped phosphate all-solid single-mode photonic crystal fiber. *Sci Rep*, 4:6139, 2014.

[258] J. Zhao, Z. Wang, Y. Liu, and B. Liu. Switchable-multi-wavelength fiber laser based on dual-core all-solid photonic bandgap fiber. *Front. Optoelectron. China*, 3:283–288, 2010.

[259] J. Cimek, R. Stępień, M. Klimczak, I. Zalewska, and R. Buczyński. Development of thermally stable glass from sio2-bi2o3-pbo-zno-bao oxide system suitable for all-solid photonic crystal fibers. *Opt. Mater.*, 73:277–283, 2017.

[260] M. J. Pascual, A. Durán, and L. Pascual. Determination of the viscosity-temperature curve for glasses on the basis of fixed viscosity points determined by hot stage microscopy. *Phys. Chem. Glas.*, 2001.

[261] P. Hlubina. White-light spectral interferometry with the uncompensated michelson interferometer and the group refractive index dispersion in fused silica. *Opt. Commun.*, 193(1):1–7, 2001.

[262] B. Tatian. Fitting refractive-index data with the sellmeier dispersion formula. *Appl. Opt.*, 23(24):4477–4485, Dec 1984.

[263] J. Cimek, N. Liaros, S. Couris, R. Stępień, M. Klimczak, and R. Buczyński. Experimental investigation of the nonlinear refractive index of various soft glasses dedicated for development of nonlinear photonic crystal fibers. *Opt. Mater. Express*, 7(10):3471–3483, Oct 2017.

[264] K. S. Kim, R. H. Stolen, W. A. Reed, and K. W. Quoi. Measurement of the nonlinear index of silica-core and dispersion-shifted fibers. *Opt. Lett.*, 19(4):257–259, Feb 1994.

[265] J. Cimek. *Wieloskładnikowe szkła krzemianowe z wysoką zawartością tlenków metali ciężkich do zastosowań fotonicznych*. PhD thesis, Faculty of Physics, University of Warsaw, 2017.

[266] L. Curilla, I. Astrauskas, A. Pugzlys, P. Stajanca, D. Pysz, F. Uherek, A. Baltuska, and I. Bugar. Nonlinear performance of asymmetric coupler based on dual-core photonic crystal fiber: Towards sub-nanojoule solitonic ultrafast all-optical switching. *Opt. Fiber Technol.*, 42:39–49, 2018.

[267] A. Rueda, F. Sedlmeir, M. C. Collodo, U. Vogl, B. Stiller, G. Schunk, D. V. Strekalov, C. Marquardt, J. M. Fink, O. Painter, G. Leuchs, and H. G. L. Schwefel. Efficient microwave to optical photon conversion: an electro-optical realization. *Optica*, 3(6):597–604, Jun 2016.

[268] G. P. Agrawal. Effect of intrapulse stimulated raman scattering on soliton-effect pulse compression in optical fibers. *Opt. Lett.*, 15(4):224–226, Feb 1990.

[269] X. Gan, C. Zhao, Y. Wang, D. Mao, L. Fang, . Han, and J. Zhao. Graphene-assisted all-fiber phase shifter and switching. *Optica*, 2(5):468–471, May 2015.

[270] C. P. Lai, A. Naughton, P. Ossieur, C. Antony, D. W. Smith, A. Borghesani, D. G. Moodie, G. Maxwell, P. Healey, A. Poustie, and P. D. Townsend. Demonstration of error-free 25gb/s duobinary transmission using a colourless reflective integrated modulator. *Opt. Express*, 21(1):500–507, Jan 2013.

[271] K. Nozaki, T. Tanabe, A. Shinya, and S. Matsuo. Sub-femtojoule all-optical switching using a photonic-crystal nanocavity. *Nat. Photonics*, 4:477–483, 2010.

[272] Y. Tamura, H. Sakuma, K. Morita, M. Suzuki, Y. Yamamoto, K. Shimada, Y. Honma, K. Sohma, T. Fujii, and T. Hasegawa. The first 0.14-db/km loss optical fiber and its impact on submarine transmission. *J. Lightwave Technol.*, 36(1):44–49, 2018.

[273] P. J. Winzer, D. T. Neilson, and A. R. Chraplyvy. Fiber-optic transmission and networking: the previous 20 and the next 20 years [invited]. *Opt. Express*, 26(18):24190–24239, Sep 2018.

[274] Dominik Dobrakowski, Anupamaa Rampur, Grzegorz Stępniewski, Dariusz Pysz, Luming Zhao, Yuriy Stepanenko, Ryszard Buczyński, and Mariusz Klimczak. Femtosecond pulse delivery around 1560 nm in large-core inhibited-coupling fibers. *J. Opt. Soc. Am. B*, 36(11):3030–3038, Nov 2019.

[275] M. Liu and Ko S. Chiang. Propagation of ultrashort pulses in a nonlinear two-core photonic crystal fiber. *Appl. Phys. B*, 98:815–820, March 2010.

[276] D. J. Kaup, T. I. Lakoba, and B. A. Malomed. Asymmetric solitons in mismatched dual-core optical fibers. *J. Opt. Soc. Am. B*, 14(5):1199–1206, May 1997.

[277] A. Kumar and T. Kurz. Switching between bistable states of a soliton in a doubly inhomogeneously doped fiber coupler. *J. Opt. Soc. Am. B*, 18(7):897–900, Jul 2001.

[278] G. Soboń, T. Martynkien, K. Tarnowski, P. Mergo, and J. Sotor. Generation of sub-100 fs pulses tunable from 1700 to 2100 nm from a compact frequency-shifted er-fiber laser. *Photon. Res.*, 5(3):151–155, Jun 2017.

[279] J.-Y. Zhang, A. P. Shreenath, M. Kimmel, E.k Zeek, R. Trebino, and S. Link. Measurement of the intensity and phase of attojoule femtosecond light pulses using optical-parametric-amplification cross-correlation frequency-resolved optical gating. *Opt. Express*, 11(6):601–609, Mar 2003.

[280] Y. Lumer, Y. Plotnik, M. C. Rechtsman, and M. Segev. Nonlinearly induced pt transition in photonic systems. *Phys. Rev. Lett.*, 111:263901, Dec 2013.

[281] B.J. Ainslie. A review of the fabrication and properties of erbium-doped fibers for optical amplifiers. *J. Lightwave Technol.*, 9(2):220–227, 1991.

[282] L. Zhao and P. Shi. Machine learning assisted aggregation schemes for optical cross-connect in hybrid electrical/optical data center networks. *OSA Contin.*, 3(9):2573–2590, Sep 2020.

[283] G. S. Zervas, M. De Leenheer, L. Sadeghioon, D. Klonidis, Y. Qin, R. Nejabati, D. Simeonidou, C. Develder, B. Dhoedt, and P. Demeester. Multi-granular optical cross-connect: Design, analysis, and demonstration. *IEEE J. Opt. Commun. Netw.*, 1(1):69–84, 2009.

[284] Y.-K. Yeo, Z. Xu, D. Wang, J. Liu, Y. Wang, and T.-H. Cheng. High-speed optical switch fabrics with large port count. *Opt. Express*, 17(13):10990–10997, Jun 2009.

[285] D. Liu, S. Sun, X. Yin, B. Sun, J. Sun, Y. Liu, W. Li, N. Zhu, and M. Li. Large-capacity and low-loss integrated optical buffer. *Opt. Express*, 27(8):11585–11593, Apr 2019.

[286] S. Yan, E. Hugues-Salas, V. J. F. Rancaňo, Y. Shu, G. M. Saridis, B. Rahimzadeh Rofoee, Y. Yan, A. Peters, S. Jain, T. May-Smith, P. Petropoulos, D. J. Richardson, G. Zervas, and D. Simeonidou. Archon: A function programmable optical interconnect architecture for transparent intra and inter data center sdm/tdm/wdm networking. *J. Lightwave Technol.*, 33(8):1586–1595, 2015.

[287] J. Gao, E. Nazemosadat, Y. Yang, S. Fu, M. Tang, J. Schröder, M. Karlsson, and P. A. Andrekson. Elliptical-core highly nonlinear few-mode fiber based oxc for wdm-mdm networks. *IEEE J. Sel. Top. Quantum Electron.*, 27(2):1–11, 2021.

[288] A. S. Kewitsch. Large scale, all-fiber optical cross-connect switches for automated patch-panels. *J. Lightwave Technol.*, 27(15):3107–3115, 2009.

[289] R. C. Figueiredo, N. S. Ribeiro, A. M. Oliveira Ribeiro, C. M. Gallep, and E. Conforti. Hundred-picoseconds electro-optical switching with semiconductor optical amplifiers using multi-impulse step injection current. *J. Lightwave Technol.*, 33(1):69–77, 2015.

[290] Rodney S. Tucker. Green optical communications - part i: Energy limitations in transport. *IEEE J. Sel. Top. Quantum Electron.*, 17(2):245–260, 2011.

[291] O. Wada. Femtosecond all-optical devices for ultrafast communication and signal processing. *New J. Phys.*, 6:183, Nov. 2004.

[292] X. Zheng, F. Liu, D. Patil, H. Thacker, Y. Luo, T. Pinguet, A. Mekis, Ji. Y., G. Li, J. Shi, K. Raj, J. Lexau, E. Alon, R. Ho, J. E. Cunningham, and A. V. Krishnamoorthy. A sub-picojoule-per-bit cmos photonic receiver for densely integrated systems. *Opt. Express*, 18(1):204–211, Jan 2010.

[293] D. A. Sidorov-Biryukov, A. Fernandez, L. Zhu, A. Verhoef, P. Dombi, A. Pugzlys, E. E. Serebryannikov, A. M. Zheltikov, J. C. Knight, and A. Baltuška. Solitonic dynamics of ultrashort pulses in a highly nonlinear photonic-crystal fiber visualized by spectral interferometry. *Opt. Lett.*, 33(5):446–448, Mar 2008.